PROCEEDINGS

OF THE

KSEEE-JSAEM 2013 INTERNATIONAL ENGINEERING CONFERENCE

ON

4th-5th SEPTEMBER, 2013

AT

DEDAN KIMATHI UNIVERSITY OF TECHNOLOGY

NYERI, KENYA

SUPPORTED BY:

Kenya Society of Electrical & Electronic Engineeers

JSAEM The Japan Society of Applied Electromagnetics and Mechanics

Jomo Kenyatta University of Agriculture and Technology

Correspondence Address

KSEEE SECRETARIAT

P.O. BOX 62000 00200, Nairobi

Website: www.jkuat.ac.ke/schools/eeie

Email: ksee.jasem@gmail.com

A Stabilized Controllability of Selemion CMV-Based IPMC Actuators in the Extremely Low Humidity Environment

H. Ngetha[1], M. Sasaki[1*], H. Tamagawa[1], K. Ikeda[2] and S. Ito[1]

[1] Department of Mechanical Engineering, Faculty of Engineering, Gifu University, Gifu, 501-1193, Japan, E-Mails: s3812007@edu.gifu-u.ac.jp, satoshi@gifu-u.ac.jp, tmgwhrhs@gifu-u.ac.jp

[2] Graduate School of Advanced Mathematical Sciences, Meiji University, 4-21-1, Nakano, Nakano-ku, Tokyo 165-8525 Japan, E-Mails: ikeda@isc.meiji.ac.jp.

* Author to whom correspondence should be addressed; E-Mail: sasaki@gifu-u.ac.jp

Abstract

Selemion CMV-based IPMC (Ionic Polymer Metal Composite) actuators have numerous promising applications in designing autonomous moving structures. This paper presents the electric properties obtained from the analysis of circuit model of Selemion CMV-based IPMC. A circuit model had been proposed for deriving the time-dependent behavior of charge, which was caused by both Faradaic and non-Faradaic currents, passing through the IPMC. In the course of derivation, electrical properties of the IPMC were obtained and analyzed. It had been established that, the bending curvature of a Selemion CMV-based IPMC is basically proportional to the total charge imposed as a result of the applied voltage. This property is the basis of controllers for the Selemion CMV-based IPMC bending behavior. Bending curvature experiments were performed on Selemion CMV-based IPMCs, obtaining the actuator's dynamics and transfer function for controlling purposes of the Selemion CMV-based IPMC actuators in the extremely low humidity environment was computed and analyzed.

Keywords: IPMC, Selemion-CMV, control, electric circuit model, compensator

1. Introduction

Ionic Polymer-Metal Composite (IPMC) is a bending mode electroactive polymer actuator (also known as artificial muscles) and has built-in actuation and sensing capabilities. Its supple motion and soft body and electroactive nature make it strikingly similar to animal muscle [1-7]. Researchers consider IPMC a promising candidate for creating artificial muscle. An IPMC sample typically consists of a thin ion exchange membrane (e.g., Nafion, Selemion), chemically plated on both surfaces with a noble metal as electrode IPMC has been widely investigated for the purpose of fabricating a practical bending mode polymer-based actuator [1-6]. IPMC is electrically activated in highly hydrated state. So, the IPMC can be activated even in an aqueous solution unlike other type of actuators, and it is one of IPMCs' featuring facets. Despite intensive efforts made by a number of researchers toward the ultimate research goal of fabricating a practical bending mode actuator of IPMC, the research progress is stagnant these days. For the practical use of IPMC, the IPMC have to be able to generate higher force and have to exhibit more precisely controllable bending behavior

Selemion CMV-based IPMC is a type of IPMC, where Selemion CMV is an ion exchange membrane manufactured by Asahi glass Co., Ltd. (Tokyo). IPMCs are usually activated in a highly hydrated state even in an aqueous solution, and it is true for the Selemion CMV-based IPMC, too. However, its bending controllability is poor.

Previous research has shown that the bending controllability could be improved greatly by dehydration treatment [8-11]. Furthermore, the bending curvature of the dehydrated Selemion CMV-based IPMC is basically proportional to the total charge imposed on it, Owing to such a proportional

relationship between the curvature and charge, bending control of Selemion CMV-based IPMC by the control of charge imposed on it has been undertaken successfully [12].

In this work, we carried out computational analysis on the bending behavior of Selemion CMV-based IPMC and discussed its bending stability in the controlled bending state.

2. Preparation of Selemion CMV-based IPMC and measurements

A Selemion CMV-based IPMC was fabricated simply by coating a Selemion CMV surface with silver through the silver mirror reaction process. Its fabrication requires several steps. First, the surfaces of a Selemion CMV sheet are crazed and sandblasted to improve silver adhesion [13-15]. Silver is then deposited by the silver mirror reaction [16]. Because the bending controllability of Selemion CMV-based IPMC deteriorates when too much water is present, as a result from being submerged in an aqueous solution, for instance [8-11], the resultant Selemion CMV-based IPMC was dehydrated by storing it in a desiccator with desiccant, resulting in a highly dehydrated (not-completely dehydrated) Selemion CMV-based IPMC. It was then cut into a strips of 20 mm × 2 mm × 120 μm as illustrated in Figure 1 (hereafter the strip of the Selemion CMV-based IPMC is called CMV IPMC for short). Water, however, is essential for electrical activation, and CMV IPMC cannot bend without it. Thus, the CMV IPMC is to reabsorb a small amount of water by exposing them to the ambient air for 30 minutes prior to any experiment. Hence, the results described below were obtained using CMV IPMCs that were slightly hydrated. Hereafter we refer to "slightly hydrated CMV IPMC" as "dehydrated CMV IPMC".

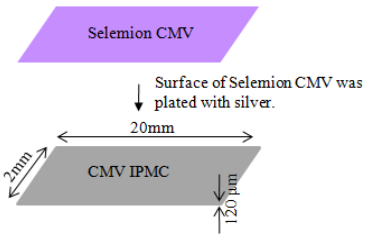

Figure 1 Structure and fabrication process of Selemion CMV IPMC.

The dehydrated CMV IPMC was horizontally clamped with a pair of electrodes as illustrated in Fig. 2 (a). Once the voltage is induced the CMV IPMC exhibits bending. Bending direction depends on the voltage polarity, and the CMV usually exhibits bending in the anode direction as illustrated in Fig. 2 (b).

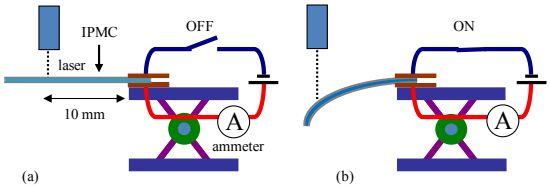

Figure 2 Experimental setup for measuring the tip displacement of CMV IPMC.

In order to see what happen to the CMV IPMC bending behavior under applied voltage, bending test in response to rectangular oscillating voltage was carried out using the setup illustrated in Fig. 2. Absolute humidity is a quite substantial factor in determining the bending behavior of IPMC in response to external electric stimulation. Hence, the test was carried out at a low absolute humidity $\sim 9\mathrm{gm}^{-3}$ [17], where the absolute humidity was monitored using a humidity sensor (Z2000, HIOKI Nagano, Japan) and a thermocouple (K type). The vertical displacement of CMV IPMC under the applied rectangular oscillating voltage was measured with the laser displacement sensor (LK-085, precision 3μm, K EYENCE, Osaka, Japan) (see Fig. 2), and the measured vertical displacement was later converted into bending curvature.

Figure 3 shows the time dependence of CMV IPMC (a) curvature and (b) current under rectangular oscillating voltage with the amplitude = 1.5 V and its frequency = 1/ 60 Hz.

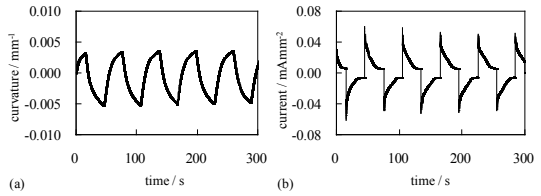

Figure 3 Experimentally obtained data of (a) bending curvature vs. time and (b) current per unit surface area vs. time about CMV IPMC

3. Computational IPMC bending analysis

To use the CMV IPMC as an actuator, it

is necessary to model it as system having the voltage as the input and bending or deformation as the output.

In this section, the bending behavior of CMV IPMC is analyzed computationally by employing a circuit model previously proposed by Ikeda et. al. [17], and the appropriateness of model is discussed.

3.1 Electrical circuit model

The following are the essential requirements for the circuit modeling of the CMV IPMC bending behavior according to the ref. [17].

a) The CMV IPMC can store a certain quantity of charge.
b) Basically change in the input current directly affects the bending curvature of CMV IPMC.
c) Effective redox reaction of $Ag \leftrightarrow Ag_2O$ is induced around at, or above 0.7 V of the applied voltage.
d) Below 0.7 V, the redox reaction is not induced effectively, but small current flows through the CMV IPMC. This current is quite small for an effective effect for the induction of CMV IPMC bending.
e) Discharge process also causes the redox reaction of $Ag \leftrightarrow Ag_2O$.

A circuit model, based on the above five requirements, was created as illustrated in Fig. 4. Explanation for the model is given below.

(i) Selemion CMV part of the CMV IPMC is approximated by a capacitor C_2 and a resistor R_3
(ii) The two silver layers on the surfaces of CMV IPMC are approximated by R_2
(iii) The charge storage in the capacitor C_2, induced by non-Faradaic current, is assumed to induce the CMV IPMC bending.
(iv) The current I_r, Faradaic current flowing through the resistor R_2, is hypothesized to cause the redox reaction, resulting in the induction of bending.
(v) It was hypothesized that the downward bending of CMV IPMC was induced, when $Q_2 > 0$ or $I_r > 0$, where Q_2 is the charge stored in C_2.
(vi) C_1 and R_1 are the path for the experimentally observed current causing ineffective bending of CMV IPMC below 0.7 V.

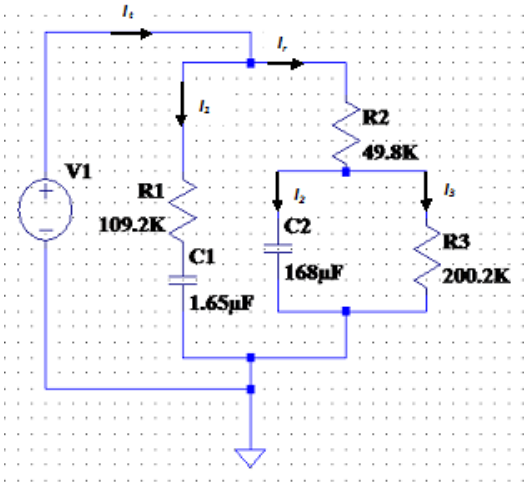

Figure 4, The CMV IPMC electric circuit model. All the numerical values for parameters are cited from the ref. [17].

3.2 The computational analysis

The experiment carried out for obtaining the data for Fig. 3 was considered and computational analysis was performed for it. For carrying out the analysis, all the parameter quantities in the circuit model should be given. Those parameter quantities are all given in the ref. [17]. Hence we use the for the computation.

Figure 5 shows the voltage imposed on the CMV IPMC vs. time. It is input for the computation.

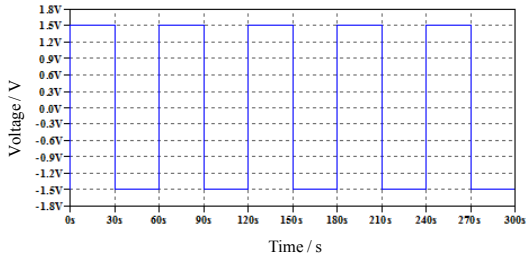

Figure 5. Voltage imposed on the CMV IPMC vs. .time

Figure 6 shows the computational result of total charge per unit surface area of CMV IPMC vs. time. It is output in response to the input voltage shown in Fig. 5. As described earlier the bending curvature is basically proportional to the total charge imposed on the CMV IPMC, the data curve of Fig. 6 is expected to be similar to that of Fig. 3 (a). Indeed significant similarity is seen between them. Figure 7 shows the computational result

of current per unit surface of CMV IPMC vs. time, where this current corresponds to I_t in Fig. 4. It is another output in response to the input voltage shown in Fig. 5.

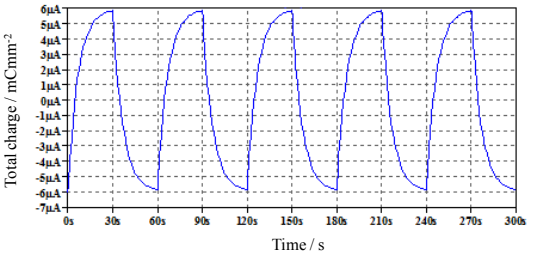

Figure 6 shows the computational result of total charge per unit surface of CMV IPMC vs. time.

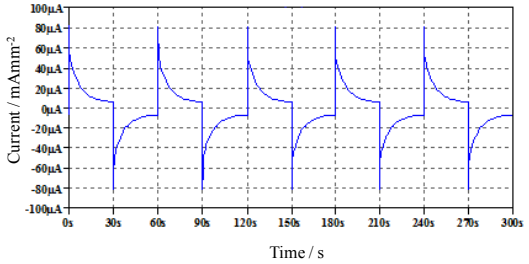

Figure 7. shows the computational result of current per unit surface of CMV IPMC vs. time, where this current corresponds to I_t in Fig. 4.

Since the computational results quantitatively well predict the characteristics of CMV IPMC, we could conclude the circuit model was appropriate as a model of CMV IPMC. Furthermore, we can say that prediction of CMV IPMC characteristics as a function of time, that is, prediction of dynamic behavior of CMV IPMC characteristics is quite successful particularly owing to considering the current as two types of currents, Faradaic and non-Faradaic currents, as the circuit model clearly suggests. .

4. Results and Discussions

Using the circuit model introduced earlier, the total current (I_t) given by Eq. (1) for the CMV IPMC was computed. The transfer function for the CMV IPMC was then derived. The derivation procedure is outlined below.

MATLAB software was used to derive the transfer function. The response of the CMV IPMC to the square waveform was simulated using LT Spice software.

$$I_{(t)} = \frac{Q_1}{\tau_1} e^{-(t/\tau_1)} + \frac{R_3C_2 - \tau_l}{\tau_2 R_3 C_2} Q_2 e^{-(t/\tau_2)} + \frac{Q_2}{R_3 C_2} \quad (1)$$

Where: $\tau_1 = r_1 Q_1$, $Q_1 = C_1 V$, $\tau_2 = \frac{C_2 r_2 R_3}{r_2 + R_3}$, $Q_2 = \frac{R_3}{r_2 + R_3} C_2 V$ (2)

Upon application of rectangular wave $(1.5V_p, 0.0167H_Z)$ to the Selemion CMV-based IPMC experimental set up, the following parameters were calculated from the measurements obtained.

$\tau_s/s = 0.18$, $\tau_l/s = 6.7$, $Q_s/(mCmm^{-2}) = 0.00247$, $Q_l/(mCmm^{-2}) = 0.202$, $C_s/(mFmm^{-2}) = 0.00165$, $C_l/(mFmm^{-2}) = 0.168$, $r_s/(K\Omega mm^{-2}) = 109.2$ $r_l/(K\Omega mm^{-2}) = 49.8$, $R/(K\Omega mm^{-2}) = 200.2$ (3)

Substituting (3) into (1) results in,

$$I_{(t)} = 13.722 * 10^{-6} e^{-(5.556t)} + 24.143 * 10^{-3} e^{-(0.149t)} + 6.006 * 10^{-3} \quad (4)$$

Using MATLAB software, the Transfer function of (4) was obtained as follows,

$$I_S = \frac{6958745971430777}{288230376151711744(S + {}^{149}/_{1000})} + \frac{4050019554871079}{29514790517935282856(S + {}^{1389}/_{250})} + \frac{6924446556668723}{11529215046068469765} \quad (5)$$

After simplification,

$$I_S = \frac{6.036 * 10^{-3}}{0.25(S + 0.149)} + \frac{3.513 * 10^{-3}}{256(S + 5.556)} + \frac{6.006 * 10^{-3}}{S} \quad (6)$$

$$I_S = \frac{24.144 * 10^{-3}}{S + 0.149} + \frac{13.723 * 10^{-6}}{S + 5.556} + \frac{6.006 * 10^{-3}}{S} \quad (7)$$

$$I_S = \frac{0.024144}{S + 0.149} + \frac{0.000013723}{S + 5.556} + \frac{0.006006}{S} \quad (8)$$

$$I_S = \frac{0.0302S^3 + 0.1443S^2 - 0.1292}{S^3 + 4.705S^2 - 4.8772S - 0.8278} \quad (9)$$

In this study, a model was built using the MATLAB. Using the simplified Transfer

function expression (9), the following results were obtained,

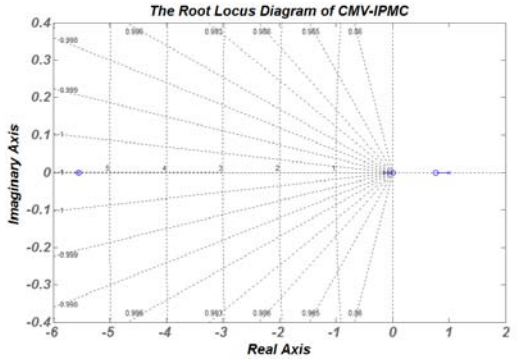

Figure 11a. The root locus diagram

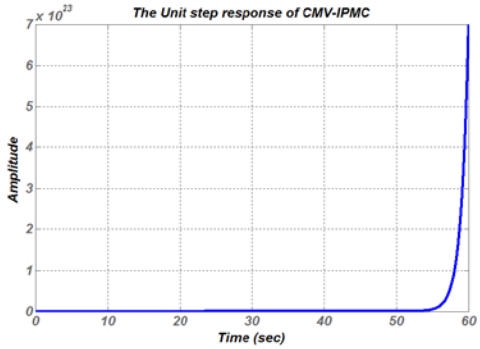

Figure 11b. The unit step response

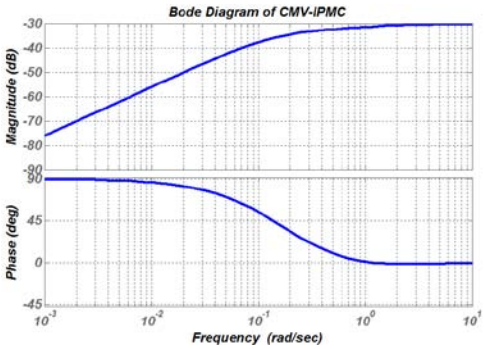

Figure 11c. The bode plot diagram

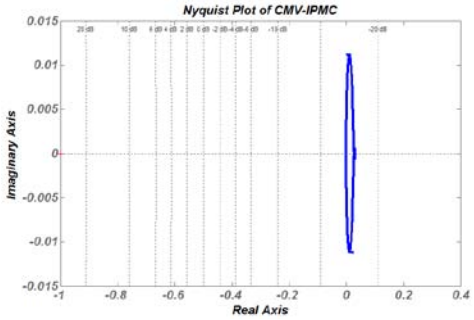

Figure 11d. The Nyquist root plot.

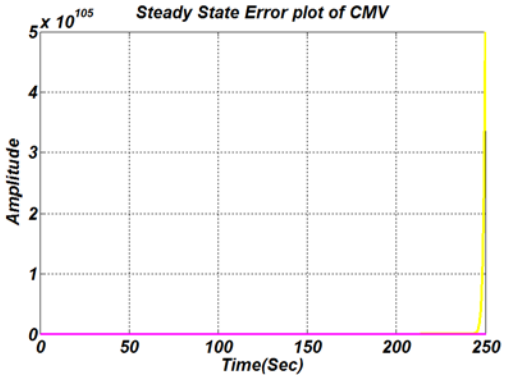

Figure 11e. The steady state error diagram.

The results obtained, indicated an unstable system. A Feedback Control system design using the SISO Design Tool was undertaken. The following are the results obtained.

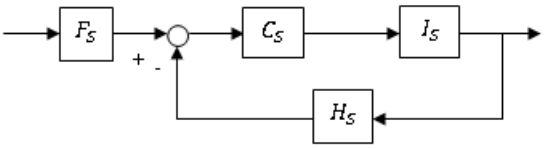

Figure 12 The Controlled CMV IPMC

The parameters:

Compensator, $C_S = \frac{79.047*10^{18}}{S+13}$

Impedance Filter, $F_S = 1$

Sensor, $H_S = 1$

After Control system design using SISO design tool, the resulting System Transfer function is given below

$$sysC_SL = C_S * I_S \qquad (10)$$

$$sysCL = \frac{2.387*10^{18}S^3+1.141*10^{18}S^2-1.021*10^{19}S}{S^4+17.7S^3+56.29S^2-64.23S-10.76} \qquad (11)$$

Using the derived System Transfer function expression (11), the following results were obtained, using the MATLAB.

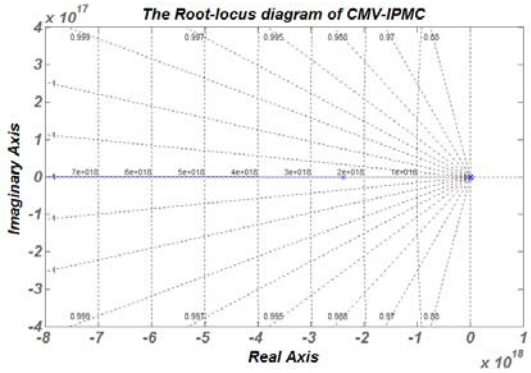

Figure 13a. The root locus diagram

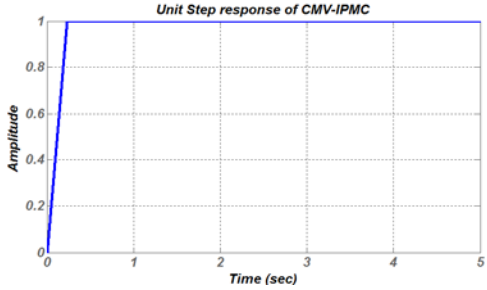

Figure 13b. The unit step response

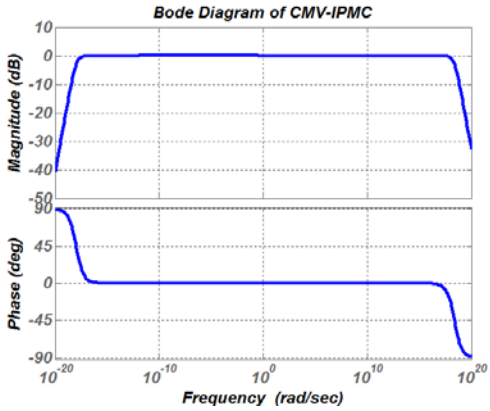

Figure 13c. The bode plot diagram

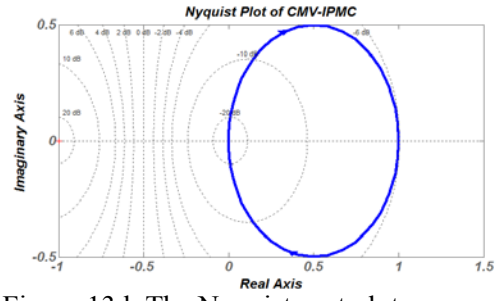

Figure 13d. The Nyquist root plot.

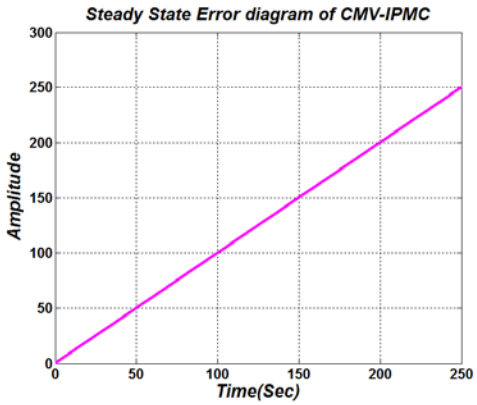

Figure 13e. The steady state error diagram.

The zeros (z) of the system are located at: 0, -5.5507, +0.7706. The poles (p) are at -12.9915, -5.5595, 1, -0.149. The gain, k = 2.387*10^018.

(For a zero steady-state error, $\lim_{S\to 0} sysCL(S) = \infty$, and for limit to be infinite, at least one pole must be at the origin ($S = 0$)).

The system has a pole in the right half –plane and thus unstable.

The time to peak is very short. Since final value is 0, the percent overshoot is infinity. This indicates a very fast response, since the rise time is zero.

The system also settles very fast since the rise time and the settling times are same.

Root locus plots illustrate how the closed loop poles of the system change as a system parameter is varied.

5. Conclusions

It was concluded that the dehydrated Selemion CMV-based IPMC exhibits linear relationship of curvature vs. charge in the extremely low absolute humidity environment. The simple linear relationship of curvature vs. charge enables a stability control of the Selemion CMV-based IPMC bending. The modeled CMV IPMC electrical circuit model conformed to the CMV IPMC under extremely low absolute humidity environment.

References and Notes

1. Oguro, K.; Kawami, Y.; Takenaka, H. Bending of an ion-conducting polymer film-electrode composite by an electric stimulus at low voltage, *Trans. J. Micromach. Soc.* **1992**, 5, 27-30.
2. Oguro, K.; Asaka K.; Takenaka, H. Polymer Film Actuator Driven by Low Voltage, *Proc. 4th International Symposium on Micro Machine and Human Science, Nagoya* **1993**, 39-40.
3. Asaka, K.; Oguro, K.; Nishimura, Y.; Mizuhara, M.; Takenaka, H. Bending of polyelectrolyte membrane-platinum composite by electric stimuli I, response characteristics to various waver forms *Polym. J.* **1995**, 27, 436-440.
4. Salehpoor, K.; Shahinpoor, M.; Mojarrad, M. Linear and Platform Type Robotic Actuators Made From Ion-Exchange Membrane-Metal Composites, San Diego, *Proc. SPIE Smart Mater. Struct.* **1997**, 3040 192-198.
5. Bar-Cohen, Y; Xue, T.; Shahinpoor, M.; Salehpoor, K.; Simpson, J.; Smith, J. Low-mass muscle actuators using electroactive polymers (EAP), *Proc. SPIE Smart Mater. Struct.* San Diego, **1998**, Paper-No. 3324-32.
6. Bar-Cohen, Y.; Leary, S.; Yavrouian, A.; Oguro, K.; Tadokoro, S.; Harrison, J.; Smith, J.; Su, J. Challenges to the transition IPMC Artificial Muscle actuators to practical application, *MRS Symposium Proceedings*, Boston, **1999**, 600, Document ID: 31295.
7. Dole, U.; Lumia, R.; Shahinpoor, M.; Bermudez, M. Design and test of IPMC artificial muscle microgripper, *J. Micro-Nano Mech.* **2008**, 4, 95-102.
8. Tamagawa, H.; Nogata, F. Bending response of dehydrated ion exchange polymer membranes to the applied voltage, *J. membrane Sci.* **2004,** 243, 229-234.
9. Tamagawa, H.; Nogata, F. Atomic structural change of silver-plating layers on the surfaces of Selemion, resulting in its excellent bending controllability, *Sens. Actuators B: Chemical* **2006**, 114, 781-787.
10. Tamagawa, H.; Nogata, F. Charge and water in need for the precise control of Selemion bending, *Sens. Actuators B: Chemical* **2007**, 121, 469-475.
11. Tamagawa, H.; Lin, W.; Kikuchi, K.; Sasaki, M. Bending control of Nafion-based electroactive polymer actuator coated with multi-walled carbon nanotubes, *Sens. Actuators B: Chemical* **2011**, 156, 375-382.
12. Sasaki, M.; Ozeki, T.; S. Ito, S.; Tamagawa, H. Position control of a dual-stage actuator, *Inter. J. Appl. Eletromagnetics and Mech.* **2010**, 33, 839-847.
13. Takeno, A.; Nakagaki, N.; Miwa, M. Anisotropic transparency of polystyrene film with crazes, *Adv. Composite Mater.* **1998**, 7, 35-46.
14. Noguchi, F.; Iwashige, Y.; Takeno, A.; Miwa, M. View field selective film of Mono-component polyester composites, *J. Advanced Science* **2001**, 13, 382-385.
15. Takeno, A.; Ozeki, T.; Miwa, M.; Yokoi, T. Periodic Micro-necking of Polyester Filament, *SEN'I GAKKAISHI* (in Japanese) **2007**, 63, 172-176.
16. Onouchi, Y.; Tamagawa, H.; Sasaki, M. Dependence of curvature of dehydrated Selemion on the total charge and environmental humidity, *Inter. J. Appl. Eletromagnetics and Mech.* **2009**, 17, 59-64.
17. Kota Ikeda, Minoru Sasaki, Hirohisa Tamagawa, "IPMC bending predicted by the circuit and viscoelastic models considering individual influence of Faradaic and non-Faradaic currents on the bending", submitted in Sensors and Actuators B: Chemical

Microcontroller Based Frequency Measurements in Isolated Generation using Magnetostrictive Amorphous Wire

C. K. Kitur[1], J. N. Nderu[2], A. M. Muhia[1], D. W. Juma[1]

[1]Dedan Kimathi University of Technology

[2]Jome Kenyatta University of Agriculture and Technology

ckitur@gmail.com

ABSTRACT

This paper presents load side power frequency measurement using magnetostrictive amorphous wire and a microcontroller. Frequency in power system is very important component that needs to be kept constant for high quality power supply however in a less rigid supply and in isolated system frequency changes with the load. Magnetostrictive amorphous wire (MAW) possess a unique property call large Barkhausen jump which results in spikes being induced every time there is reversal of magnetization. The spikes are picked by the pickup coil wound around the MAW and are amplified to appropriate level for Transistor-Transistor logic circuit. The amplified and conditioned signal is fed to a microcontroller for further processing and display. The displayed measurements are compared with other measurement method using power generation meter.

INTRODUCTION

Energy has been the main challenge hindering development especially in the rural areas the world over. Greater percentage is obtained from biomass which is the energy derived from organic or plant matter, which include energy stored in trees, grass crops, forestry waste, agricultural waste, urban waste amongst others [1], but it cannot be converted to electrical form easily. Electrical energy for use in electronic units is therefore obtained from batteries which are expensive. Lighting energy is obtained mainly from petroleum (which is fast getting depleted coupled with unpredictable international prices and pollution effects) fueled lantern and burning of wood fuel. This is in itself very unhygienic and produces serious pollutions and associated ailments. Proliferation electronic equipments like mobile phones and entertainment systems call for some source of energy which is cheaper and renewable. Hydro power is a proven technology that has been used over several centuries especially to electrify remote locations where utility power is well out of reach. In an Isolated power plant, the input power is nearly constant but the load to which the generator supply is continuously varying this causes variations in frequency and the generated voltage. Any increase in load causes a decrease in voltage and speed and hence the frequency of generated voltage. Similarly, a decrease in load causes an

increase in speed hence frequency and voltage as can be deduced from the equations below. But issues of voltage variations are addressed by the automatic voltage regulators (AVR). Hence the voltage will relatively be maintained constant within some accepted limits.Frequency is a basic and important operating parameter of an electrical power system, which is required to be maintained constant. Under steady-state conditions the total power generated by a generator in an isolated system or power stations in grid connected systems is equal to the system load and losses. Due to sudden appearance of generation-load mismatches the frequency can deviate from its nominal value [2]. Power system protection and control equipment are installed to mitigate these variations, for example load-frequency controller and frequency relay for load shedding require accurate and fast estimation of the frequency [2].

In our paper [3] it was shown that frequency of uncontrolled turbine generator can be sense using magnetostrictive amorphous wire (MAW), and the results compare well with other frequency measurements methods. In paper [4] it was shown that there is a critical length which the signal obtained from MAW is strongest and also relative position with respect to the rotor. From these conclusions, effort is made to operate the frequency measurements at its strongest position so that the results can be processed further for connection to the microcontroller and finally to the digital display. From these frequency measurements, the sense signal is also measured by the digital oscilloscope and the results are compared.

SYNCHRONOUS GENERATOR

Generators world over are mainly synchronous machines this means that these machines operate in step with the mechanical rate of rotation of the prime mover [5]. In a rigid system the frequency is maintained constant whereas in a less rigid system, the frequency may vary with the load. The equation below describes the operation of the synchronous generator.

$$N_s = \frac{120f}{P}$$

Where N_s Synchronous speed in revolutions per minute (rpm)
f System frequency in hertz (Hz)
P Number of poles

This relates the speed of rotation and the frequency of generated power. An increase in load on the generator causes an increase in load angle which translated to lower speed of the generator so that the torque of the machine can increase.
The voltage generated by the generator is a function of applied magnetic field which can be as a result of using permanent magnet (which is rarely used because of voltage control) or supplied from the DC excitation system which can easily be controlled so as to obtain regulated voltage supply. The induced voltage in the generator is given by

$$e = -N\frac{d\emptyset}{dt}$$

Where e induced voltage per coil
Φ fluxes
N number of turns
t time

MAGNETOSTRICTIVE AMORPHOUS WIRE

Magnetostriction is the changing of a material's physical dimensions in response to changing its magnetization. In other words, a magnetostrictive material will change shape when it is subjected to a magnetic field [6]. Magnetostrictive amorphous wire present outstanding peculiarities; those with large and positive magnetostriction exhibit bistable behaviour with magnetization reversal through a large Barkhausen jump(LBJ) originating in the propagation of single domain wall [7]. Others show a vanishing magnetostriction with giant magneto impedance effect. These unique properties have made these materials to have wide applications in sensors and other industrial applications.

MAW are produced by ejecting the molten metal stream through an orifice of quartz tube into a water layer formed by centrifugal force on the internal surface of a rotating drum. The quenching rate (about $10^5 Ks^{-1}$) is required to achieve amorphous structure which restricts the diameter ranges to typically 80 to 200μm [7]

EXPERIMENTAL PROCEDURE

The figure Fig.1 below shows the experimental set up of the system. DC series motor is used in this experiment because as the motor is loaded, the torque developed by it must increase. The increase in the torque necessitates an increase in the armature current. The increase in the armature current causes an increase in the voltage drop across the armature-circuit resistance, the field-winding resistance, and the external resistance. For a fixed applied voltage, the back emf must decrease with load. Since the back emf is also proportional to the armature current, the speed of the motor must drop [8]. As the speed drops, the frequency of generated power in the generator terminals drops just as what would happen in a less rigid electrical power generation system.

A magnet is attached to the shaft as shown; as the shaft rotates, the magnetic field associated with magnets rotates inducing some voltage in the MAW placed 2cm from the magnet this distance is selected since this is the position where we have the strongest signal [4]. The signal is picked by the by the pickup coil of 3000 turns wound around the wire. These spikes are based on the Large Backhausen Jump (LBJ). The signals induced are so weak in the range of 200mV peak to peak. This signal is passed through the amplifier so that they are amplified to some level that can easily switch on the transistor in TTL logic. The transistor only allows the signal only on the positive side edge hence the negative signals is eliminated. The signal is then fed to the microcontroller programmed to interpret the signal for measurement and display. A program is written that interprets the signal and displays the frequency and the speed of the rotation of the generator based on the signal captured. The properties of the signal are then displayed as in the result below

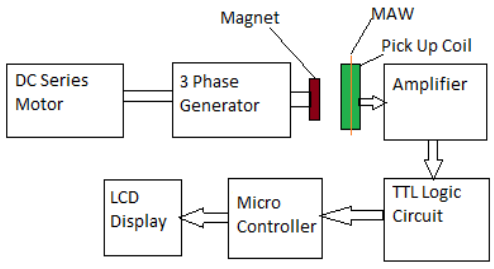

Fig 1: Block Diagram of the set up

RESULTS AND DISCUSSIONS

Figure 2 shows the raw signal as induced in the MAW and picked by the pick up coil wound around it with 3000 windings as indicated in the figure 1 above. This signal is as a result of LBJ resulting in the stable pulses. These pulses are very weak with peak to peak signal value in the ranges of between 140mV to 300mV with some noise as can be seen in the figure. The noise is as a result of nonlinearity in magnetization of the MAW. This needs to be amplified to a range that it can switch a transistor in a TTL logic circuit. This signal is amplified and then connected directly to TTL since the range of the signal can trigger a transistor. The measured signal by the digital oscilloscope gives the properties of the signal which includes the peak to peak value and the fequency. The interest in this reaseach is on the frequency measurements since this directly relates power delivered and frequency of the operation.

$$e(t) = -\frac{d\theta(t)}{dt}$$

Where $e(t) \rightarrow induced\ emf\ in\ MAW$

$\theta \rightarrow flux\ of\ rotating\ field$

$t \rightarrow time$

Several sets of measurement were done with the comparison to show the measurements. In Figure 3, the raw signal and conditioned signal is shown this shows the signal after passing through the amplification circuit and the TTL circuit the negative part of the signal is removed since during such part, the transistor is reversed biased hence there is no conduction during this time. The frequency reading will not be affected after the chopping of negative side of the signal this is because when programming the microcontroller, it only counts the pulses hence the measured quantity will not be affected. The code used is is such that the program reads number of pulses per second. The two signals are shown side by side as in the Figure 3. It is also important to point out that as the frequency and the speed of rotation of rotor affects the peak to peak signal, this can be explained by faradays law.

Any change in the magnetic environment of a coil of wire will cause a voltage (emf) to be "induced" in the coil. No matter how the change is produced, the voltage will be generated. The change could be produced by changing the magnetic field strength, moving a magnet toward or away from the coil, moving the coil into or out of the magnetic field, or rotating the coil relative to the magnet, in this situation, magnetic field changes with respect to the time.

The higher the speed of the rotor the higher will be the value of induced electromotive force (emf). This explains the strength of signal dependence on the speed. It is also worth noting that this does not affect the conditioned signal over the range of

operation but may effect at much lower speeds. This is when the induced emf is so weak that it cannot switch the transistor.

The figure 6 below shows the snapshot of the set up with liquid crystal display of the frequency measurements. The reading of the three measurements is compared as presented. The measured quantities displayed are digital and can easily be incorporated in control of power generated.

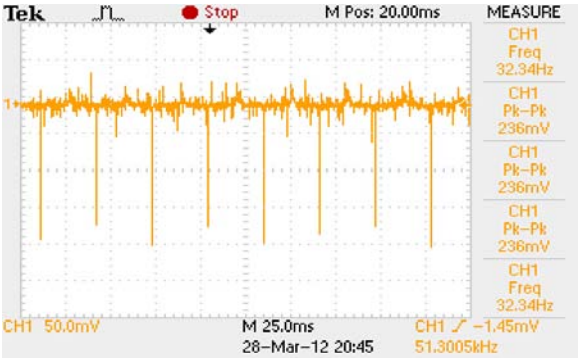

Figure 2: Raw signal as picked by the MAW

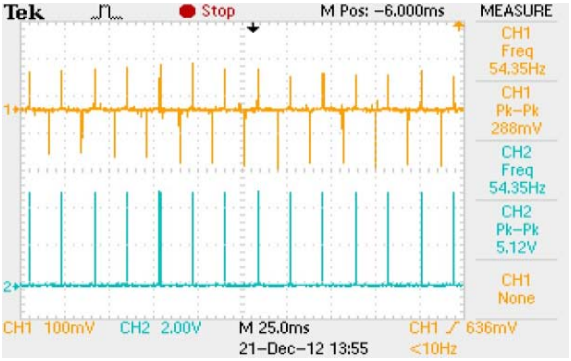

Figure 3: Raw signal and amplified signal side by side at no load condition

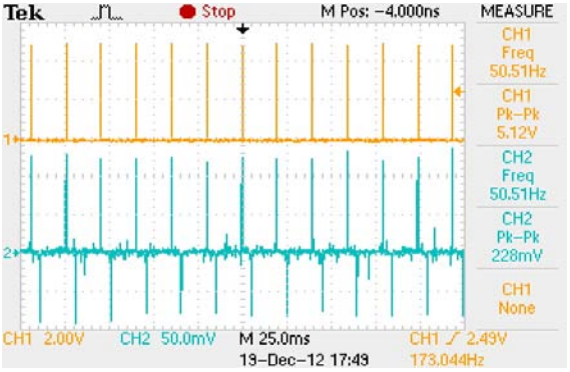

Figure 4: Raw signal and conditioned signal when the generator is supplying optimum load.

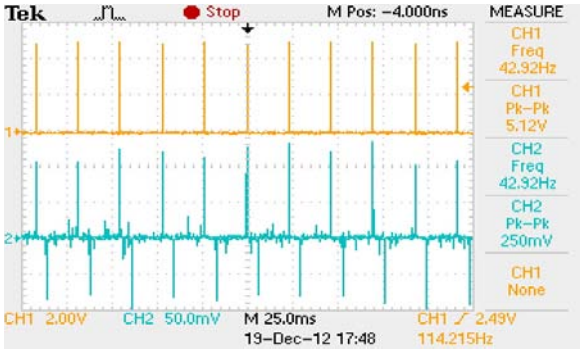

Figure 5: Raw signal and conditioned signal when the generator is overloaded

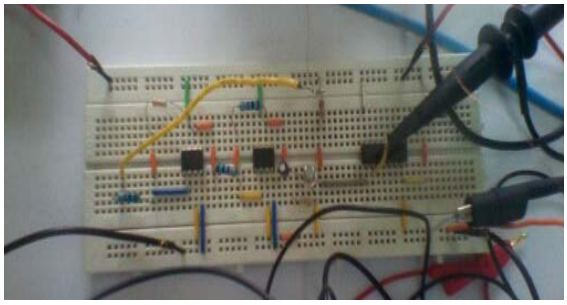

Figure 6: Amplifying circuit for the signal.

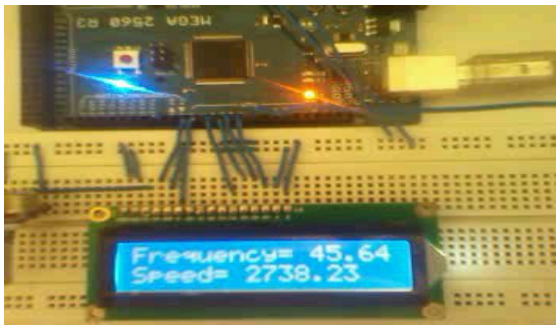

Figure 7: Snapshot of the frequency and speed measurements displayed on a digital display

CONCLUSIONS

In this paper it was shown that,

i) Signal induced in the MAW and picked by the pickup coil can be processed using TTL logic so that it can be directly connected to microcontroller for display on a liquid crystal display and for control action.
ii) Using the processed signal, the frequency can be displayed on a digital display which closely matches the raw signal frequency as measured by the digital oscilloscope.
iii) The signal obtained has been processed to be compatible with the micro controller and this will be used for digital power generation control in isolated power generation plants and island power plants.
iv) The frequency measured is accurate to 0.01Hz this means that the measured quantity can be used accurately in generation control providing very fine controls hence enhancing power quality.

REFERENCE

[1] L. W. and P. Y. Lin, "Analysis of a commercial Biogas Generation System Using a Gas Engine-Induction Generator set," *IEEE Transactions on Energy Conversion*, vol. 24, no. 1, pp. 230-239, March 2009.

[2] T. Lobos and J. Rezmer, "Real Time Determination of Power System Frequency," in *IEEE Proceedings*, Wroclaw, Poland, 1997, pp. 877-881.

[3] C. K. Kitur, J. N. Nderu, A. M.Muhia "Frequency sensing of an isolated Pico Hydro power Generation using Magnetostrictive Amorphous Wire," *IJETAE*, vol. 2, no. 8, pp. 70-74, August 2012.

[4] A. M. Muhia, J. N. Nderu, P. K. Kihato and C. K. Kitur "Effect of length and Position Relative to the Rotor of the Magnetostrictive Amorphous wire Motor speed sensing," in *KSEEE Conference Proceedings*, JKUAT Nairobi, 2012, pp. 61-64.

[5] S. J. Chapman, *Electric Machinery Fundamentals*, 4th ed., Baesystems, Ed. New York, United States of America: McGraw Hill Publishers, 2005.

[6] A. E. Clark, "Ferromagnetic materials," in *Ferromagnetic materials*, E. P. Wolfhart, Ed. Amsterdam, North Holland, vol. 1, p. 531.

[7] M. Vazquez, "Advanced Magnetic Microwires," in *Handbook of Magnetism and Advanced Magnetic Materials*, Helmut and Stuart Parkin Kronmuller, Ed. Madrid, Spain: John Willey and sons ltd, 2007, ch. 1, pp. 1-34.

[8] B. S. Guru and H. R. Hiziroglu, *Electric Machinery and Transformers*, 3rd ed. New York, United States of America: Oxford University Press, 2001.

Motor Vehicle Speed Measurement using Magnetostrictive Amorphous Wire Sensor

M. N. Kiio[1], J. N. Nderu[1], S. I. Kamau[1], A. M. Muhia[2]

[1]Jomo Kenyatta University of Agriculture and Technology, [2]Dedan Kimathi University of Technology

mercyndinda@gmail.com

***Abstract*—** This paper presents the application of Magnetostrictive Amorphous Wire (MAW) sensor in motor vehicle speed measurement. The sensor comprises of permanent magnets attached on the vehicle hub and a stationary coil wound on a magnetostrictive amorphous wire. The wire causes Large Barkhausen Jump (LBJ), a unique feature of the wire and the coil detects magnetic change in the wire to generate pulse signals in response to large Barkhausen Jump .The pulse signals are indicative of the frequency which corresponds to the average rotational speed of the driveshaft and therefore the vehicle speed. The frequency is measured using an oscilloscope and vehicle speed can be calculated from the frequency obtained. This sensor has the advantage of determining the speed of a rotating shaft without the sensor physically contacting the shaft.

***Keywords*—** Large Barkhausen Jump, Magnetostrictive Amorphous Wire, Motor vehicle, speed,

I. INTRODUCTION

Rotational speed sensors involving a variety of mechanisms have been used to detect the rotational speed of a vehicle wheel to control an Anti-lock Braking System (ABS) or detect rotational speed of a shaft. Generally speed sensors involve a sensor wherein an emf induced in a coil changes in accordance with changes in magnetic flux density. The drawback of such systems is that the output of the sensor at low speeds is small, hence unavoidable increase in the cost of the controller for accurate speed detection. Speed sensors which give an output of a constant magnitude regardless of the rotational speed enable speed detection at extremely low speed. Such sensors include the Magnetostrictive Amorphous Wire sensor and Wiegand wire Sensor [1].

It is important to understand that in using Amorphous wire or the Wiegand wire sensor, the induced voltage amplitude is not totally dependent on excitation field strength and orientation. It is the alternating positive and negative magnetic field of equal saturating strength that magnetize and trigger the wire sensors. The alternating magnetic fields are produced by magnets attached to a rotating shaft or moving equipment. Amorphous wire sensor has been used successfully in motor speed sensing in [2] and [3].

A. Principal operation of the sensor

The sensor is a Magnetostrictive Amorphous wire with the composition $(Fe_{50}Co_{50})_{78}Si_9B_{13}$, 7cm in length and 125µm diameter, placed in a pick-up coil. Operation of the sensor is based on Large Barkhausen Jump (LBJ) [4], an effect which is a discontinuity in the magnetic hysteresis loop of the wire sensor corresponding to polarity switching of the core. To achieve magnetic switching, a coil is wound around the amorphous wire and placed in the presence of an alternating external magnetic field parallel with the axis of the wire, the resultant hysteresis loop shown in figure 1(a) contains large discontinuous jumps known as Barkhausen discontinuities that occur due to shell and core polarity switching. The magnetic switching action of the amorphous wire induces a voltage pulse across the pickup coil due to sudden magnetic flux reversal of the wire. This sudden magnetic flux reversal is termed as Large Barkhausen Jump. Due to the LBJ, magnetostrictive amorphous wires generate very sharp and stable voltage spikes in acfield s as shown in figure 1(b).

Advantages of sensors employing amorphous wire sensor include high stability against temperature variation, Small size, high reliability and small aging over long time usage, excellent digital output and electromagnetic properties, insensitivity to mechanical vibrations and good corrosion resistance.

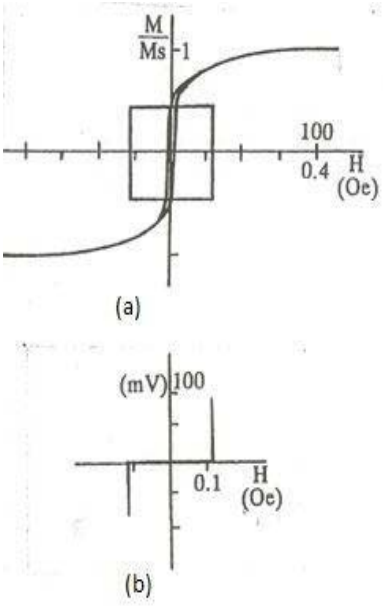

Figure.1: (a) Low and High field M-H loops for ($F e_{50}Co_{50})_{78}Si_7B_{15}$wire (b) Voltage pulse induced in a pick-up coil around the wire during LBJ

B. Experimental setup

To measure the speed of a car, one must be able to measure the rotational speed of either the wheels or the transmission and send the information to some sort of a gauge. Generally vehicle speed sensor is mounted on the transmission output shaft or to the crankshaft and consists of a toothed metal disk and a stationary detector that covers a magnetic coil.

In this paper the vehicle wheel hub is used whereby two permanent magnet are attached on a rotating shaft on the vehicle's hub with the unlike poles facing each other. A pick-up coil of 3000 turns, with amorphous wire placed inside is placed about 4.5 cm from the magnets. End of the coils are connected to a digital oscilloscope. The experiments were conducted at varying values of vehicle speed and frequency of the signal from the pick-up coil measured with the oscilloscope.

II. RESULTS AND DISCUSSION

The results of experiment using amorphous wire sensor and digital oscilloscope to read the frequency are as shown in figures 2, 3, 4, 5 and 6 below. In all the cases frequency increase is observed with speeds between 10 km/h and 80 km/h. The frequency of the voltage pulses obtained is equivalent to number of revolutions of the wheel per second; hence the frequency can be used to calculate the vehicle speed.

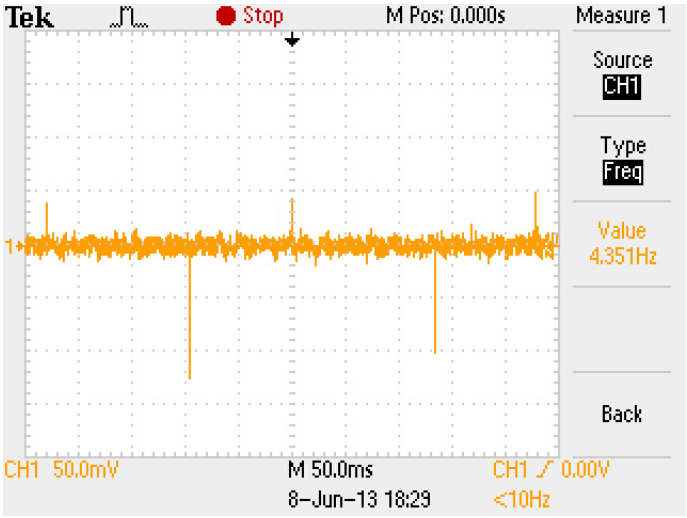

Figure 2 : Vehicle speed at 10 km/h

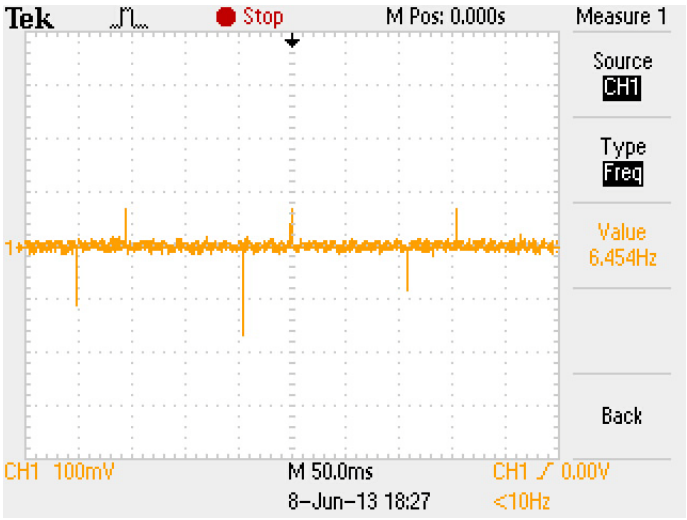

Figure 3: Vehicle speed at 20 km/h

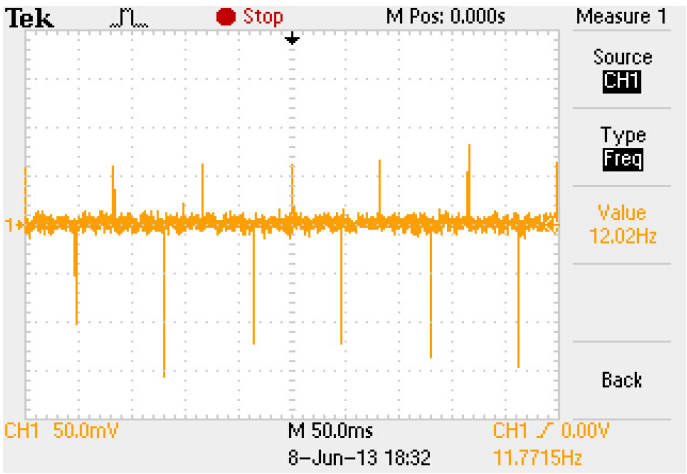

Figure 4: Vehicle speed at 40 km/h

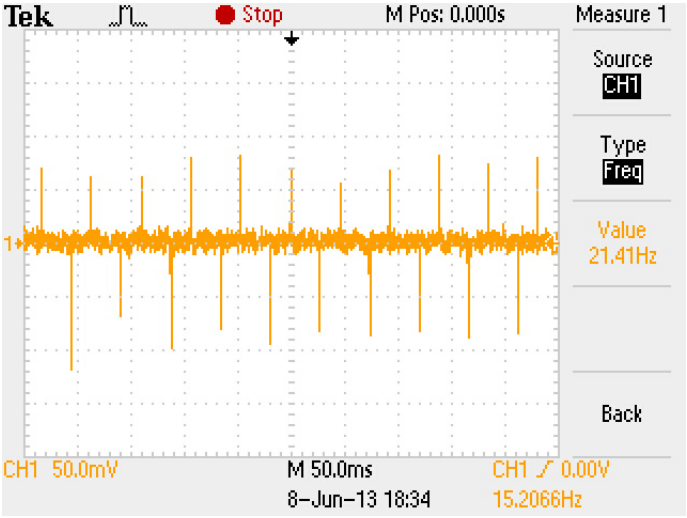

Figure 5: Vehicle speed at 70 km/h

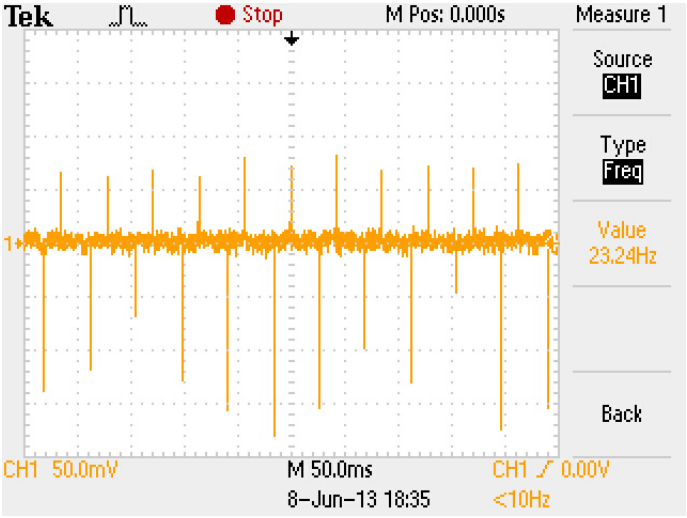

Figure 6: Vehicle speed at 80 km/h

Calculation of vehicle speed from frequency obtained.

If D is the wheel diameter, the vehicle speed V as shown in equation (2) could be determined taking into consideration the wheel frequency f and the wheel diameter. Using the vehicle wheel dimension 195/65R15, the vehicle diameter was determined using (1)

$$D = 15*25.4 + 0.65*195*2 = 634.5\ mm = 0.6345m \quad (1)$$

$$V = 2 \cdot \pi \cdot R \cdot f \quad (2)$$

Equation (2) gives the calculated speed in m/s which is hence converted to km/h. Table 1 shows the calculated values of the vehicle speed in Km/h.

Frequency (HZ)	Calculated Speed (m/s)	Calculated Speed (Km/h)	Speedometer Reading (Km/h)
4.35	8.2	29.5	10
6.45	12.16	43.8	20
8.87	16.72	60.2	30
12.02	22.66	81.6	40
14.86	28.01	100.8	50
17.29	32.59	117.3	60
21.41	40.36	145.3	70
23.24	43.81	157.7	80

Table 1: Results obtained using amorphous wire.

The results from Table 1 are plotted in Figure 7. It is observed that the calculated speed is double the speedometer speed. This can be attributed to the differential ratios where locking one wheel doubles the speed of the free- spinning wheel.
This was because during experiment, the vehicle was jacked only allowing one wheel to spin freely. The estimated vehicle speed is thus half the calculated speed.
The slight difference between the speedometer speed and estimated vehicle speed may also be attributed to the calibration allowance on speedometers.

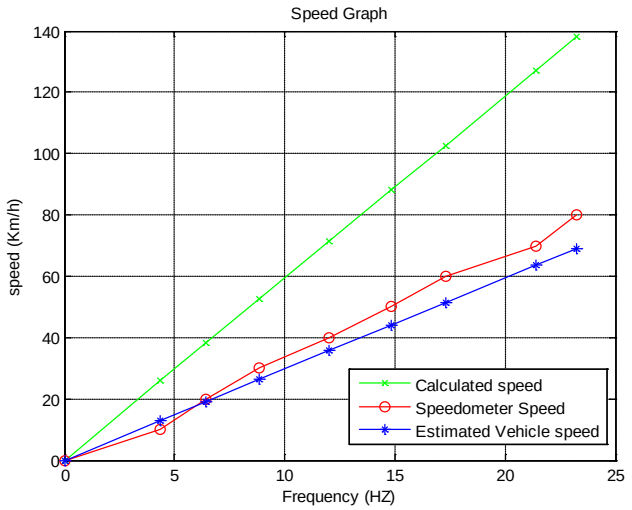

Figure 7: Vehicle speed versus MAW measured frequency

III. CONCLUSION

- It was possible to measure the wheel revolution frequency using the magnetostrictive amorphous wire which offers more advantages over existing speed sensors.
- Taking into consideration the issue of differential ratios, the calculated speed using amorphous wire compares well with the speedometer reading hence suitable for vehicle speed measurement.
- It was observed that with only one drive wheel spinning freely, the speed measured is twice the speedometer speed.

REFERENCES

[1] W. J. Flemming, "Overview of Automotive Sensors". *IEEE Sensors Journal* , Vol.1, No. 4, pp.296-308, 2001.

[2] J. N. Nderu, A. M. Muhia, P. K. Kihato and C. K. Kitur, "Microcontroller Based Magnetostrictive Amorphous Wire Motor Speed Sensor," *Proceedings of the 2012 mechanical Engineering Conference on Sustainable Research and innovation*, pp.173-175, May 2012.

[3] P. K. Kihato, J. N. Nderu, and G. M. Hinga, "Motor speed measurement using magnetostrictive amorphous wire,"*Proceedings of 2007 JKUAT Scientific and Technological and Industrialization Conference*, pp. 315–319,October 2007.

[4] J. N. Nderu and P. K. Ruirii, "Speed Sensing by Amorphous Magnetostrictive Metal Wires," *Proceedings of the 5th International Annual Mechanical Engineering Seminar (J.K.U.A.T)*, June 2000.

SINGLE CONTROLLER ALGORITHM FOR AUTONOMOUS CAR BASED ON BACKSTEPPING AND SINUSOIDAL INPUT

Mr. Inno Odira, Dr. P. K. Kihato and Dr. S. I. Kamau

innoodira@gmail.com, kamitakhat1@gmail.com and sikamau@gmail.com

Department of Mechatronic Engineering, School of Engineering, Dedan Kimathi University of Technology (DeKUT) P.o Box 657-10100Nyeri-Kenya

Department of Electrical and Electronics Engineering, School of Electrical and Telecommunniction Engineering, Jomo Kenyatta University of Agriculture and Technology (JKUAT), P.o box 62000-01000 Nairobi-Kenya

Department of Electrical and Electronics Engineering, School of Electrical and Telecommunniction Engineering, Jomo Kenyatta University of Agriculture and Technology (JKUAT), P.o box 62000-01000 Nairobi-Kenya

ABSTRACT

Autonomous car requires situational sensors to facilitate path planning which generates trajectory or path following control problem. Focusing on a case where the path is predetermined as waypoints and interacts with obstacles between waypoints. We seek to develop a single controller that can operate virtually on any type of trajectory opposed to the conventional multi-model controller approach. We formulate our problem as a trajectory tracking control problem which is also adaptable to path following problem. The design is based on backstepping method with sinusoidal input signal on the car's non-holonomic kinematic model. Simulation results demonstrates that backstepping and sinusoidal input is quite effective for this particular application and also enables easy adaptability of the controller to operate on a path following problem without changing controller parameters.

Index Terms—Backstepping controller, Sinusoidal input, trajectory tracking, path following, autonomous driving, non-holonomic constraints.

1. INTRODUCTION

Much work has been done on designing intelligent vehicle systems, which belongs to one of three categories: 1) hierarchical control system design for fully automated traffic, in which vehicles are all automated and are organized into platoons through interactive vehicle-to-vehicle communication 2) autonomous intelligent cruise control, i.e., keeping a desired velocity when there is no vehicle in front and keeping a desired spacing (possibly velocity dependent) when there is a vehicle in front and 3) autonomous vehicle guidance, which requires sensing, actuation, and computational intelligence on board the vehicle. Specifically, we are interested in designing the system of the third category. Once the feasible path is obtained the navigation and control process enters the tracking phase. In this paper we seek to develop a single controller that ensures that every path can be followed accurately opposed to conventional multi-model approach. We consider a case where the path is predetermined as waypoints and interacts with objects between waypoints.

2. PROBLEM STATEMENT

The motion planning problem for car-like vehicles has been investigated intensively and is still an open problem [1], [2] and [3]. When the desired path has been planned from the in-vehicle vision system, the next step is to plan the motion that brings the car from the current position to follow the planned path. There exist two different categories of approaches. The first category is skill-based. The control commands are generated in real-time according to the current state. Fuzzy logic and neural networks are used to transfer skills of human beings to the intelligent vehicle [4], [5] and

[6]. The second category aims at first planning the whole motion series in advance and then sending these commands to the controller constituting plan-and control process. The plan-and-control methods include two standard steps. The first step is path planning and second step is called trajectory planning.

Existing solutions offer multiple control strategies to the corresponding specific trajectory features which are classified for different control strategies. Depending on the different trajectory, corresponding control strategy is selected [7] and [8]. A number of solution to this problem has employed PD algorithm based on PID controllers while operating on a road path following problem based on prediction of forward path based on markings on the road [9].

Here we propose a control strategy exploiting the path planning method using Single deformable polyline tentacle [10] which presents the path as a trajectory (time indexed), thus the controller algorithm can be designed as a straight trajectory tracking controller without path planning but is also adaptable to car speed modifications along the trajectory. We employ backstepping control algorithm applied on non-holonomic vehicle kinematic model considering that the model is a nonlinear model.

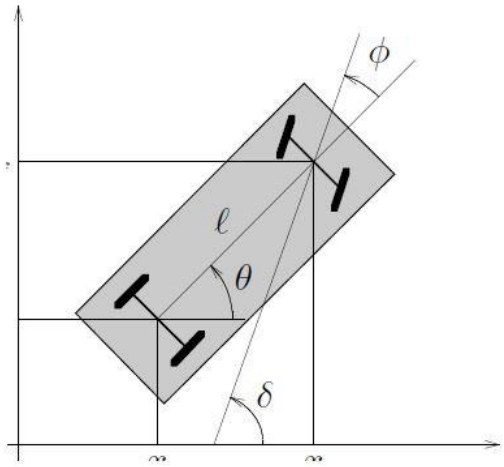

Fig. 1. Generalized coordinate of a car

For a rear-wheel driving, the kinematic model is derived as follows.

$$\begin{bmatrix}\dot{x}\\ \dot{y}\\ \dot{\theta}\\ \dot{\phi}\end{bmatrix} = \begin{bmatrix}\cos\theta\\ \sin\theta\\ \frac{tan\ \phi}{l}\\ 0\end{bmatrix} V_1 + \begin{bmatrix}0\\0\\0\\1\end{bmatrix} V_2 \quad (1)$$

Where $V1$ and $V2$ are the driving and the steering velocity input respectively. There is a model singularity at $\phi = \pm\frac{\pi}{2}$, where the first vector field has a discontinuity [11] and [12]. This corresponds to the car becoming jammed when the front wheel is normal to the longitudinal axis of the body. However, the importance of this singularity is limited due to the restricted range of the steering angle φ in most practical cases

3. BACKSTEPPING TRAJECTORY TRACKING DESIGN

3.1 Transforming the kinematic model to chained form

The existence of canonical forms for kinematic models of non-holonomic vehicles is essential for the systematic development of both open-loop and closed loop control strategies. The most useful canonical structure is the chained form. The two -input thriftless control system

$$\begin{aligned} \dot{x_1} &= u_1 \\ \dot{x_2} &= u_2 \\ \dot{x_3} &= x_2 u_1 \\ &\vdots \\ \dot{x_n} &= x_{n-1} u_1 \end{aligned} \quad (2)$$

is called (2,n) single-chain form [11]. Using the change of coordinates

$$\begin{aligned} x_1 &= x \\ x_2 &= \frac{1}{l\cos^3\theta}\tan\ \phi \\ x_3 &= \tan\ \theta \\ x_4 &= y \end{aligned} \quad (3)$$

together with the input transformation

$$V_1 = \frac{u_1}{cos\ \theta}$$

$$V_2 = \frac{-3u_1\ sin\ \theta\ \overset{2}{sin}\ \phi}{l\ \overset{2}{cos}\ \theta} + lu_2\ \overset{3}{\cos}\ \theta\ \overset{2}{\cos}\ \phi \quad (4)$$

the system is transformed into (2,4) chained form

$$\dot{x_1} = u_1$$

$$\dot{x_2} = u_2$$

$$\dot{x_3} = x_2 u_1 \quad (5)$$

$$\dot{x_4} = x_3 u_1$$

3.2. Reference tracking

Assume that a feasible and smooth desired output trajectory is given in terms of the cartesian position of the car

$$x_d = x_d(t), \quad y_d = y_d(t) \quad \forall \quad t \geq t_0 \quad (6)$$

From this information we are able to derive the corresponding time evolution of the remaining coordinates (state trajectory) as well as of the associated input commands (input trajectory). The desired output trajectory is feasible when it can be obtained from the evolution of reference vehicle model

$$\dot{x_d} = \cos\ \theta_d\, V_{d1} \quad (7)$$

$$\dot{y_d} = \sin\ \theta_d\, V_{d1} \quad (8)$$

$$\dot{\theta_d} = \frac{tan\ \phi_d\, V_{d1}}{l} \quad (9)$$

$$\dot{\phi_d} = V_{d2} \quad (10)$$

for suitable initial conditions $x_d(t_0), y_d(t_0), \theta_d(t_0)$, $\phi_d(t_0)$ and piecewise continuous inputs $V_d(t)$ for $t \geq 0$. Solving for $V_{d1}(t)$, from equation (7) gives the first input

$$V_{d1} = \pm\sqrt{\dot{x_d}^2(t) + \dot{y_d}^2(t)} \quad (11)$$

Dividing equation (8) by (7) and keeping the sign of linear velocity input into account, we compute the desired orientation of the car as

with codomain in all four quadrants.

Differentiating equation (7) and (8) and combining the results so as to eliminate V_{d1}

$$\dot{\theta_{d1}}(t) = ATA2\left\{\frac{\dot{y_d}(t)}{V_{d1}(t)}, \frac{\dot{x_d}(t)}{V_{d1}(t)}\right\} \quad (12)$$

we obtain

$$\dot{\theta_d}(t) = \frac{\ddot{y_d}(t)\dot{x_d}(t) - \ddot{x_d}(t)\dot{y_d}(t)}{V_{d1}^2} \quad (13)$$

Plugging this into equation (9) provides the desired steering angle which takes values in $(-\frac{\pi}{2}, \frac{\pi}{2})$

$$\phi_d(t) = \arctan\frac{B}{V_{d1}^3} \quad (14)$$

Where

$$B = l[\ddot{y_d}(t)\dot{x_d}(t) - \ddot{x_d}(t)\dot{y_d}(t)]$$

Finally differentiating equation (13) and substituting the result in equation (10) yields the second input

$$V_{d2}(t) = lV_{d1}\frac{(\dddot{y_d}\dot{x_d} - \dddot{x_d}\dot{y_d})V_{d1}^2 - A}{V_{d1}^6 + l^2(\ddot{y_d}\dot{x_d} - \ddot{x_d}\dot{y_d})^2} \quad (15)$$

Where

$$A = 3(\ddot{y_d}\dot{x_d} - \ddot{x_d}\dot{y_d})(\dot{x_d}\ddot{x_d} + \dot{y_d}\ddot{y_d})$$

Where we dropped for compactness the time dependence in the right hand side. Equation (11) to (14) provide the unique state and input trajectory needed to reproduce the desired output trajectory. These expressions depend only on the values of the output trajectory (6) and its derivatives up to the third order. Therefore in order to guarantee its exact reproducibility, the cartesian trajectory should be three times differentiable almost everywhere. This fact should be taken into account at the motion planning level.

Denote the tracking error as $x_e = x - x_d$. The error differential equations are

$$\begin{aligned} \dot{x_{e1}} &= u_1 - u_{d1} \\ \dot{x_{e2}} &= u_2 - u_{d2} \\ \dot{x_{e3}} &= x_{e2}u_{d1} + x_2(u_1 - u_{d1}) \\ \dot{x_{e3}} &= x_{e3}u_{d1} + x_3(u_1 - u_{d2}) \end{aligned} \quad (16)$$

The goal is to find a Lipschitz continous time-varying state-feedback controller $\tilde{u}$ such that

$$u = \begin{bmatrix} u_1 \\ u_2 \end{bmatrix} = u(x_e, u_{d1}, u_{d2}) \quad (17)$$

such that the tracking error x_e converges to zero asymptotically ie. $lim|x - x_d| = 0$ under appropriate conditions on the reference control functions u_{d1} and u_{d2} and the initial tracking error $x_e(0)$, with good choice of damping coefficient λ .

We first introduce change of coordinates and rearrange system into a triangular like form so that the integrator backstepping can be applied.

Denote $\widetilde{x_d} = (x_{d2} \cdots x_{d4})$ and let $\eta_1(\widetilde{x_d})$: $R^4 \to R_4$ be a mapping defined by

$$\begin{aligned} \zeta_1 &= x_{e4} - (x_{e3} + x_{d3})x_{e1} \\ \zeta_2 &= x_{e3} - (x_{e3} + x_{d3})x_{e1} \\ \zeta_3 &= x_{e2} \\ \zeta_4 &= x_{e1} \end{aligned} \quad (18)$$

In the new cordinate $\zeta = (\zeta_1, \zeta_2, \zeta_3, \zeta_4)$ the system is transformed into

$$\begin{aligned} \dot{\zeta_1} &= u_{d1}\zeta_2 - x_2(u_1 - U_{d1})\zeta_4 \\ \dot{\zeta_2} &= u_{d1}\zeta_3 - u_2\zeta_4 \\ \dot{\zeta_3} &= u_2 - u_{d2} \\ \dot{\zeta_1} &= u_1 - u_{d1} \end{aligned} \quad (19)$$

The basic design idea for backstepping based control law is to take for every dimension subsystem some state variables as virtual control inputs and at the same time recursively select an appropriate Lyapunov function candidate. Thus each step results in a new virtual controller. In the end of the overall procedure the true control law results which achieve the original design objective.

Consider the ζ_1 subsystem of equation (18)

We consider the variable ζ_2 as a virtual control input and the variable u_{d1} and ζ_4 as time varying functions.

$$\dot{\zeta_1} = u_{d1}\zeta_2 - x_2(u_1 - U_{d1})\zeta_4 \quad (20)$$

Denote $\bar{\zeta_1} = \zeta_1$ Differentiating the function $V_1 = \frac{1}{2}\zeta_1^2$ along the solution of equation (19) yields

Since variable ζ_2 is a virtual control input,

$$\dot{V_1} = u_{d1}\bar{\zeta_1}\zeta_2 - x_2\bar{\zeta_1}(u_1 - u_{d1})\zeta_4 \quad (21)$$

selecting $\zeta_2 = -k_1\zeta_1$ for $k_1 \geq 0$ then $\dot{V_1} = -k_1u_{d1}^2\bar{\zeta_1}^2$ whenever $\zeta_4 = 0$.

From above equation we observe that function $\alpha_1(\zeta_1) = 0$ is a stabilizing function ie. the desired value of virtual control ζ_2 for which V_1 is negative semi definite for subsystem (20). This desired value is called stabilizing functionand ζ_2 is called virtual control. As in this case

$$\dot{V_1} = -2k_1u_{d1}^2V_1$$

Above implies that $V_1 \to 0$ as $t \to \infty$ and $\zeta_1 \to 0$ as $t \to \infty$ ie $V_{1lim} = 0$ So the origin $\zeta_2 = 0$ is a stabilizing function

Define $\bar{\zeta_2} = \zeta_2 - \alpha_1(\zeta_1)$

Differentiating the function

$$V_2 = V_1 + \frac{1}{2}\bar{\zeta_2}^2 = \frac{1}{2}\bar{\zeta_1}^2 + \frac{1}{2}\bar{\zeta_2}^2$$

along the solution of equation (19)yields

$$\dot{V_2} = u_{d1}\bar{\zeta_2}\bar{\zeta_3} - x_2\zeta_1(u_1 - \bar{}ud1)\zeta_4$$

As

$$\begin{aligned} \bar{\zeta_2} &= \zeta_2 - \alpha_1(\zeta_1) \\ \dot{\bar{\zeta_2}} &= \dot{\zeta_2} - \frac{\partial\alpha_1}{\partial\zeta_1}\zeta_1 \\ &= \dot{\zeta_2} - u_{d1}\zeta_3 - u_{d1}\zeta_1 + u_{d1}\zeta_1 - u_{d1}\zeta_1 \\ &= u_{d1}\zeta_3 - u_2\zeta_4 - u_2\zeta_4 - u_{d1}\zeta_1 \end{aligned}$$

$$= u_{d1}(\zeta_3 + \zeta_1) - u_2\zeta_4 - u_{d1}\zeta_1$$
$$= u_{d1}(\zeta_3 + \alpha_2) - u_2\zeta_4 - u_{d1}\zeta_1$$

Where

$$\alpha_2(\zeta_1, \zeta_2) = -\zeta_1$$

Again define

$$\bar{\zeta_3} = \zeta_3 - \alpha_2(\zeta_1.\zeta_2)$$
$$\dot{\bar{\zeta_3}} = \dot{\zeta_3} - (\frac{\partial \alpha_2}{\partial \zeta_1}\zeta_1 + \frac{\alpha_2}{\zeta_2})\zeta_2$$
$$= \dot{\zeta_3} - (-\dot{\zeta_1}) = \dot{\zeta_3} + \dot{\zeta_1}$$
$$= u_2 + u_{d2} + u_{d1}\zeta_2 - x_2(u_1 - u_{d1})\zeta_4$$

Consider the positive definite and proper function

$$V_3 = V_2 + \frac{1}{2}\bar{\zeta_3}^2 = \frac{1}{2}\bar{\zeta_1}^2 + \frac{1}{2}\bar{\zeta_2}^2 + \frac{1}{2}\bar{\zeta_3}^2$$

Differentiating the function V_3 along the solution of equation (19) yields

$$\dot{V_3} = \bar{\zeta_3}(u_{d1}\bar{\zeta_2} + u_2 - u_{d2} + u_{d1}\zeta_2) - (x_2\zeta_1 + x_2\zeta_3)(u_1 - u_{d1})\zeta_4 - u_2\bar{\zeta_2}\zeta_4$$

In order to make V_3 negative definite we choose the following control input

$$u_{d1}\bar{\zeta_2} + u_2 - u_{d2} + u_{d1}\zeta_2 = c_3\bar{\zeta_3} \quad (22)$$

Where $c_3 > 0$

Thus we have

$$V_3 = -c_3\bar{\zeta_3}^2 \cdot - C - u_2\bar{\zeta_2}\zeta_4$$

Where

$$C = (x_2\zeta_1 + x_2\zeta_3)(u_1 - u_{d1})\zeta_4$$

Finally consider the positive definite and proper function which serves as a candidate lyapunov function for the whole system (19)

$$V_4 = V_3 + \frac{\lambda}{2}\zeta_4^2 = \frac{1}{2}\bar{\zeta_1}^2 + \frac{1}{2}\bar{\zeta_2}^2 + \frac{1}{2}\bar{\zeta_3}^2 + \frac{\lambda}{2}\zeta_4^2$$

Where $\lambda > 0$ is a design parameter. Differentiating the function V_4 along the solution of (19) yields

$$\dot{V_4} = -c_3\bar{\zeta_3}^2 - (x_2\bar{\zeta_1} + x_2\bar{\zeta_3})(u_1 - u_{d1})\zeta_4 - u_2\bar{\zeta_2}\zeta_4 + \lambda\zeta_4(u_1 - u_{d1})$$

$$\dot{V_4} = -c_3\bar{\zeta_3}^2 + [\lambda - (x_2\bar{\zeta_1} + x_2\bar{\zeta_3})(u_1 - u_{d1}) - u_2\bar{\zeta_2}]\zeta_4$$

$$\lambda - (x_2\bar{\zeta_1} + x_2\bar{\zeta_3})(u_1 - u_{d1}) - u_2\bar{\zeta_2} = -c_4\zeta_4 \quad (23)$$

In order to make V_4 negative definite we

$$u_1 = u_{d1} + \frac{-c_4\zeta_4 + u_2\zeta_2}{\lambda - (2x_2\zeta_1 + x_2\zeta_3)} \quad (24)$$

$$u_2 = u_{d1} - c_3(\zeta_3 + \zeta_1) - 2u_{d1}\zeta_2 \quad (25)$$

choose the following control input

From equation (22) and (23) we get the following control law

4. RESULTS

To examine the effectiveness of the proposed trajectory control methodology, the simulation for the vehicle was performed in MATLAB/SIMULINK for three different cases; 1.) Smooth lane changing 2.) Trajectory with obstacle avoidance and 3.) Worst scenario (High frequency Sinusoidal trajectory)

The simulations validates the robustness of this backstepping algorithm.

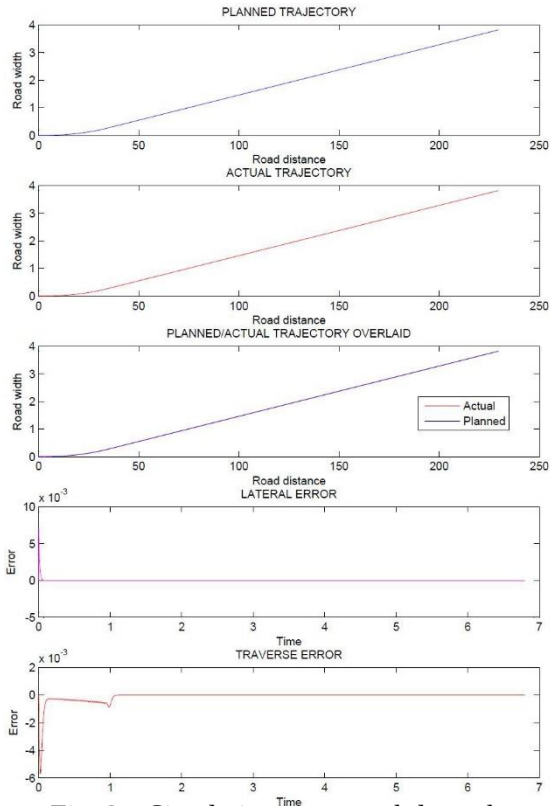

Fig. 2. Simulation on smooth lane change manoeuvre

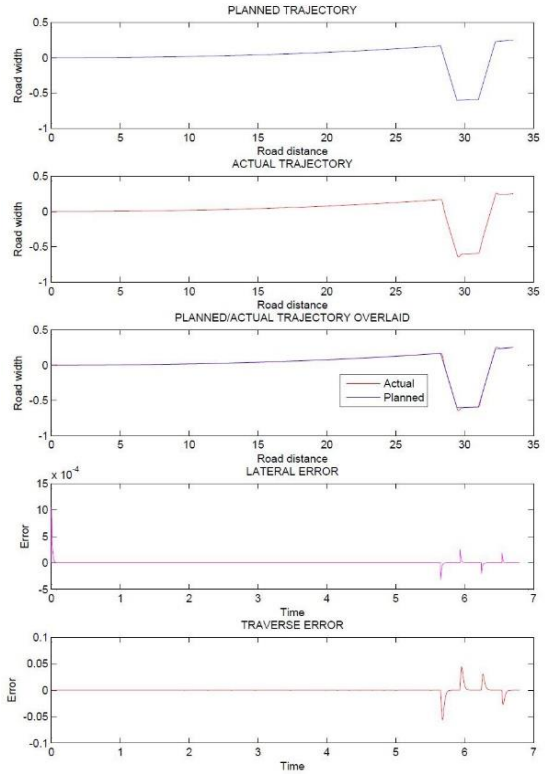

Fig. 3. Simulation on obstacle avoidance manoeuvre

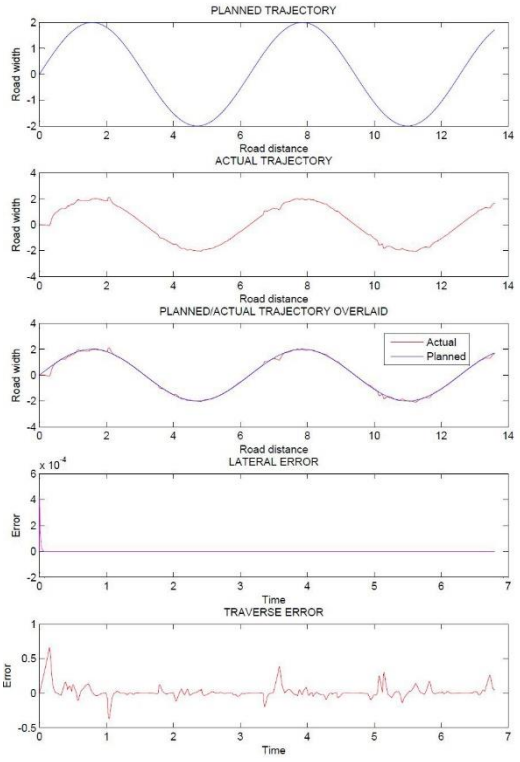

Fig. 4. Simulation on worst case of wavy manoeuver

5. DISCUSSION AND CONCLUSION

The simulation results shows excellent performance particularly, the transient errors are significantly reduced even for continuously changing trajectory. It is only notable that errors are observed only at the start of trajectory tracking but are significantly diminished even at points where there are sudden changes in desired trajectory.

The use of sinusoidal input in the controller design guaranteed representation of all possible trajectories. This is supported by the theory of Fourier transforms of signal decomposition. Hence, any control law that satisfied trajectory tracking of this input would be applicable to any feasible trajectory ranging from straight lines, smooth curves, sharp curves, etc.

The backstepping algorithm idealized the trajectory function and control law by eliminating errors which are normally

attributed to approaches that employ linearization or approximation of functions. This facilitates reduction of unmodelled disturbances and hence ensures fast transient responses and reduced steady state errors.

The combination of sinusoidal input in the controller design and the backstepping method enabled realization of a single controller that is able to track any feasibly trajectory without the need of multi-model controller approach.

REFERENCES

[1] T. Dang, S. Kammel, C. Duchow, B. Hummel, and C. Stiller, "Path planning for autonomous driving based on stereoscopic and monoscopic vision cues," in *Multisensor Fusion and Integration for Intelligent Systems, 2006 IEEE International Conference on*, 2006, pp. 191–196.

[2] M. Cherif, "Motion planning for all-terrain vehicles: a physical modeling approach for coping with dynamic and contact interaction constraints," pp. 202–218, 1999.

[3] B. Hummel, S. Kammel, T. Dang, C. Duchow, and C. Stiller, "Vision-based path-planning in unstructured environments," in *Intelligent Vehicles Symposium, 2006 IEEE*. IEEE, 2006, pp. 176–181.

[4] Z. L. Z. Lu, J. L. J. Li, and Z. M. Z. Minghui, "Intelligent control research based on the smart car," 2010.

[5] W. Y.-d. W. Yong-ding and N. L.-n. N. Li-na, "Design of smart car speed control system based on fuzzy control," 2010.

[6] S. Huang and W. Ren, "Use of neural fuzzy networks with mixed genetic/gradient algorithm in automated vehicle control," *Industrial Electronics, IEEE Transactions on*, vol. 46, no. 6, pp. 1090–1102, 1999.

[7] Z. Wang and Y. Liu, "Design of road tracing navigation control for smart car use ccd sensor," in *E-Health Networking, Digital Ecosystems and Technologies (EDT), 2010 International Conference on*, vol. 1, 2010, pp. 345–348.

[8] R. Li, "Study of control algorithm for smart car system," pp.184–187, 2011.

[9] W. Xiuquan, S. Xiaoliu, C. Xiaoming, and C. Ying, "Route iden- tification and direction control of smart car based on cmos image sensor," in *Computing, Communication, Control, and Management, 2008. CCCM '08. ISECS International Colloquium on*, vol. 2, 2008.

[10] I. Odira, P. K. Kihato, and S. I. Kamau, "Driving with single deformable polyline tentacle and velocity obstacles," *Accepted for presentation by MKU Research and Innovation Conference 2013, Nairobi-Kenya.*

[11] O. De Luca, "Robot motion planning and control. Spring, 1998, ch," *Feedback Control of a Nonholonomic Car-like Robot*, pp. 343–427.

[12] G. Campion, G. Bastin, and B. Dandrea-Novel, "Structural properties and classification of kinematic and dynamic models of wheeled mobile robots," *Robotics and Automation, IEEE Transactions on*, vol. 12, no. 1, pp. 47–62, 1996.

Real-time Motor Speed Monitoring in MATLAB using Magnetostrictive Amorphous Wire as the Speed Sensor

A. M. Muhia, J. N. Nderu and C. K. Kitur

***Abstract*—This paper presents a real-time motor speed monitoring approach in MATLAB using magnetostrictive amorphous wire as the speed sensor. The principle operation of the sensor is based on Large Barkhausen Jump, a unique feature of the wire. The wire generates stable voltage pulses in alternating fields which correlate well with the rotary speed of the motor hence can be used to measure the speed of the motor. The pulses are signal conditioned and fed into a microcontroller on arduino board for measurement of frequency. The arduino is linked to MATLAB using inbuilt blocks with capability of receiving and sending data via the serial port. A model is then developed in MATLAB with the blocks for receiving data from the arduino and displaying both frequency and motor speed. The design presents a simple, real-time motor speed monitoring system that can be useful in speed control.**

***Index Terms*—Real-time motor speed monitoring, Magnetostrictive Amorphous Wire, MATLAB, Arduino**

I. INTRODUCTION

In our work [1], we presented a microcontroller based magnetostrictive amorphous wire motor speed sensor. The sensor was tested and found to be reliable in motor speed sensing. In [2], we presented a successful application of the sensor in frequency sensing of a pico-hydro.

In any control system, real-time acquisition of data is important for fast response. Our present work explores the possibility of real-time monitoring of motor speed in MATLAB using the sensor with the ultimate aim of achieving real-time speed control. Arduino board is used in this work due to its ability to interface with MATLAB using inbuilt blocks in Simulink. MATLAB 2012a provides for interfacing with Arduino Uno and Arduino Mega 2560. Arduino Mega 2560 is used in this work. Communication is achieved via the serial port.

A. Operation

Speed Sensor: The operation of the sensor is discussed in our previous work [1]. A Liquid Crystal Display (LCD)is incorporated in this work for displaying the values of motor frequency and speed.

J. N. Nderu, Department of Electrical and Electronic Engineering, JKUAT (e-mail: djainderugac@gmail.com. jkuat.ac.ke).

A. M. Muhia, Department of Electrical and Electronic Engineering, JKUAT (e-mail: ammuhia@gmail.com).

C. K. Kitur, Department of Electrical and Electronic Engineering, JKUAT (e-mail: cleophaskitur@gmail.com).

MATLAB interface with arduino: MATLAB 2012a provides for direct communication with arduino Uno and arduino Mega in simulink. The arduino digital and analog pins are modelled into blocks in MATLAB. Communication is through the USB-serial port cable. Digital and analaog data can be easily sent from arduino to MATLAB and vice versa through these pins. Other provisions include blocks for servo motor control, pulse width modulated signals and serial transmission of data between MATLAB and arduino. Figure 1 below gives a description of the blocks in MATLAB, simulink.

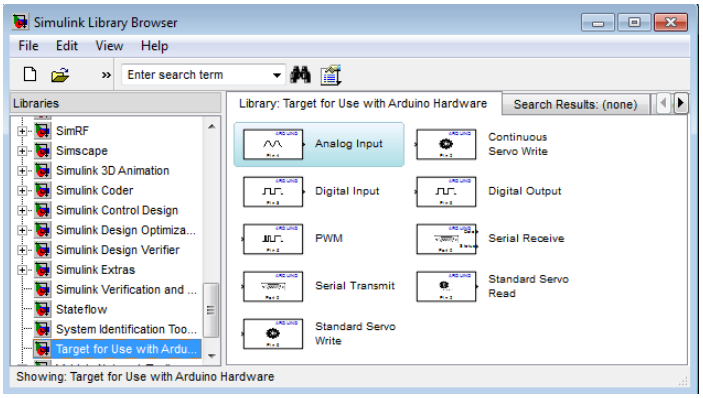

Fig. 1. Inbuilt blocks for use with arduino in simulink

B. Experimental Procedure

Two arduino boards are used and are connected as shown in Fig 2.

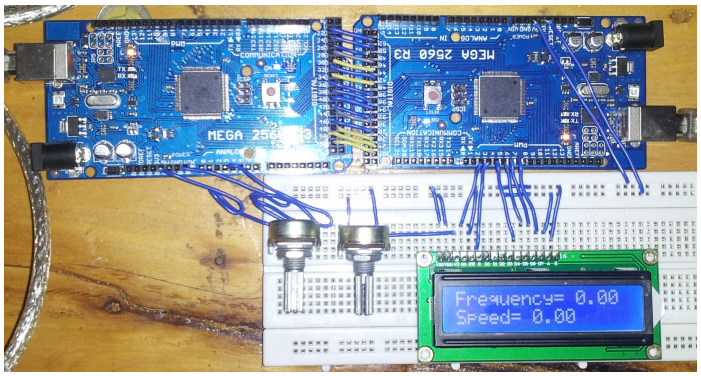

Fig. 2. Physical connections of the arduino and LCD

The first arduino is used for measuring the motor speed from the frequency of the signal of the magnetostrictive amorphous wire sensor and displaying this speed onto a liquid crystal display. The second arduino is used in reading the frequency and speed in MATLAB through a model of the arduino pins developed in simulink.

The signal obtained from the sensor after signal conditioning is fed into a digital pin of the first arduino. The frequency of the signal is determined from which motor speed is calculated and displayed on the LCD. The frequency obtained is converted into binary form and fed to the second arduino via digital pins. A model of the digital pins receiving the binary digits in the second arduino is modelled in MATLAB. The binary bits are received in MATLAB through the model and converted into decimal form from which the frequency is reassembled. Motor speed is then calculated from the frequency and both the frequency and speed displayed. The model in simulink is as shown in 3

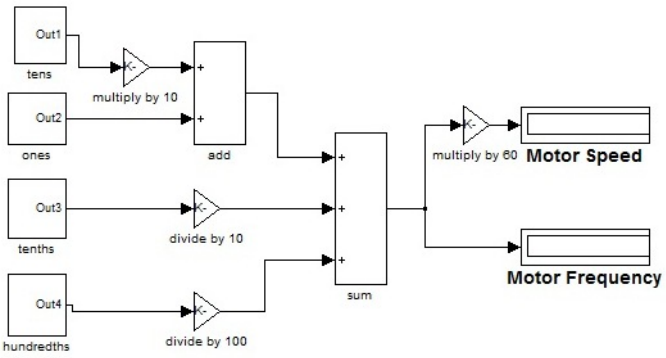

Fig. 3. Model in MATLAB, simulink

Comparison is made between the values of frequency and speed on the Oscilloscope, LCD and MATLAB display at different motor speeds.

II. Results and Discussion

The values of frequency and speed at three different motor speeds using the oscilloscope, LCD and MATLAB are as shown in Fig. 4, Fig. 5 and Fig. 6

In Fig. 4, the motor is set at approximately 2250 rpm. The frequency obtained using the oscilloscope is 37.59 Hz. This compares well with the value of 37.53 Hz recorded using the arduino and in MATLAB. The motor speed is calculated and obtained to be 2252 rpm which matches the set speed of 2250 rpm.

In Fig. 5, the motor is set at approximately 1560 rpm. The frequency obtained using the oscilloscope is 26.04 Hz. This compares well with the value of 26.02 Hz recorded using the arduino and in MATLAB. The motor speed is calculated and obtained to be 1561 rpm which matches the set speed of 1560 rpm.

In Fig. 6, the motor is set at approximately 895 rpm. The frequency obtained using the oscilloscope is 14.93 Hz. This compares well with the value of 14.91 Hz recorded using the arduino and in MATLAB. The motor speed is calculated and obtained to be 894 rpm which matches the set speed of 895 rpm.

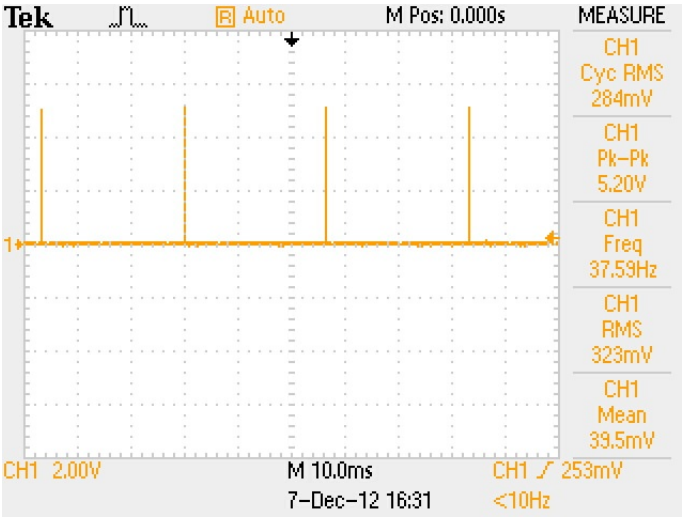

(a)

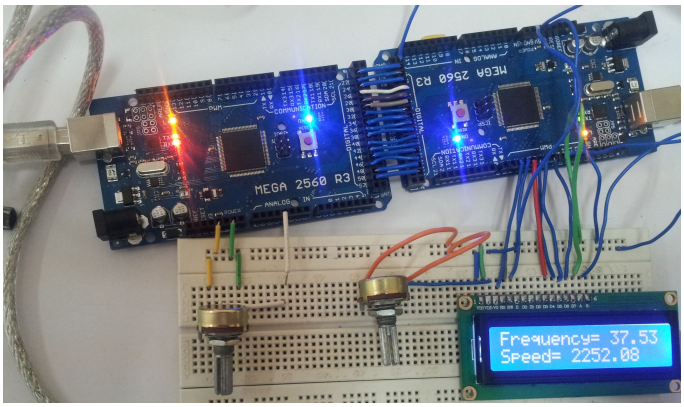

(b)

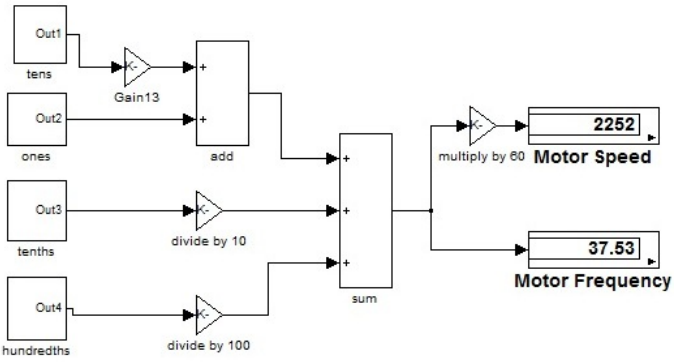

(c)

Fig. 4. Frequency and motor Speed at 2250 rpm using (a)Oscilloscope (b) LCD (c) MATLAB

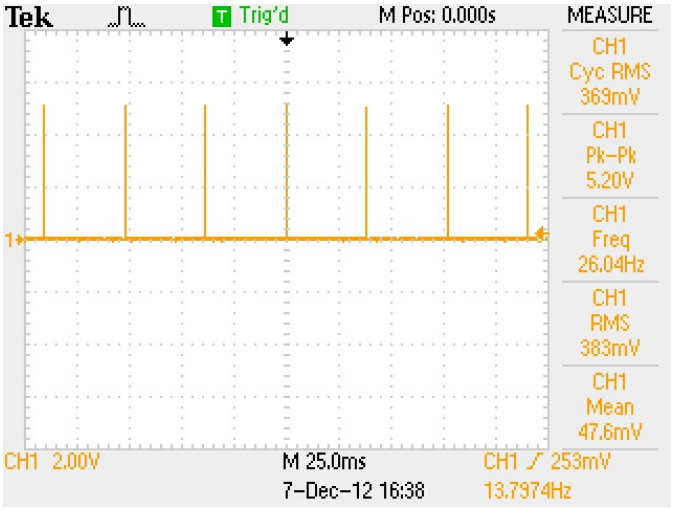

(a)

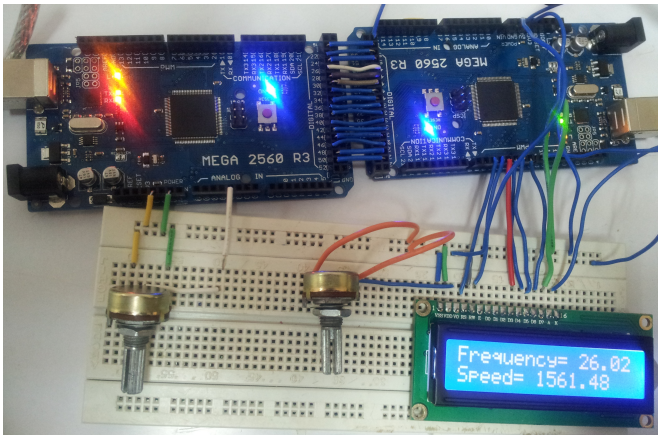

(b)

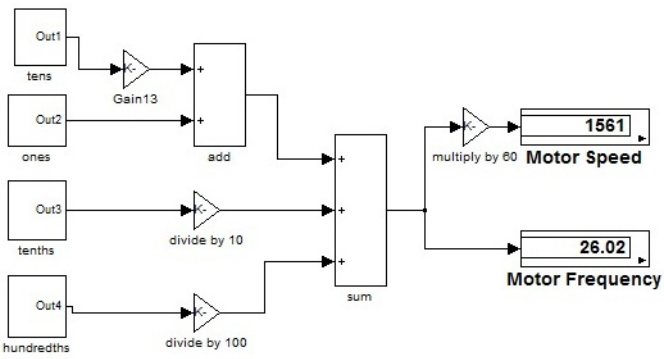

(c)

Fig. 5. Frequency and and motor Speed at 1560 rpm using (a)Oscilloscope (b) LCD (c) MATLAB

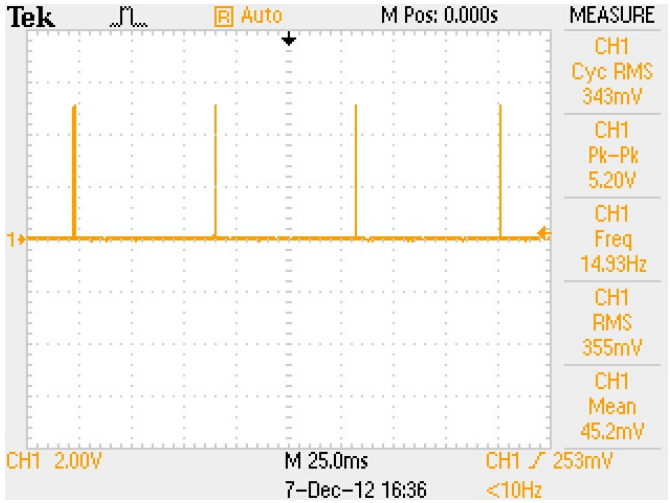

(a)

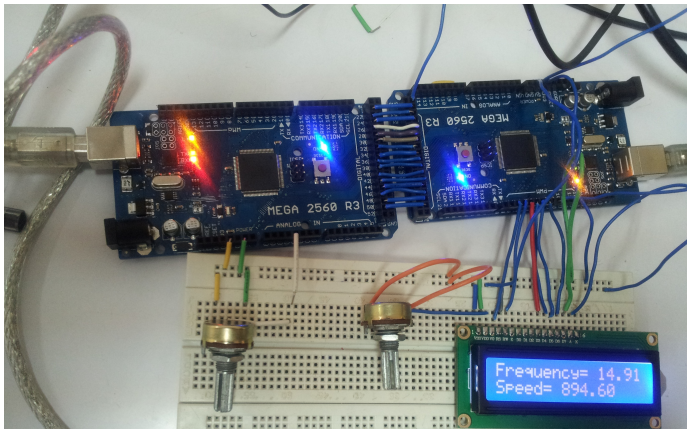

(b)

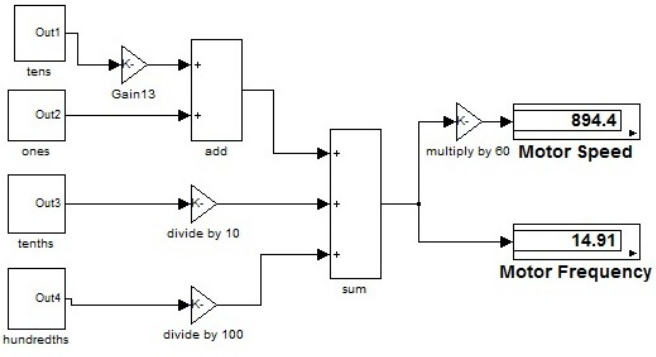

(c)

Fig. 6. Frequency and and motor Speed at 895 rpm using (a)Oscilloscope (b) LCD (c) MATLAB

III. Conclusion

In this work, real-time monitoring of motor speed in MATLAB has been achieved using magnetostrictive amorphous wire as

the speed sensor.
At different motor speed, the frequencies and speeds obtained and displayed on the oscilloscope, LCD and MATLAB compare well.
This work can be extended to real-time control of motor speed in MATLAB.

REFERENCES

[1] J. N. Nderu, A. M. Muhia, P. K. Kihato, and C. K. Kitur, "Microcontroller based magnetostrictive amorphous wire motor speed sensor," *Proceedings of the 2012 Mechanical Engineering Annual Conference on Sustainable Research and Innovation*, vol. 4, pp. 173–175, May 2012.

[2] C. K. Kitur, J. N. Nderu, and A. M. Muhia, "Microcontroller based power generation control in an isolated pico-hydro plant using magnetostrictive amorphous wire," November 2012.

Using EOG Signal to Operate Robot Manipulator System for Tracking Objects in 2D Space.

M. I Rusydi[1], T. Okamoto[2], M. Sasaki[1], S. Ito[1]

q3812204@edu.gifu-u.ac.jp, r3128004@edu.gifu-u.ac.jp sasaki@gifu-u.ac.jp satoshi@gifu-u.ac.jp

[1] Department of Mechanical Engineering, Gifu University, Gifu, Japan

[2] Department of Human and Information System, Gifu University, Gifu, Japan

Abstract

Performing some special tasks using electro-oculograph (EOG) in daily activities is being developed in various areas. In this paper, the tracking object technique using EOG as the input is introduced to help operator moving robot to desired positions. First, experiments in horizontal (right and left) and vertical (up and down) eye movement were performed to establish the correlations between EOG and gaze motions. After evaluating the equations, rotation matrixes were attached to combine the signals from horizontal (right or left) and vertical (up or down), so it was also feasible used for diagonal tracking object. To test this system, there were 3 operators tracking an object indicated by the robot manipulator movement. This test section had five routes and each route had 4 gaze motions. The result shows that this system could track an object with the average error about 0.82 cm and 1.02 cm along the X and Y-Axis.

Keywords: EOG signal, robot manipulator, tracking, eye movement, rotation matrix.

1 INTRODUCTION

Nowadays, in daily activity, people are used to working with computer or machine to improve the quality of work. But for some paralysis patients, armless person[1], older adults[2], and locked up syndrome; they face some difficulties in controlling device because of their limitation. To solve this problem, people try to establish the alternative ways to transmit and receive signal between human and machine[3].

One of the ways to handle this problem is through the biosignal technology for communication. There are many kinds of biosignal; such as electromyographic(EMG) [4], electroencephalographic(EEG)[5], and electrooculographic[6].

In this study, EOG signal is used to control robot manipulator movement in 2 dimensions for tracking object. To achieve the aim, the primarily experiment to calculate the relationship between EOG and eye gaze distance was developed. After that, using rotation matrix, the improvement of accuracy was proposed, so the equations were available not only for horizontal or vertical gaze motion but also diagonal movements.

2 EOG BASED HUMAN MACHINE INTERFACE

EOG is a weak signal that naturally occurs because the difference potential between cornea and retina. This difference arises due to the eye activity such as gaze motion and blink[7]–[9]. So, EOG signal can be recorded although in darkness condition by placing electrode around the eyes. A vertebrate has more positive polarity in cornea than retina. It is a vice versa condition for invertebrate[10].

EOG signal can be obtained by placing electrode in appropriate position around the eyes[11].This experiment used NF Instrument as the EOG sensor. This devices had 4 electrodes (ground, minus, Ch1 and Ch2) put around the eyes. Fig 1 illustrates the polarity

of eye and the attachment position of NF Instrument.

EOG is easily influenced by recording technique, environmental and the operator condition. Even a slight facial muscle activities and visual stimulation can give impact to the EOG signal form[12].

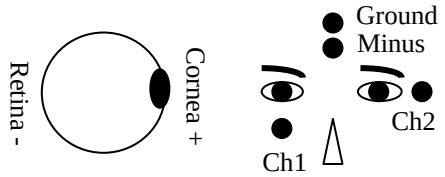

Fig 1. The polarity of eye components and the electrode positions.

3 METHODOLOGY

This present study had three main steps to achieve its goal after setting up the experiment environment. Fig. 2 shows that the first action to do is calculate the relationship between EOG and gaze motion in horizontal or vertical eye movement. Since the performance improvement is needed, so the equations were corrected after evaluating section. Rotating the equations was applied not only to raise the accuracy of the system but also to make this system working well in diagonal movement. Finally, after examining the equations which were rotated, we tried to move the robot using EOG signal.

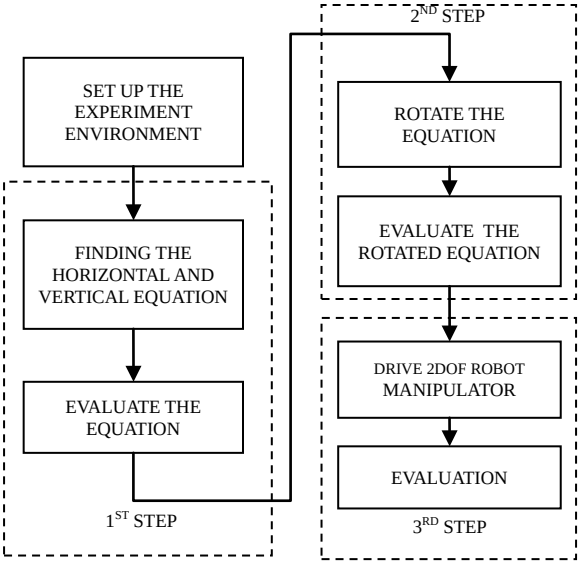

Fig 2. The flowchart of experiment.

3.1 Experiment Setup

Constructing the experiment environment set up was very necessary since this research was done in fixed head position. There are 5 points (point 1 to point 5) each in horizontal and vertical as the target (Fig. 3) which were 40 cm in front of the operator (Fig. 4). As long as this system is used in free target position, those points were needed as the primarily study respecting the relationship between EOG and gaze motion.

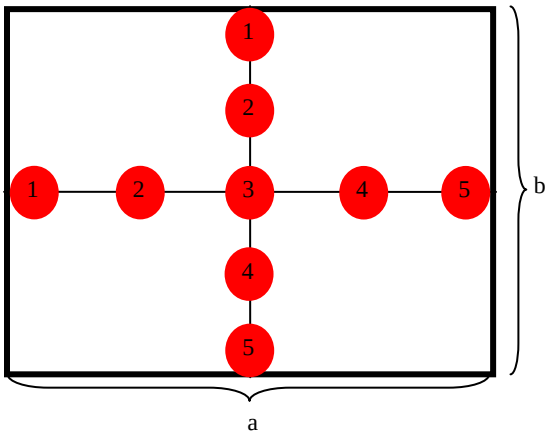

Fig 3. Five target points each in horizontal and vertical. The target point area is a = 1020 pixel/34 cm wide and b = 720 pixel/27 cm height.

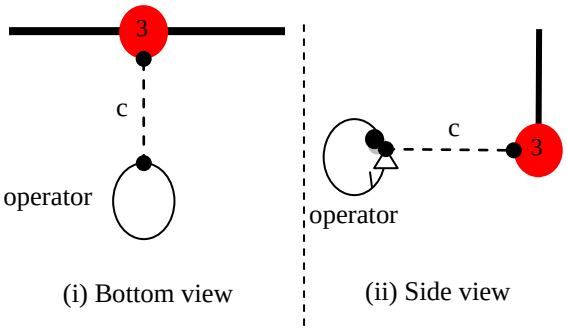

Fig 4. The normal length between operator and points is c= 40 cm.

To establish the relationship between gaze motion and EOG, there were 4 types of distance, the shortest was 1-point movement and the farthest was 4-point movement. Tab.1 shows that in vertical it is available from 180 pixels to 720 pixels and in horizontal it is from 255 pixels to 1020 pixels.

Operator was given maximum 4 areas to examine the linearity of EOG signal from them. Especially for area 1, this area was used to conclude the active area that was used for the further experiment. From Tab. 2, eye movement from point 1 to point 2 stands in area 1, from point 2 to point 3 is area 2, from point 3 to point 4 is area 3 and from point 4 to point 5 is area 4. The same idea applies to the other movements.

Table 1. The distance between 2 points in pixel.

	1-point	2-point	3-point	4-point
Vertical	180	360	540	720
Horizontal	255	510	765	1020

Table 2. Four kinds of gaze motion distance and the areas.

	Area 1	Area 2	Area 3	Area 4
1-point	1-2	2-3	3-4	4-5
2-point	1-3	2-4	3-5	
3-point	1-4	2-5		
4-point	1-5			

This test was used NF5201 instrument to drive the eye signal. The sensor had 4 electrodes that were put on specific place around eyes. Fig 5 illustrates the location where channel 1 (Ch1) is put under the left eye, channel 2 (Ch2) right side of the right eye and both of minus and ground electrode are attached on the middle of brow.

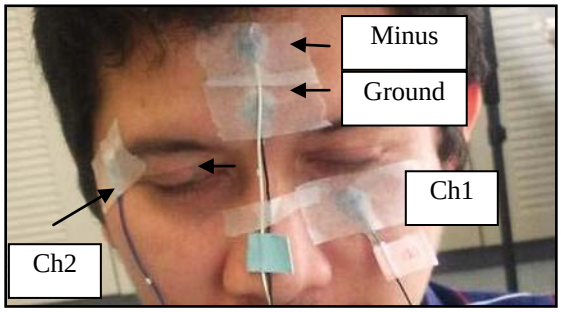

Fig 5. Position of 4 electrodes.

After that all, the EOG was used to drive robot manipulator as indicator that the tracking system ability. This robot has 2 planar joints connected to EOG computer by serial communication via ardiuno microcontroller.

3.2 Linearity of EOG and Gaze Motion

In this section, the study about horizontal and vertical gaze motion were described to get the relationship between them and EOG. The first slope of EOG when a movement occurred and the integral EOG were used as the signal features. If the signal more than positive threshold (th +) or less than negative threshold (th -), so it meant the system detecting a gaze movement. There are 2 signal patterns that can be used later to distinguish gaze motion. Fig.7 gives information about the patterns of EOG signal from Ch1 or Ch2. First wave is called negative (-) pole signal as its first slope is negative and the second one is positive (+) pole signal since the first slope is positive.

Fig 6. degree of freedom planar Robot Manipulator.

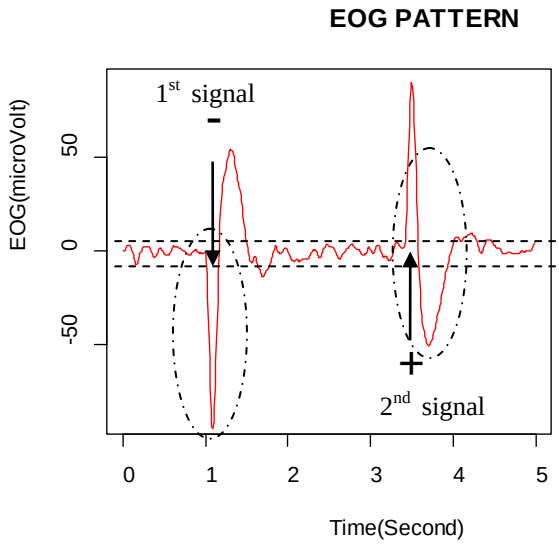

Fig 7. Signal shapes from Ch1 or Ch2 when gaze motion is detected.

As mentioned earlier, choosing active areas from the experiment design were necessary to be decided at the beginning in order to get the linear area of target. This inspection especially was focused on 1-point gaze motion. If the values of EOG were equal among the 1-point eye movements, then the next movement distance would be scanned. But, if there was found a difference in an area with others, so the next movement would be skipped. To analyze the difference between EOG among the areas, we used analysis of variance method (ANOVA) for movements that had more than 2 areas (Appendix 1(a)) and Z-score method especially for movement which had 2 areas only (Appendix 1(b)).

Using ANOVA and Z-Score could ensure that for horizontal, all areas were available for any kind of movement distances. But for vertical, we could not use them all, because there were differences between EOG values among 4 areas in 1-point movement distance. To conclude the active areas which were used, Appendix 1 (c) shows that horizontal movement can use all areas in this experiment but not for vertical and Fig 9 illustrates the active area with the pixel coordinate, which the X value ranges from -510 to 510 and the Y value ranges from 0 to 360.

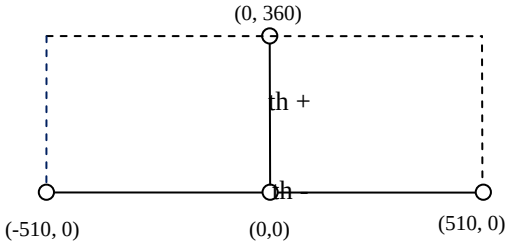

Fig 9. Pixel coordinate of active area.

To develop this system into diagonal movement detection, the experiment that could recognize EOG into 4 basic directions (right, left, up and down) had been already obtained. These basic directions are important since diagonal movement is the combination of them.

The first thing that was needed to establish the relationship between EOG and pixel was absolute integral of EOG. It was counted first when there was a signal bigger than positive threshold or smaller than negative threshold until the full wave formed (see (1) and (2)). The integral value from Ch1 belonged to up or down gaze motion and Ch2 was in the interest of right or left gaze motion. Normalization of integral EOG which was used in this system could be calculated by dividing the EOG signal with average of maximum EOG(see (3)). Table 3 provides the average maximum value of EOG for right, left, up and down from 3 operators. Finally, the linear relationship between normalized EOG and pixel are formulated from (4) to (7). The constant variable of those equations could be seen from Table 4.

Table 3. Average Maximum EOG in 4 directions from 3 operators.

	$\overline{Maximum\_\text{int}\_EOG_{ch_{i,i=1,2}}}$	Standard Deviation
Right	2094	189
Left	2031	220
Up	2398	259
Down	2370	201

Table 4. Parameter of linear equation from 3 operators.

	Ch2			
	Right		Left	
	A	B	C	D
Operator 1	1092	-108	-1091	104
Operator 2	1124	-185	-1142	207
Operator 3	1241	-278	-1113	195
	Ch1			
	Up		Down	
	E	F	G	H
Operator 1	553	-72	-546	83
Operator 2	537	22	-511	10
Operator 3	450	15	-476	17

$$\left| \int_{EOG>th+}^{EOG<th+} EOG_{Ch1} \right| + \left| \int_{EOG<th-}^{EOG>th-} EOG_{Ch1} \right| = \text{int\_}EOG_{Ch1} \quad (1)$$

$$\left| \int_{EOG>0}^{EOG<0} EOG_{Ch2} \right| + \left| \int_{EOG<0}^{EOG>0} EOG_{Ch2} \right| = \text{int\_}EOG_{Ch2} \quad (2)$$

$$Norm\_EOG_{Chi,i=1,2} = \frac{\text{int\_}EOG_{Chi,i=1,2}}{Maximum\_\text{int\_}EOG_{Chi,i=1,2}} \quad (3)$$

$$X\_right = A * Norm\_EOG_{Ch2} + B \quad (4)$$

$$X\_left = C * Norm\_EOG_{Ch2} + D \quad (5)$$

$$Y\_up = E * Norm\_EOG_{Ch1} + F \quad (6)$$

$$Y\_down = G * Norm\_EOG_{Ch1} + H \quad (7)$$

3.3 Rotation Matrix

Although we wanted to separate 2 channels into horizontal which was detected by Ch2 and vertical determined by Ch1, in fact both of the channels always drove signal when we looked at right, left, up or down. Table 5 shows the pole combinations from each of 4 basic directions. In case left eye movement, Ch1 pole was negative even the Ch2 was positive. This condition was vice versa for right gaze motion. In vertical, both of the channels gave the same pole signs as they were negative for up eye movement and negative for down gaze motion.

Fig 10. shows how the signals from Ch1 and Ch2 give the pixel value for vertical and horizontal direction. X-axis belongs to gaze movement in horizontal and Y-axis indicates the movement in vertical. In a glance, we can see that although we just only look at to a certain right or left only, there are always another signal from Ch1 that shown by the pixel in Y-axis. The same condition also occurs in vertical gaze motion.

Table 5. Channel pole detection

	Left	Right	Up	Down
Ch1	(-)Up	(+)Down	(-)Up	(+)Down
Ch2	(+)Left	(-)Right	(-)Right	(+)Left

Because value of α1, α2, α3, and α4 were founded, we proposed to rotate the X-Y coordinate in clock wise direction (see (8)), so that the X-axis exactly was on the right to left line and Y-axis was on the up to down line.

Appendix 2. shows the influence of rotation matrix on 4 basic directions. In a glance, it shows that error pixel after rotating is smaller than before this action.

$$\begin{pmatrix} X_{ar} \\ Y_{ar} \end{pmatrix} = \begin{pmatrix} \cos\alpha_i & -\sin\alpha_i \\ \sin\alpha_i & \cos\alpha_i \end{pmatrix} \begin{pmatrix} X \\ Y \end{pmatrix} i = 1,2,3,4 \quad (8)$$

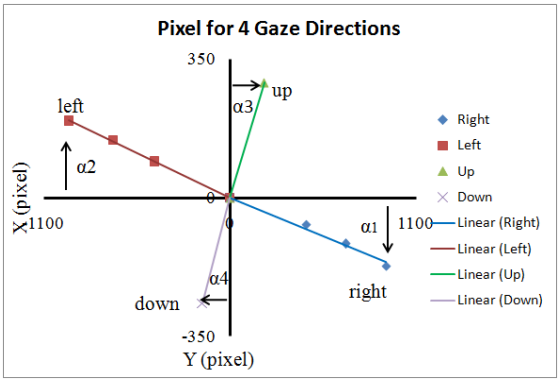

Fig 10. Pixel positions for right, left, up and down, before rotating the X-Y axis (α1 = 13.00^0, α2= 12.97^0, α3 = 52.25^0, and α4= 42.07^0).

4 RESULT

Several experiments were performed to examine the tracking object system using EOG to drive robot manipulator. There were three operators who tried to track object using EOG. The relationship between their EOG signal and pixel has already been explained in

the previous section. To examine those equations, there were 5 routes which tested not only the horizontal and vertical direction but also diagonal gaze motion. Each route experiment was performed 4 times for the eye gaze motion, where the reference point was the centre of pixels (X, Y) = (0, 0), to the target points in pixel. The routes were:
Route 1 was (400,0) → (0,0) → (400,0) → (0,0),
Route 2 was (-400,0) → (0,0) → (-400,0) → (0,0),
Route 3 was (0,300) → (0,0) → (0,300) → (0,0),
Route 4 was (200,200) → (0,0) → (200,200) → (0,0),
Route 5 was (-200,200) → (0,0) → (-200,200) → (0,0).

Appendix 3. shows that all operators success in operating the robot. The robot position always moves toward the target point. Nevertheless, there are still errors in calculating the target position. Appendix 4. gives information about the errors from all operator in 5 tracking object routes. Since 1 cm is equal to 30 pixels in horizontal or 26 pixels in vertical, this system has ability to work with the biggest error is about 76 pixels in horizontal or around 2.5 cm and 90 pixels in vertical or around 3.5 cm. This system has good potential to be improved because the average error along the X-axis is around 0.82 cm and Y-axis is 1.02 cm.

5. Conclusion

In this experiment, an EOG system which was used to drive robot manipulator for tracking object was developed not only for horizontal or vertical gaze motion but also in diagonal movement. To reduce pixel error, the rotation matrix was attached to the process based on the 4 basic directions. This system tested many times by 3 operators in 5 routes shows that it successfully tracked an object indicated by the movement of robot manipulator.

Although this system could tracks freely moving object with the level of accuracy about 1 cm, there are still many challenges to improve it. One of them is about its robustness, because the variance of EOG from an operator is big and the importance of calibration.

REFERENCE

[1] H. Harun and W. Mansor, "EOG signal detection for home appliances activation," in *5th International Colloquium on Signal Processing Its Applications, 2009. CSPA 2009*, 2009, pp. 195–197.

[2] A. Murata, "Eye-gaze input versus mouse: Cursor control as a function of age," *Int. J. Hum.-Comput. Interact.*, vol. 21, no. 1, pp. 1–14, 2006.

[3] C. G. Pinheiro, E. L. Naves, P. Pino, E. Losson, A. O. Andrade, and G. Bourhis, "Alternative communication systems for people with severe motor disabilities: a survey," *Biomed. Eng. OnLine*, vol. 10, no. 1, p. 31, Apr. 2011.

[4] A. B. Barreto, S. D. Scargle, and M. Adjouadi, "A practical EMG-based human-computer interface for users with motor disabilities," *J. Rehabil. Res. Dev.*, vol. 37, no. 1, pp. 53–63, Feb. 2000.

[5] J. R. Wolpaw, D. J. McFarland, G. W. Neat, and C. A. Forneris, "An EEG-based brain-computer interface for cursor control," *Electroencephalogr. Clin. Neurophysiol.*, vol. 78, no. 3, pp. 252–259, Mar. 1991.

[6] E. Magosso, M. Ursino, A. Zaniboni, and E. Gardella, "A wavelet-based energetic approach for the analysis of biomedical signals: Application to the electroencephalogram and electro-oculogram," *Appl. Math. Comput.*, vol. 207, no. 1, pp. 42–62, Jan. 2009.

[7] S. Aungsakun, A. Phinyomark, P. Phukpattaranont, and C. Limsakul, "Robust Eye Movement Recognition Using EOG Signal for Human-Computer Interface," in *Software Engineering and Computer Systems*, J. M. Zain, W. M. bt W. Mohd, and E. El-Qawasmeh, Eds. Springer Berlin Heidelberg, 2011, pp. 714–723.

[8] R. Barea, L. Boquete, S. Ortega, E. López, and J. M. Rodríguez-Ascariz, "EOG-based eye movements codification for human computer interaction," *Expert Syst. Appl.*, vol. 39, no. 3, pp. 2677–2683, Feb. 2012.

[9] R. J. Croft and R. J. Barry, "EOG correction of blinks with saccade coefficients: a test and revision of the aligned-artefact average solution," *Clin. Neurophysiol.*, vol. 111, no.

3, pp. 444–451, Mar. 2000.

[10] J. Malmivuo and R. Plonsey, *Bioelectromagnetism: principles and applications of bioelectric and biomagnetic fields*. New York: Oxford University Press, 1995.

[11] N. Nöjd, M. Hannula, N. Narra, and J. Hyttinen, "Electrode position optimization for facial EMG measurements for human-computer interface," *Methods Inf. Med.*, vol. 47, no. 3, pp. 192–197, 2008.

[12] N. Timmins and M. F. Marmor, "Studies on the stability of the clinical electro-oculogram," *Doc. Ophthalmol. Adv. Ophthalmol.*, vol. 81, no. 2, pp. 163–171, 1992.

Appendix 1. (a). ANOVA table to test the equality EOG in 4 areas. The hypothesis are $H_0 : \mu_1 = \mu_2 = ... = \mu_i$ and $H_a : \mu_1 \neq \mu_2 \neq ... \neq \mu_i$. (b). Z Statistical Method with 95% confidence. The hypothesis are $H_o : \mu_1 = \mu_2$ and $H_a : \mu_1 \neq \mu_2$. (c). Availability of area to be used in this research.

(a)

	1-Point Movement (i = 4 areas)								2-Point Movement (i = 3 areas)			
	Right		Right		Left		Up		Right		Left	
	Between	Between	Within	Between	Between	Within	Between	Within	Between	Within	Between	Within
Sum of Squares	22384.34	22384.34	841768.9	2392.11	22384.34	841768.9	2392.11	918031.7	22384.34	841768.9	2392.11	918031.7
DoF	3	2	158	2	2	158	2	156	2	158	2	156
Mean Squares	7461.447	7461,447	9021.95	7974.038	7461,447	9021.95	7974.038	5884.819	7461.447	9021.95	7974.038	5884.819
F-Statistic	1.400513		1.400		1.355		23.35908		1.400		1.355	
F-Table	2.67		3.05		3.05		2.67		3.05		3.05	
Conclusion	H_0 is accepted		H_0 is accepted		H_0 is accepted		H_0 is not accepted		H_0 is accepted		H_0 is accepted	

b)

	3-Point Movement (2 areas)			
	Right		Left	
	Area 1	Area 2	Area 1	Area 2
Mean	1627.955	1600.243	1581.544	1600
Variance	9711.407	9711.207	15933.79	5867.577
Sample	45	41	45	50
Z-statistic	1.302		-0.83156	
Z-Table	1.64		1.64	
Conclusion	H_0 is accepted		H_0 is accepted	

(c)

Horizontal	Area 1	Area 2	Area 3	Area 4
1-point	O	O	O	O
2-point	O	O	O	O
3-point	O	O	O	O
4-point	O	O	O	O

Vertical	Area 1	Area 2	Area 3	Area 4
1-point	O	O	X	X
2-point	O	X	X	X
3-point	X	X	X	X
4-point	X	X	X	X

O = Available
X = Not availabl

Appendix 2. Comparison between position of pixel before and after attaching the rotation matrix.

	Signal		Desired Pixel		Actual Pixel before Rotation		Actual Pixel after Rotation		Error Pixel before rotation		Error Pixel after rotation	
	$Norm\_EOG_{Ch1}$	$Norm\_EOG_{Ch2}$	X_d	Y_d	X_{br}	Y_{br}	X_{ar}	Y_{ar}	$X_{d\text{-}br}$	$Y_{d\text{-}br}$	$X_{d\text{-}ar}$	$Y_{d\text{-}ar}$
Right	0.42	0.52	510	0	461	-147	483	3	39	147	27	-3
Left	0.59	0.53	-510	0	-476	255	-540	-27	34	-255	30	27
Up	0.73	0.36	0	360	207	332	43	389	-207	24	-43	29
Down	0.69	0.26	0	-360	-180	-296	-35	-345	180	-74	35	-15

Appendix 3. Pixel positions of robot manipulator while tracking an object in 5 routes.

		1		2		3		4	
		x	y	x	y	x	y	x	y
Route 1	Op 1	379	40	17	0	369	0	64	0
	Op 2	373	26	31	7	377	31	15	0
	Op 3	393	12	-70	0	383	0	59	0
Route 2	Op 1	-375	41	-12	0	-390	39	-14	0
	Op 2	-350	24	-43	0	-377	7	-40	0
	Op 3	-442	13	-36	0	-420	15	-21	0
Route 3	Op 1	11	283	21	12	-5	317	-27	0
	Op 2	4	246	4	0	52	248	16	35
	Op 3	20	315	8	14	5	272	8	5
Route 4	Op 1	180	189	24	32	190	180	0	0
	Op 2	222	250	31	0	230	230	76	0
	Op 3	167	282	70	0	185	174	31	0
Route 5	Op 1	-190	190	8	4	-240	208	2	0
	Op 2	-250	250	4	4	-230	240	6	4
	Op 3	-196	248	6	0	-190	204	0	0

Appendix 4. Absolute error pixel position of robot manipulator while tracking an object in 5 routes.

		1		2		3		4	
		x	y	x	y	x	y	x	y
Route 1	Op 1	21	40	17	0	31	0	64	0
	Op 2	27	26	31	7	23	31	15	0
	Op 3	7	12	70	0	17	0	59	0
Route 2	Op 1	25	41	12	0	10	39	14	0
	Op 2	50	24	43	0	23	7	40	0
	Op 3	42	13	36	0	20	15	21	0
Route 3	Op 1	11	17	21	12	5	17	27	0
	Op 2	4	54	4	0	52	52	16	35
	Op 3	20	15	8	14	5	23	8	5
Route 4	Op 1	20	11	24	32	10	20	0	0
	Op 2	22	50	31	0	30	90	76	0
	Op 3	33	82	70	0	15	26	31	0
Route 5	Op 1	10	10	8	4	40	8	2	0
	Op 2	50	50	4	4	30	40	6	4
	Op 3	4	48	6	0	10	4	0	0

FUZZY C-MEANS OPTIMIZATION FOR BASE STATION CLUSTERING

Antony Onim[1], P. K. Kihato [1], Stephen Musyoki[2]

onim.antony@gmail.com, smusyoki@jkuat.ac.ke, kamitazv@yahoo.co.uk

[1]Jomo Kenyatta University of Agriculture and Technology, Department of Telecommunication Engineering

[2]Jomo Kenyatta University of Agriculture and Technology, Department of Electrical Engineering

ABSTRACT- This paper addresses the problem of optimal distribution of Base Transceiver Stations (BTS) in a geographical area. Expansion of telecommunication industry results in stiff competition among service providers which leads to focus on quality of services delivered. Increase in number of mobile phone usage has also led to unprecedented increase in network traffic. This paper focuses on using Fuzzy C-means (FCM) to distribute the BTSs. The FCM has to be optimized to achieve the best results.

Key words- BTS Optimization, Cell tower placement, Path loss, Link budget

I. INTRODUCTION

Network optimization is an important aspect of networking since it allows for: [1]

- Proper resource and capital allocation: Optimization encourages efficient allocation of capital in networks to use of bandwidth and equipment profitably. Telecommunication equipment such as BTS, cell towers etc. are costly to purchase, deploy and maintain. Allocation of equipment where they are required leads to massive savings for service providers.
- Operation cost reduction: Operation costs are expenses incurred during the lifetime of equipment to keep them in service. Optimization reduces the number of equipment required to a minimum and as a result reduces costs such as power consumption, repair and maintenance.

Link budget is an account of all gain and losses beginning from transmitter, propagation medium to the receiver in a telecommunication network. A simple representation of the link budget can be represented by the equation below: [2]

Received Power (dBm) = Transmitted Power (dBm) + Gains (dB) − Losses (dB) (1)

Typical transmission power for both BTS and MS can be summarized as:

TABLE I
MOBILE STATION AND BTS POWER CATEGORIZATION
BTS [3]

CLASS	POWER
1	320W (55 dBm)
2	160W (52 dBm)
3	80W (49 dBm)
4	40W (46 dBm)
5	20W (43 dBm)
6	10W (40 dBm)
7	5W (37 dBm)
8	2.5W (34 dBm)

MS		
CLASS	**POWER**	**TYPE**
1	20W (43 dBm)	Vehicle & Portable
2	8W (39 dBm)	Vehicle & Portable
3	5W (37 dBm)	Hand held
4	2W (33 dBm)	Hand held
5	0.8W (29 dBm)	Hand held

Gains arise mainly from antenna gains at transmitter and receiver ends. Transmitter gain boosts the power of transmitter signal and is normally directed toward the receiver. Receiver gain increase power of weak signal received. [4]

Losses arise from transmission line losses as well as transmitter and receiver antenna inefficiencies.
Transmission line losses can be due to:

i. Free space loss
ii. Refraction
iii. Diffraction
iv. Reflection
v. Absorption
vi. Buildings and vegetation
vii. Multi-path

Path losses are due to transmission medium. Path loss is important in telecommunication link budget calculations because it determine the range of a BTS cell. MS is the largest determinant of the cell radius. MS limitations are:

i. Fixed and low power supply
ii. Low transmitter antenna gain
iii. Low receiver antenna gain
iv. Limited signal processing compared to the BTS

Coupled with path losses, the range of the transmitter is reduced. The aim is to optimize BTS location by minimizing path loss and retain it at an acceptable level. This is achieved by putting network equipment and other resources close areas to where they are most required thereby reducing transmission losses.

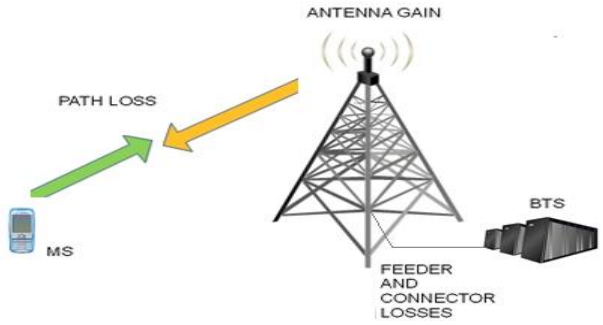

Fig. 1 BTS – MS gains and losses

Networking equipment cannot always be in the most optimal position due to social, political, economic and geographic factors. For example if population center shift as a due to construction new buildings such as schools, hospitals, apartments etc. which concentrate mobile stations in a small space. In such cases micro-cells are advisable. In the event of large changes, new cell have to be created since UMTS BTS can handle a finite number of users. This paper depicts a situation in which population grows and how it affects optimal location of BTS.

Optimum BTS locations change with time as population centers change. Whether or not service providers decide to add equipment or decommission others is a judgment that is left to the engineers. Equipment can be added if funds are available and also the new population to be covered is profitable and can return the investment in the new equipment. This decision differs from place to place and one engineer to the other and cannot be made by machinery as it is one of a social nature.

II. MATHEMATICAL FORMULATION

A. Link Budget

A link budget equation is given below: [5]

$$P_{RX} = P_{TX} + G_{TX} + G_{RX} - L_{TX} - L_{FS} - L_{FM} - L_{RX} \quad (2)$$

Where:
PRX= received power (dBm)
PTX = transmitter output power (dBm)
GTX = transmitter antenna gain (dBi)
GRX = receiver antenna gain (dBi)
LTX = transmit feeder and associated losses (feeder, connectors, etc.) (dB)
LFS = free space loss or path loss (dB)
LFM = many-sided signal propagation losses due to the transmission medium(dB)
LRX = receiver feeder losses (dB)

Free space loss is given by:

$$L_{FreePathloss} = 32 + 20 \cdot \text{Log}(f) + 20\text{Log}(d) \quad (3)$$

Where: d = Distance in meters

Downlink power should be equal or less than uplink power. When downlink power is greater than the uplink power, the range cells increase. Calls at the edge of the cell are dropped because BTS will be out of range of MS transmitter.

TABLE II
LIST OF CONSTANTS IN HATA PATH LOSS EAUATION

AREA	a(hm)	K
Open	[1.1Log10(fMHz)-0.7]hm - [1.56Log10(fMhz)-0.8]	4.78[Log10(fMHz)]2 – 18.33Log10(fMHz) + 40.94
Suburban	[1.1Log10(fMHz)-0.7]hm - [1.56Log10(fMhz)-0.8]	2[Log10(fMHz/28)]2 + 5.4
Small city	[1.1Log10(fMHz)-0.7]hm - [1.56Log10(fMhz)-0.8]	0
Large city	3.2[Log10(11.75hm)]2 – 4.97	0

1) Uplink budget:

a) Transmission from MS to BTS

$$EIRP = P_{TX} + L_{AF} + G_{ME} \quad (4)$$

Where:
- EIRP = Effective Isotropic Radiated Power
- P_{TX} = Power transmitted by the MS
- L_{AF} = Antenna feeder and connector losses
- G_{ME} = MS antenna gain

b) Receiver side: BTS is receiver

$$R_S = EIRP – L_P - I_M – F_M - L_C + G_{BTS} \quad (5)$$

Where:
- R_S = Receiver sensitivity
- L_P = Path loss
- I_M = Interference
- F_M = Fast fade margin
- L_C = Connector losses
- G_{BTS} = BTS antenna gain

2) Path loss calculation

Path loss can be calculated from the above equation by making L_P subject.
From Hata model path loss equation: [6]

$$L_P = 69.55 + 26.16Log10\ (f_{MHz}) - 13.82Log10\ (h_b) – a(h_m) + [44.9-6.55Log10\ (h_b)]Log10\ (d_{km}) – K \quad (6)$$

To get maximum cell size, make distance d subject of Hata path loss equation to yield Hata maximum distance equation:

$$d = antiLog10\ \{[P_t + G_{tot} - R - 69.55 - 26.16Log10\ (f_{MHz}) + 13.82Log10\ (h_b) + a(h_m) + K] / [44.9 – 6.55Log10(h_b)]\} \quad (7)$$

Where:
- G_{tot} = Total gain
- hb = Base antenna height over street level in meters
- hm = Mobile station antenna height in meters
- hB = Nominal height of building roofs in meters

Minimizing distance d between the BTS and MS while keeping path loss less than 140 dB:
1. Number of BTS are reduced to a minimum
2. Power required to run BTS and MS reduces
3. Number of calls dropped due to high path loss values reduces.

III. FUZZY CLUSTERING

Fuzzy c-means (FCM) is a data clustering technique in which a dataset is grouped into n clusters with every data point in the dataset belonging to every cluster to a certain degree. For example, a certain data point that lies close to the center of a cluster will have a high degree of belonging or membership to that cluster and another data point that lies far away from the center of a cluster will have a low degree of belonging or membership to that cluster.

FCM starts with an initial guess for the cluster centers, which are intended to mark the mean location of each cluster. The initial guess for these cluster centers is most likely incorrect. Next, FCM assigns every data point a membership grade for each cluster. By iteratively updating the cluster centers and the membership grades for each data point, FCM iteratively moves the cluster centers to the right location within a data set. This iteration is based on minimizing an objective function that represents the distance from any given data point to a cluster center weighted by that data point's membership grade.[9]

$$J(U,V) = \sum_{i=1}^{n}\sum_{j=1}^{c}(u_{ij})^m ||x_i - v_j||^2 \quad (8)$$

Where,

$||x_i - v_j||$ is the Euclidean distance between i^{th} data and j^{th} cluster center.

n = number of data points.

$v_j = j^{th}$ cluster center

m = fuzziness index m $\in [1, \infty]$

c = number of cluster center.

u_{ij} = membership of i^{th} data to j^{th} cluster center.

$U = (u_{ij})n*c$ is the fuzzy membership matrix.

J = objective function.

A. Algorithmic steps for Fuzzy c-means clustering [7] [8]:

If X = {x_1, x_2, x_3 ..., x_n} is set of data points and V = {v_1, v_2, v_3 ..., v_c} the set of centers.

1) Select c cluster centers randomly.

2) Calculate the fuzzy membership u_{ij} using:

$$u_{ij} = 1/\sum_{k=1}^{c}(d_{ij}/d_{ik})^{(\frac{2}{m}-1)} \quad (9)$$

Where:

k = iteration step.

d_{ij} = Euclidean distance between i^{th} data and j^{th} cluster center.

3) Compute the fuzzy centers v_j using:

$$v_j = \frac{\left(\sum_{i=1}^{n}(u_{ij})^m x_i\right)}{\sum_{i=1}^{n}(u_{ij})^m}, \forall j = 1,2,\ldots c \quad (10)$$

4) Repeat step 2) and 3) until the minimum J value is achieved or $||U^{(k+1)} - U^{(k)}|| < \beta$.

Where:

β = termination criterion between [0, 1].

B. Advantages of Fuzzy-C-Means

1. Gives best result for overlapped data set and comparatively better then k-means algorithm.
2. Unlike k-means where data point must exclusively belong to one cluster center here data point is assigned membership to each cluster center as a result of which data point may belong to more than one cluster center.

IV. RESULTS

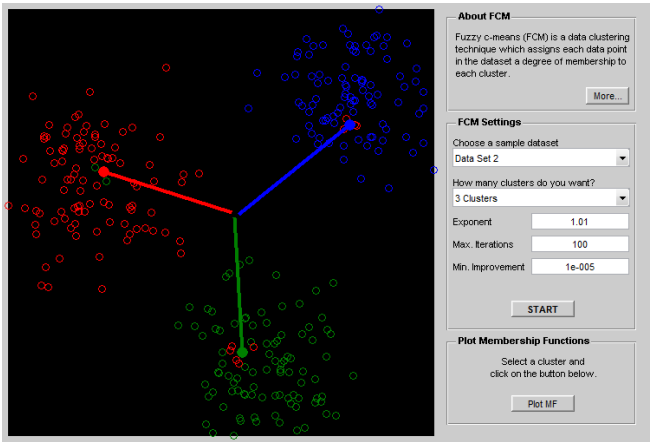

Fig. 2 Clustering using exponent value of 1.01

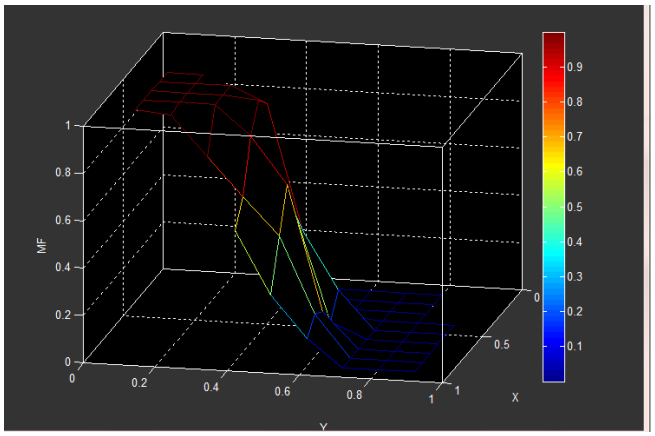

Fig. 3 Membership function of exponent value of 1.01

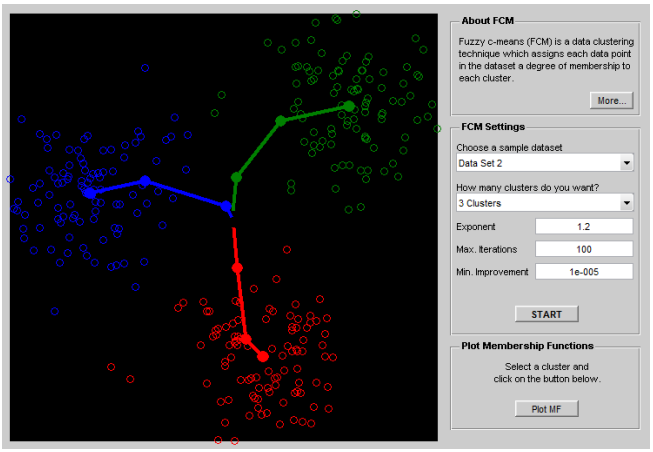

Fig. 3 Clustering using exponent value of 1.2

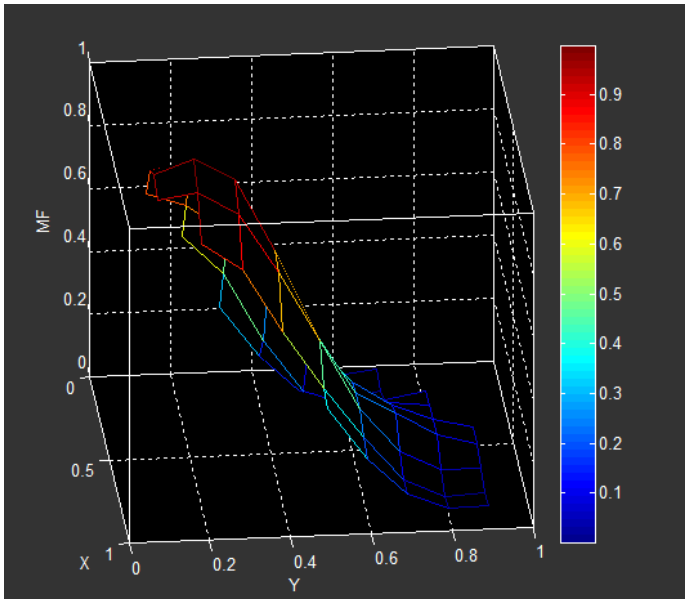

Fig. 4 Membership function of exponent value of 1.2

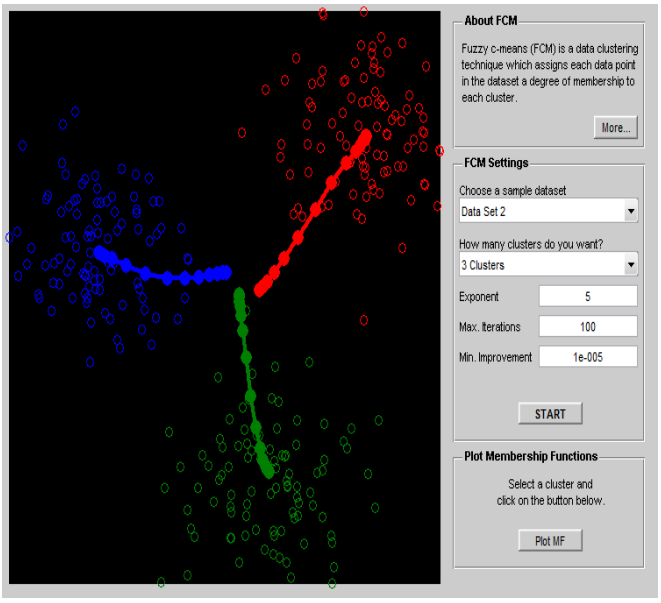

Fig. 7 Clustering using exponent value of 5

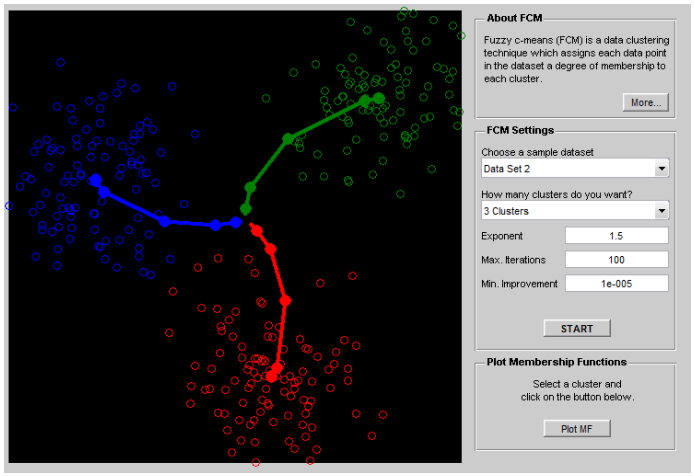

Fig. 5 Clustering using exponent value of 1.5

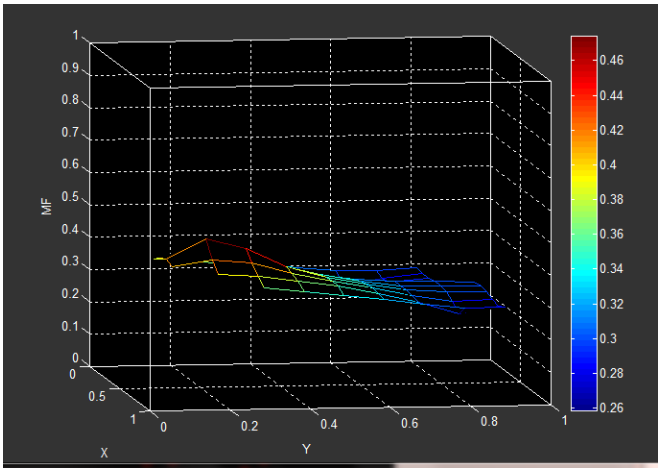

Fig. 8 Membership function of exponent value of 5

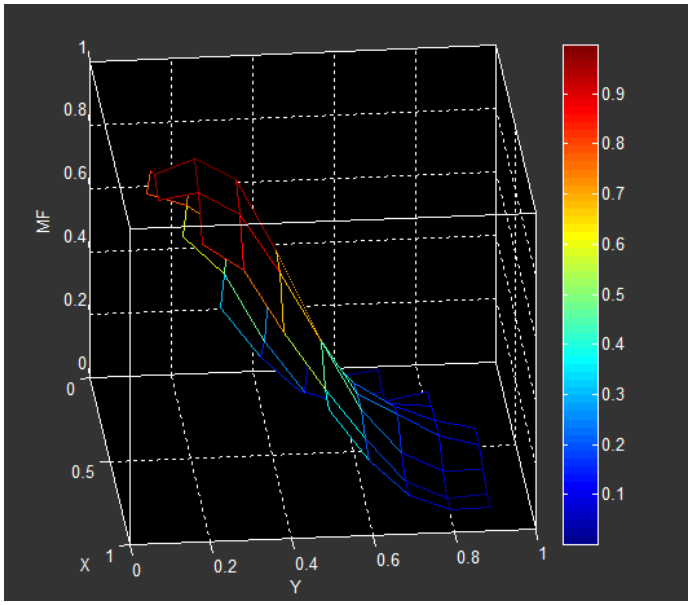

Fig. 6 Membership function of exponent value of 1.5

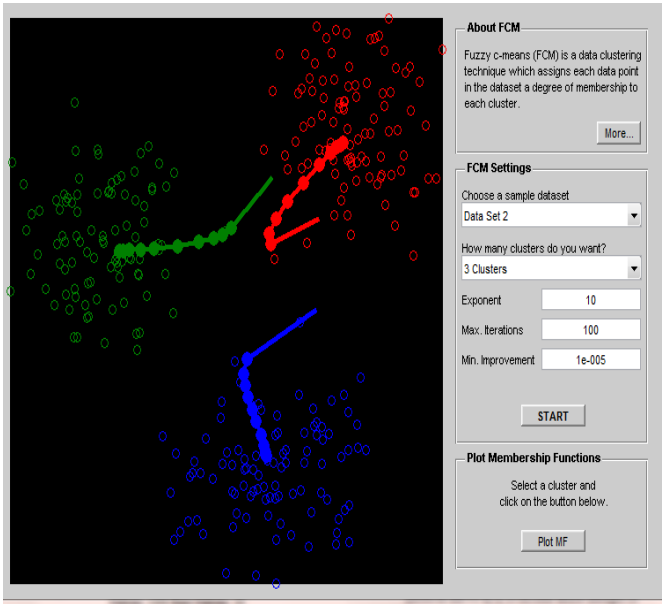

Fig. 9 Clustering using exponent value of 10

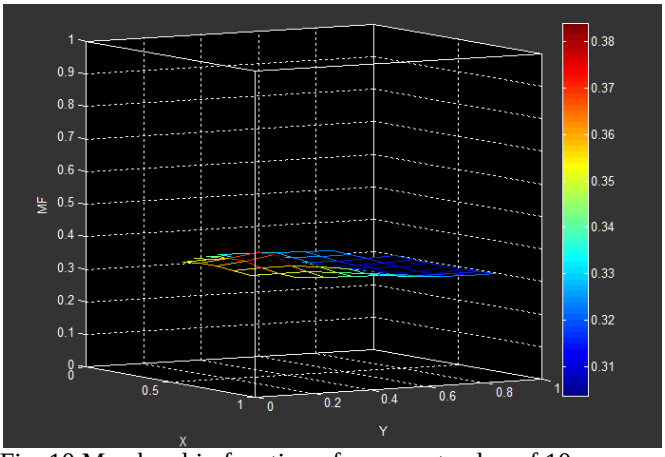

Fig. 10 Membership function of exponent value of 10

V. EXPALANATION OF RESULTS

FCM takes in inputs of mobile station distribution, exponent value, maximum number of iterations and minimum improvement. This paper mainly focuses on the effect of the fuzzy exponent value. The values of maximum iterations and minimum improvement are set as default of 100 and 1e-005 respectively. The values for the exponent investigated are 1.01, 1.2, 1.5, 5 and 10. At value of 1.01 the FCM allocates the centres but fails to properly assign some points to the correct clusters. Some points belonging to the 'red' cluster are in the 'blue' cluster. Exponent values of 1.2 and 1.5 shows the best results since all members in each cluster are properly assigned. The membership function (MF) is also ranging from 0.1 – 0.9 meaning points closer to the centre have more membership to the center than those farther away. Exponent values of 5 and 10 shows that the clustering is fairly done. However the MF graphs range from 0.26-0.46 and 0.31-0.38 respectively. This shows poor membership at these values since the expected values should range from 0-1.

This therefore shows that the membership values in the range of 1.2-1.5 would produce the best results when considering correct location of centres, proper assignment of the points to their respective centres and proper membership function representation.

REFERENCES

[1] M. R. Karim, *W-CDMA and cdma2000 for 3G Mobile Networks*.: McGraw-Hill Telecom., 2002, ch. 1-4.

[2] Purnima K. Sharma and R. K. Singh, "Cell Coverage Area and Link Budget Calculations in GSM System," in *International Journal of Modern Engineering Research (IJMER)*, vol. Vol.2,Issue.2 , 2012, pp. 173-174.

[3] Dr. S. A. Mawjoud, "Evaluation of Power Budget and Cell Coverage," in *Al-Rafidain Engineering*, vol. Vol.16, 2008, pp. 37-47.

[4] Rappaport, *Wireless Communications*. Upper Saddle River, New Jersey: Prentice-Hall, 1996, ch. 3.

[5] Radio-Electronics.com. Radio-Electronics.com. [Online]. http://www.radio-electronics.com/info/propagation/path-loss/rf-signal-loss-tutorial.php.

[6] Directorate-General for Communications Networks,Content and Technology,European Commission, "DIGITAL MOBILE RADIO TOWARDS FUTURE GENERATION SYSTEMS," in *COST 231 Final Report.*, 1999, ch. 3-4. [Online]. http://www.lx.it.pt/cost231/final_report.htm

[7] James Keller, Raghu Krisnapuram, Nikhil R. Pal James C. Bezdek, "Fuzzy Models and Algorithms for Pattern Recognition and Image Processing," in *Fuzzy Models and Algorithms for Pattern Recognition and Image Processing*.: Kluwer Academic Publishers, 1999, ch. 2-4.

[8] ROBERT EHRLICH, WILLIAM FULL JAMES C. BEZDEK, "FCM: THE FUZZY c-MEANS CLUSTERING ALGORITHM," *Computers & Geosciences*, vol. 10, no. 2-3, pp. 191-203, 1984.

[9] Data Clustering Algorithms. (2012) Data Clustering Algorithms. [Online]. https://sites.google.com/site/dataclusteringalgorithms/fuzzy-c-means-clustering-algorithm

System Level Performance of Interference Alignment in LTE using the Vienna LTE System Level Simulator

Luke Oduor Otieno, Philip Kibet Langat, Stephen Musyoki

luke.otieno@hotmail.com, *kibetlp@gmail.com*

Abstract: Since its introduction, Interference Alignment (IA) has witnessed a lot of interest and research at its improvement and potential inclusion into practical wireless networks continues. However, the simulated assessment of its performance has often been based upon proprietary simulators. Reproducibility of research results therefore becomes a big challenge. The Vienna LTE (Long Term Evolution) System level simulator is an open source simulator that promises reproducibility of results across the research community, in academy and industry. Whereas IA performance in LTE evaluations has been made before using proprietary simulators, this, to the best of our knowledge, provides the first attempt at producing results that will be reproducible. A campaign of simulations are conducted using MATLAB® and the bit error rates (BER) and capacity under varying traffic conditions, channel conditions and scheduling is evaluated. In conclusion, this work presents the first, to the best of our knowledge, truly reproducible performance evaluation of IA in a realistic LTE network cellular network.

Keywords: Vienna LTE System Level Simulator, LTE, Reproducibility, System Level Simulator

Malignant Tumor Detection using Finite Volume Time Domain

Kenneth O.Dinga[1], D.B.O Konditi[2], H. Ouma[3]

[1]Graduate Student, Faculty of Engineering, Jomo Kenyatta University of Agriculture and Technology, P. O. Box 62000-00200, Nairobi, Kenya

Corresponding Author Email: Kendinga@yahoo.com

[2]Professor, Faculty of Engineering, Multi-Media University College of Kenya, P. O. Box 30305-00100, Nairobi, Kenya

[3]Lecturer, School of Engineering, Nairobi University, P. O. Box 30197-00100, Nairobi, Kenya

ABSTRACT

For a long time microwave engineers have dreamed of using non-ionizing electromagnetic waves to image the human body in order to detect cancer. Over the past several years, significant progress has been made towards making this dream a reality for breast cancer detection. In the next decade, microwave systems are likely to become viable diagnostic option for many women and men alike. More so than for any other cancers, breast tumors have electrical properties at microwave frequencies that are significantly different from those of healthy breast tissues. The breast can easily be accessed from outside, while internal organs are much less accessible. Normal breast tissue is also more translucent to microwaves than many other tissues, such as muscle or brain. Phenomenal progress in computers and numerical techniques during the past decade allows us to effectively process data acquired through measurements. This paper proposes a new methodology for analyzing malignant tumors. The methodology will be based on finite volume time domain (FVTD) modeling approach. In the past finite difference time domain modeling schemes have been used to detect tumors. However, though it is simple and has wide frequency coverage, its main drawback is that it is computationally intensive. To overcome this drawback finite volume time domain (FVTD) is proposed as a suitable modeling technique for the problem.

Keywords: Conformal microwave technology; finite difference time domain, malignant tumor; permittivity; conductivity; finite volume time domain

1.0 INTRODUCTION

There is considerable recent debate as to whether or not women under 50 years of age should have X-ray mammograms. This debate arises from the need to detect breast cancer in its earliest stage. Early detection leads to longest survival and greatest patient comfort. While mammography is recognized as the preferred method to detect breast cancer, it fails to detect as many as 20% of the malignant tumors. Further, it may be uncomfortable or threatening to many of the patients, especially with the public perception that repeated X-ray mammograms increase the risk of cancer. Other modalities such as ultrasound and magnetic resonance imaging (MRI) are either less effective or too costly. Pulsed confocal microwave technology can complement mammography by remedying most of the above noted deficiencies.

1.1 Physical Basis of the method

The confocal, microwave breast cancer detection technology is based upon two fundamental properties of breast tissues at microwave frequencies. Microwaves interact with biological tissues primarily according to the tissue water content. This is a different interaction mechanism than for X-rays. The relevant physical properties contrast between malignant tumors and normal breast tissues is significantly greater for microwaves than for either X-rays or ultrasound, approaching an order of magnitude. This large dielectric contrast causes malignant tumors to have significantly greater microwave scattering cross sections than normal tissues of comparable geometry.

Microwave attenuation in normal breast tissue is less than 4 dB/cm up to 10 GHz. This may permit existing microwave equipment having standard sensitivity and dynamic range to detect tumors located up to about 5 cm beneath the skin. The microwave attenuation and phase characteristic of normal breast tissue is such that constructive addition is possible for wide-bandwidth backscattered returns using broad aperture confocal-imaging techniques. The confocal technique suppresses returns from spurious scatterers such as a vein interposed between the tumor and the surface of the breast.

1.2 BREAST TISSUE DIELECTRIC PROPERTIES

Gabriel *et al.* [1]–[4] indicates that the relative dielectric permittivity ε_r, and conductivity σ, of high-water-content tissues (such as muscle or malignant tumors) are about an order of magnitude greater than those of low-water-content tissues (such as fat or normal breast tissue). As illustrated in Figures 1 and 2, this contrast between high- and low-water-content tissues persists over the entire radio frequency (RF) spectrum from power frequencies through millimeter waves.

.

1.2.1 Malignant Tumor Properties

Foster and Schepps [5], Rogers *et al.* [6], and Peloso *et al.* [7] separately measured ε_r and σ of malignant tumors and found values above 1 GHz that are almost the same as for normal high-water-content tissues such as muscle. In some cases, ε_r and σ for malignant tumors were significantly greater than for normal muscle tissues, especially at frequencies below 1 GHz.

Swarup *et al.* [8] studied the onset of the high values of ε_r and σ in malignant tumors by measuring MCA1 fibro sarcoma mouse tumors at 7, 15, and 30 days after inception. No significant variation of ε_r and σ was seen with tumor age. While the larger tumors exhibited a necrotic interior, they showed little difference in ε_r and σ above 0.5 GHz.

Surowiec *et al.* [9] performed measurements of cm-size malignant human breast tumors and adjacent tissues and found an increase in ε_r and σ of the normal breast tissue near malignant tumors. This effect may be caused by infiltration or vascularization. It could enlarge the microwave scattering cross-section and thereby aid in the confocal microwave detection of the tumor.

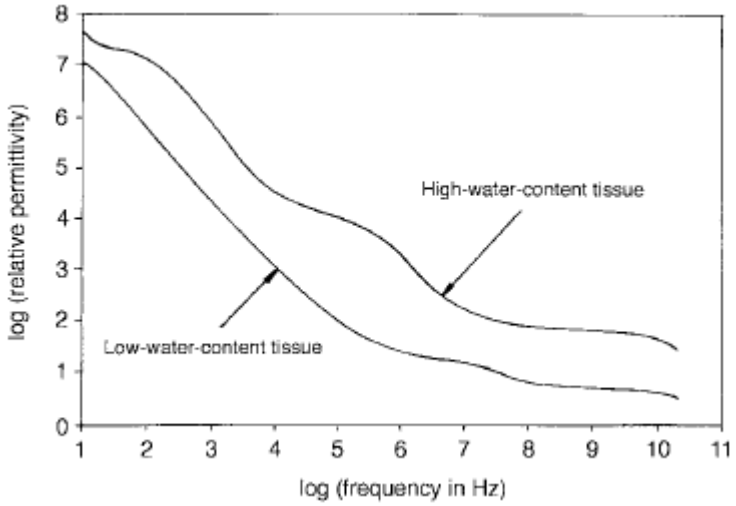

Figure 1: Comparison of the permittivity of high water content tissue with low water content tissue as a function of frequency

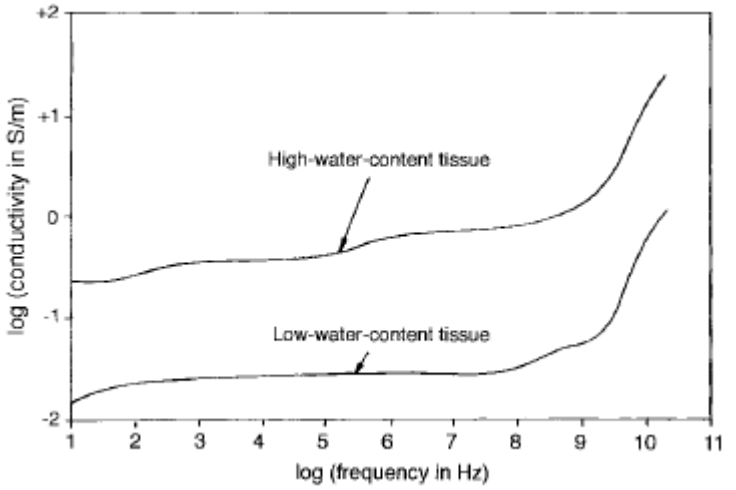

Figure 2: Comparison of the conductivity of high water content tissue with low-water content tissue as a function of frequency

1.3. 2-D Finite Difference Time Domain of a Pulsed Microwave System

1.3.1 Modeling of the Fixed Focus Elliptical System

As the first step in the systems analysis, a fixed focus confocal microwave system employing a metal elliptical reflector was computationally modeled in two dimensions using the finite-difference time-domain (FDTD) solution of Maxwell's equations, for the transverse magnetic case. The reflector was specified with one focal point at a monopole antenna element and one in a breast half-space 3.8 cm below the surface. (In such two-dimensional (2-D) models, all material structures in the computational space, including the antenna, are assumed to be infinitely long. Thus, there is no ground return for the antenna and it is termed a "monopole.")

Figure 3 illustrates the FDTD model of this system. This model used a uniform grid with square unit cells as fine as 0.2 mm in the highest-resolution simulations. The reflector was assumed filled with lossless dielectric ($\varepsilon_r = 9$, $\sigma = 0$) matching the nominal breast permittivity,

and was located at the surface of a half-space of normal breast tissue ($\varepsilon_r = 9$, $\sigma = 0.4$ S/m). No skin layer was modeled. The monopole antenna was excited by a 270-ps Gaussian pulse multiplying a 6-GHz sinusoid that passed through zero at the peak of the Gaussian. This signal has zero dc content and a Gaussian, double sideband (DSB) suppressed-carrier spectrum symmetric about 6 GHz. The full-width spectral bandwidth at half-maximum extends from 4 to 8 GHz. A circular tumor extends from 4 to 8 GHz. A circular tumor ($\varepsilon_r = 50$, $\sigma = 7$ S/m) was assumed located at the in-breast focus.

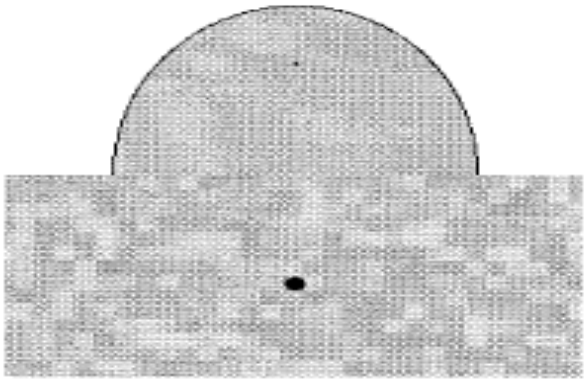

Figure 3: 2-D FDTD Computational model of the elliptical reflector system showing the heterogeneous breast tissue model and 0.5cm diameter tumor located at the in breast focus 3.8cm beneath the surface.

Figure 4 depicts the calculated time waveforms of the backscattered power response for this model with and without the 0.5-cm-diameter tumor present at the in-breast focus 3.8 cm below the surface.

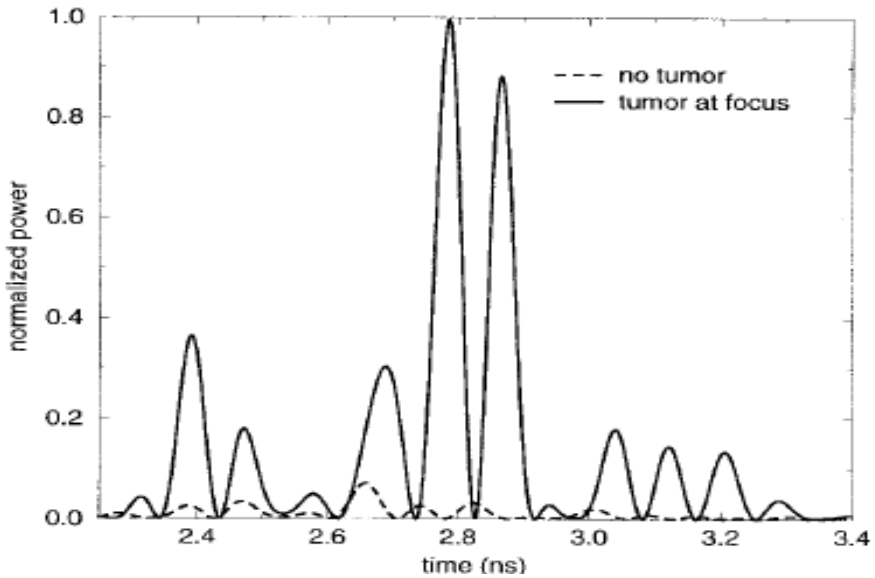

Figure 4: FDTD-computed time domain waveforms of the backscattered response with and without the 0.5cm diameter tumor present at the in-breast focus

1.4 FINITE VOLUME TIME DOMAIN

The Finite-Volume Time-Domain (FVTD) method, as a general time-domain field solver, has successfully been applied to a variety of electromagnetic structures. The advantage of an unstructured mesh with tetrahedral volume elements places the FVTD method somewhat in between the Finite Element Time-Domain (FETD) method and the Finite-Difference Time-Domain (FDTD) method. Since the FVTD method is still in its infancy in computational electromagnetic application – at least in comparison to the FDTD method – the potential of this relatively new approach has not been fully unfolded yet. Although several authors have illustrated the capability of the FVTD method for the analysis of large scale problems [10] or problems with fine details surrounded by curved linear boundaries [11], the achievable accuracy for the FVTD method in particular for problems requiring a large dynamic range, has not been demonstrated so far. The FVTD method is inherently applied in unstructured meshes and thus is able to approximate complex geometries naturally without additional effort. In contrast, methods using structured meshes, e.g. a classic stair casing FDTD approach, may need to incorporate artificial treatment of boundaries to meet certain accuracy requirements.

1.4.1 Electromagnetic wave diffraction using a finite volume method

Simulation of near fields scattered by an aircraft illuminated by an incident plane wave will be discussed. An exciting Gaussian pulse in the time domain is used for the following example in the computational time interval. The scatterer is assumed to be perfectly conductive. In Figures: 5 and 6, we present the meshes used for the numerical simulations. For the FDTD, the computational domain is composed of 4144000 volumes and for FVTD, the discretization leads to 79361 volumes with the same minimum mesh size. The results presented in Figure. 7 shows the x-component of the electric field and the y-component of the magnetic field computed at points A and B with the two methods. In this example the use of FVTD permits an important gain in memory and a gain of 3 in time compared with FDTD, despite a smaller time step to ensure the scheme's stability and a larger number of operations in FVTD than in FDTD.

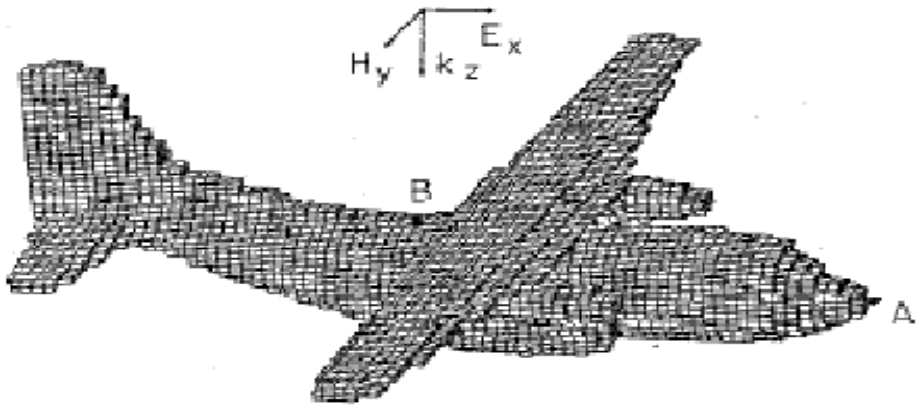

Figure 5: FDTD Meshing

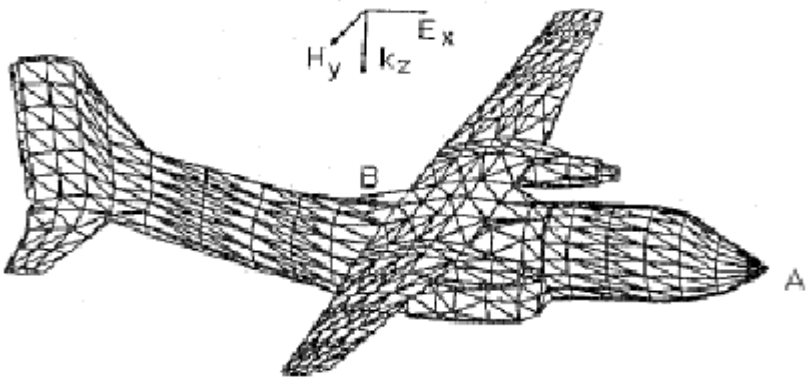

Figure 6: FVTD Meshing

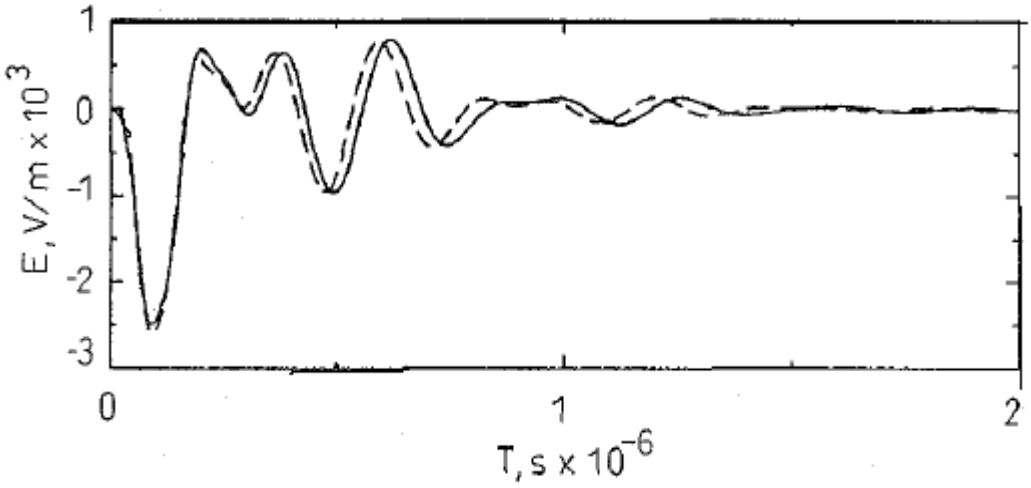

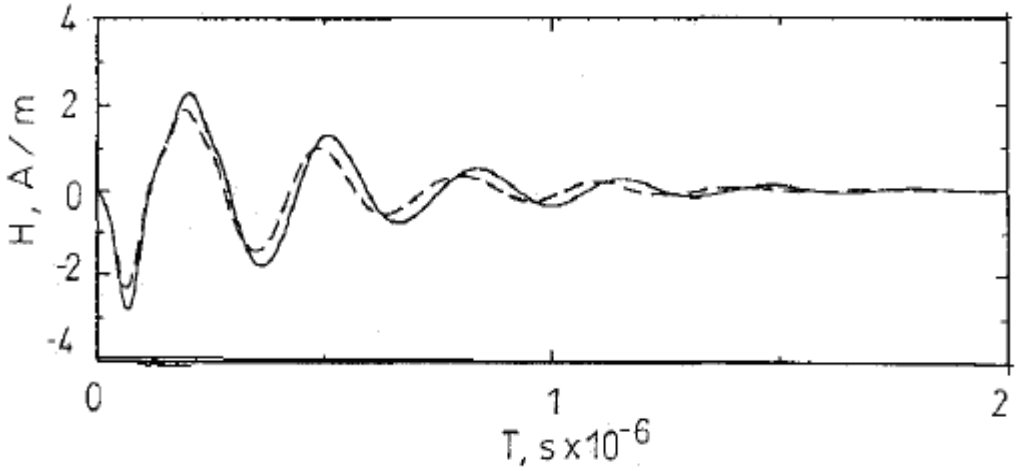

- - - - - FDTD
_____ FVTD

Figure 7: Comparison between FDTD and FVTD

1.5 Conclusion

The finite volume technique seems to be an interesting approach for the study of electromagnetic wave diffraction. Scatterers with 'complex' surfaces can be treated. The higher computational time required in FVTD can be compensated by a conformal unstructured meshing of the objects allowing local refinement mesh easier than in FDTD. Moreover with the finite volume scheme, thin material with finite conductivity and dielectric part can be taken into account easily. With dielectric properties of the breast tissue and malignant tumor it is possible to use the Finite Volume Time Domain.

1.6 REFERENCES

1. C. Gabriel, "A compilation of the dielectric properties of body tissues at RF and microwave frequencies," Radiofrequency Radiation Division, Brooks AFB, San Antonio, TX, Contract AL/OE TR-1996-0037, 1996.
2. C. Gabriel, S. Gabriel, and E. Corthout, "The dielectric properties of biological tissues: I. Literature survey," *Phys. Med., Biol.,* vol. 41, no. 11, pp. 2231–2249, Nov. 1996.
3. S. Gabriel, R. W. Lau, and C. Gabriel, "The dielectric properties of biological tissues: II. Measurements on the frequency range 10 Hz to 20 GHz," *Phys. Med., Biol.,* vol. 41, no. 11, pp. 2251 2269, Nov. 1996.
4. ____"The dielectric properties of biological tissues: III. Parametric models for the dielectric spectrum of tissues," *Phys. Med., Biol.,* vol. 41, no. 11, pp. 2271–2293, Nov. 1996.
5. K. R. Foster and J. L. Schepps, "Dielectric properties of tumor and normal tissue at radio through microwave frequency," *J. Microwave Power,* vol. 16, pp. 107–119, 1981
6. J. A. Rogers, R. J. Shepard, E. H. Grant, N. M. Bleehen, and D. J. Honess, "The dielectric properties of normal and tumor mouse tissue between 50 MHz and 10 GHz," *Br. J. Radiol.,* vol. 56, pp. 335-338, 1983.
7. R. Peloso, D. Tuma, and R. K. Jain, "Dielectric properties of solid tumors during normothermia and hyperthermia," *IEEE Trans. Biomed.Eng.,* vol. BME-31, pp. 725–728, 1984.
8. S. Swarup, S. S. Stuchly, and A. Surowiec, "Dielectric properties of mouse MCA1 fibro sarcoma at different stages of development," *Bioelectromagn.,* vol. 12, pp. 1–8, 1991.
9. A. J. Surowiec, S. S. Stuchly, J. R. Barr, and A. Swarup, "Dielectric properties of breast carcinoma and the surrounding tissues," *IEEE Trans. Biomed. Eng.,* vol. 35, pp. 257–263, Apr. 1988.
10. P. Bonnet, X. Ferrieres, F. Paladian, J. Grando, J. Alliot, and J. Fontaine, "Electromagnetic wave diffraction using a finite volume method," *IEE Electr. Letters*, vol. 33, no. 1, pp. 31–32, 1997.
11. C. Fumeaux, D. Baumann, and R. Vahldieck, "Advanced FVTD simulations of dielectric resonator antennas and feed structures," *ACES Journal*, vol. 19, no. 3, pp. 155–164, 2004.

Comparative Beamforming Analysis between Circular and Rectangular Antenna Array Systems

Robert Macharia Maina[1], Kibet Langat[1], P. K. Kihato[2]

[1]Jomo Kenyatta University of Agriculture and Technology, Department of Telecommunication Engineering

[2]Jomo Kenyatta University of Agriculture and Technology, Department of Electrical Engineering

robertisaacm@gmail.com, kibetlp@jkuat.ac.ke, kamitazv@yahoo.co.uk

ABSTRACT- Antenna Array Systems utilize beamforming algorithms based on particular criterions to optimize radiation patterns in wireless communication links. Common array geometrical arrangements are linear, circular and rectangular. Circular and rectangular antenna array arrangements yield radiation patterns with 3-dimension scanning capability. In this paper, adaptive beamforming using circular and rectangular array approaches is studied. The beamforming algorithm of choice is the Particle Swarm Optimization (PSO) algorithm. The weights of the adaptive beamformer are synthesized to directly steer the main radiation beam towards any direction of interest and steer nulls towards undesired directions. The resultant beam shapes are used as measures of success. The rectangular array is found to be highly effective in adaptive beamforming as compared to the circular array in a large set of beam/ null steering directions.

Key words- Circular Antenna Array, Rectangular Antenna Array, Beam/ Null Steering, PSO

1. INTRODUCTION

Radio antennas couple electromagnetic energy from space to another medium (for example: wire, coaxial cable, or waveguide) or vice versa. Antennas can be generally categorized into omnidirectional and directional antennas [1].

An omnidirectional antenna radiates electromagnetic energy equally in all directions. This approach scatters signal energy with only a small percentage of the entire energy sent out reaching desired users.

A directional antenna in general has preferential transmission and reception directions (radiation directions are coupled with different gain values) [1] - [2].

Such antennas are usually built using a number of antenna elements arranged in a particular desired geometric pattern (e.g. linear, circular, and planar). Phase and amplitude differences between the element paths govern the resultant array radiation pattern. Directional antenna categories are fixed beam and adaptive beam classes [3].

Adaptive antennas have gained supremacy over fixed beam antennas, especially due to the ever increasing computer processing power.

Circular and rectangular array geometries are of significant importance in that they allow three dimension beam/ null steering.

The application of numerical optimization techniques in beamforming is an ongoing area of research stimulated by the ever increasing computer processing power. Among the favorite optimization techniques is the Particle Swarm Optimization (PSO) algorithm. PSO technique has been proven highly effective in a wide range of multidimensional problems compared to other techniques. PSO is based on the search behavior of a swarm of particles in a multidimensional search space.

An overview of wireless communication networks utilizing adaptive antennas can be found in [4] - [5].

2. ANTENNA ARRAYS

In a transmitting antenna array, each antenna

element radiates radio waves at a particular phase and amplitude. The radio waves build upon each other or cancel each other when they cross paths. The manner in which the waves interfere with each other depends on the phase of each contributing wave (whether the wave is at its crest, its trough or somewhere in between).

A map of interference (destructive/ constructive) between the radio waves is referred to as a radiation pattern. It is the radiation pattern that portrays the relative radiation strengths in all directions [1].

The main beam is formed at the line where the greatest number of waves projected by the antenna array elements constructively overlap to form a composite waveform. An illustration of beamformed radiation is shown in Fig. 1 below.

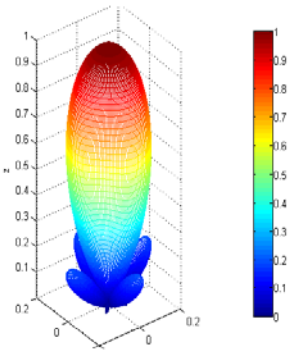

Fig. 1 An illustration of beamformed radiation

3. RECTANGULAR ANTENNA ARRAY

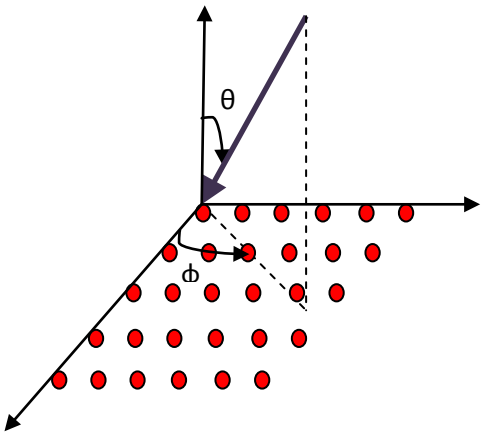

Fig. 2 Rectangular Antenna Array

Fig.2 depicts an M by N rectangular array with uniform element spacing distance. A planar wave front impinges on the array. The resultant array factor is given by:

$$AF(\theta,\emptyset) = \sum_{m=1}^{M}\sum_{n=1}^{N} w_{mn}\, e^{j\left[(m-1)(kd_x \sin(\theta)\cos(\emptyset)+\beta_x)+(n-1)(kd_y \sin(\theta)\sin(\emptyset)+\beta_y)\right]} \quad (1)$$

Where: AF: Array Factor, k: wave number, d: element separation distance, θ, Ø: wave front angle of arrival, β: phase difference between adjacent elements, w: element amplitude.

The total radiation pattern is the product of individual element radiation pattern and the array factor. [3].

4. CIRCULAR ANTENNA ARRAY

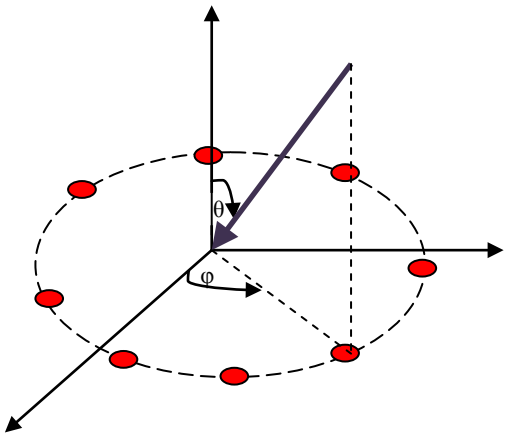

Fig.3 Circular Antenna Array

Fig.3 depicts an N element circular array with uniform element spacing distance. A planar wave front impinges on the array. The resultant array factor is given by:

$$AF(\theta,\emptyset) = \sum_{n=1}^{N} w_n e^{-j\left[ka\sin(\theta)\cos(\emptyset-\frac{2\pi}{N}(n-1))+\delta_n\right]} \quad (2)$$

Where: AF: Array Factor, k: wave number, a: array radius, θ, Ø : wave front angle of arrival, δ: electrical phase difference between adjacent elements, w: element amplitude.

The total radiation pattern is the product of individual element radiation pattern and the array factor [3].

5. BEAM/ NULL STEERING

An adaptive beamformer automatically adapts its response to different scenarios. A criterion has to be defined to allow adaption to take place. In this paper, the criterion of choice is the beam/ null steering approach. Fig. 4 below

is an illustration of a beam/ null steering based adaptive beamformer.

The weights of the null steering beamformer are chosen to synthesize a beam with unit gain in the direction of the desired signal and nulls in the direction(s) of interferer(s) [6].

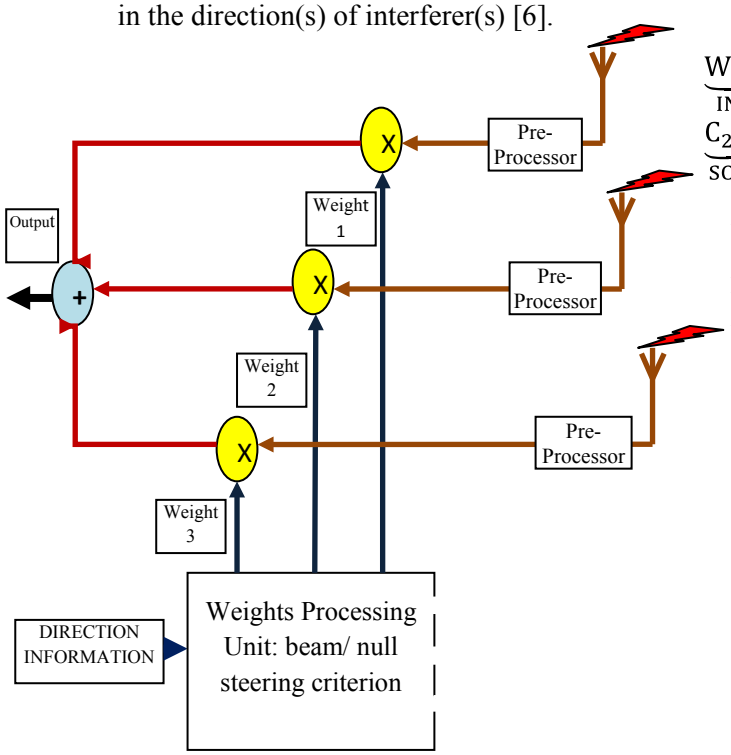

Fig. 4 Beam/ Null Steering based Adaptive Beamformer

6. PARTICLE SWARM OPTIMIZATION ALGORITHM

PSO is an optimization technique based on the search behavior of a swarm of particles in a multidimensional search space [7]. It is an iterative algorithm in which the velocities and positions of the swarm particles are updated per iteration in a controlled manner. For each particle i, the respective velocity vector V is updated according to (3) where inertia weight W controls the influence of the previous velocity vector. Parameter C_1 controls the influence of the personal best position achieved so far (the position at which the particle has resulted in the smallest objective function value so far (assuming that the objective function has to be minimized)). Parameter C_2 determines the influence of the best position that has been found so far by any of the particles in the neighborhood of particle i. Random values R_1 and R_2 are usually drawn with uniform probability from the number set [0, 1].

$$V_i(t+1) = W * V_i(t) + C_1 * R_1.(Y_i - X_i) + C_2 * R_2.(\tilde{Y}_i - X_i) \quad (3)$$

$$X_i(t+1) = X_i(t) + V_i(t+1) \quad (4)$$

$$V_i(t+1) = \underbrace{W * V_i(t)}_{\text{INERTIA}} + \underbrace{C_1 * R_1.(Y_i - X_i)}_{\text{PERSONAL INFLUENCE}} + \underbrace{C_2 * R_2.(\tilde{Y}_i - X_i)}_{\text{SOCIAL INFLUENCE}} \quad (5)$$

V_i : velocity vector
X_i : position vector
Y_i : "personal best" position vector
$\hat{Y}_i$: "neighborhood" best position vector

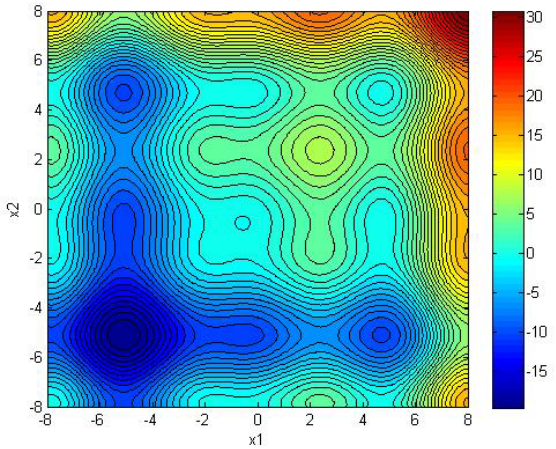

Fig. 5 Typical search region

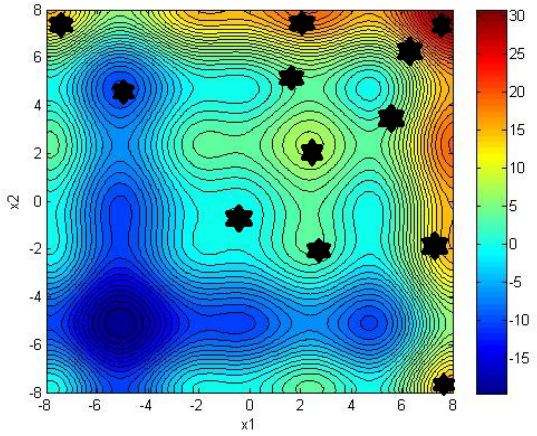

Fig.6 Random particle distribution

Fig. 5 – Fig. 7 are contour plots illustrating the PSO concept. Fig. 5 depicts a function with a minimum value at point (-5,-5). Fig. 6 depicts an initial random distribution of PSO particles. Fig. 7 depicts the positions of the particles after a number of algorithm iterations (this is at the region with the minimum function value).

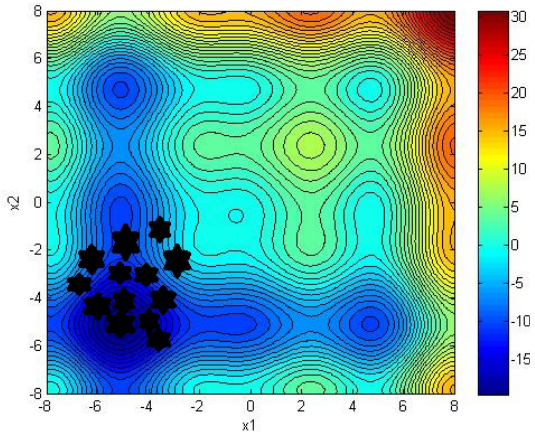

Fig. 7 Final solution

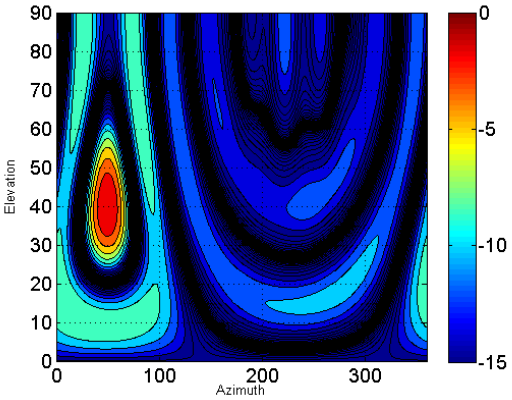

Fig. 8 Contour plot using circular array

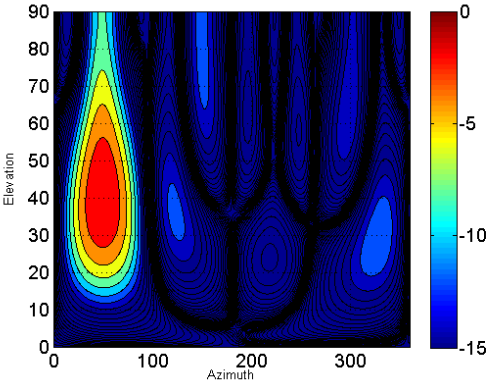

Fig. 9 Contour plot using rectangular array

7. METHODOLOGY

The general idea is to ensure maximum array factor magnitude in desired directions and minimal array factor magnitude in undesired directions. As such, the problem is formulated as a maximization problem of the relationship defined in Equation 5 below.

Objective function = AF (desired directions) - AF (undesired directions) (5)

AF denotes Array Factor.

In this format, this objective function is easily maximized using the PSO algorithm. The weight in each and every array path is taken as the function variable. A 4x4 element rectangular and 16 element circular arrays are used.

8. RESULTS

Results obtained from sets of one desired direction and three undesired directions are presented below.

8.1 Direction set one

The set of angles in Table 1 below is used in the first set of simulations.

Table 1: Direction set 1

	Desired direction	Undesired 1	Undesired 2	Undesired 3
Elevation angle	40	30	60	50
Azimuth angle	50	100	230	300

8.2 Direction set two

The set of angles in Table 2 below is used in the second set of simulations.

Table 2: Direction set 2

	Desired direction	Undesired 1	Undesired 2	Undesired 3
Elevation angle	50	10	20	70
Azimuth angle	100	50	250	310

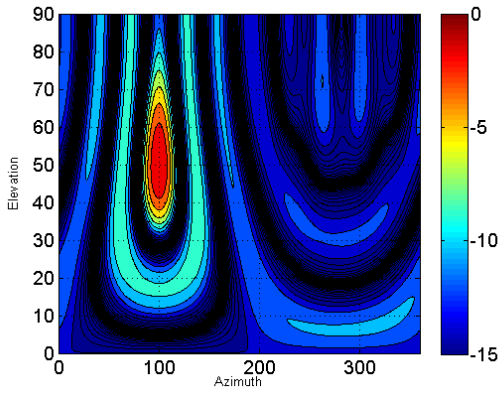

Fig. 10 Contour plot using circular array

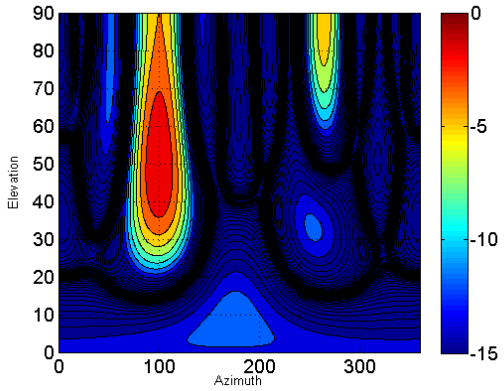

Fig. 11 Contour plot using rectangular array

8.3 Direction set three

The set of angles in Table 3 below is used in the third set of simulations.

Table 3: Direction set 3

	Desired direction	Undesired 1	Undesired 2	Undesired 3
Elevation angle	30	60	80	10
Azimuth angle	250	60	180	350

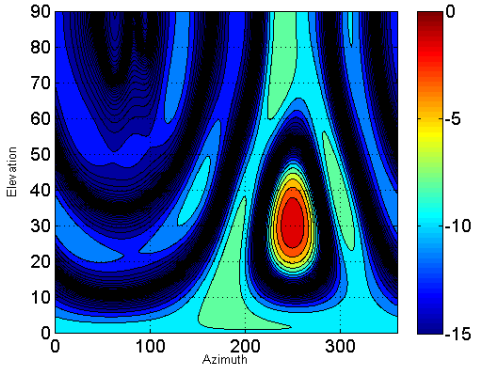

Fig. 12 Contour plot using circular array

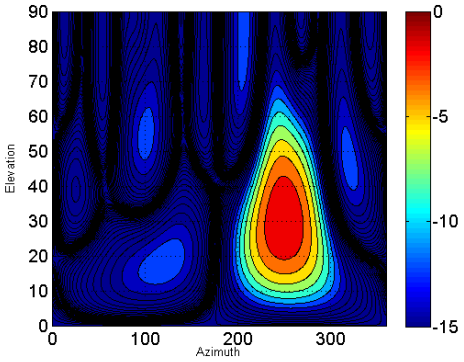

Fig. 13 Contour plot using rectangular array

8.4 Direction set four

The set of angles in Table 4 below is used in the fourth set of simulations.

Table 4: Direction set 4

	Desired direction	Undesired 1	Undesired 2	Undesired 3
Elevation angle	80	70	85	30
Azimuth angle	40	50	200	325

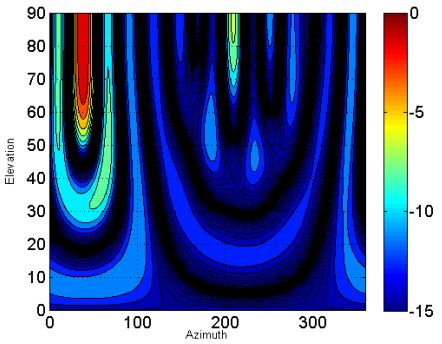

Fig. 14 Contour plot using circular array

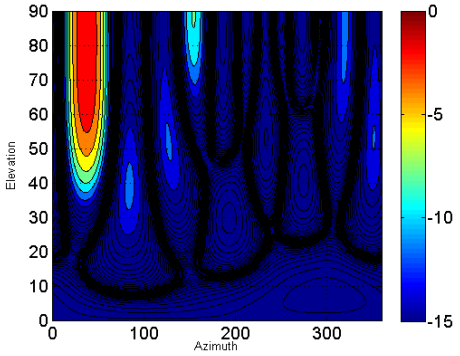

Fig. 15 Contour plot using rectangular array

8.5 Direction set five

The set of angles in Table 5 below is used in the fifth set of simulations.

Table 5: Direction set 5

	Desired direction	Undesired 1	Undesired 2	Undesired 3
Elevation angle	70	45	55	45
Azimuth angle	140	60	190	310

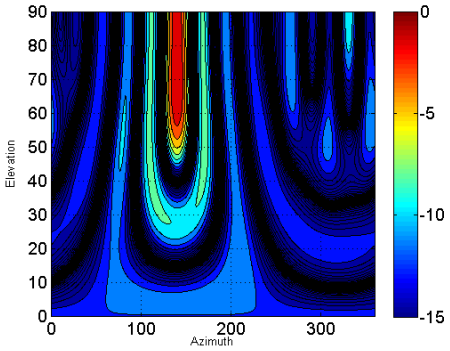

Fig. 16 Contour plot using circular array

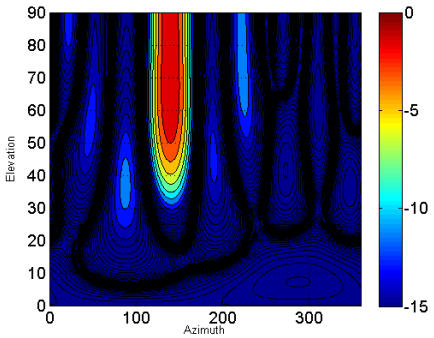

Fig. 17 Contour plot using rectangular array

8.6 Direction set six

The set of angles in Table 6 below is used in the sixth set of simulations.

Table 6: Direction set 6

	Desired direction	Undesired 1	Undesired 2	Undesired 3
Elevation angle	60	25	70	20
Azimuth angle	290	55	175	330

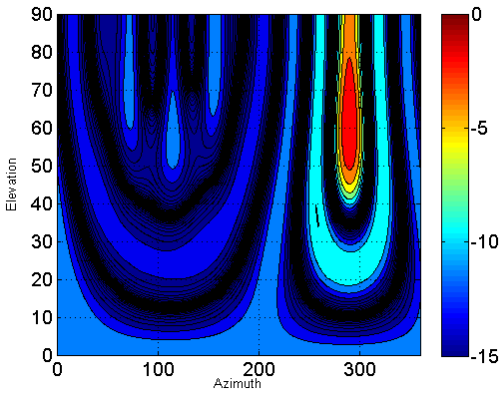

Fig. 18 Contour plot using circular array

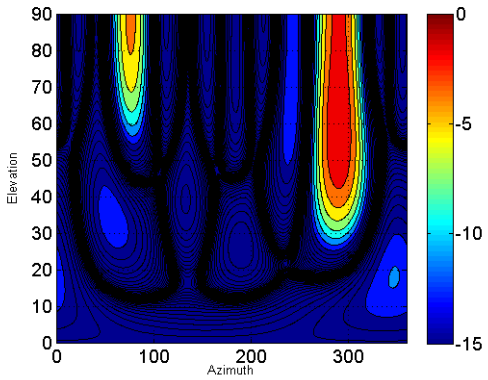

Fig. 19 Contour plot using rectangular array

Table 7: Tabulated results

ARRAY RESPONSE MAGNITUDE IN DECIBELS						
	DIRECTION SET 1		**DIRECTION SET 2**		**DIRECTION SET 3**	
DIRECTION	*RECT.*	*CIRC.*	*RECT.*	*CIRC.*	*RECT.*	*CIRC.*
DESIRED	-7.15E-04	0	-0.0024	0	0	-0.0078
UNDESIRED 1	-52.1531	-9.2542	-18.2574	-27.5682	-28.1863	-17.1002
UNDESIRED 2	-43.9044	-26.1953	-20.4986	-27.007	-36.0386	-23.6041
UNDESIRED 3	-15.3069	-17.5731	-38.4905	-13.3147	-26.4916	-11.707
TOTAL I. LEVEL	**-111.3644**	**-53.0226**	**-77.2465**	**-67.8899**	**-90.7165**	**-52.4113**
OTHER STATISTICAL PARAMETERS IN DECIBELS						
	DIRECTION SET 1		**DIRECTION SET 2**		**DIRECTION SET 3**	
PARAMETER	*RECT.*	*CIRC.*	*RECT.*	*CIRC.*	*RECT.*	*CIRC.*
MAX. RESPONSE	0	0	0	0	0	0
MIN. RESPONSE	-103.1012	-87.5421	-87.0741	-88.5247	-89.98	-83.2074
MEAN	-24.5643	-16.058	-22.4797	-15.9501	-22.4242	-15.3723
MEDIAN	-21.4736	-14.154	-21.8708	-14.32	-20.0868	-12.9732

ARRAY RESPONSE MAGNITUDE IN DECIBELS						
	DIRECTION SET 4		**DIRECTION SET 5**		**DIRECTION SET 6**	
DIRECTION	*RECT.*	*CIRC.*	*RECT.*	*CIRC.*	*RECT.*	*CIRC.*
DESIRED	-0.1006	-0.0816	-7.27E-04	-7.03E-04	-0.0067	0
UNDESIRED 1	-2.6562	-6.7188	-22.311	-30.5018	-18.2513	-16.2803
UNDESIRED 2	-29.2043	-13.3282	-13.1019	-17.9453	-27.9992	-25.7564
UNDESIRED 3	-28.1051	-14.4579	-27.2939	-11.7774	-17.9872	-18.5012
TOTAL I. LEVEL	**-59.9656**	**-34.5049**	**-62.7068**	**-60.2245**	**-64.2377**	**-60.5379**
OTHER STATISTICAL PARAMETERS IN DECIBELS						
	DIRECTION SET 4		**DIRECTION SET 5**		**DIRECTION SET 6**	
PARAMETER	*RECT.*	*CIRC.*	*RECT.*	*CIRC.*	*RECT.*	*CIRC.*
MAX. RESPONSE	0	0	0	0	0	0
MIN. RESPONSE	-99.0982	-81.9751	-82.2455	-83.4157	-95.3614	-97.4296
MEAN	-25.3964	-16.7023	-25.1616	-16.3029	-23.8018	-16.1318
MEDIAN	-23.2296	-15.0666	-22.8027	-14.2847	-23.441	-13.5277

Table 8: Averaged results

ARRAY RESPONSE MAGNITUDE IN DECIBELS		
	AVERAGES	
DIRECTION	*RECT.*	*CIRC.*
DESIRED	-0.018523643	-0.015017157
UNDESIRED 1	-23.63588333	-17.90391667
UNDESIRED 2	-28.45783333	-22.30605
UNDESIRED 3	-25.61253333	-14.55521667
TOTAL INTERFERENCE LEVEL	-77.70625	-54.76518333
OTHER STATISTICAL PARAMETERS IN DECIBELS		
	AVERAGES	
PARAMETER	*RECT.*	*CIRC.*
MAXIMUM RESPONSE	0	0
MINIMUM RESPONSE	-92.81006667	-87.01576667
MEAN	-23.97133333	-16.08623333
MEDIAN	-22.15075	-14.05436667

9. DISCUSSION

The maximum response depicts the highest array response level achieved. The minimum response depicts the lowest array response level achieved. The response mean depicts the average array response achieved. The response mean alongside the response median gives an indication of overall sidelobe contributions. The contour plots give a visual illustration of response strength spread across all possible directions (elevation along y-axis and azimuth along x-axis) as depicted by the color bars. Maximum response (pure red color) is set at 0 dB. The dark blue regions have minimal response (to the extent of -103 dB in Figure 3.5 (b)).

Maximal radiation is directed towards the desired direction and minimal radiation towards the undesired directions as depicted by Figures 8- 19. The rectangular array performs better than the circular array as depicted by the total interference levels and other statistical parameters as tabulated in Tables 7 and 8. It is worthwhile to note that the performance of the circular array in steering the main beam/ nulls is largely hampered by high sidelobe levels.

10. CONCLUSION

Quantitatively and qualitatively, the rectangular array arrangement is found to generate better results in all simulated radiation/ reception directions. The rectangular array generally yields lower sidelobe levels.

11. BIBLIOGRAPHY

[1] Constantine A. Balanis, *Antenna Theory, Analysis and Design*, 3rd ed. Hoboken, New Jersey: John Wiley & Sons, Inc., 2005.

[2] Ahmed El Zooghby, *Smart Antenna Engineering*, 1st ed. Norwood, United States of America: Artech House, 2005.

[3] Constantine A. Balanis, "Smart Antennas," in *Antenna Theory Analysis and Design*, 3rd ed. New Jersey, United States of America: John Wiley & Sons, Inc., Hoboken, New Jersey, 2005, ch. 16, pp. 945 - 999.

[4] S. Anderson, "An adaptive array for mobile communication systems," *IEEE Trans. Vehicular Technol.*, vol. 40, pp. 230–236, 1991.

[5] Inc. Network World. (2010) Networkworld. [Online]. http://networkworld.com/news/2010/101910-smart-antennas-wifi-performance.html

[6] Lal Chand Godara, *Smart Antennas*, 1st ed. Florida, United States of America, 2004.

[7] Thomas Weise, *Global Optimization Algorithms: Theory and Applications.*, 2009.

Patch Antennas with Enhanced Bandwidth by Ground Plane Modification

E. K. Miring'u [1], D. B. O. Konditi [2], P. L. Kibet [3]

[1] miringu4edwin@gmail.com, [2] onyango_d@yahoo.co.uk, [3] kibetlp@gmail.com

[1] Department of Electrical and Electronic Engineering
School of Engineering,
Dedan Kimathi University of Technology
P. O. Box 657-10100,
Nyeri, Kenya

[2] Department of Electrical and Communication Engineering
Faculty of Engineering,
Multimedia University of Kenya
P. O. Box 15653-00503,
Nairobi, Kenya

[3] Department of Telecommunication and Information Engineering
School of Electrical, Electronic and Information Engineering
Jomo Kenyatta University of Agriculture and Technology
P. O. Box 62000 – 00200,
Nairobi, Kenya

Abstract - In this paper, an antenna design method for improvement of patch antenna bandwidth is investigated by partial modification of the ground plane of the antenna on a multi-dielectric substrate. The modification is done in the radiating, non-radiating and a combination of both with respect to the patch antenna. Compared to the conventional patch antennas, this technique is found to improve the bandwidth of the antenna. Such a technique is applicable for high frequencies, where a frequency of 6.646GHz has been employed in this work. Antenna parameters such as gain, bandwidth, Voltage Standing Wave Ratio and radiation efficiency have been used to analyze the performance of the antennas. An improvement in bandwidth of 223.1 MHz is achieved for a patch size of $7.13 \times 9.09\text{mm}^2$.

Keywords - Patch antenna, ground plane modification

1.0. INTRODUCTION

One example of an antenna finding increased usage in wireless communication systems is the microstrip antenna [1]. In a world where personal wireless communication is evolving rapidly, the design of antennas with increased bandwidth, while maintaining high efficiency is paramount. In addition, designing low profile and light weight antennas is requisite to meet wireless systems needs of portability and economy of space. Microstrip antennas meet such requirements and as such are attractive for application in wireless communication systems. Further, they have inherent additional advantages such as low cost, ease of fabrication, conformability to mounting surfaces and are easily integrable [2] - [3]**.** In spite of the above advantages, the patch antennas are faced with the drawback of narrow bandwidth due to their small size. The bandwidth can albeit be increased through increasing the size of the patch, which is not desirable in most wireless communication applications.

This paper explores ways of increasing the bandwidth of the antenna by ground plane modification.

2.0. PATCH ANTENNAS WITHOUT MODIFICATION

In this section, conventional microstrip-line fed rectangular patch antennas without ground plane modification are designed to resonate at 6.646GHz. The first design is undertaken on a single layer Glass substrate with $\varepsilon_r = 4.6$ and patch dimensions L= 10mm, W=9.523mm and height 2mm. The second design is done using a single layer Silicon substrate with $\varepsilon_r = 11.9$ and with patch dimensions L =5mm, W =8.5mm and height 2mm. The third design is done using a combination of both substrates where the glass substrate is sandwiched between the two layers and with a patch size of L=7.126mm and W=9.093mm.

For the silicon-glass-silicon substrate design, the glass substrate had a height of 1mm whereas each of the two layers of silicon had 0.5mm each. The three designs are illustrated in Fig 1. This was done in order to establish the optimum configuration in terms of the antenna parameters-patch size trade off. It was discerned that the Si-Glass-Si configuration gave the best optimum parameters with respect to the patch size and the antenna parameters such as bandwidth, gain, directivity, Voltage Standing Wave Ratio (VSWR) and radiation efficiency, compared to the other two single layer substrate antenna designs. Thus the design with the combined substrates will be employed in subsequent designs.

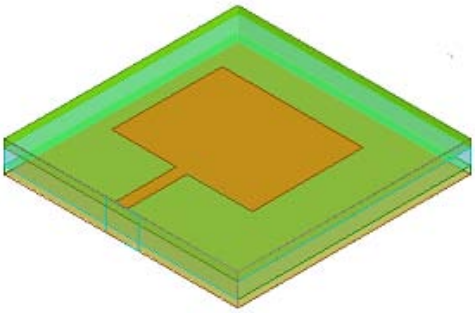

(c)

Fig. 1. Patch Antennas without modification at 6.646GHz (a) Glass substrate (b) Silicon substrate (c) Silicon-Glass-Silicon Substrates

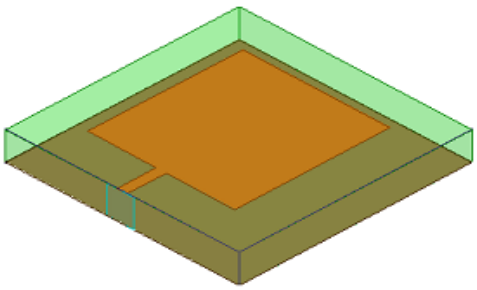

(a)

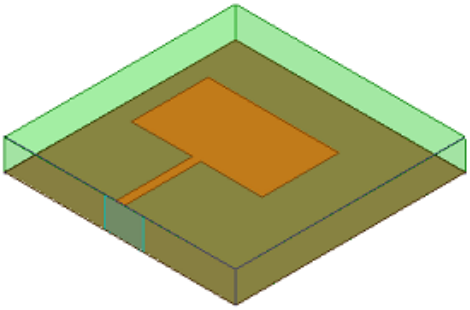

(b)

3.0. PATCH ANTENNAS WITH GROUND PLANE MODIFICATION

In this section, the ground plane of the antenna is modified in various configurations. A width of 2mm of the ground plane is modified in the radiating, non-radiating and a combination of both configurations. Fig. 2 below depicts the three configurations.

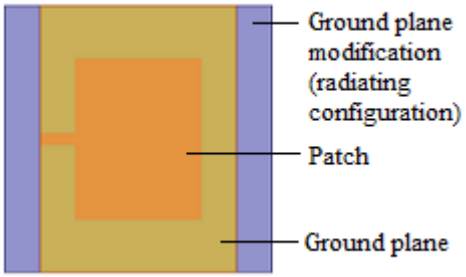

(a)

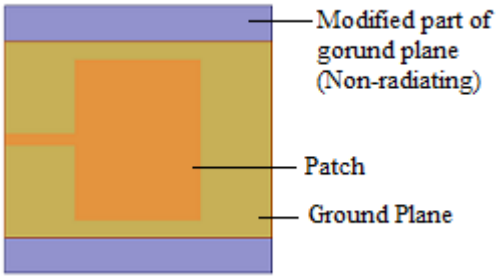

(b)

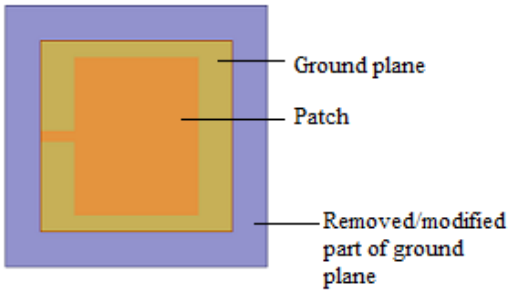

(c)

Fig. 2. Bottom views showing the ground plane modification in (a) Radiating (b) Non-radiating (c) Both radiating and Non-radiating configurations.

Modification of portions of the ground plane is carried out by changing the material from a perfect electric conductor (pec) to air which in turn reduces the conductivity in certain portions of the ground plane. Performance parameters such as return loss, gain and VSWR are analyzed for the proposed designs.

4.0. RESULTS AND DISCUSSION

After an in-depth analysis of the proposed designs, it was discerned that all the three designs gave an in improvement in bandwidth when comparison was undertaken with the single layered glass, single layered silicon substrates and the Silicon-Glass-Silicon substrates antenna designs. The design with a single substrate of glass (Fig. 1(a)) gave a bandwidth of 432.2MHz, as shown in Fig. 3, a gain of 0.9103 dB and a patch size of 10×9.52 mm^2 whereas that with a single substrate of silicon (Fig. 1(b)) gave a bandwidth of 389.2MHz (Fig. 4), a gain of 0.6734dB and a patch size of 5×8.5 mm^2. The glass substrate gave a higher bandwidth but with a larger patch size. The silicon substrate on the other hand gave a lower bandwidth but with reduced patch size. Thus a bandwidth-patch size trade-off had to be established by combining the two substrates in one antenna, where the glass substrate was sandwiched between two silicon layers, as illustrated in Fig. 1(c) This design gave a bandwidth of 405.1MHz as shown in Fig. 5, a gain of 1.712 dB and a patch size of 7.13×9.09 mm^2. Thus this design gave the best bandwidth-patch size trade-off and was employed in the subsequent designs.

As illustrated in Fig. 2(a), the modification of the ground plane was first done for the radiating configuration. This was adopted as such since the ground plane was modified with respect to the radiating sides of the patch antenna. This configuration gave a bandwidth of 469.2MHz, as illustrated in Fig. 6, which was an improvement of 64.1MHz. In Fig. 2(b), the modification of the ground plane was done for the non-radiating configuration. This design had a bandwidth of 453.7MHz, as shown in Fig. 7, an improvement of 48.6MHz. The final design in Fig.2(c) involved modification in both the radiating and non-radiating directions. The modification for this configuration was annular. This gave the highest bandwidth of 612.3MHz, as illustrated by the return loss plot of Fig. 8, which was an improvement of 223.1 MHz when compared to a single layered silicon substrate, which exhibited the lowest bandwidth prior to modification. All the designs exhibited a VSWR < 2.Table 1 gives a summary of the results in terms of the performance parameters for each of the designs undertaken above.

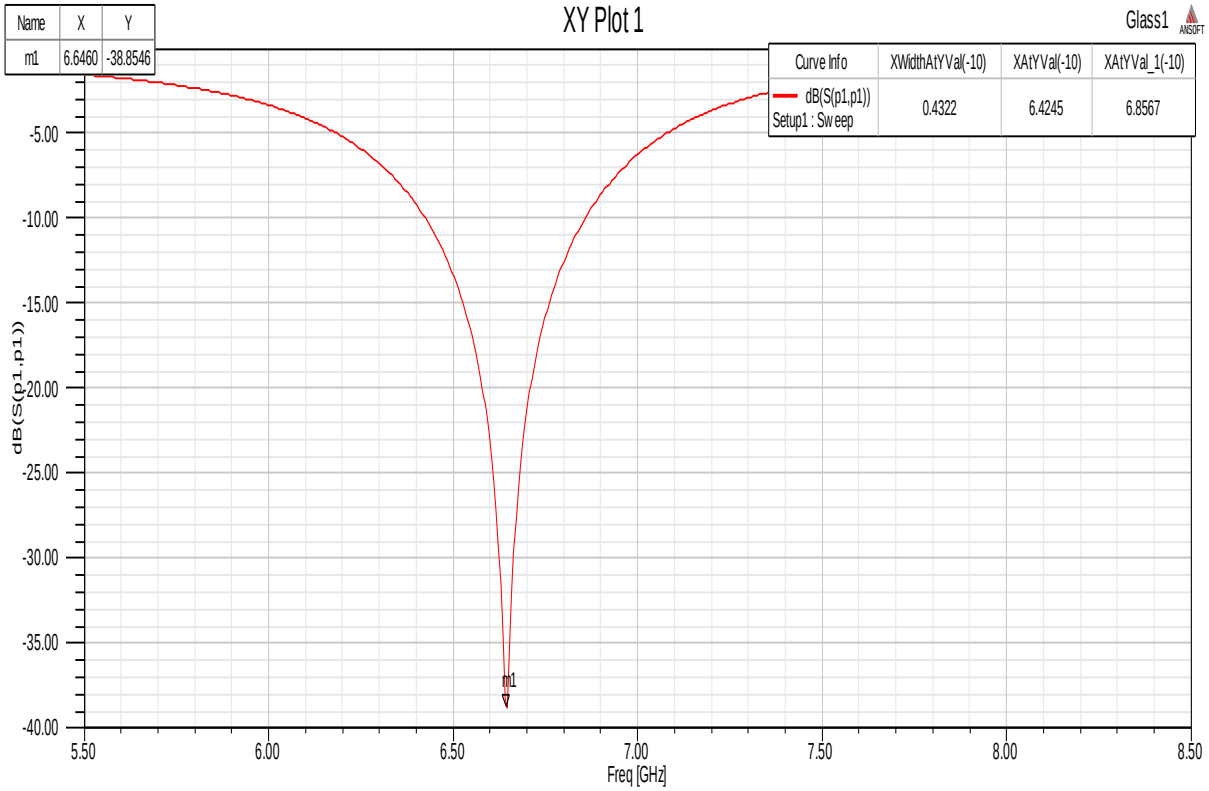

Fig. 3. Return Loss plot against Frequency for the Glass substrate patch antenna

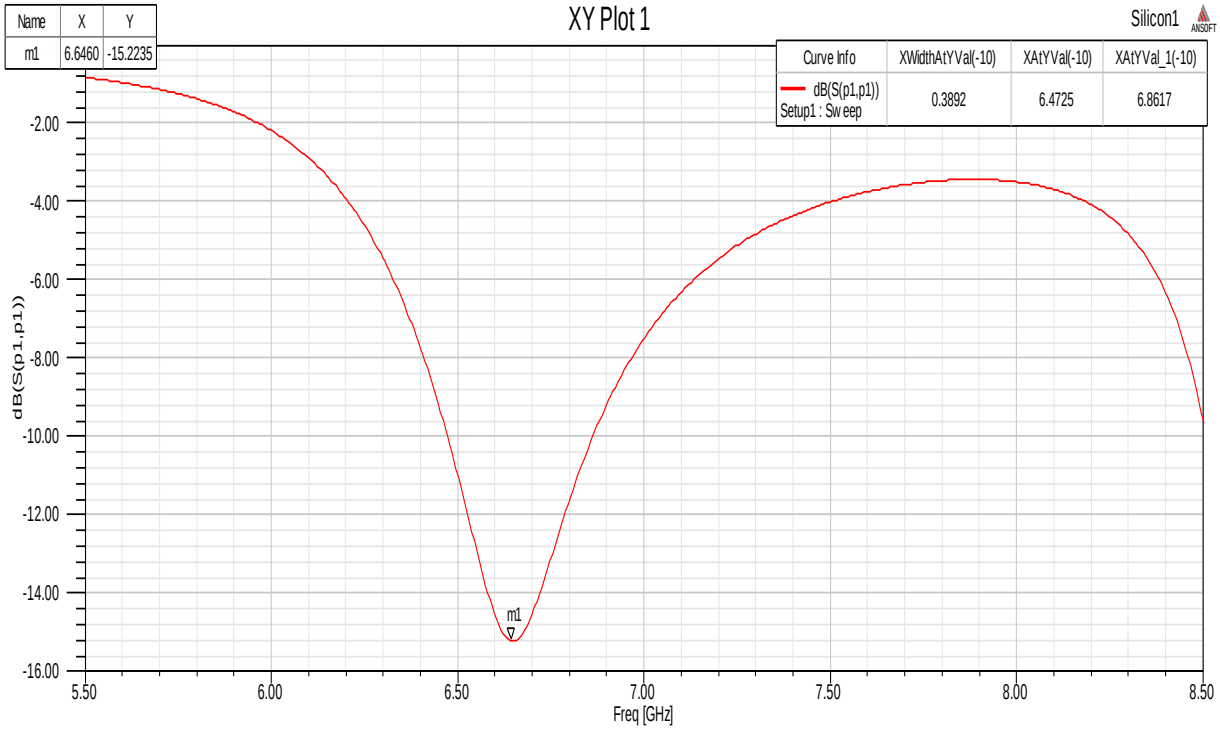

Fig. 4. Return Loss plot against Frequency for the Silicon Substrate patch antenna

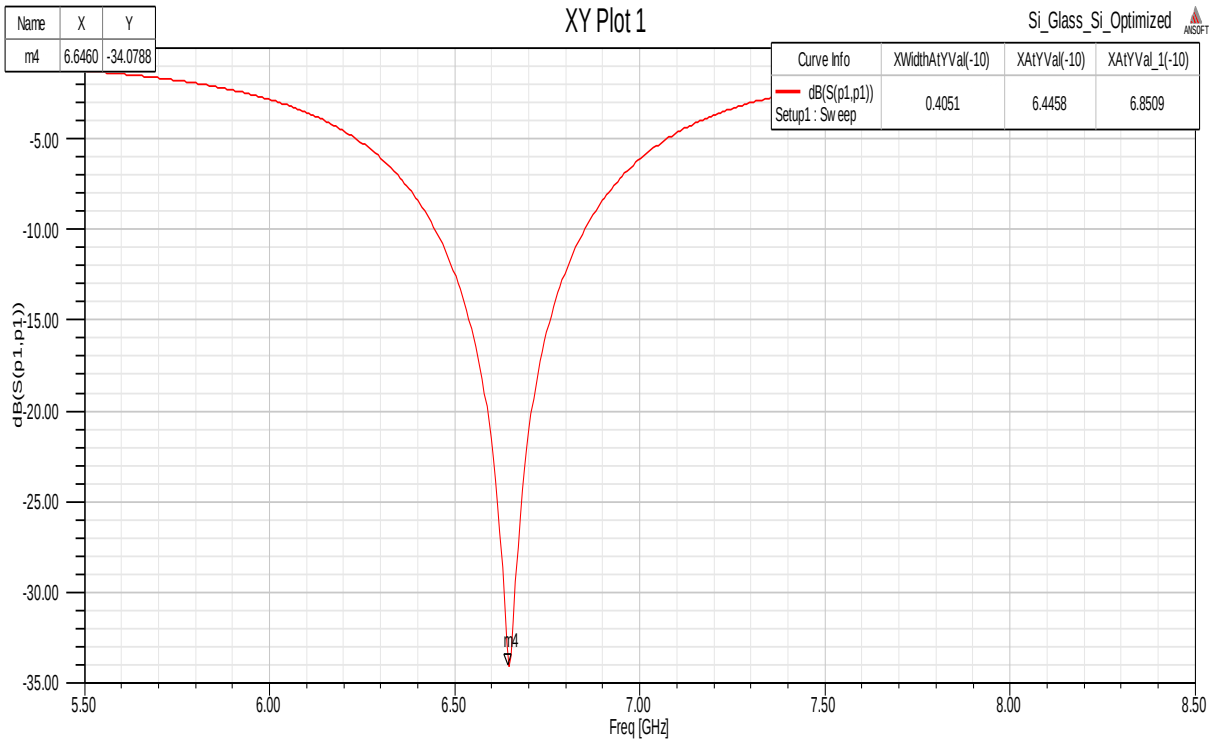

Fig. 5. Return Loss plot against Frequency for the Silicon-Glass-Silicon Substrate patch antenna

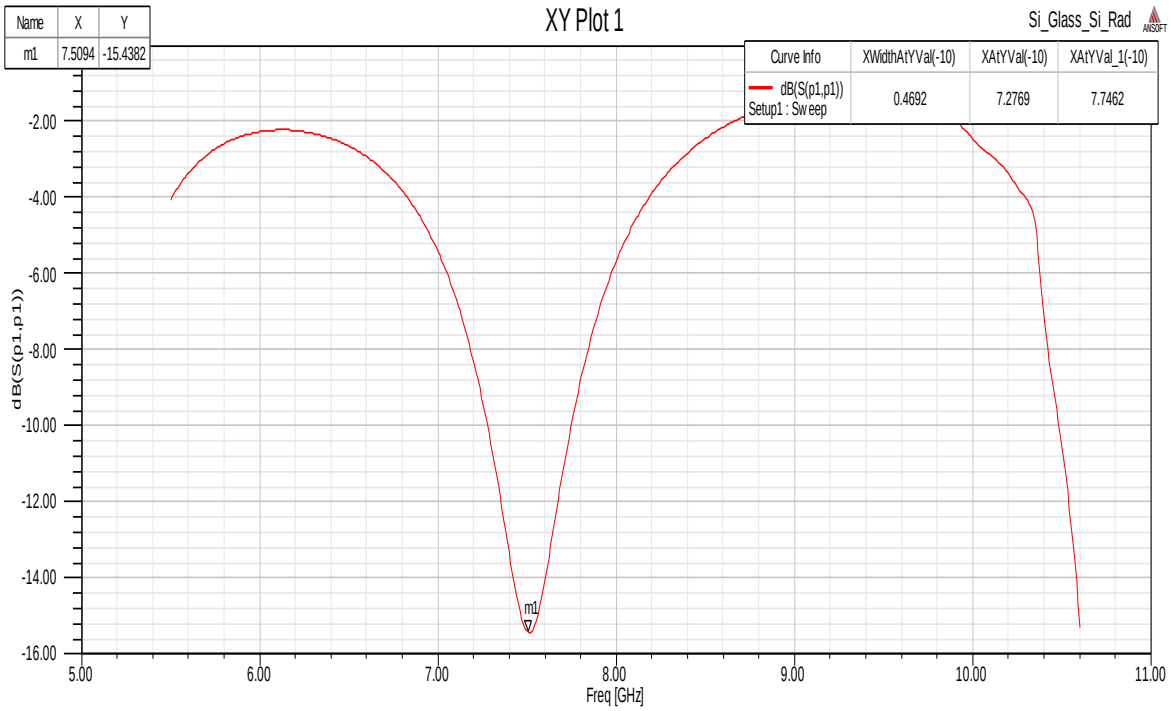

Fig. 6. Return Loss plot against Frequency for the modified ground plane (Si-Glass-Si Substrate patch antenna -Radiating side configuration)

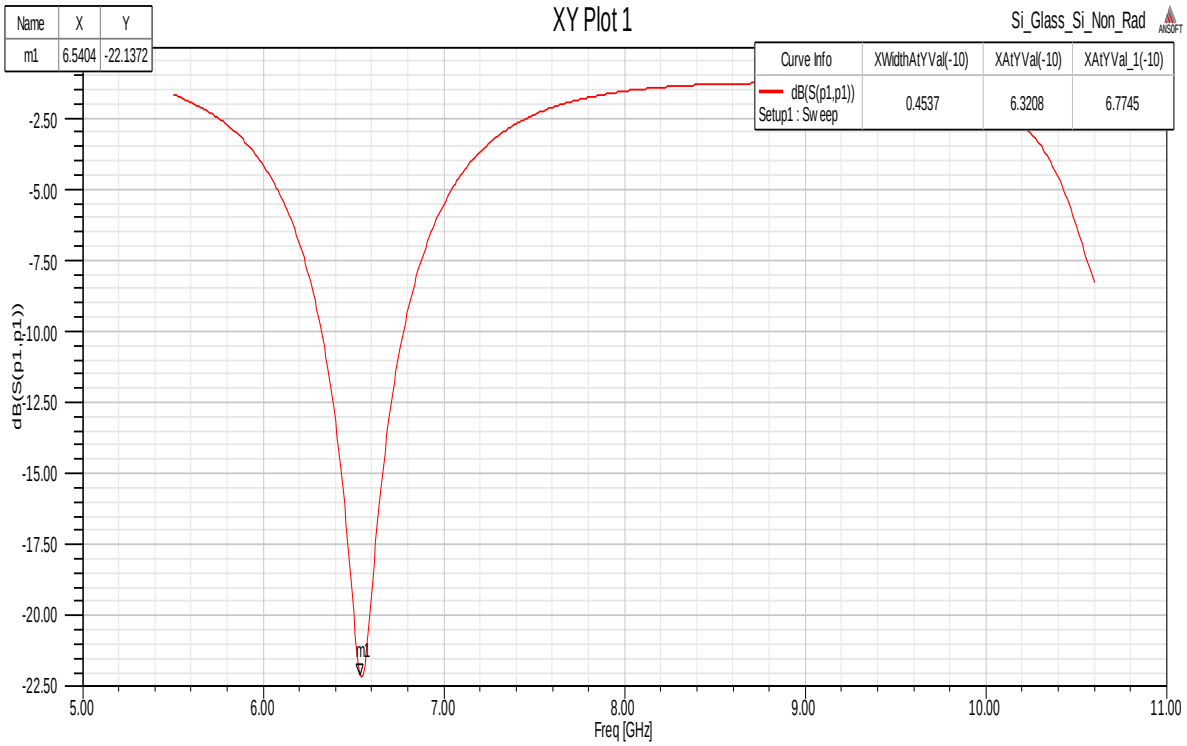

Fig. 7. Return Loss against Frequency for the modified ground plane (Si-Glass-Si Substrate patch antenna-Non-radiating side Configuration)

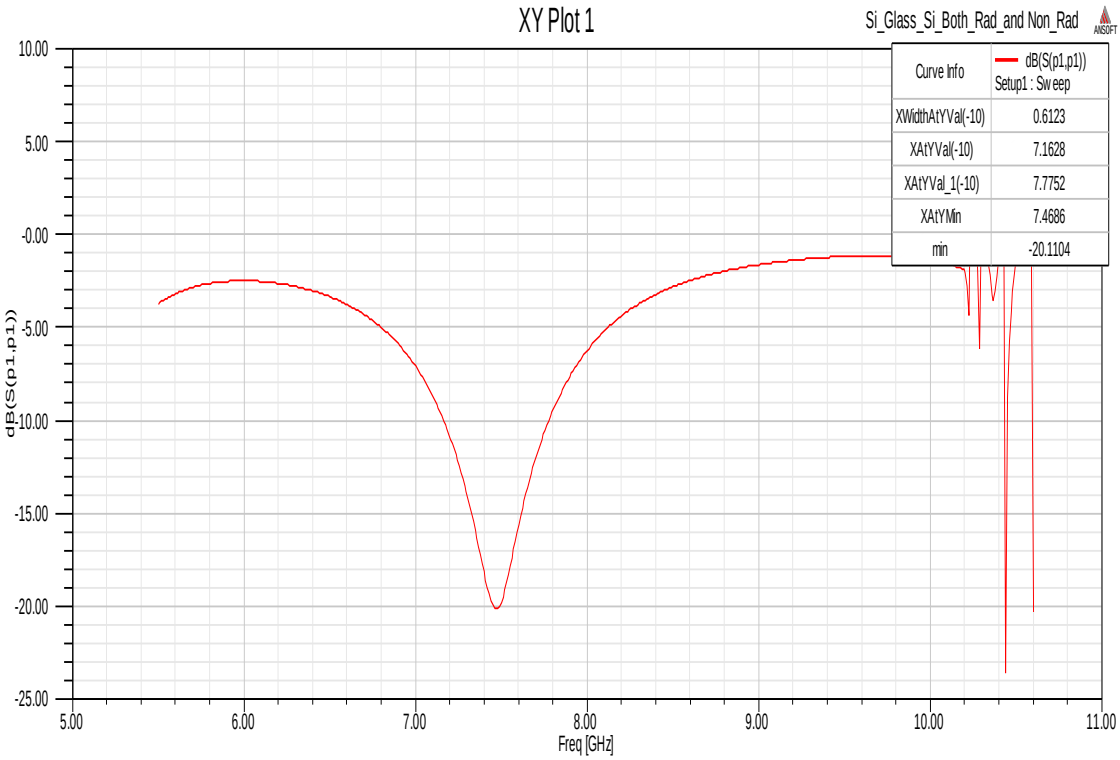

Fig. 8. Return loss against frequency for the modification of ground plane in both configurations (Si-Glass-Si Substrate patch antenna-Radiating and Non-radiating configurations)

Table 1: Comparison of antenna parameters for patch antennas with and without ground plane modification

Design	Dielectric Constant, ε_r	BW (MHz) (-10dB)	Return Loss, S11, Min (dB)	Size of Patch, (mm^2)	VSWR (Min)	Gain (dB)
Glass	4.6	432.2	-38.8546	10 × 9.52	1.0231	0.9103
Silicon	11.9	389.2	-15.2235	5 × 8.5	1.4193	0.6734
Si-Glass-Si_ without ground plane modification	11.9_4.6_11.9	405.1	-34.0788	7.13 × 9.09	1.0403	1.712
Si-Glass-Si (Modification in Radiating Configuration)	11.9_4.6_11.9	469.2	-15.4382	7.13 × 9.09	1.407	1.4419
Si-Glass-Si (Modification in Non-Radiating Configuration)	11.9_4.6_11.9	453.7	-22.1372	7.13 × 9.09	1.1696	1.6712
(Modification in Both configurations)	11.9_4.6_11.9	612.3	-20.1104	7.13 × 9.09	1.2191	1.4002

5.0. CONCLUSION

The effect of partial ground plane modification in a patch antenna with multi dielectric substrate has been analyzed. This method gives a peak improvement in bandwidth of 223.1 MHz when compared to a single layered silicon substrate patch antenna, which exhibited the lowest bandwidth prior to modification while maintaining the robustness of the antennas. The proposed approach can be extended further by combining it with the substrate modification technique to simultaneously enhance the gain and bandwidth of the patch antennas.

REFERENCES

[1] C. A. Balanis, "Microstrip antennas ," in *Antenna Theory: Analysis and Design*. New Jersey, USA: John Wiley and Sons, 2005, ch. 14, pp. 811-872.

[2] K. N. Malik et al., "A compact microstrip patch antenna with triangular snipped slot for wireless applications," *International Journal of Engineering and Advanced Technology*, vol. 1, no. 4, pp. 116-119, April 2012.

[3] L. Mokalled, M. Al-Husseini, A. Ramadan, K. Y. Kabalan, and A. El-Hajj, "A frequency reconfigurable microstrip rectangular patch antenna using stubs," *Progress In Electromagnetics Research Symp. Proc.*, Mar. 2011.

Analyzing Transmission Control Protocol and User Datagram Protocol Using Wireshark-Transport Layer

Amdany K. Amdany, N. P. Waweru
Electrical & Electronic Engineering Department, Dedan Kimathi University of technology
$amdanyk88@gmail.com$, $waweru@ymail.com$

***Abstract*—Transfer layer matches up to the fourth layer of the Open Systems Interconnection (OSI) reference model. In an Internet Protocol environment, TCP provides reliable data transmission, transfer of stream data, full-duplex operation, multiplexing and efficient flow of control while UDP is more or less a null protocol with check-summing of data and multiplexing by port numbers as the only service the protocol over IP. In order to understand the whole concept of TCP and UDP, this paper provides an experimental result on the performance of TCP and UDP in a network model using the Wireshark software. A detail observation on the TCP and UDP segments indicate that there is a well elaborated and essential presentation of transport protocol from the transport layer for which the reliability performance of the transport protocol is satisfactory for data transmission.**

***Index Terms*—transmission control protocol (TCP), transport layer, internet protocol (IP), network, Wireshark.**

I. INTRODUCTION

TRANSPORT layer is the fourth layer in the Open Systems Interconnection (OSI) reference model; more specifically it is the middle layer [1]. It is the last layer directly under the user control[2]. The OSI reference model was created, in late 1970s, by the International Organization for Standardization (ISO) to make it possible for computers, from different manufacturers, to typically communicate with other computers. The OSI model was designed to aid vendors craft interoperable network software and devices in form of protocols, therefore ensuring close relation between different vendor networks. The transport layer can be considered part of both upper and lower groups of layers in the OSI model. The layer connects the application software in the application layer with the network layer and is fully responsible for the end-to-end delivery of the message [2]. It performs the said function by accepting the outgoing messages from the application layer for instance, E-mail, Web and segments them for transmission. When application layer sends a Simple Mail Transfer Protocol (SMTP) packet, the transport layer splits the into smaller TCP segments [3]. SMTP is a procedure that makes the transfer of possible electronic mail between source and destination hosts possible. The main responsibility of SMTP is to provide message transfer and not to manage mailboxes or mail systems [4]. On the other hand, a segment is a Protocol Data Unit (PDU) at the transport layer. Once the transport layer splits the SMTP, the network layer takes the messages from the transport layer and forwards them via the network by selecting the most excellent route from one computer to the other through the network [3].

In computer networking, layer 4 provides end-to-end reliable communication services for application purpose within a structured architecture protocols and various network components. For general networking, the TCP/IP model, a foundation of the OSI model and Internet, engulfs the entire concept of transport layer [2]. The layer provides services support such as reliability, flow control, connection-oriented data stream and multiplexing. It is required for transporting data clear of boundaries of an address space through segmentation and reassembling data into a data stream [5]. The services, sited in the fourth layer, segment and reassemble upper-layer application data and bind them to form the same data stream. By doing so, the layer presents end-to-end data transport services while at the same time providing logical internetwork connections between source host and the destination host. For transport layer to fully perform its reliable connection responsibility, it makes use of different transport protocol. The main transport protocols are Transmission Control Protocol (TCP) and User Datagram Protocol (UDP). Other examples include Fibre Channel Protocol (FCP), Stream Control Transmission Protocol (SCTP), AppleTalk Transmission Protocol (ATP), and Reliable Datagram Protocol (RDP).

A. Transmission Control Protocol (TCP)

TCP match up the transport layer of the OSI reference model and is planned for use as a highly reliable source-to-destination host protocol between packet-switched communication networks. In an IP environment, TCP provides reliable data transmission [6]. The protocol is responsible for transferring data stream, providing reliable host-to-host communication, ensuring efficient and effective flow control to ensure that data does not flood the station, guaranteeing multiplexing, and full-duplex operation. Data transmitted between the source and the destination is sent as a series of packets. Once at the receiving end, the packets are reassembled in the correct sequence to recreate the initially transmitted data stream [7]. Along the transmission channel, packets can be duplicated, corrupted, lost or received out of order. To make sense of all these, the transport layer breaks up the request into TCP segments, add some extra sequence numbers and checksums to the data before passing the message to the internet layer [2, 7].

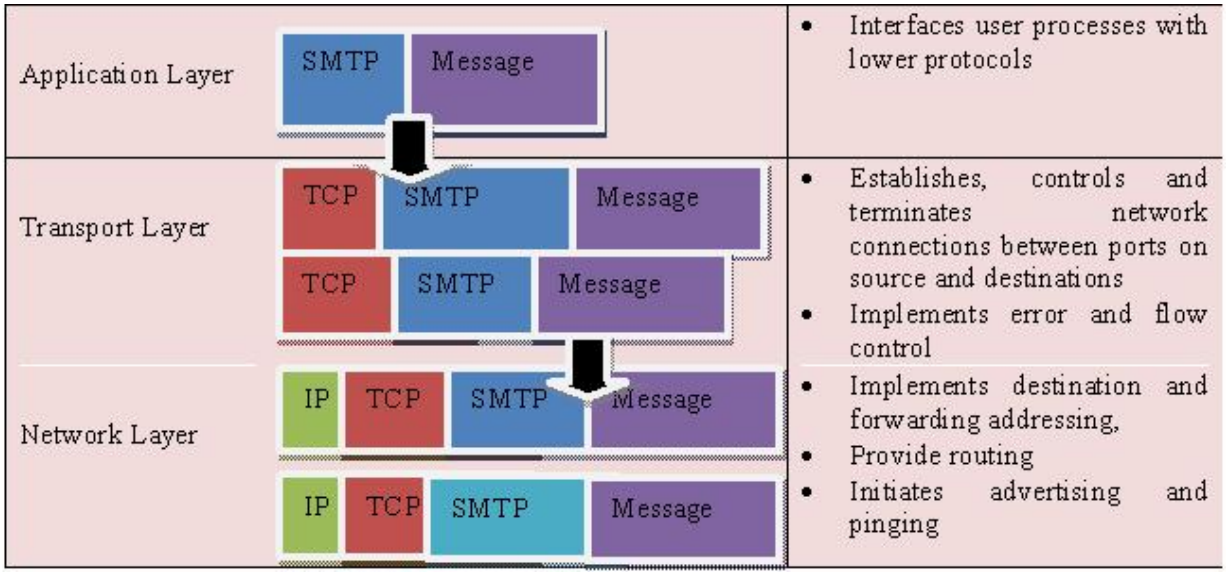

Fig. 1: Message transmission using layers in an Internet Protocol stack. [3, 4]

B. User Datagram Protocol (UDP)

The User Datagram Protocol (UDP) is a transport layer protocol defined for application with the IP network layer protocol. TCP is generally superior in terms reliability than UDP, but UDP does a great job when it comes to transporting information that usually do not require reliable delivery[6]. This transport protocol tenders least transport services, non guaranteed datagram delivery while at the same time giving applications direct access to datagram service of the IP layer. UDP does not provide acknowledgement to the sender, hence providing a connectionless and unreliable transport of message. The integrity of data suffers from lost packets, missequenced packets and receipt of duplicate packets. Such situations occur without the knowledge of the sender [6, 8]. UDP introduces the idea of port numbers, used by application layer which resides above UDP. Port numbers are of great importance in terms of actions that call for specific response by the receiving station and requested by the application itself [7]. Lastly, UDP is well-known transport protocol used by several application layer protocols, including Domain Name System (DNS), Network File System (NFS), and Trivial File Transfer Protocol (TFTP) [8].

II. PROCEDURE

i. Visit http://www.wireshark.org. and download the latest version of Wireshark and its user guide.

ii. Discover the network settings on your computer before running Wireshark. Run the command prompt on your windows machine and enter the command *ipconfig/all* to display all network settings. From the information displayed in the figure 2 below (command prompt), one is able to identify the IP address of your computer's link to the LAN, the subnet mask, the MAC address of your NIC, and the network's range of IP addresses.

iii. Run Wireshark and click on the icon referred to as list available capture interfaces, located on the top left corner of your computer screen. This will display all relevant network interfaces that can be captured by Wireshark.

iv. Choose the identified network interface in Step (ii), the network connection to capture from. This is done by clicking the pertinent start button; from the appearing Wireshark: Capture Interface dialog.

v. The Wireshark will start capturing packets. The captured packets are displayed in real time on the main window as they appear.

vi. Select an individual packet by clicking on the coloured section of the packet. Details of the displayed packet will appear in the middle section showing information enclosed in layer 7 to layer 2 of the OSI model.

vii. Randomly select and examine captured packets in the transport layer, Transmission Control Protocol and User Datagram Protocol.

III. RESULTS AND ANALYSIS

a. Transmission Control Protocol Figure 3 shows the TCP segment format. The figure displays different fields contained by the TCP header. The TCP header is 20-24 bytes long with options.

i. **Sources Port (2 Bytes):** It is the application's port number of the host sending the data. The source IP address and source port tasks as the return address of the packets.

ii. **Destination Port (2 Bytes):** It is the port number of the requested application on the destination host. This port includes the interface address of the application on the computer of the recipient's for which the data in the packets will be transferred. The source and destination ports identify points where TCP services are received by upper-layer source and destination processes.

iii. **Sequence number (4 Bytes):** The 4-bytes (32-bits) sequence number is used by the receiver computer

```
Microsoft Windows [Version 6.1.7601]
Copyright (c) 2009 Microsoft Corporation.  All rights reserved.

C:\Users\Nimrod>ipconfig/all

Windows IP Configuration

   Host Name . . . . . . . . . . . . : Nimrod-PC
   Primary Dns Suffix  . . . . . . . :
   Node Type . . . . . . . . . . . . : Hybrid
   IP Routing Enabled. . . . . . . . : No
   WINS Proxy Enabled. . . . . . . . : No
   DNS Suffix Search List. . . . . . : kuct.ac.ke

Wireless LAN adapter Wireless Network Connection:

   Media State . . . . . . . . . . . : Media disconnected
   Connection-specific DNS Suffix  . :
   Description . . . . . . . . . . . : Realtek RTL8187B Wireless 802.11b/g 54Mbp
s USB 2.0 Network Adapter
   Physical Address. . . . . . . . . : 70-F1-A1-3A-E8-04
   DHCP Enabled. . . . . . . . . . . : Yes
   Autoconfiguration Enabled . . . . : Yes

Ethernet adapter Local Area Connection:

   Connection-specific DNS Suffix  . : kuct.ac.ke
   Description . . . . . . . . . . . : Realtek RTL8102E/RTL8103E Family PCI-E Fa
st Ethernet NIC (NDIS 6.20)
   Physical Address. . . . . . . . . : 70-5A-B6-88-DA-4B
   DHCP Enabled. . . . . . . . . . . : Yes
   Autoconfiguration Enabled . . . . : Yes
   Link-local IPv6 Address . . . . . : fe80::7966:ffd3:1302:66f8%10(Preferred)
   IPv4 Address. . . . . . . . . . . : 192.168.117.156(Preferred)
   Subnet Mask . . . . . . . . . . . : 255.255.224.0
   Lease Obtained. . . . . . . . . . : Thursday, August 01, 2013 10:56:37 AM
   Lease Expires . . . . . . . . . . : Friday, August 02, 2013 11:19:56 AM
   Default Gateway . . . . . . . . . : fe80::3851:688c:778a:8ade%10
                                       192.168.96.1
   DHCPv6 IAID . . . . . . . . . . . : 242244278
   DHCPv6 Client DUID. . . . . . . . : 00-01-00-01-16-C6-10-C8-70-5A-B6-88-DA-4B

   DNS Servers . . . . . . . . . . . : 192.168.96.1
   NetBIOS over Tcpip. . . . . . . . : Enabled

Tunnel adapter Local Area Connection* 9:

   Media State . . . . . . . . . . . : Media disconnected
   Connection-specific DNS Suffix  . :
   Description . . . . . . . . . . . : Teredo Tunneling Pseudo-Interface
   Physical Address. . . . . . . . . : 00-00-00-00-00-00-00-E0
   DHCP Enabled. . . . . . . . . . . : No
   Autoconfiguration Enabled . . . . : Yes

Tunnel adapter isatap.{1F791F33-D28C-41A3-8631-6CA35D5C9BEE}:

   Media State . . . . . . . . . . . : Media disconnected
   Connection-specific DNS Suffix  . :
   Description . . . . . . . . . . . : Microsoft ISATAP Adapter #2
   Physical Address. . . . . . . . . : 00-00-00-00-00-00-00-E0
   DHCP Enabled. . . . . . . . . . . : No
```

Fig. 2: Network settings of my computer.

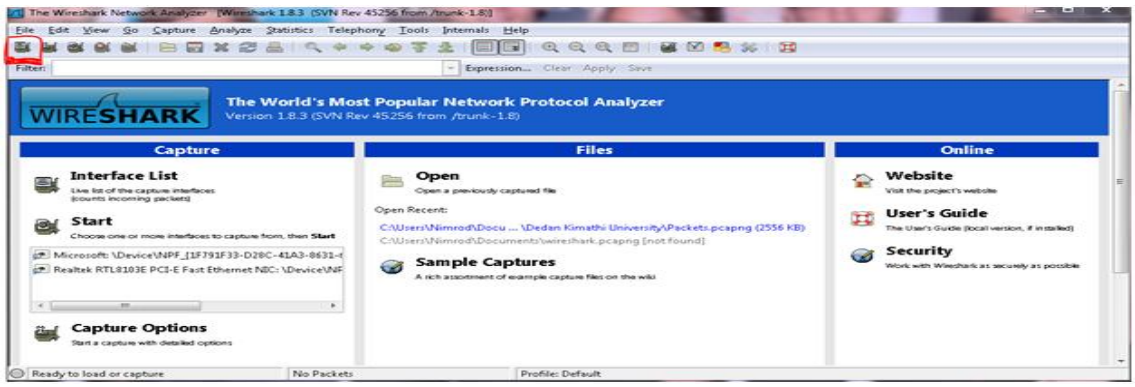

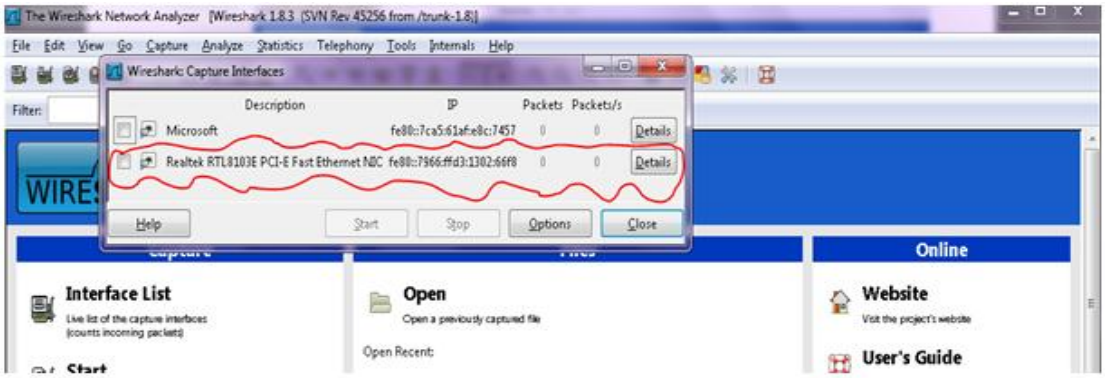

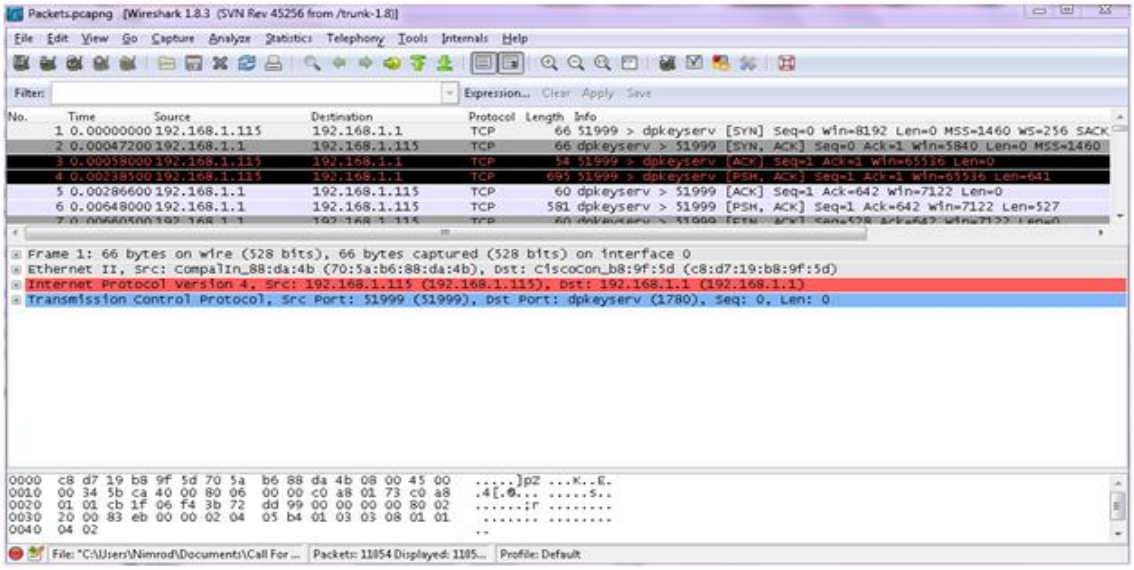

to reassemble the patchy data back into its original form. It is possible for packets to take different transfer channels and arrive out of order at the destination, especially in a dynamically routed network. This field compensates for the lost packets, out of order packets, and inconsistency of delivery in a process called sequencing.

iv. **Acknowledgement number (4-bytes):** TCP make use of the 32-bit acknowledgement (ACK) of the first octet of data held in the subsequently supposed segment. However, it may seem spontaneous contradictive to acknowledge something that has not transpired still, nevertheless a TCP/IP source machine that receives an ACK understands that all the data, except that particular received segment. The sequence number of the packet being acknowledged is used to identify each ASK. This field is only applicable if the ACK flag is set.

v. **Header Length (4-bits):** This field corresponds to the number of 32-bits words within the TCP header and indicates where the data begins. The TCP header is the basic number of 32-bits in length.

vi. **Reserved (6-bits):** this field is always set to zero and reserved for up to now unspecified future use. Nevertheless, at present some bits in this field are used to transfer flow control flags which make it possible for TCP to adapt the number of segments that can be sent before an ACK is received from the recipient.

vii. **Code/Flag bits (6 bits):** this field contains control functions used to set up and terminate a session. The 6-bit code field comprises of 6 1-bit flags namely URG, ACK, PSH, RST, SYN, and FIN that enable the control functions of urgent field, acknowledgement of important field, push, reset, synchronize sequence numbers and finished sending data respectively.

viii. **Window (4-bytes):** It is a 16-bit field used by the destination machine to inform the source host the amount of data the destination host is prepared to acknowledge in octets for each TCP segment.

ix. **Checksum (2 bytes):** This field indicates whether the header was lost, duplicated or damaged while on transit. The field also employs Cyclic Redundancy Check (CRC) since TCP is not confident with the lower layers thereby checking the validity of every transmitted segment. The CRC checks and confirms the header and data fields. The source and destination host calculates the checksum based on the contents of the segment. If the contents are intact, not altered,

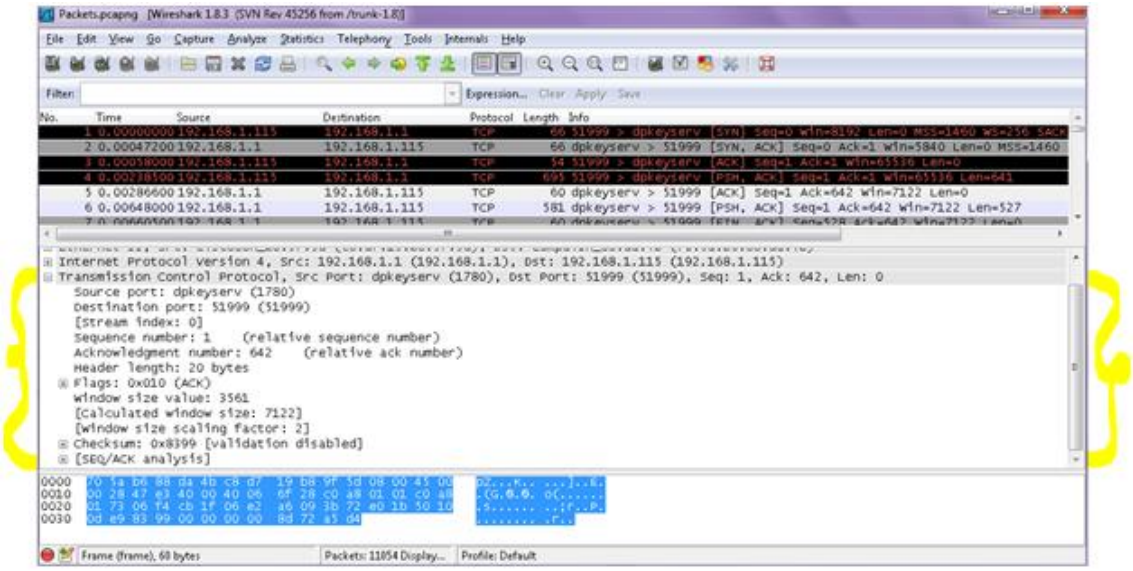

Fig. 3: A captured UDP Segment, using packet sniffer in Wireshark 1.8.3

while in transmission and the final results of the two calculations are similar then the validity of data is proved.

x. **Urgent Pointer (2 bytes):** This field points to the primary urgent data byte in the packet i.e. the sequence number of the octet following the urgent data. The urgent field can only be interpreted in segments with set URG control bit.
Padding will pre-empt the urgent field if the said flag is not set. Data segments that are acknowledged as urgent are treated to accelerate handling by the entire TCP/IP devices that lie in the network between the source and destination machines.

xi. **Option:** It implies that no options have to be present (Option size of 0). This field may comprise of 0 or a multiple of 32-bits, if any exist. However, padding of 0's must be applied to ensure that data starts on a 32-bit boundary, especially where used options do not cause the option field to sum a multiple of 32-bits. To ensure reliable establishment and termination of connections, TCP uses a three-way handshake process. The process is necessary and sufficient for correct synchronization between two ends, Host-A and Host-B, of a TCP connection.

xii. **Data:** It includes the upper layer headers and is normally dropped to the TCP protocol at the transport layer.

A. Connection Establishment

For communication to take place, Host-A sends a segment with SYN bit set and a random Initial Sequence Number (ISN). After receiving the segment, Host-B sends back a segment with SYN bits set, ACK, and random ISN to Host-A for communication process. This implies that it acknowledges the first SYN segment and the handshake process continues. Eventually, Host-A sends ACK to Host-B informing that connection between the two hosts has been established.

B. Connection Termination

It is worth noting that connections can be established or terminated from either Host-A and Host-B of simultaneously from both hosts. Figure 6 above Host-A provides an active close while Host-B a passive close. Since the termination of half-duplex connections is completely independent of each other, connection termination is a four-way handshake [9].

b. User Datagram Protocol From the above packet capture, it is clear that the UDP packet has four fields. These include the source and destination ports- each containing 2 bytes (16 bits) and the length and checksum fields- containing 16 bits each.

i. **Source port (2 Bytes):** It is a Service Access Point (SAP) used by UDP packets from clients to indicate the session on the local client where the packet originated from. If the UDP packets are from a server, they would carry the server SAP in source port.

ii. **Destination port (2 Bytes):** UDP packets from a client make use of the destination port as a SAP to point out the required services from any remote server. It is from this field that the server's UDP packets carry the server SAP.

iii. **UDP Length (2 Bytes):** This refers to the number of bytes comprising of a combination of payload data and UDP header information.

iv. **UDP Checksum (2 Bytes):** A Checksum is used to verify that end-to-end data has not being corrupted during transfer by either network routers or bridges or during processing process by an end system. Standard Internet Checksum is an algorithm used to

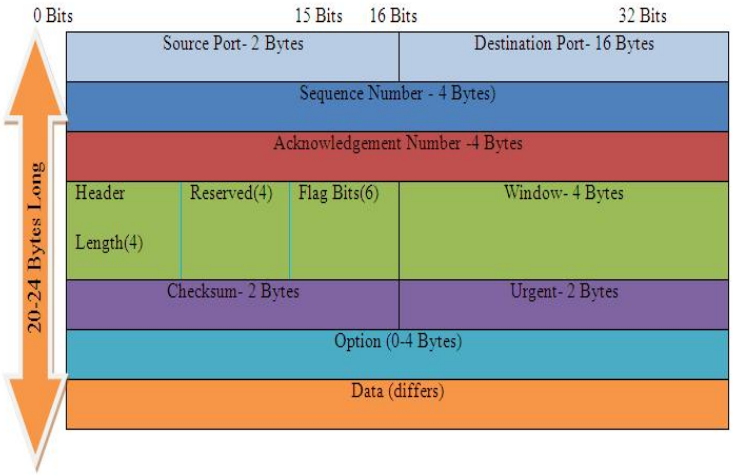

Fig. 4: TCP segment Structure from the Results

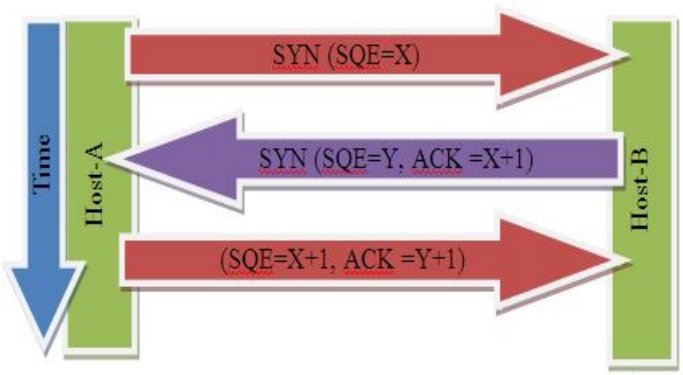

Fig. 5: Connection Termination Process [9]

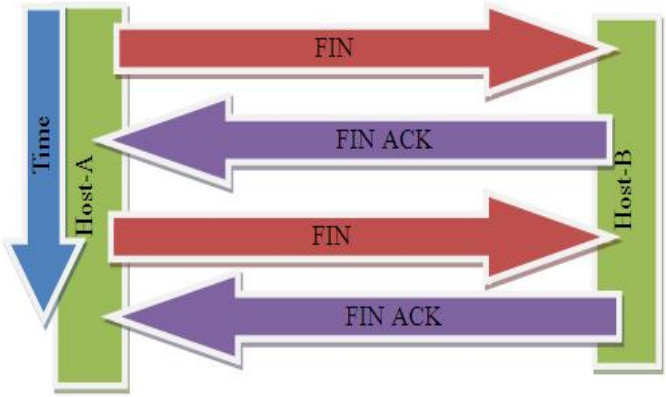

Fig. 6: Connection establishment Process [9]

compute the checksum and it operates by allowing the receiver to verify that:

- The packet destination was intended since it covers the IP addresses, port and protocol numbers.
- The packet is not padded or truncated since it covers the size field.

Lastly, there is an optional data field which differs in the number of bits. From the above explanations, we can deduce a UDP segment format as shown below.

IV. CONCLUSION

In transport layer of the OSI reference model, TCP and UDP transport protocol stands out from the other protocols.

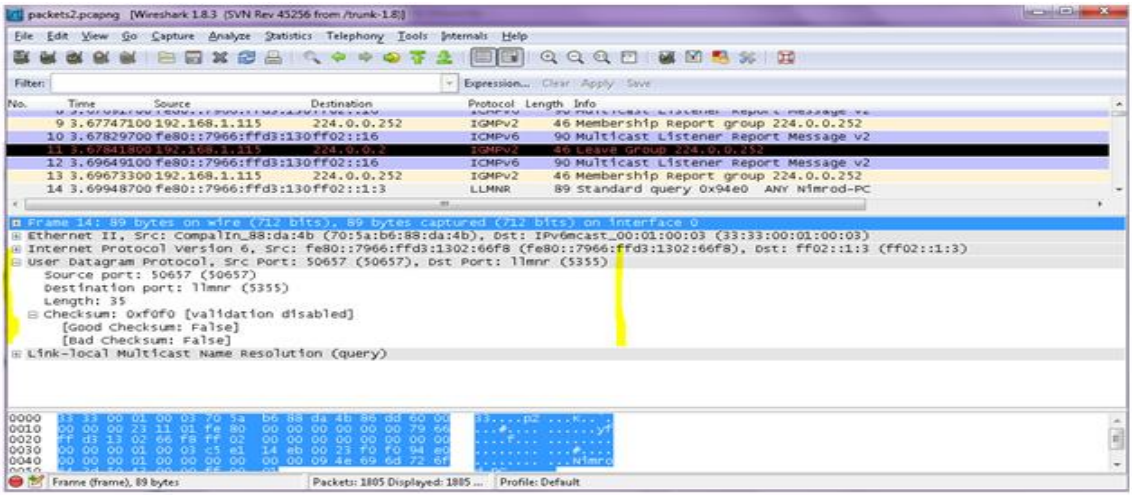

Fig. 7: A captured UDP Segment, using packet sniffer in Wireshark 1.8.3

Source Port- 2 Bytes	Destination Port- 2 Bytes
Length- 2 Bytes	Checksum- 2 Bytes
Data (Differs)	

Fig. 8: A captured UDP Segment, using packet sniffer in Wireshark 1.8.3

Though TCP is the most reliable than UDP, UDP can be relatively efficient and effective if the upper-layers can handle retransmission and error checking. TCP is the best choice for those applications that require precedence and security. The inclusion of 32-bit sequence number, acknowledgement number, and flag bits in the TCP header makes it easier for the protocol to ensure flow control, error checking and multiplexing unlike UDP. However, both the TCP and UDP use port numbers and create unique pockets definitions when used with IP addresses, across the network, but TCP remains the suitable transfer protocol for data communication.

REFERENCES

[1] C. M. Kozierok., "The TCP/IP guide.," tech. rep., 2005. www.tcpipguide.com/free/TransportLayerLayer4.htm.
[2] L. N. Cassel and R. H. Austing, *Computer Networks and Open Systems: An Application Development Perspective.* Burlington: Jones & Bartlett Learning, 2000.
[3] J. FitzGerald and A. Dennis, *Business Data Communications and Networking.* John Wiley & Sons Inc, Hoboken, New Jersey, 2009.
[4] B. E. Carne, *A Professional's Guide to Data Communication in a TCP/IP World*. London, United Kingdom: Artech House, 2004.
[5] A. Pude and K. Rmer, *Distributed Systems Architecture: A Middleware Approach.* Amsterdam: Elsevier Group, 2011.
[6] R. Braden, *Requirements for Internet Hosts - Communication Layers*. Marina del Rey, CA, 1989.
[7] G. Thomas, "Introduction to the transmission control protocol: How does tcp and udp impact control transmission?," *The Extension: A Technical Supplement to Control Network*, vol. 1, no. 5, pp. 1–4, 2000.
[8] G. C. Kessler, *TCP/IP*. 2011.
[9] P. R. Egli, *TCP - Transmission Control Protocol*. 2011.

IMPROVED NETWORK SECURITY THROUGH KERNEL TRANSFORMATION

Vincent Omollo, Dr. Kibet Langat, Stephene Musyoki
Email: vincentyoung88@gmail.com

Department of Telecommunication and Information Engineering
Jomo Kenyatta University Of Agriculture and Technology.
Tel: +254725818924

Abstract

Network security is a field that has drawn a lot of attention lately. This can be attributed to the importance and vulnerabilities of data communication networks. Many illegal groups of hackers have developed applications that enable them gain unauthorized access to private networks and computer systems. Various mechanisms have been developed to curb these intrusions. These include authentication, authorization, intrusion detection systems (IDS), firewalls and gateways. The adoption and use of these measures has proven ineffective. Authorization and authentication protocols can be easily cracked by software. IDS do not always detect all intrusions. Firewalls and gateways can be bypassed by advanced algorithms, and may slow down traffic flow. In this paper, a secure LAN architecture based on router internetworking operating system (IOS) hiding is suggested as a more effective means of preventing network intrusions.

1. INTRODUCTION

One of the features of the 21st century is the rapid increase in the number of data communication networks. Today, virtually every company, university, college, business and individual premises have connections to the internet. This can be attributed to the fact that the internet provides them with the required information concerning business advertisement, educational forums, entertainment facilities, weather updates, news from any part of the world and even information on their current location by use of the Global Positioning Systems (GPS). On the flip-side, any leak of information to their direct competitors could spell disaster, from a business perspective.

The need to protect information has forced many institutions to think about the security of their network infrastructure more seriously. Particularly, these organizations have to deal with attacks on their networks (either from curios snoopers or malicious attackers), and also data protection from their competitors.

The traditional solution involves the usual fundamental security services; an authentication service, an authorization service and an administrative service. The combination of these components may lead to a high-level of assurance of protection for the company. Authentication [1] is defined as the formal identification of a user. This requires a user to provide proof of their identity. Authorization [1] is the release of access to the users, based on their authentication credentials. Using both of these, an institution gains control over those who access its network resources.

Another solution to network intrusion involves the use of Honeypots. The idea of this mechanism is to catch malicious network activity with a prepared machine [2]. This computer is used as a bait. The intruder is meant to detect the Honeypot and try to break into it [3]. The network administrator is then able to monitor the intruder activities including which system files he accesses and the tools he uses to attack the network. Using this information, the network can be made more secure.

Cryptography is the art of encoding network data in a way that only the intended recipient can decode it, and know that the message is authentic and unchanged. Strong encryption is not a technical standard; it simply implies that one's encryption cannot be broken by current known methods. It can be used to protect data against organized crime, government and multinational corporations [4].

More recently, network traffic has been used to boost cyber security [5]. However, some of these radical changes to the current internet approaches to clean-slate architecture run the risk of introducing new opportunities for attacks. These attacks range from new forms of denial-of-service to attacks against other user's privacy. This is particularly true for general-purpose caches that are shared by a small number of users [6]. For speed optimization, several web browsers pre-fetch domain names appearing in links on web pages. This information can however be used to exploit pre-fetching Domain Naming System (DNS) names found on search engine result pages. This is done by inferring the keywords that have been used during searches [7]. Attackers can build a list of domain names that would be resolved for a given keyword, and probe DNS caches for these domains.

While the above technologies provide security to networked devices to some extent, they still lack in feature to support current and future advancements in devices that was be connecting to a network. This paper explores a new security approach through the transformation of the host system kernel.

II. METHODOLOGY

Introduction

In this paper, a secure LAN architecture is presented. The design in Figure 1 below was used for the study.

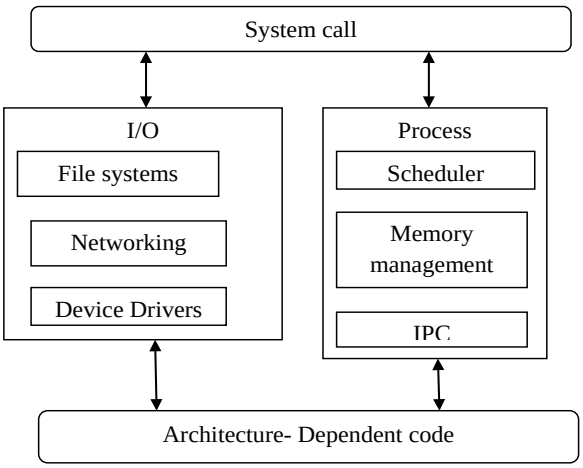

Figure 1: Architecture of the kernel

Choosing an IOS kernel to transform

For this paper, QUAGGA network router was selected. This is because it is open source; hence it can be changed and recompiled as any custom system.

Designing the initial IOS stack configuration.

The initial process of changing the routing stack of the QUAGGA IOS was to determine its exact architecture. Figure 2 below shows the architecture of the QUAGGA router.

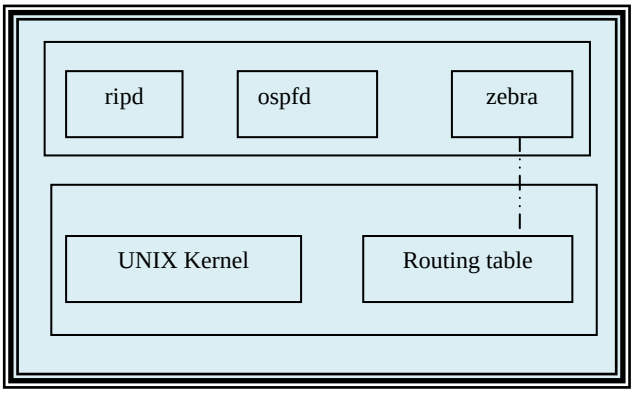

Figure 2: Design Architecture

The zebra daemon kernel controls the communication process. We configured it is as shown in Table 1 below. From the table below, the network manager communicates with the routing protocols via its interfaces. These are 192.168.1.1/24, 192.168.10.1/24 and 192.168.20.1/24.

We ran Nmap scan on one of these interfaces and the information in Figure 3 below was revealed. From the figure, the router model, version, services and the state of our interface was successfully detected.

```
!
hostname netmanager
password omollo
enable password omollo
!
interface eth0
 description LINK TO ETH0
 link-detect
 ip address 192.168.1.1/24
 ipv6 nd suppress-ra
!
interface lo
 description LINK TO LO
 link-detect
 ip address 192.168.10.1/24
!
interface wlan0
 description LINK TO WLAN
```

Table 1: Configuration of the Zebra daemon.

The router model is Quagga, its version is 0.99.21 (Derivative of GNU Zebra), service is Quagga and one port (TCP) was reported open. Since we installed our router in Ubuntu 12.04, this information was also revealed. In the OS guess, the network scanner is 96 % sure that the host OS is Ubuntu.

Probing the changes in the IOS kernel to conceal router identity

The operating system in the host system determines how the TCP/IP packets are packaged. Different operating systems implement the IP header and the associated protocols in their own style. It is this implementation procedure that network scanners look for and try to compare with their databases criteria that leads to effective identification of a network device.

scan against this address and the information similar to the one in Figure 3 above was obtained. As can be seen from Figure 3, the Nmap tool managed to match the host system with 96% accuracy (Ubuntu 7.10, x86_64). It is interesting to note that the network scanner managed to give such accuracy, although its version results are wrong.

The next task was to study and experiment with the Ubuntu kernel, TCP options and

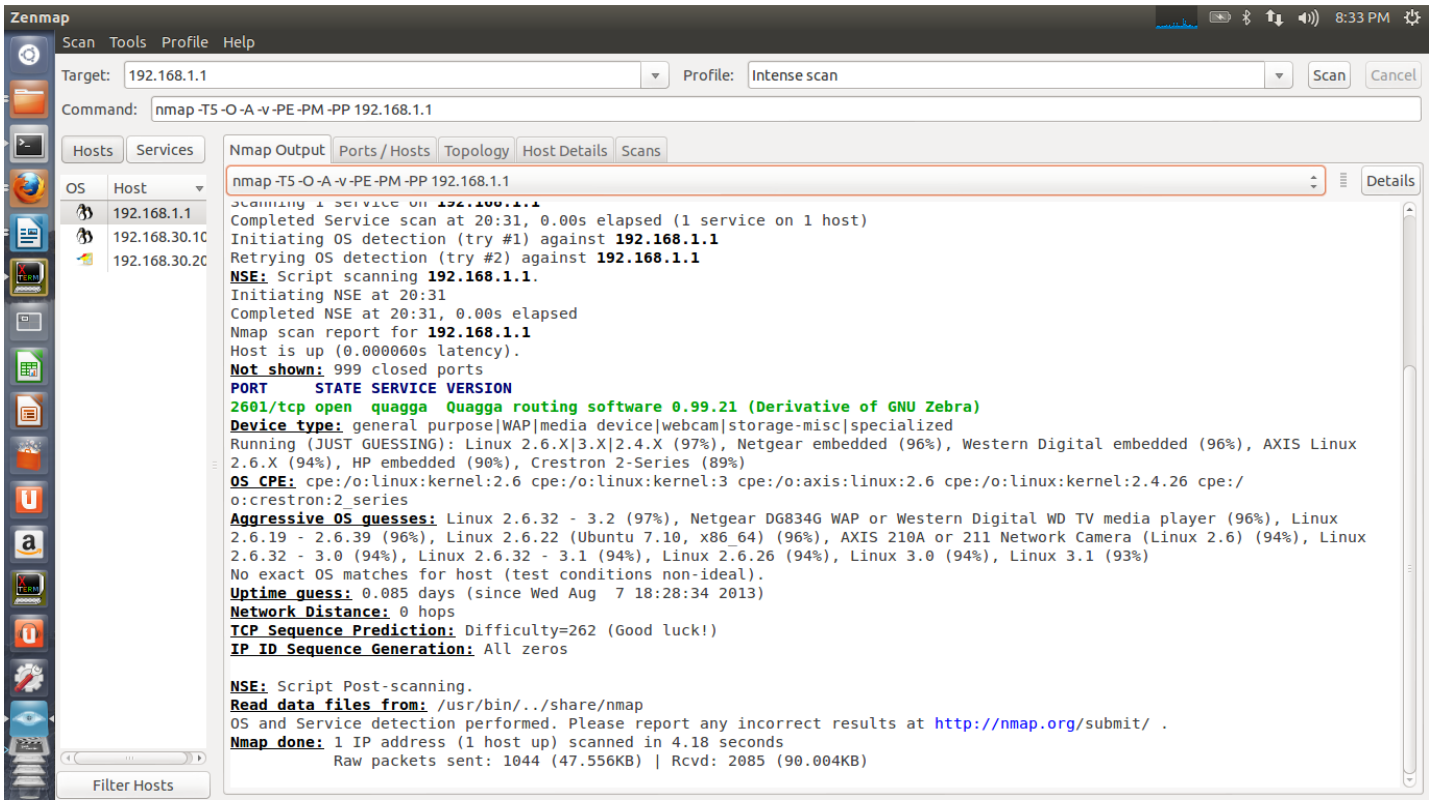

Figure 3: Responses of Nmap scan against Interface 192.168.1.1

Therefore rigorous study and experiments were carried out to determine what part of the kernel produced them and how it could be re-structured and re-compiled to hide this crucial information from untrusted systems and users. In the following sub-sections, we discuss these procedures.

Disguising Ubuntu 12.04 host operating system

We installed our router in Ubuntu version 12.04. It therefore acted as our host operating system. Its IP address was set to 192.168.30.10, its network being 192.168.30.0. We first ran the network

flags in an effort to understand the components responsible for revealing the above information.

TCP Timestamp

This TCP option tracks the current time in a TCP packet that is sent over the internet. When the packet is sent to its destination, upon arrival, the time value is echoed back to the sender. For Ubuntu 12.04, its default value was found to be 1.

TCP window scaling

This option allows the window size to be increased above its normal value of 32,767. This is achieved by multiplying the advertised window size by the value of the window scale. In this way, the performance of fast networks can be increased. Its value was found to be 0.
We changed these two values by setting timestamp=0 and window scaling =0. This was done by issuing the commands shown in Table 2 below from the terminal.

Sudo nano /proc/sys/net/inpv4/tcp_timestamps
Sudo nano /proc/sys/net/inpv4/tcp_window_scaling

Table 2: Commands to open TCP options files
The above command opened files from which the new values were inserted and saved. We then ran a network scan on the host address and obtained the information shown in Figure 4 below.

It can be observed that the network scanner's accuracy has reduced by 2 %(from an initial value of 96% to 94%). It now indicates that the host is a Netgear DG834G WAP or Western Digital WD TV media player. Interestingly enough, Ubuntu does not appear in its OS guesses. However, this gap of 2% is small. Hence further experimentations were carried out to increase this gap.

TCP time wait Recycle and TCP time wait Reuse
They enable fast recycling of TIME_WAIT sockets. The TCP_TW_REUSE flag allows reusing sockets in TIME_WAIT state for new connections. Its default value was found to be 0. It is a good option when dealing with a web server that has to handle many short TCP connections left in TIME_WAIT state.

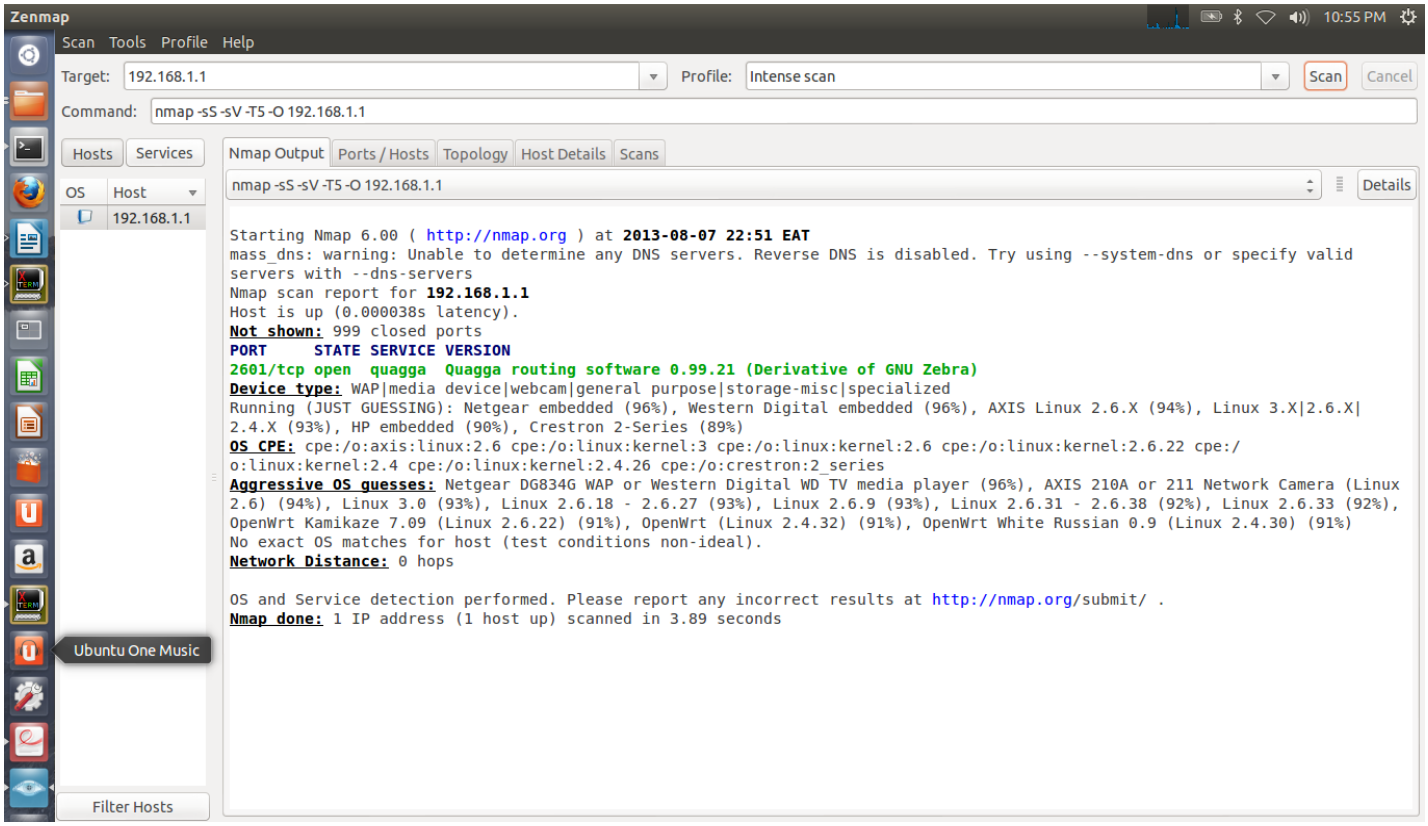

Figure 4: Nmap scan against the host system

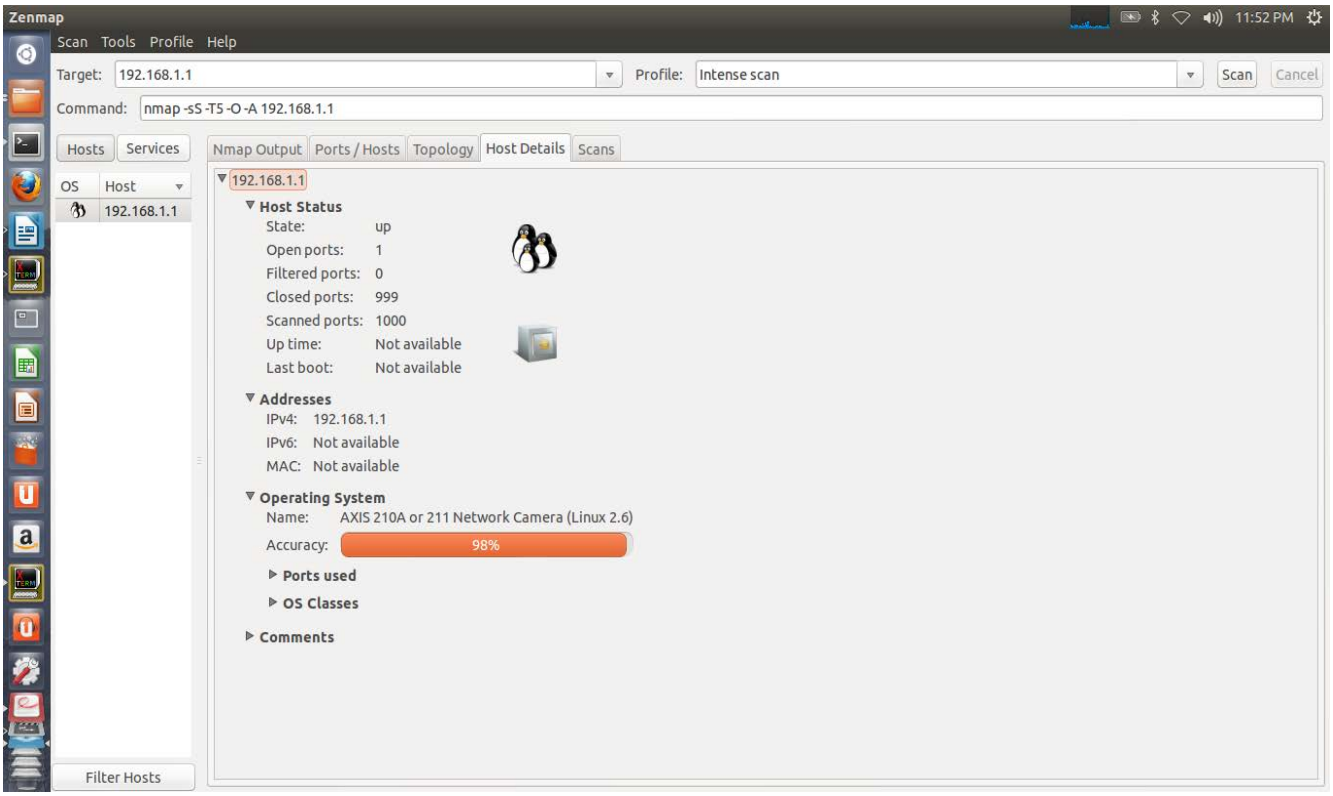

Figure 5: Responses from an Nmap scan of the host (tcp_tw_recycle=1)

However, the TCP_TW_RECYCLE could cause some problems when using load balancers. Its default value was found to be 0. We changed these values to 1 and ran a scan. The information in Figure 5 was observed.

The network scanner is now strongly convinced that the host operating system is a network scanner (with accuracy of 98%). Note that this is 1% more than the original Linux guess and 2% more for Ubuntu guess. The accuracy of the scanner reduced by 2% (from 97% to 95%) as shown in Table 3 below.

Aggressive OS guesses: AXIS 210A or 211 Network Camera (Linux 2.6) (98%), Linux 2.4.26 (Slackware 10.0.0) (95%), Linux 2.6.24 (95%), AXIS 211A Network Camera (Linux 2.6) (95%), AXIS 211A Network Camera (Linux 2.6.20) (95%), Check Point SBox-200 firewall (95%), Check Point VPN-1 UTM appliance (95%), Linux 2.6.31 (95%), Linux 2.6.32 (95%), Android 2.2 (Linux 2.6) (95%) No exact OS matches for host (test conditions non-

Table 3: Responses from Nmap scan of the host (Percentage reduction)

We performed a number of re-writing in the TCP flags, options and in the kernel. Quite a number of these kernel and TCP flags produced no changes in the OS guess. A combinational change of TCP flags tcp_ecn, tcp_tw_recycle, tcp_abc, tcp_fin_timeout, tcp_timestamps, tcp_window_scaling, tcp_fack and tcp_dfack produced the information shown in Table 4 below. At this point, it can be seen that the network scanner is totally confused about the host operating system. From the figure below, it is clear that we have managed to conceal the host operating system.

2601/tcp open quagga Quagga routing software 0.99.21 (Derivative of GNU Zebra)
No exact OS matches for host (If you know what OS is running on it, see http://nmap.org/submit/).
TCP/IP fingerprint:
OS:SCAN(V=6.00%E=4%D=8/17%OT=2601%CT=1%CU=34063%PV=Y%DS=0%DC=L%G=Y%TM=520F1
OS:7C5%P=x86_64-unknown-linux-gnu)SEQ(SP=FA%GCD=1%ISR=109%TI=Z%CI=Z%II=I%TS
OS:=8)OPS(O1=M400CST11NW7%O2=M400CST11NW7%O3=M400CNNT11NW7%O4=M400CST11NW7%
OS:O5=M400CST11NW7%O6=M400CST11)WIN(W1=8000%W2=8000%W3=8000%W4=8000%W5=8000
OS:%W6=8000)ECN(R=Y%DF=Y%T=41%W=8018%O=M400CNNSNW7%CC=Y%Q=)T1(R=Y%DF=Y%T=41
OS:%S=O%A=S+%F=AS%RD=0%Q=)T2(R=N)T3(R=N)T4(R=Y%DF=Y%T=41%W=0%S=A%A=Z%F=R%O=
OS:%RD=0%Q=)T5(R=Y%DF=Y%T=41%W=0%S=Z%A=S+%F=AR%O=%RD=0%Q=)T6(R=Y%DF=Y%T=41%

Table 4: Responses of Nmap scan after multiple tcp value changes

III. Results and discussions

The responses shown in Table 3 and Table 4 above show that the target IOS has been successfully hidden. Network intrusion mechanisms are not generic; they work on certain IOS versions, models, and in some instances, for particular device manufacturers. Hence any network intruder will first try to get this crucial information. However, from the above responses, it will be infeasible to get this.

Firstly, the intruder needs to know the IP address of the host system. This can be done by network scanner. However, the quagga router runs independent of the host system IP address. This means that gaining access to the host system does not guarantee access to the router. The router is controlled by a network manager, which is zebra daemon. The zebra daemon defines an interface through which other routing daemons can be accessed. This information cannot be accessed by network scan. Even if this interface is known, it doesn't reveal the networks to which the communications are directed towards. The running protocols and networks are not displayed in the network manager.

To remotely access and control the router, one normally needs a virtual teletype (VTY) password. However for this new architecture, a socket (a combination of port number and IP address) is needed. Moreover, it will be difficult to launch a generic attack against the target host because its internetworking operating system (IOS), manufacturer, model and version are hidden.

IV. Conclusion

The router IOS configuration information is very important for everyone who is interested in learning more about the router and the devices it controls. This makes this configuration the first target for network intruders, who are out to steal the organizational information or do any malicious activities. Therefore concealing the router IOS information is one of the ways of preventing network intrusions and the consequent damages. One of the methods of these mechanisms is the modification of the IOS architecture.

The prototype developed managed to confuse the network scanner; making it harder for someone to launch a specific attack or against the host system and the router installed in it. This is in recognition of the fact that network attacks are not generic; they work in certain IOS and specific versions.

References

[1] Committee on National Security Systems, "National Information Assurance (IA) Glossary", CNSS

Secretariat-National Security Agency ,June 2006.

[2] The Honeynet Project, “Know Your Enemy: Learning about Security Threats”, 2nd Edition, Addison-Wesley, 2004.

[3] Christian Doring, “Improving network security with Honeypots”, Masters Thesis report, University of Wisconsin-Platteville, Department of Computer Science, 2006.

[4] A. Dahlgren and O. Jonsson, “IPsec, the future of Network security?”, Göteborg University, 2000.

[5] Wasiam F. Major, “Statistical Analysis of the Skaion Network Security Dataset”, Naval Postgraduate School, 2012.

[6]Tobias Lauinger: “Security and Scalability of Content-Centric Networking” , Masters Thesis report,Technische University Darmstadt, 2010.

[7] S. Krishnan and F. Monrose, “DNS pre-fetching and its privacy implications: When good things go bad,” in *LEET ’10: Proceedings of the 3rd Usenix workshop on large-scale exploits and emergent threats*. Usenix, 2010.

[8] Kunihiro Ishiguro, et al., “Quagga, a routing software package for TCP/IP networks”, January 2013.

Use of Cost Analysis to Assess the Viability of Deploying Voice Quality Assessment on Mobile Phones

Kevin Mwongera, Kibet Langat, S Musyoki

Telecommunication & Information Engineering, JKUAT, 62000-00200, Nairobi Kenya

kmwongera@jkuat.ac.ke, kibetlp@jkuat.ac.ke, smusyoki@yahoo.com

Abstract

The measurement of Quality of Service (QOS) from the end user in mobile communication has been acclaimed as the most viable replacement for the use of drive tests. This study will show that despite the considerations of the method, the implementation of the methods has by far other concerns that would limit the use of the method. Despite using the User Equipment (UE), the retrieval of the data can be a costly affair if not done carefully. A cost analysis will be done to demonstrate this; and recommendations will be drawn that include multi-level selective reporting, to ensure that the method is utilized effectively and with manageable costs to operators. This will be of benefit to operators and developers of voice quality assessment application software to be deployed in the UE.

1 INTRODUCTION

When selecting a service provider, mobile phone consumers base their decisions on dependability and call quality. However, the quality of service is not as good as expected for all geographical regions. The conventional way of assessing the strength of the service has been drive tests.

KPIs (Key Performance Indicators) used to assess voice and video quality by regulatory agencies do not represent the real situation experienced by consumers. Use of QoE (Quality of Experience), for example, is not sufficient since consumers who might even be from the same geographical location may give different feedback.

Measuring the Quality of Service (QoS) from the users' end would be a better alternative. An emerging QoS technique in monitoring cellular networks is speech or voice quality assessment. It uses parametric models to estimate voice quality in GSM (Global System for Mobile Communications) networks. MDTs (Minimization of Drive Tests) have been used to reduce operators' costs by collecting users' RF (radio frequency) parameters from their devices. The new method will turn to fixing voice quality test tools in end user devices (mobile phones) to complement MDTs in assessing voice quality.

This method, though much better than getting consumers' opinions, has its limitations in terms of cost. The cost will be in the form of installing the voice quality test tools and retrieving data from the consumers' devices.

2 MINIMIZATION OF DRIVE TESTS (MDTs)

To find out which geographical regions do not experience the expected service quality, network operator's conduct drive tests. These drive tests involve literally driving from place to place to find out signal strength and other

RF parameters. Clearly, these drive tests require a lot of investment: many staff, vehicles and fuel. MDTs serve to reduce these costs, and are being adopted by many network operators.

MDTs were introduced in 2008 by NGMN (Next Generation Mobile Networks), an alliance of network operators [1]. They were further researched by 3GPP (3rd Generation Partnership Project) from 2009. 3GPP aimed to come up with principles and procedures that would enable network operators to collect data regarding coverage from UEs (user equipments) [2]. By 2010, a feasibility study was done. It mainly focused on coming up with measurement entities, specifically QoS verification and optimization of coverage [2]. According to [2], coverage optimization involved noting the prevalent problems which include but not limited to weak coverage, overshoot coverage, coverage holes, pilot pollution and uplink coverage. Figure 1 shows how MDT works:

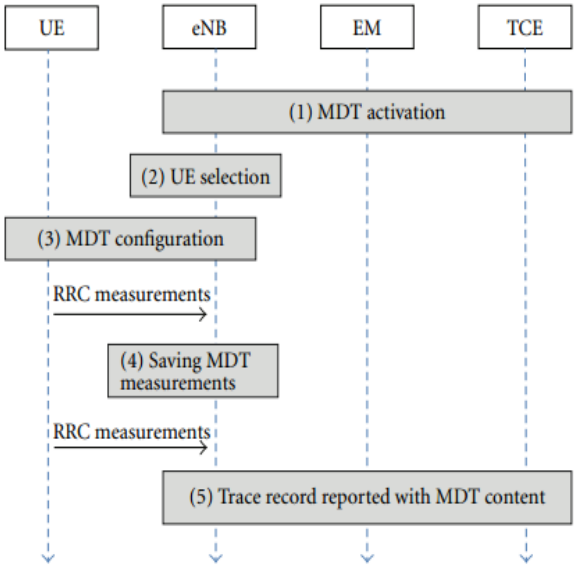

Figure 1: Immediate MDT Reporting [3]

After the feasibility study, attention was shifted to measurement and reporting schemes for the MDTs[4]. These include logged MDT as well as immediate MDT.

2.1 Logged MDT

This enables gathering of data from UEs which are usually in RRC (Radio Resource Control) idle state. A list of configuration parameters used is contained in[4]. RRC signaling provides the MDT configuration to UEs while they are connected to RRC. When UEs change to RRC idle state, measurement data is logged to the UE memory. UEs then report the data that had been logged when they switch back to the RRC connected state.

2.2 Immediate MDT

Immediate MDT uses the RRC measurement procedures that are already in existence, with an addition of location information. For example, when a condition has been fulfilled in RRC measurement, a set timer will expire. This sends RSRP (reference signal received power) and RSRQ (reference signal received quality) measurements to the E-UTRAN NodeB (eNB), with the addition of *LocationInfo* IE (information element) to the report[5].

3 ADDING VOICE QUALITY TEST (VQT) TOOLS TO IMPROVE MDT

MDT can be improved by analyzing voice quality using VQT tools and a Wireless Measurement Software such as the E6474A, which use the ITU-T Recommendation P.862 [6].

VQT tools are installed to a microcomputer, which is then put into a UE and an audio card. Audio files are then sent and received by the server over the network. The weak signals are compared to the original, stronger signals to come up with an MOS (Mean Opinion Score). A mobile phone call made to the server will trigger estimation of voice quality using PESQ (perceptual evaluation of speech quality) algorithm. This enables estimation of MOS for every test call. The figure below shows the architecture of MDT which incorporates VQT tools:

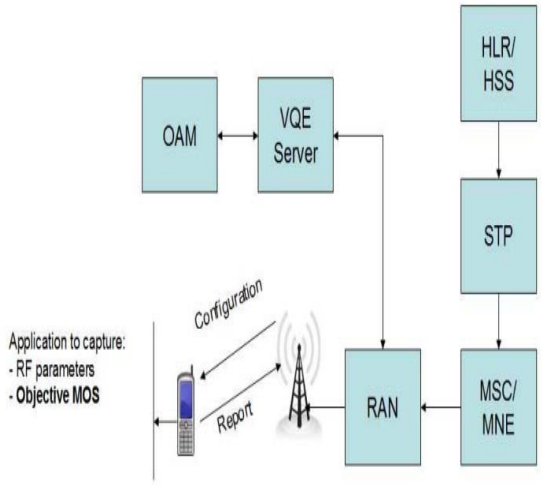

Figure 2: Architecture of VQT incorporated in MDT[7]

4 DEVELOPMENT AND DEPLOYMENT COSTS

Current MDT methods involve embedding application software into SIM cards to enable reporting of the RF parameters. In that case, the development of the program/software itself is a cost incurred. To add the VQT tools, it means that there should be investment in making both operations work together and fit them either on the SIM card or in application stores for today's smartphones.

There is no doubt that the algorithm which will be used may be part of the costs that will be accrued. This is due to the fact that the current market situation indicates that they are not free ware. Coding and embedding of the two functions will be done in such a way that they do not interfere with each other's functions. Tests also form a cost factor, with major investment going into conversion of user SIM cards so that they can accommodate both MDT and VQT.

To suit several points of installation, the cost may vary across several points of consumer access.An example would be a scenario that would use both SIM cards and application store utilization. Other costs include support systems like databases and servers to cater for such implementations. Staff too may be needed to look into these functions.

These costs are common for such investments. The fact that the implementation of the MDTs has been assimilated by the operators shows that the cost does not raise alarms as compared to the conventional drive test. Therefore, the costs have been limited by the scope of this research whose interest is in the operational costs. To be specific, this study is interested in the variable cost in such a project which gets information from the UE to the operator for analysis.

5 DATA RETRIEVAL COSTS

In the operation of VQT tools embedded on MDT solutions, there are two scenarios that can emerge. The data can be uploaded in raw format which will be large, consequently reducing the work load of the UE. In the case of tunneling the data to the databases, the cost will be accrued by the operator. The operator will have to provide for processing services when the data is obtained to detect areas that have gone below the expected KPI.

Arguably, the nature of the data and cost will vary depending on the amount of data that will be retrieved as well as the frequency and number of subscribers that are in the network.

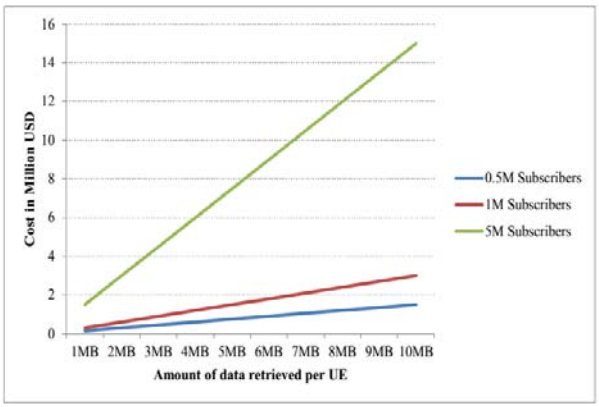

Figure 3: Varying costs depending on data and subscribers/UE

In figure 3, the cost per MB has been calculated as $0.03. For this case, an assumption of frequency was adopted to be 10. As the data indicates, the costs can be quite high if the main variables are not kept in check. Particularly, if the number of UEs/subscribers goes beyond 5million, the costs go even higher. For most operators, the number can go beyond that since some operators have about 12-20 million subscribers.

This analysis is for particular data retrieval techniques which have been outlined in this paper. Higher costs are caused by retrieval of raw unprocessed information; especially voice related. Therefore, it is better for the operators to develop applications that process the Voice Quality Index (VQI) within the UE. This will reduce the size of the data uploads by even more than 100 times. For example, a 1MB voice recording upon processing can be in the form of a 10KB score.

Additionally, the method can be made even cheaper by determining the methods of reporting used. These include situations where:

i. Data is reported upon request by the KPI and VQT analysis servers.

ii. Data is processed in the UE, and the report is only made when the KIP and VQT results are below an expected operational figure.

iii. Data collection by the operator is spread in regions in such a way that the frequency is reduced to acceptable limits per region in a given period.

In this method, the UE will process the voice and produce a score among other RF parameters. If either RF parameters or the VQI is below a certain expected amount, the UE stores the data on an expiry cycle to avoid too much accumulation. The reporting is not done until a request for that region is made. At that point, the records stored are reported on the predetermined cycle. The operators can do this on determined frequencies and in different regions all year round.

In this case, cost reduction will be done in the three-fold process recommended so that the project to be viable.

6 CONCLUSIONS

MDTs are very effective tools in helping operators achieve desired QoS. The need to deploy them in UEs is at the best of times since the ability of the UE has improved; and the spread projections show they are taking over the market. The deployment of VQT tools is thus made possible. This study has shownthat operational costs should be put into consideration. Using UEstogether with selective reporting to process the data will reduce costs as indicated in this study.

REFERENCES

[1] NGMN Alliance, "Next generation mobile networks use: Cases related to self organising network, overall description," v.2.02, Decemeber 2008.

[2] 3GPP TR 36.805, "Study on minimization od drive-tests in Next Generation Networks," v.9.0.0, December 2009.

[3] J Turkka, F Chernogorov, K Briggatti, T Ristaniemi, and J Lempiainen, "An approach for network outage detection from drive-testing databases," *Journal of Computer networks and communications*, vol. 2012, no. 163184, 2012.

[4] 3GPP TS 37.320, "Radio measurement collection for Minimization of Drive Tests," v.0.7.0, June 2010.

[5] 3GPP TS 36.331, "Evolved Universal Terrestrial Radio Access (E-UTRA), Radio

Resource Control (RRC) Protocol specification," v.10.4.0, December 2011.

[6] ITU-T Rec. P.862, "Perceptual Evaluation of Speech Quality (PESQ): An objective method for End-to-End speech quality assessment of norrowband telephone networks and speech codecs," Available on: www.itu.int/rec/T-REC-P862/en, April, 2005.

[7] Demostenes Z Rodriguez and Bressan G, "Improving the minimization drive tests using voice quality index," *Foundation for research support of Sao Paulo*, pp. 1-4, January 2011.

EVOLUTION OF MOBILE TELECOMUNICATION

Antony Onim[1], P. K. Kihato [1], Stephen Musyoki[2]

Onim.antony@gmail.com, smusyoki@jkuat.ac.ke, kamitazv@yahoo.co.uk

[1]Jomo Kenyatta University of Agriculture and Technology, Department of Telecommunication Engineering

[2]Jomo Kenyatta University of Agriculture and Technology, Department of Electrical Engineering

ABSTRACT- Mobile telecommunication is fast evolving. There is rapid technology growth driving the data rates that can be transmitted in the telecommunication networks. The drive for faster data rates is fuelled by a number of factors like the improvement of ability of mobile devices to handle higher data rates as they run applications that are more demanding on data like video calls. There is also an increase on the development of more mobile value chain through applications based on mobile operating system platforms like Android and Windows 8. This paper explores the various developments as well as the drivers for these developments.

Key words- Mobile telecommunication, Data rates, Mobile applications, Developments.

1. INTRODUCTION

Over the last two decades, mobile radio has emerged from being a niche technology to becoming ubiquitous throughout much of the world. Most people come directly in touch with the technology through mobile phones and the networks that serve them. Mobile communication uses base stations to transmit information between mobile phones. Multiple users can access the same channels by being allocated a time slot, a different frequency or a specific code.

Mobile Generations:

The First Generation System (Analog) [1]

In 1980 the mobile cellular era started, and since then mobile communications have undergone significant changes and experienced enormous growth. First-generation mobile systems used analog transmission for speech services. In 1979, the first cellular system in the world became operational by Nippon Telephone and Telegraph (NTT) in Tokyo. This system offered handover and roaming capabilities but the cellular networks were unable to interoperate between countries. This was one of the disadvantages of first-generation mobile networks. The system was allocated bandwidth within the 800 to 900 MHz frequency range by the Federal Communications Commission (FCC) and traffic was multiplexed onto an FDMA (frequency division multiple access) system.

The Second-generation Systems (Digital)[2]

Second-generation (2G) mobile systems were introduced in the end of 1980s. Low bit rate data services were supported as well as the traditional speech service. Compared to first-generation systems, second-generation (2G) systems use digital multiple access technology, such as TDMA (time division multiple access) and CDMA (code division multiple access). Consequently, compared with first-generation systems, higher spectrum efficiency, better data services, and more advanced roaming were offered by 2G systems. New technologies have been developed based on the original GSM system, leading to some more advanced systems known as 2.5 Generation (2.5G) systems. (Global System for Mobile Communication): The main element of this system are the BSS

(Base Station Subsystem), in which there are BTS (Base Transceiver Station) and BSC (Base Station Controllers); and the NSS (Network Switching Subsystem), in which there is the MSC (Mobile Switching Centre); VLR (Visitor Location Register); HLR (Home Location Register); AC (Authentication Centre) and EIR (Equipment Identity Register). This network is capable of providing all the basic services up to 9.6kbps. This GSM network also has an extension to the fixed telephony network. GSM and GPRS (General Packet Radio Services): added new elements such as SGSN (Servicing GPRS) and GGSN (Gateway GPRS) to the existing GSM system. These elements made it possible to send packet data on the air-interface. This enables wireless access to the internet and bit rate reaching to 150 kbps in optimum conditions. GSM and EDGE (Enhanced Data rates in GSM Environment): increased the data rate up to 384 kbps.

The Third-generation (WCDMA in UMTS, CDMA2000 & TD-SCDMA)[3]

The International Telecommunication Union (ITU) defined the demands for 3G mobile networks with the IMT-2000 standard. In Europe 3G was called UMTS (Universal Terrestrial Mobile System. IMT2000 is the ITU-T name for the third generation system, while cdma2000 is the name of the American 3G variant. WCDMA is the air-interface technology for the UMTS. The main components includes BS (Base Station) or node B, RNC (Radio Network Controller), apart from WMSC (Wideband CDMA Mobile Switching Centre) and SGSN/GGSN. Services include wide-area wireless voice telephony, video calls, and broadband wireless data, all in a mobile environment. Additional features also include HSPA (High Speed Packet Access) data transmission capabilities able to deliver speeds up to 14.4 - 42 Mbps on the downlink and 5.8 Mbps on the uplink.

Fourth Generation (All-IP)[4]:

In contrast to 3G, the new 4G framework to be established will try to accomplish new levels of user experience and multi-service capacity by also integrating all the mobile technologies that exist. The current agreements on the requirements for IMT-Advanced are:

• Peak data rate of 1 Gbps for downlink (DL) and 500 Mbps for uplink (UL).

• Backward compatibility and inter-working with legacy systems.

2. Mobile evolution drivers

2.1. World Demographics

World population is projected to increase from 6.1 billion in 2000 to 7.7 billion in 2020 (an increase about 1.6 billion over 20 years). 95% of the increase comes from developing countries and especially from Asia and Africa regions. India significantly contributes to this growth with more than 17 million new inhabitants per year.

In the less developed countries, a CAGR (Compound Annual Growth Rate) of 1.33% is forecasted between 2000 and 2020 (vs 0.30% in more developed economies). In India, the population will grow from 1.04 billion to more than 1.37 billion in 2020, adding more than 230 million inhabitants during this period. In China, there will see a net addition of 164 million inhabitants to reach a global population of 1.43 billion in 2020. [5]

2.2 Urbanization level

Urbanization is steadily increasing with more than 50% world population living in cities today. In 2020, it is expected that this number will reach 55%. Moreover, the number of people living in mega-cities (more than 10 million inhabitants) will double to more than 400 million.[5]

2.3 Economic trends

Developing economies are catching up with the large economy countries with the entry of developing countries like Russia and Brazil into the top ten biggest economies in 2010. They have all fared well during the global economic recession. Chinese share in world GDP has increased from 7.1% in 2000 to 13.3% in 2010 and India has become the world's fourth largest economy in 2010.

Moreover, based on IMF and the United Nations forecasts, most developing economies in the top ten largest economies will be ranked higher than high income countries by 2020. Indeed, it is forecasted that China will be the world's largest economy accounting for more than 20.7% of global GDP. [5]

2.4 Evolutions in the mobile value chain

There are five main sections in the mobile value chain: contents and applications, application store, connectivity, mobile OS and the mobile terminal. Of these, the "application store" component is a significant change to

the mobile value chain; it did not exist (at least significantly) until the arrival of the App Store by Apple. The mobile OS is also worthy of interest, as the arrival of Google Android in this area has opened it up considerably.[6]

2.4.1 Mobile terminal

The role of the smart phone is increasingly important for the mobile internet as these devices are specifically designed to optimize such usage.[6]

2.4.2 Mobile OS

The importance of mobile OS has changed considerably with smart phones. The operating system is now at the heart of the system layer within the mobile phone, and is a vital interface between the applications and the mobile terminal. Google have the Android OS while Microsoft are playing catch-up with their Windows 08 OS.[6]

2.4.3 Connectivity

This is perhaps the one area which has changed the least and is unlikely to change very much in the future. After all, it is only the mobile telcos which can provide the connectivity for mobile Internet. Potentially there are other technologies such as WiFi which could replace mobile operators by offering the connection. In practice, however, WiFI-coverage will always remain "patchy" and true mobility will not be achieved.[7]

2.4.4 Application store

This is the part of the chain that has received most of the limelight in recent times and has seen the arrival of new entrants, due to the arrival of Apple App Store and the Google playstore. Players from all over the mobile ecosystem have latched onto this part of the chain. It is worth noting that a similar model – although not exactly the same – has in fact existed in Japan since the early 2000s; there, developers could create their own applications and have them available through operator portals. Currently this part of the chain is being hotly competed, with many big players from handset vendors.[8]

2.4.5 Contents and applications

With all the talk of application stores and the tens of thousands of developers and their applications, it is easy to forget that in fact all the main players offer their own applications too. For example, Apple iTunes is available on the iPhone, and in fact at the initial launch of the App Store, developer applications which threatened iTunes were not accepted onto the store (although this stance appears to be changing). Internet giants too are also present; Google, for example, whilst offering the Android Market Place for developer applications also offers their own mobile version of Google services. All the same, it is crystal clear that this part of the chain is now highly innovative and easily accessible to any startup with ideas for mobile applications.

3. MOBILE FORECASTS

Worldwide device mix[9]

The hypothesis regarding device mix take into account the growing share for mid-range and high-end smart phones, bringing low-end phones' share down below the 20% mark in 2020. According to this hypothesis, high-end smart phones will represent a little bit more than 20% of the total devices in 2010. Low-end phones will see their share falling from 76.6% in 2010 to 17.2% in 2020.

Worldwide mobile traffic

Total mobile traffic will reach more than 127 EB in 2020, representing an x33 increase over 2010. In 2020, it is forecast that Asia will represent 34.3% of total world mobile traffic, Europe 22% and Americas 21.4%.

Mobile data usage is estimated to be surpassing that of the Personal Computer. In developing countries where few people own a computer this is already the case. Cheapness of mobile phones with internet capability is driving up data usage and mobile phones are now used more for data then voice or SMS.

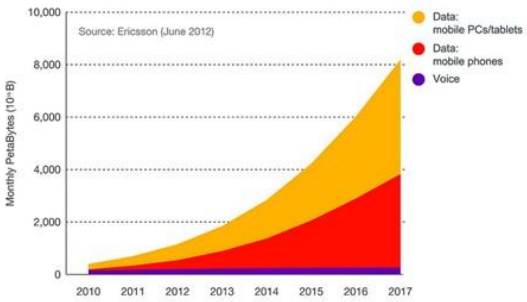

Fig. 1 Data usage for laptops and mobile phones[10]

Mobile devices are already widely available in the market and their popularity is increasing. As of 2012 according to Cisco report, global mobile data traffic grew 70 percent in 2012. Average mobile phone usage grew 81%. This

trend is set to increase from current 0.9 EB to 11.2 EB in 2017.

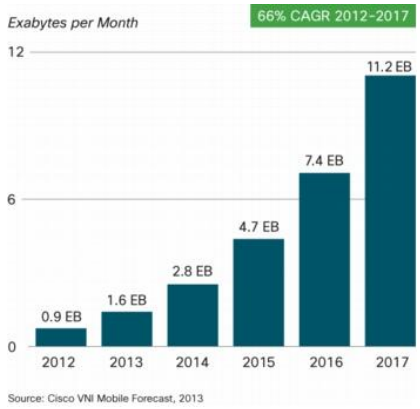

Fig. 2 Mobile monthly data usage 2012-2017[10]

Cisco Forecasts 11.2 Exabytes per Month of Mobile Data Traffic by 2017.

4G mobile device connections comprise 0.9% of mobile connection and generate 14% of mobile data traffic. 4G is forecast to grow to be 10% in 2017 and generate 45% of mobile traffic.

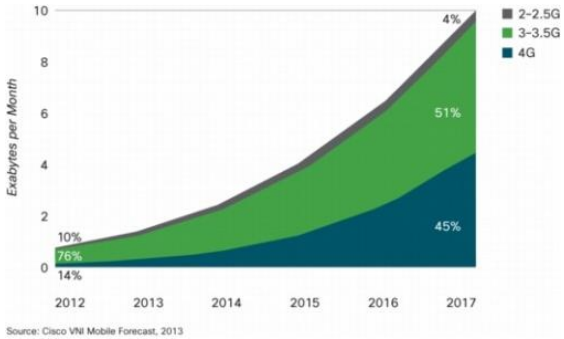

Fig. 3 Growth of the various technologies in terms of generated data traffic. [11]

However, 3G connection is set to surpass 2G with 4G gaining ground slightly.

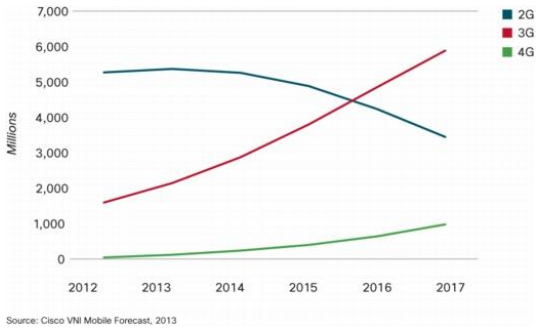

Fig. 4 Growth of the various technologies in terms of mobile device connections. [11]

Smart phones comprise 18% of mobile connections and generate 92% of mobile data traffic. The number of mobile connected tablets has also grown and continues to rise. The average smart phone will generate 2.7 GB of traffic per month in 2017, an 8-fold increase over the 2012 average of 342 MB per month. Aggregate smart phone traffic in 2017 will be 19 times greater than it is today, with a *Compounded Annual Growth rate* (CAGR) of 81 percent.

Tablets can generate 2.4 times more traffic than smart phones. While laptops can generate 7 times more traffic than smart phones. The population of smart phones is expected to surpass that of Personal Computers and laptops.

Furthermore, smart phones are set to become most popular mobile data communication device and remain so until 2017

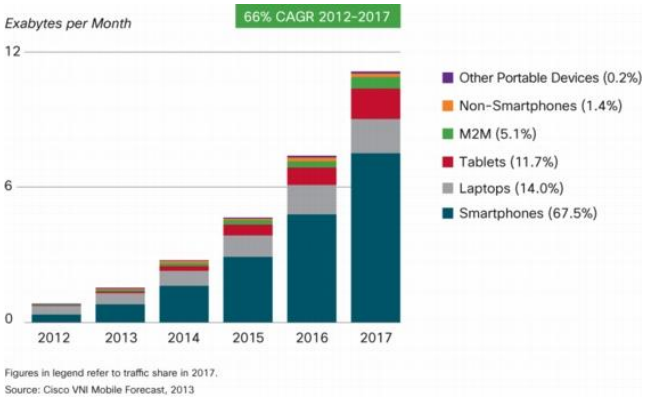

Fig.5 Projected device data usage until 2017[12]

Basic handsets are still most dominant with 82% of mobile connections. By the end of 2013, the number of mobile-connected devices will exceed the number of people on earth, and by 2017 there will be nearly 1.4 mobile devices per capita. There will be over 10 billion mobile-connected devices in 2017, including machine-to-machine (M2M) modules-exceeding the world's population at that time (7.6 billion).

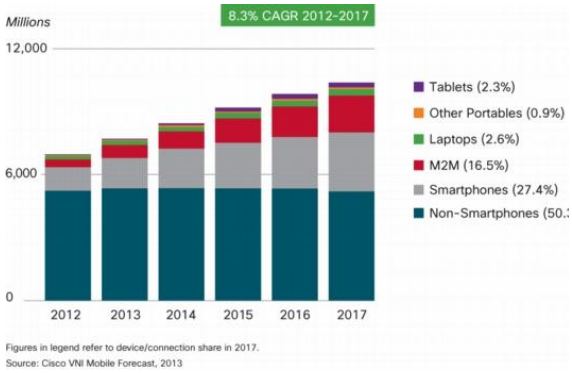

Fig.6 Global Mobile Devices[12]

Mobile network connection speeds will increase 7-fold by 2017. The average mobile network connection speed (526 kbps in 2012) will exceed 3.9 megabits per second (Mbps) in 2017.

By 2017, 41 percent of all global mobile devices and connections could potentially be capable of connecting to an IPv6 mobile network. Over 4.2 billion devices and connections will be IPv6-capable in 2017.

Two-thirds of the world's mobile data traffic will be video by 2017. Mobile video will increase 16-fold between 2012 and 2017, accounting for over 66 percent of total mobile data traffic by the end of the forecast period.

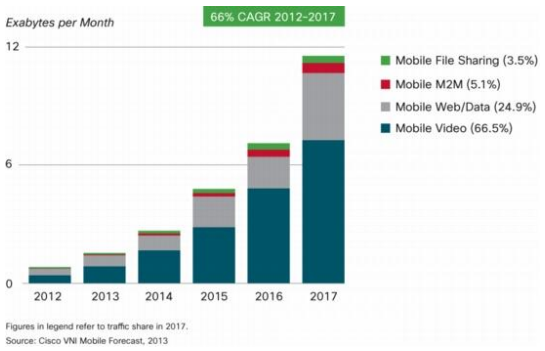

Fig.7 Mobile Data Traffic by 2017[13]

Mobile-connected tablets will generate more traffic in 2017 than the entire global mobile network in 2012. The amount of mobile data traffic generated by tablets in 2017 (1.3 exabytes per month) will be 1.5 times higher than the total amount of global mobile data traffic in 2012 (885 petabytes per month).

By 2017, almost 21 exabytes of mobile data traffic will be offloaded to the fixed network by means of Wi-Fi devices and femtocells each month. Without Wi-Fi and femtocell offload, total mobile data traffic would grow at a CAGR of 74 percent between 2012 and 2017 (16-fold growth), instead of the projected CAGR of 66 percent (13-fold growth).

Fig.8 Mobile Data Traffic to be offloaded to fixed network until 2017[13]

Mobile devices have memory and speed limitations that might prevent them from acting as media consumption devices, were it not for cloud applications and services. Cloud applications and services such as Netflix, YouTube, Pandora, and Spotify allow mobile users to overcome the memory capacity and processing power limitations of mobile devices. Globally, cloud applications will account for 84 percent of total mobile data traffic in 2017, compared to 74 percent at the end of 2012.

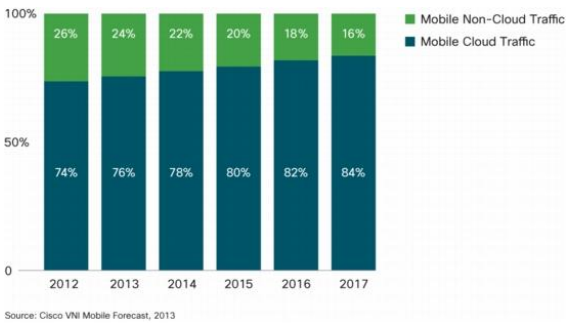

Fig.9 Mobile cloud traffic usage projection[14]

4. CONCLUSION

Mobile traffic will increase by a factor of 33 (worldwide) from 2010 to 2020, total worldwide traffic will grow from 3.86 EB to 127.8 EB. For a representative European country, total daily traffic will grow from 186 TB to 12,540 TB. This growth will come from the combination of a higher number of subscriptions and the importance of video traffic.

The traffic will be dominated by video, i.e. user related content. As a result, the traffic will continue to be unevenly distributed with a significant unbalance between busy and non busy hours, along with very large variations across the different parts of the globe. Traffic is likely to vary parallel to peaks in population density, coupled with the peak of leisure time. This in turn would see an expansion of the existing mobile infrastructure like Base Stations.

5. BIBLIOGRAPHY

[1] ITU (2009). "Measuring the Information Society; The ICT Development Index", [Online] Available: http://www.itu.int/ITU-D/ict/publications/idi/2009/material/IDI2009_w5.pdf

[2] Mishra, Ajay K. "Fundamentals of Cellular Network Planning and Optimization, 2G/2.5G/3G…Evolution of 4G", John Wiley and Sons, 2004.

[3] Chen, Yue (2003). "Soft Handover Issues in Radio Resource Management for 3G WCDMA Networks", Queen Mary, University of London, [Online] Available: www.elec.qmul.ac.uk/research/thesis/YueChen2003.pdf

[4] ITU-R PDNR WP8F. "Vision, Framework and Overall Objectives of the Future Development of IMT-2000 and Systems beyond IMT-2000", 2002.

[5] Toh, C. K. "Ad Hoc Mobile Wireless Networks: Protocols and Systems", Prentice Hall, New Jersey, USA, 2002.

[6] Pereira, Vasco & Sousa, Tiago. "Evolution of Mobile Communications: from 1G to 4G", Department of Informatics Engineering of the University of Coimbra, Portugal 2004.

[7] ITU (2010). "Measuring the Information Society, 2010". [Online] Available: http://www.itu.int/ITU-D/ict/statistics/material/graphs/2010/Global_ICT_Dev_00-10.jpg

[8] UMTS World (2009). "UMTS / 3G History and Future Milestones", [Online] Available: http://www.umtsworld.com/umts/history.htm

[9] Kamarularifin Abd Jalil, Mohd Hanafi Abd. Latif, Mohamad Noorman Masrek, "Looking Into The 4G Features", MASAUM Journal of Basic and Applied Sciences Vol.1, No. 2 September 2009

[10] 3gamericas (2010). "Transition to 4G: 3GPP Broadband Evolution to IMT-Advanced", Rysavy Research/3G Americas. [Online]Available:www.rysavy.com/PR/3GA_PR_2010_09.pdf

[11] Fumiyuki Adachi, "Wireless past and Future: Evolving Mobile Communication Systems". IEICE Trans. Findamental, Vol. E84-A, No.1, January 2001.

[12] ITU (2010). "ITU Paves the Way for Next-Generation 4G Mobile Broadband Technologies". [Online] Available: http://www.itu.int/net/pressoffice/press_releases/2010/40.aspx

[13]Giannini,Vito;Craninckx,Jan; Baschirotto, Andrea,"Baseband Analog Circuits for Software Defined Radio", Springer, USA, 2008. ISBN: 978-1-4020-6537-8

[14] Allot, Mobile trends, global mobile broadband traffic report, 2010

UMTS Forum, 3G offered traffic characteristics, Report No. 33, November 2003

Interference Alignment vs Blind Interference Alignment: diversity and multiplexing gain in a 4G Cellular Network

Luke Oduor Otieno, Philip Kibet Langat, Stephen Musyoki

luke.otieno@hotmail.com, *kibetlp@gmail.com*

Abstract: Incorporation of multi-input multi-output orthogonal frequency division multiplexing (MIMO-OFDM) and universal frequency reuse in fourth generation cellular network standards has brought with it increased interference. One of the promising methods for interference mitigation is Interference Alignment (IA). IA is being considered for inclusion as one of the driving technologies for the fourth generation wireless networks. It promises increased capacity in the presence of interference yet requires much by way of channel state information at the transmitter (CSIT). Blind interference alignment (BIA) promises improved capacity under some conditions with no requirement for CSIT. This work compares, through simulation, the diversity (in terms of bit error rate (BER)) and capacity (in terms of bits/sec/Hz) performance of IA and BIA in similar environments of a fourth generation cellular network. Multiple users at the cell edge are considered and scheduling incorporated. Simulations are done using MATLAB®. In conclusion, this work presents the trade-offs between linear-IA precoding and staggered antenna based BIA in a fourth generation cellular network in a potential deployment for link level simulation.

Keywords: interference alignment, blind interference alignment, channel state information at the transmitter

Beamforming with Side-Lobe Level Control in an Antenna Array System

Robert Macharia Maina[1], Kibet Langat[1], P. K. Kihato[2]

[1]Jomo Kenyatta University of Agriculture and Technology, Department of Telecommunication Engineering

[2]Jomo Kenyatta University of Agriculture and Technology, Department of Electrical Engineering

robertisaacm@gmail.com, kibetlp@jkuat.ac.ke, kamitazv@yahoo.co.uk

ABSTRACT- The shape of the radiation beam in an antenna array depends upon the phase and amplitude difference between array elements. Therefore it is possible to continuously steer the main beam and/or nulls in any direction by adjusting the progressive phase and amplitude difference between the elements. Unwanted side lobes usually arise in the resultant radiation pattern. In this paper, an approach to minimize side lobe levels is brought forward. The approach is implemented using Particle Swarm Optimization (PSO) algorithm. The weights of the beam/ null steering beamformer are synthesized to directly produce minimum side lobe level. The resultant beam shape and the side lobes' magnitude are used as measures of success. A comparative beamforming analysis is done between a system without side lobe level control and a system with side lobe level control. The PSO algorithm is found to be highly effective in generating array weights required in the array channels to produce optimal side lobe level performance.

Key words- Antenna Array, Main lobe, Side lobe, Null steering, Beam steering, PSO

1. INTRODUCTION

Radio antennas couple electromagnetic energy from space to another medium (for example: wire, coaxial cable, or waveguide) or vice versa. Antennas can be generally categorized into omnidirectional and directional antennas [1].

An omnidirectional antenna radiates electromagnetic energy equally in all directions. This approach scatters signal energy with only a small percentage of the entire energy sent out reaching desired users.

A directional antenna in general has preferential transmission and reception directions (radiation directions are coupled with different gain values) [1] - [2].

Such antennas are usually built using a number of antenna elements arranged in a particular desired geometric pattern (e.g. linear, circular, and planar). Phase and amplitude differences between the element paths govern the resultant array radiation pattern. Directional antenna categories are fixed beam and steerable beam [3].

Beam steerable antennas have gained supremacy over fixed beam antennas, especially due to the ever increasing computer processing power.

Antenna arrays usually result in radiation in undesired directions (side lobes). It is thus of paramount importance to minimize side lobe levels.

The application of numerical optimization techniques in beamforming is an ongoing area of research stimulated by the ever increasing computer processing power. Among the favorite optimization techniques is the Particle Swarm Optimization (PSO) algorithm. PSO technique has been proven highly effective in a wide range of multidimensional problems compared to other techniques. PSO is based on the search behavior of a swarm of particles in a multidimensional search space.

Studies on wireless communication networks utilizing beam steerable antennas can be found in [4] - [5].

2. ANTENNA ARRAYS

In a transmitting antenna array, each antenna element radiates radio waves at a particular

phase and amplitude. The radio waves build upon each other or cancel each other when they cross paths. The manner in which the waves interfere with each other depends on the phase of each contributing wave (whether the wave is at its crest, its trough or somewhere in between).

A map of interference (destructive/ constructive) between the radio waves is referred to as a radiation pattern. It is the radiation pattern that portrays the relative radiation strengths in all directions [1].

The main beam is formed at the line where the greatest number of waves projected by the antenna array elements constructively overlap to form a composite waveform. An illustration of beamformed radiation is shown in Fig. 1 below.

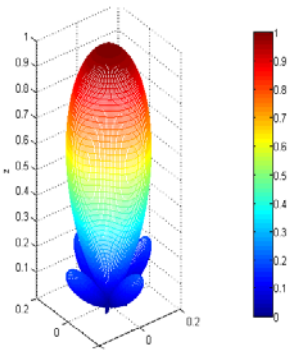

Fig. 1 An illustration of beamformed radiation

3. LINEAR ANTENNA ARRAY

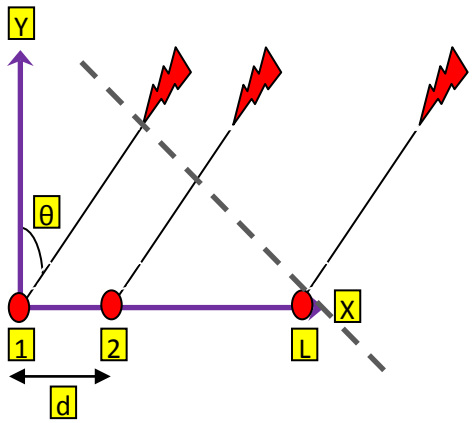

Fig. 2 Linear Antenna Array

Fig.2 above depicts an L element linear array with uniform element spacing distance. A planar wave front impinges on the elements. The wave front arrives at element L way before it arrives at element 1 (the extra distance being $((L-1)*d*\sin(\theta))$. The resultant array factor is given by:

$$AF(\theta) = \sum_{n=1}^{L} w_n \, e^{j(n-1)(kd\sin(\theta)+\delta)} \qquad (1)$$

Where: AF: Array Factor, k: wave number, d: element separation distance, θ: wave front angle of arrival, δ: phase difference between adjacent elements, w: element amplitude.

The total radiation pattern is the product of individual element radiation pattern and the array factor. [3].

4. SIDE LOBES

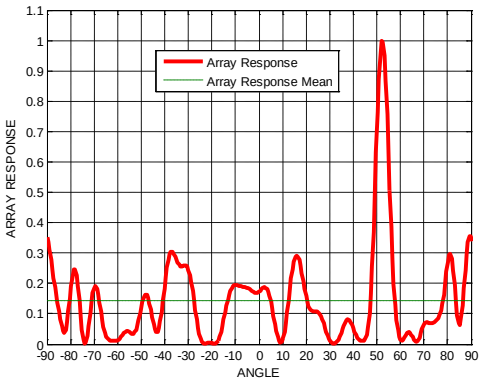

Fig. 3 Array response plot with high SL

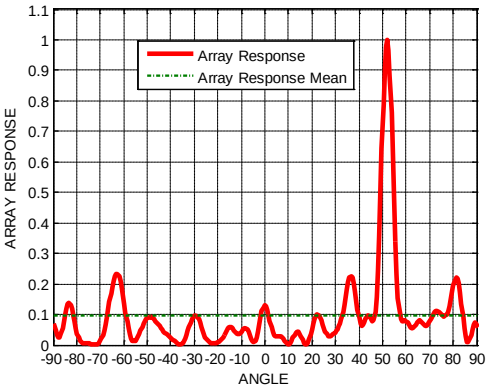

Fig. 4 Array response plot with low SL

Fig. 3 and Fig. 4 above portray beamformed radiation with high side lobe levels and low side lobe levels respectively.

5. BEAM/ NULL STEERING

An antenna array beamformer automatically adapts its response to different scenarios. A criterion has to be defined to allow adaption to take place. In this paper, the criterion of choice is the beam/ null steering approach. Fig. 5 below is an illustration of a beam/ null steering based adaptive beamformer.

The weights of the null steering beamformer are chosen to synthesize a beam with unit gain in the direction of the desired signal and nulls in the direction(s) of interferer(s) [6].

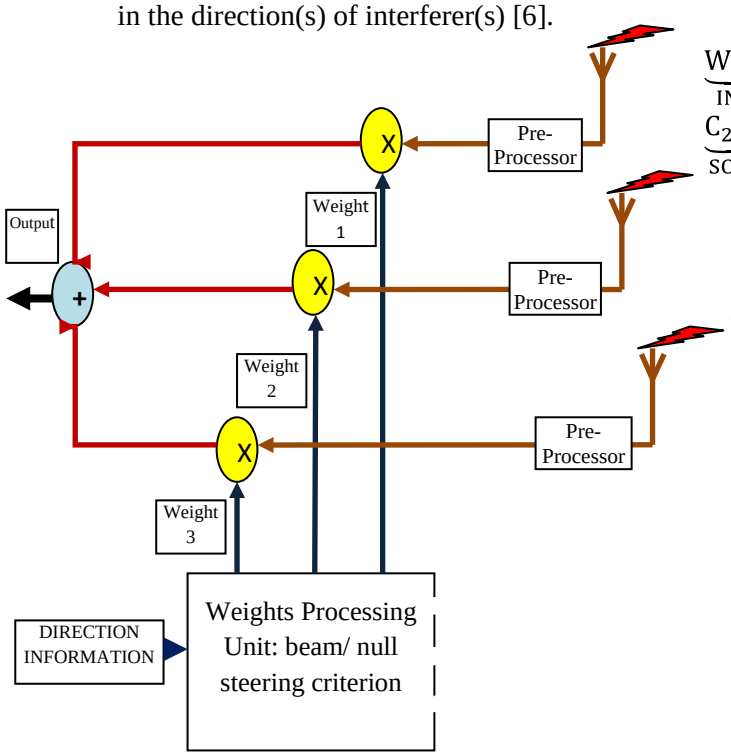

Fig. 5 Beam/ Null Steering based Adaptive Beamformer

6. PARTICLE SWARM OPTIMIZATION ALGORITHM

PSO is an optimization technique based on the search behavior of a swarm of particles in a multidimensional search space [7]. It is an iterative algorithm in which the velocities and positions of the swarm particles are updated per iteration in a controlled manner. For each particle i, the respective velocity vector V is updated according to (2) where inertia weight W controls the influence of the previous velocity vector. Parameter C_1 controls the influence of the personal best position achieved so far (the position at which the particle has resulted in the smallest objective function value so far (assuming that the objective function has to be minimized)). Parameter C_2 determines the influence of the best position that has been found so far by any of the particles in the neighborhood of particle i. Random values R_1 and R_2 are usually drawn with uniform probability from the number set [0, 1].

$$V_i(t+1) = W * V_i(t) + C_1 * R_1.(Y_i - X_i) + C_2 * R_2.(\tilde{Y}_i - X_i) \quad (2)$$

$$X_i(t+1) = X_i(t) + V_i(t+1) \quad (3)$$

$$V_i(t+1) = \underbrace{W * V_i(t)}_{\text{INERTIA}} + \underbrace{C_1 * R_1.(Y_i - X_i)}_{\text{PERSONAL INFLUENCE}} + \underbrace{C_2 * R_2.(\tilde{Y}_i - X_i)}_{\text{SOCIAL INFLUENCE}} \quad (4)$$

V_i : velocity vector
X_i : position vector
Y_i : "personal best" position vector
$\hat{Y}_i$: "neighborhood" best position vector

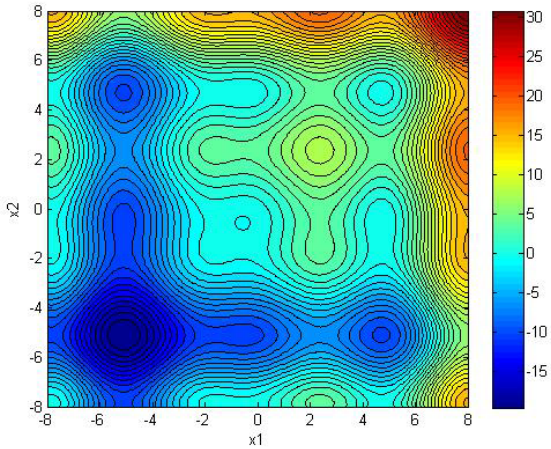

Fig. 6 Typical search region

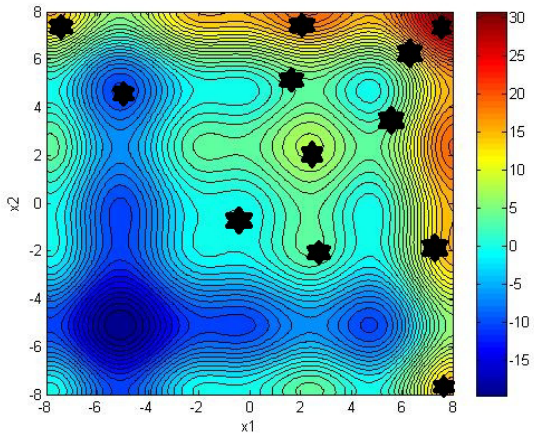

Fig.7 Random particle distribution

Fig. 6 – Fig. 8 are contour plots illustrating the PSO concept. Fig. 6 depicts a function with a minimum value at point (-5,-5). Fig. 7 depicts an initial random distribution of PSO particles. Fig. 8 depicts the positions of the particles after a number of algorithm iterations (this is at the region with the minimum function value).

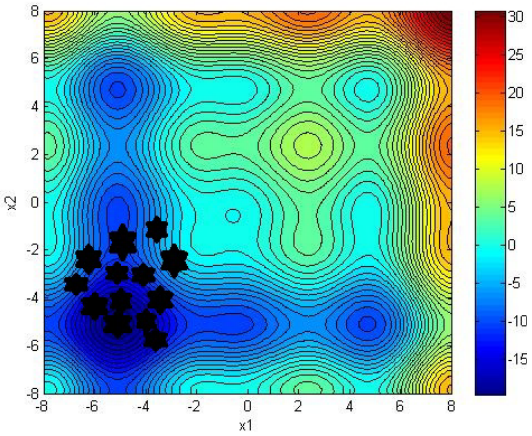

Fig. 8 Final solution

7. METHODOLOGY

7.1 Without sidelobe level control

The general idea is to ensure maximum array factor magnitude in desired directions and minimal array factor magnitude in undesired directions. As such, the problem is formulated as a maximization problem of the relationship defined in Equation 5 below.

Objective function = AF (desired directions) - AF (undesired directions) (5)

AF denotes Array Factor.

In this format, this objective function is easily maximized using the PSO algorithm. The weight in each and every array path is taken as the function variable.

7.2 With sidelobe level control

The objective function is modified to include a third component, the average sidelobe level in a viable set of directions (less the direction bearing the main beam).

The techniques defined in both 7.1 and 7.2 are processed for equivalent periods of time in the same processing machine. Matlab is used in all simulations.

8. RESULTS

Results obtained from a set of four directional sources defined in Table 1 below are presented below.

Table 1: Direction information

	Desired signal	Interferer 1	Interferer 2	Interferer 3
Set 1	-76	23	45	-10
Set 2	-53	45	-70	20
Set 3	-23	-87	7	35
Set 4	-12	-23	-75	45

8.1 Direction set one

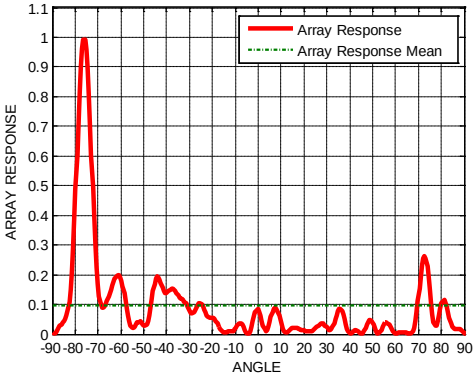

Fig. 9 Array response plot with SL control

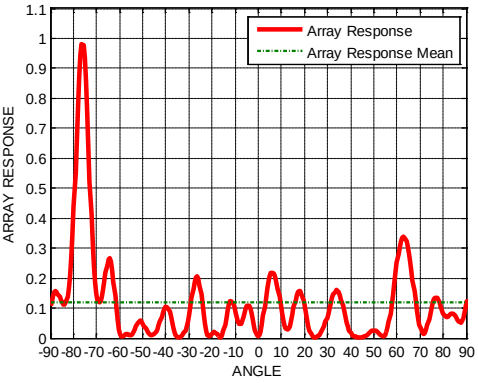

Fig. 10 Array response plot without SL control

Table 2: Set 1 results

ARRAY RESPONSE MAGNITUDE IN DECIBELS		
DIRECTION	*WITH SL CONTROL*	*WITHOUT SL CONTROL*
DESIRED	-0.034813232	-0.1324
INTERFERER 1	-40.44552789	-40.358
INTERFERER 2	-62.15654908	-49.9606
INTERFERER 3	-34.37933266	-20.7992
TOTAL I. L.	-136.9814096	-111.1178
OTHER STATISTICAL PARAMETERS IN DECIBELS		
PARAMETER	*WITH SL CONTROL*	*WITHOUT SL CONTROL*
ARRAY RESPONSE MAX.	-0.054894204	-0.159
ARRAY RESPONSE MIN.	-65.87793958	-63.0599
ARRAY RESPONSE MEAN	-20.33649856	-18.5816
ARRAY RESPONSE MEDIAN	-27.70205568	-22.5185
ALGORITHM ITERATIONS	365	2109

8.2 Direction set two

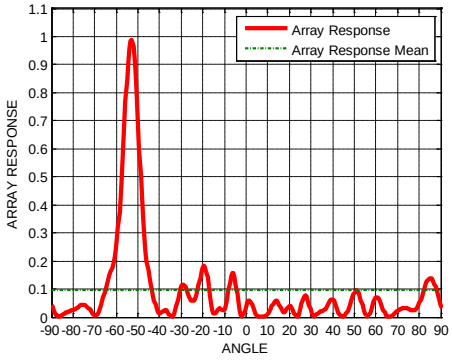

Fig. 11 Array response plot with SL control

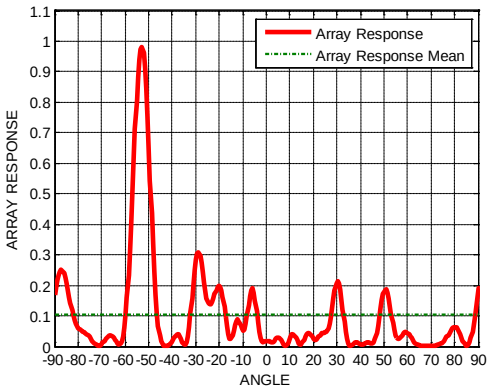

Fig. 12 Array response plot without SL control

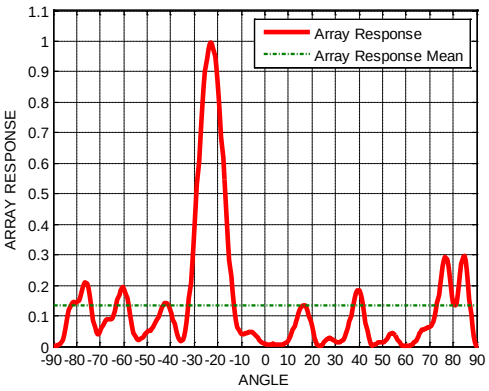

Fig. 14 Array response plot without SL control

Table 3: Set 2 results

ARRAY RESPONSE MAGNITUDE IN DECIBELS		
DIRECTION	*WITH SL CONTROL*	*WITHOUT SL CONTROL*
DESIRED	-0.0963	-0.1509
INTERFERER 1	-54.3549	-40.916
INTERFERER 2	-42.7562	-43.1461
INTERFERER 3	-28.0849	-31.7252
TOTAL I. L.	-125.196	-115.7873
OTHER STATISTICAL PARAMETERS IN DECIBELS		
PARAMETER	*WITH SL CONTROL*	*WITHOUT SL CONTROL*
ARRAY RESPONSE MAX.	-0.1008	-0.15
ARRAY RESPONSE MIN.	-79.8917	-64.7312
ARRAY RESPONSE MEAN	-20.4778	-19.7463
ARRAY RESPONSE MEDIAN	-28.4041	-28.1112
ALGORITHM ITERATIONS	365	2104

Table 4: Set 3 results

ARRAY RESPONSE MAGNITUDE IN DECIBELS		
DIRECTION	*WITH SL CONTROL*	*WITHOUT SL CONTROL*
DESIRED	-0.018	-0.0319
INTERFERER 1	-45.1853	-43.152
INTERFERER 2	-80.8667	-46.7151
INTERFERER 3	-41.3279	-25.5329
TOTAL I. L.	-167.3799	-115.4
OTHER STATISTICAL PARAMETERS IN DECIBELS		
PARAMETER	*WITH SL CONTROL*	*WITHOUT SL CONTROL*
ARRAY RESPONSE MAX.	-0.018	-0.0321
ARRAY RESPONSE MIN.	-81.5431	-106.0943
ARRAY RESPONSE MEAN	-20.0333	-17.3791
ARRAY RESPONSE MEDIAN	-24.3345	-23.9646
ALGORITHM ITERATIONS	350	2105

8.3 Direction set three

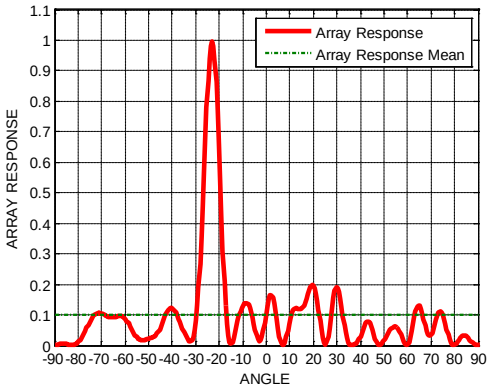

Fig. 13 Array response plot with SL control

8.4 Direction set four

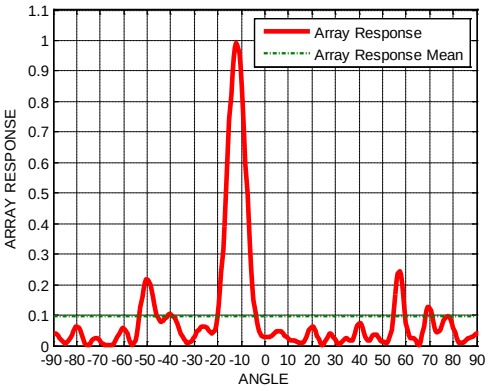

Fig. 15 Array response plot with SL control

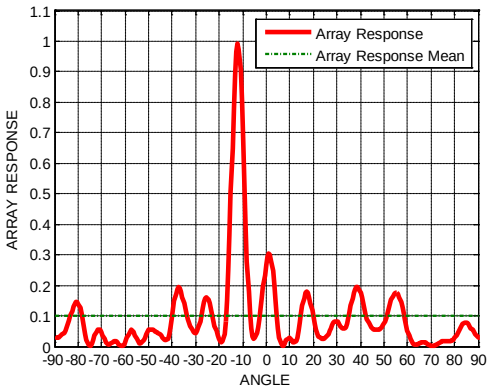

Fig. 16 Array response plot without SL control

Table 5: Set 4 results

ARRAY RESPONSE MAGNITUDE IN DECIBELS		
DIRECTION	*WITH SL CONTROL*	*WITHOUT SL CONTROL*
DESIRED	-0.0635	-0.0573
INTERFERER 1	-27.5583	-19.6399
INTERFERER 2	-58.5511	-61.1033
INTERFERER 3	-33.1084	-24.4901
TOTAL I. L.	-119.2178	-105.2333
OTHER STATISTICAL PARAMETERS IN DECIBELS		
PARAMETER	*WITH SL CONTROL*	*WITHOUT SL CONTROL*
ARRAY RESPONSE MAX.	-0.0669	-0.0545
ARRAY RESPONSE MIN.	-73.8546	-86.188
ARRAY RESPONSE MEAN	-20.4414	-20.0308
ARRAY RESPONSE MEDIAN	-28.1561	-25.0926
ALGORITHM ITERATIONS	362	2091

9. DISCUSSION

Array response max depicts the highest array response level achieved. Array response min depicts the lowest array response level achieved. Array response mean depicts the average array response achieved. The response mean alongside the response median give an indication of overall sidelobe contributions (the lower, the better). The array response plots give a visual illustration of response strength spread across all possible directions. Maximal radiation is directed towards the desired direction and minimal radiation towards the undesired directions as depicted by Figures 9- 16. Better performance is observed when using sidelobe level control mechanisms (lower array response mean values and lower interferer direction array response values) as depicted in Tables 2-5.

10. CONCLUSION

Quantitatively and qualitatively, the sidelobe level control mechanism is found to generate better results in all simulated radiation/ reception directions. It is advisable that all beamforming approaches incorporate sidelobe level control. Further research needs to be done pertaining to the use of sidelobe level control mechanisms in circular and rectangular arrays.

11. BIBLIOGRAPHY

[1] Constantine A. Balanis, *Antenna Theory, Analysis and Design*, 3rd ed. Hoboken, New Jersey: John Wiley & Sons, Inc., 2005.

[2] Ahmed El Zooghby, *Smart Antenna Engineering*, 1st ed. Norwood, United States of America: Artech House, 2005.

[3] Constantine A. Balanis, "Smart Antennas," in *Antenna Theory Analysis and Design*, 3rd ed. New Jersey, United States of America: John Wiley & Sons, Inc., Hoboken, New Jersey, 2005, ch. 16, pp. 945 - 999.

[4] S. Anderson, "An adaptive array for mobile communication systems," *IEEE Trans. Vehicular Technol.*, vol. 40, pp. 230–236, 1991.

[5] Inc. Network World. (2010) Networkworld. [Online]. http://networkworld.com/news/2010/101910-smart-antennas-wifi-performance.html

[6] Lal Chand Godara, *Smart Antennas*, 1st ed. Florida, United States of America, 2004.

[7] Thomas Weise, *Global Optimization Algorithms: Theory and Applications.*, 2009.

Micro-stereolithography process for fabrication of mask onto a 3D freeform workpiece

[1] J. B. Byiringiro, [2] D.W. Juma, [1,3]J.N. Keraita

[1] Department of Mechatronic Engineering, Dedan Kimathi University of Technology
[2] Department of Electrical & Electronic Engineering, Dedan Kimathi University of Technology

E-mail: [1]jean.bosco@dkut.ac.ke, [2]juma.wabwire@dkut.ac.ke, [3]james.keraita@dkut.ac.ke

Abstract — This paper presents the fabrication of a photoresist mask onto the surface of a 3D freeform workpiece. Though sensitivity variation of the SU-8 photoresist is not well known, previous researchers focused on 2D-fabrication.Two-dimensional fabrication techniques are difficult to directly adapt to 3D curved surfaces, so the fabrication of SU-8 masks onto 3D freeform workpieces has been an ill-defined problem. Moreover, there is not much known about the variation of the main mask properties (hardness and surface roughness) and the ranks of the controlling parameters. Additionally, both spinning and soft-baking are not feasible for 3D curved workpieces. In this work, the most influential input variables on the mask hardness and surface roughness were ranked by the Taguchi approach. The maximum mask hardness attained was 9.9 HV with a corresponding surface roughness of 1.36 μm.

Keywords — 3D freeform workpiece, micro-stereolithography, SU-8 photoresist mask

1. INTRODUCTION

Modeling and fabrication of the photoresist mask structure are key processes in highly accurate micro-blasting [1, 2]. There are a number of commercially available photoresists suitable for high aspect ratio (HAR) applications. SU-8, an epoxy-based negative photoresist, has become the favorite photoresist for HAR and 3-D lithographic patterning due to its excellent coating, planarization, and processing properties as well as its mechanical and chemical stability. However, as feature sizes get smaller and pattern complexity increases, a number of material-related issues need to be carefully considered [3 - 6]. For instance, after Lee et al [7] compared the SU-8 mask and the Watershed 11110 mask for use in the micro-abrasive jet machining process; they concluded that the SU-8

photoresist (highly sensitive and viscous epoxy resin) can be used for accurate and precise fabrication of a photoresist mask onto a 2-D planar workpiece at reasonable cost. Nevertheless, high viscosity (45,000 – 80,000 cSt) of the SU-8 photoresist, as determined by the UV range, requires both spin coating and soft-backing processes to acquire uniform thickness for UV illumination [4 - 9]. But both spin coating and soft-baking are not feasible for 3D freeform workpieces.

A few decades ago, micro-stereolithography (SL) was developed as a prototyping method that cures photosensitive resin under ultraviolet (UV) light of the proper wavelength. SL can be used to fabricate 3-D solid parts. After the first micro-SL apparatus was developed, a number of micro-SL devices have been used. They operate with similar principles but vary in the prototyping materials, light sources, and curing processes used, thus resulting in many subfamilies of micro-SL methods [10 - 12]. For instance, Choi et al [10] introduced the micro-SL system using a UV lamp and optical fibers instead of UV laser beam because the UV lamps are cheaper compared to UV lasers. Although the developed micro-SL systems demonstrated high performance, previous studies only focused on 2D planar workpieces. Micro-mask fabrication processes are well suited and have been optimized for producing micro-features on planar (2-D) workpieces. However, the demand for micro-features on 3D freeform surfaces in micro-electromechanical systems (MEMs) and lab-on-a-chip devices (e.g., micro-lenses and other micro-optical components, and contoured micro-fluidic channels), requires alternative non-planar micro-manufacturing processes to be developed.

Kim et al [11] introduced a modeling algorithm that can generate a 3D CAD mask model from the cross-sectional images of an arbitrary shaped workpiece by computed tomography (CT) or magnetic resonance imaging (MRI) scanners. Although the concept of a mask modeling algorithm is promising, its applicability still needs to be tested and verified by experiments.

In this paper, a tunable micro-SL technique was introduced to fabricate SU-8 resist mask onto 3D freeform workpieces. The most influential input variables on the mask hardness and surface roughness were ranked by the Taguchi approach as it requires fewer numbers of tests.

2. CAD MODELING OF 3D FREEFORM WORKPIECE

In this research, CAD modeling was used to visualize the design of a 3D freeform mask model (Figure 1) and predict problems that could arise before the mask model was made into a physical form, as shown in Figure 2. For instance, the modeling algorithm recognizes white and black colors for masked and unmasked zones, respectively. The CAD modeling was also used to computerize the mask model to generate the NC code necessary in the micro-SL process and simulate the whole process before the designed mask model was physically produced. Figure 3 show a model of the 3D sliced mask and tool path and computation of the mask.

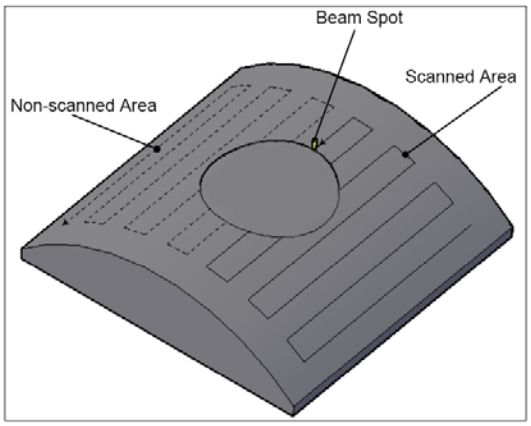

Figure 1: Design concept for fabrication of a micro-hole

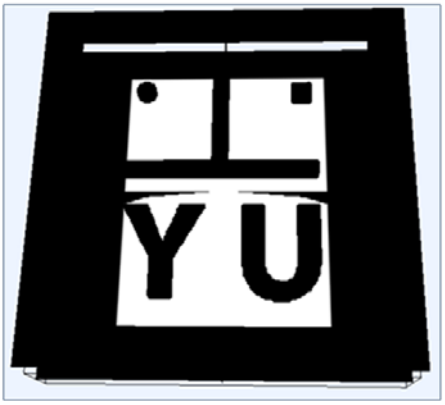

Figure 2: Masked (white) against unmasked (black) areas

As illustrated in the Figure 3 (a), the model of 3D freeform mask was designed by using layer by layer strategy. Figure 3 (b) demonstrates the hatching technique for computation of the 3D freeform mask model (masked and unmasked zones).

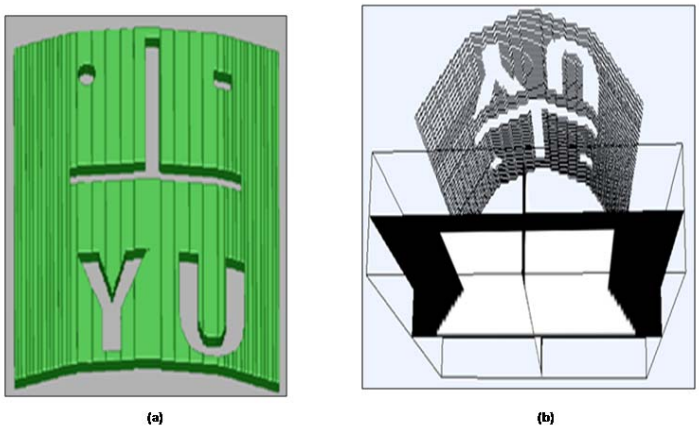

Figure 3: (a) Model of the 3D sliced mask; (b) Tool path and computation of the mask

In this work, the generated NC code was skillfully customized for compatibility with each machine controller. In the design, mathematical (rectangular/circular hole, channel, etc.) and non-mathematical (arrow, YU, CAY, etc.) shapes were scaled down to a minimum of 0.02 inches (around 500μm) and 10 points (Myriad professional), respectively. The details of the CAD modeling procedures and steps are provided in [11].

3. FABRICATION STEPS OF THE PHOTORESIST MASK

The sensitivity variation of the SU-8 photoresist is still an ill-defined problem, invoking the intuition of the experienced user. Therefore, before the UV exposure process, sensitivity related parameters such as UV spectrum, spot size, and UV power were investigated. Scientific procedures were used to rank the controlling parameters of the developed tunable micro-SL system. Figure 4 illustrates the experimental set-up for fabrication of the SU-8 resist mask onto 3D curved workpiece surface through developed micro-SL system.

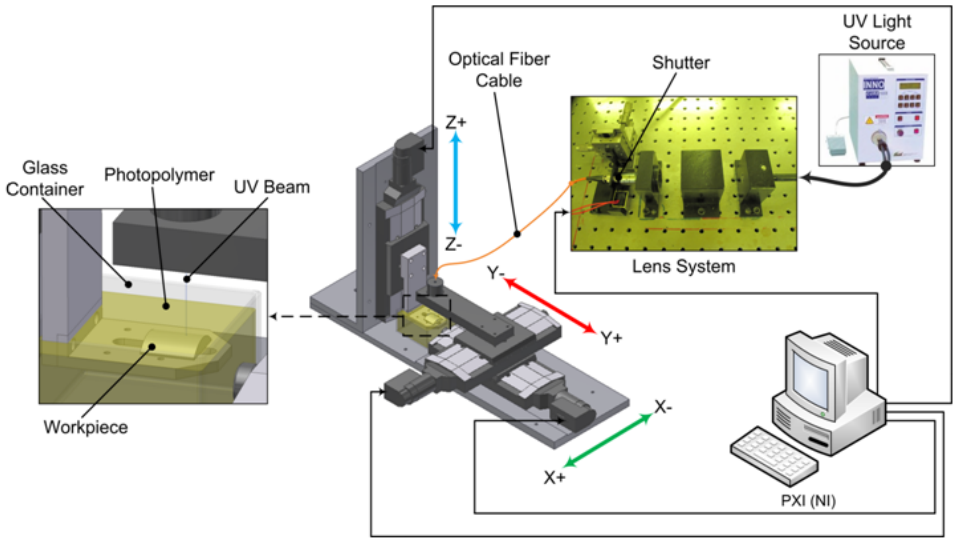

Figure 4: Experimental set-up for fabrication of the SU-8 resist mask onto 3D curved workpiece

3.1 Analysis of the UV spectrum

Previous studies suggested that UV lasers should not be used for SU-8 photoresist exposure, except for very thin layers [2-7]. However, because the tunable micro-SL used a UV lamp instead of a UV laser, it was imperative to ensure that the UV spectrum complied with the recommended sensitivity range. Therefore, the UV spectrum (wavelength) of the micro-SL system was measured by using a UV radiometer (Model: JP-9710) and the results are provided in Table 1 and plotted in Figure 7. Analysis of the wavelength results demonstrated that the tunable micro-SL supplied effective UV light in the wavelength range of 360nm ~ 600nm. Even though, the UV spectrum was not fixed to 365nm, it was still within the optimal condition range for fabrication of the SU-8 photoresist mask by using UV illumination because there is no radiation below 350nm [13-15].

3.2 Analysis of the spot size and UV light power

From the basic concept, for a converging lens of thickness (d), a focal length (f) is a positive distance at which the beam of collimated light is focused to a single point (Figure 5). To implement this convergence, the tunable micro-SL system used in this research was designed so that it would converge the UV light beam to scale it down for fabrication of the desired micro-shapes.

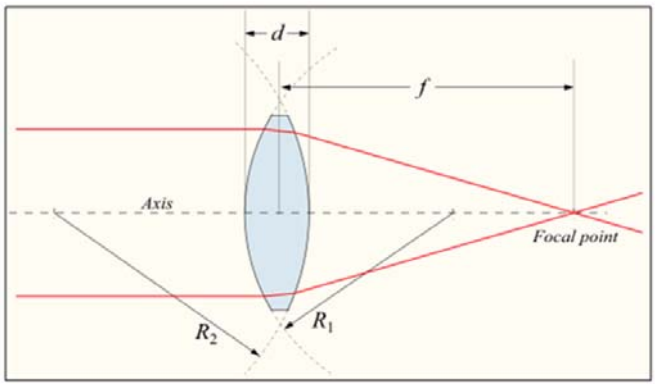

Figure 5: Schematic diagram UV system

For verification of the design concept, a laser beam profiler (LBP-1-USB: UV Laser Beam Profiler, 190-1100nm, USB 2.0 interface) was used to provide graphical representations and the parameter range of the tunable micro-SL system (spot size and focal length). Therefore, at a focal length of 18mm, the LBP series showed that the minimum spot sizes were 321.84 µm and 324.19 µm in the vertical and horizontal direction, respectively, and that the spot was of nearly circular shape (Figure 6).

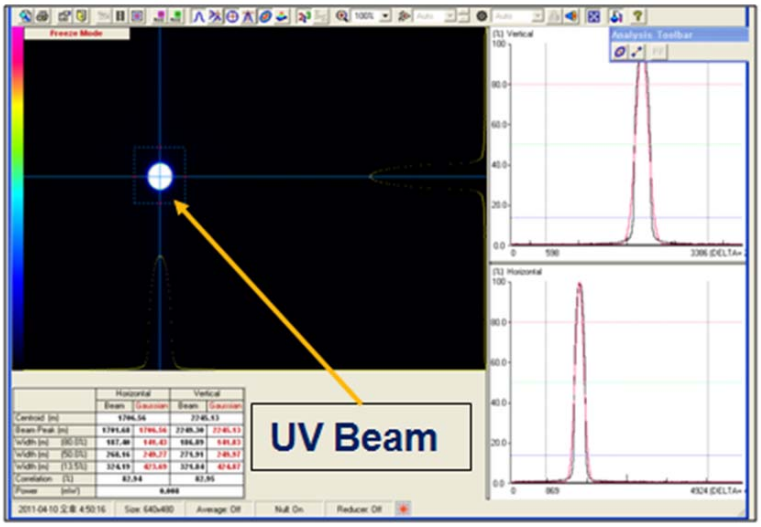

Figure 6: Measurement of UV spot size and power

Moreover, a laser power meter (FieldMaxll - Coherent) was used to measure the scanning UV power. The results demonstrated that the developed tunable micro-SL system delivered the maximum output UV power of 27.5µW. Analysis of the spot size verified the preliminary experimental results, proving that hatched spacing of 200µm made

lines that always overlapped during mask fabrication. More results on the variation of spot size are given in Table 1 and plotted in Figure 7.

TABLE I
SYSTEMATIC MEASUREMENT OF THE SPOT POINT

Focal distance (mm)	Beam width (13.5%)		Correlation (%)	
	Horizontal (µm)	Vertical (µm)	Horizontal	Vertical
10	777.86	780.67	88.05	89.73
15	494.16	506.13	84.36	86.09
17	357.6	362.68	82.54	82.34
18	324.19	321.84	82.94	89.95
19	332.75	328.78	84.66	84.36
20	394.00	394.22	86.85	86.63
22	502.90	505.49	87.48	87.77
27	795.69	801.20	93.07	93.06

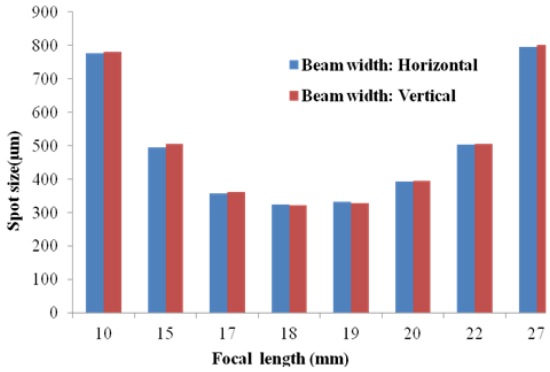

Figure 7: Plot of the UV beam profiles

3.3 Fabrication process

MicroChem Corp. [15], a renowned SU-8 manufacturer, recommends SU-8 2100 when a stable image of a micro-fabrication is desired. However, uniformly coating the SU-8 2100 photoresist onto a 3D freeform workpiece surface is extremely tricky because of its high viscosity (45,000cSt). In 2D fabrication, spinning and soft-baking technique is applied to allow the SU-8 photoresist to acquire a uniform thickness. In 3D freeform fabrication, both the spinning and the soft-baking are not feasible. In this research, the viscosity problem was adeptly handled by diluting the viscous SU-8 2100 with another chemical product known as cyclopentanone (C_5H_8O) at defined ratio (Table II). After dilution, the mixed solution was stabilized for 30 min in a yellow room. Finally, the 3D curved workpiece was cautiously immersed into the mixed solution for UV scanning. In the preliminary experiments, an unstable solution led to a fabrication of a useless punched-like photoresist mask.

UV scanning consisted of overflowing fabrication steps [11, 15], which affected the mask hardness as well as the surface roughness. Due to the lack of knowledge about the mask fabrication mechanism, its required steps as well as the effect of each step are still unknown. Based on our preliminary experimental work, some of the recommended fabrication steps were considered awkward and not viable. Eliminating these useless steps, we have derived the required steps and experimentally verified them, as shown in Figure 8.

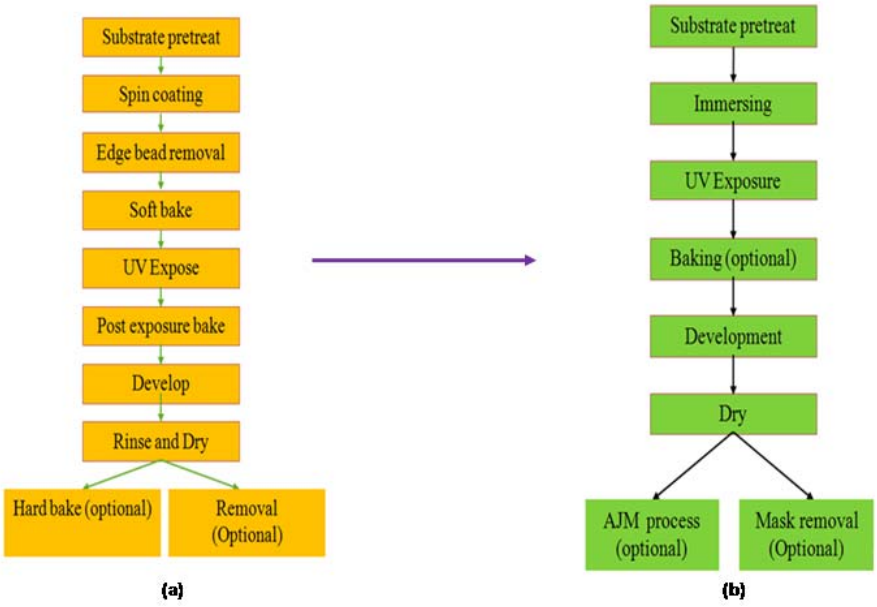

Figure 8: Fabrication process (a) 2D fabrication, (b) Proposed 3D fabrication

3.4 Experimental procedure

By using the Taguchi approach [17], an L16 orthogonal array (five input variables with four levels) was used in 16 tests as shown in Table II. This array was very efficient because instead of the 1024 (4^5) testing required for the factorial method, only a systematic set of 16 tests was carried out to rank the most significant parameters that influenced photoresist mask hardness and surface roughness (Ra).

4. EXPERIMENTAL RESULTS

As predicted in the experimental design set up, various designed photoresist mask models (mathematical and non-mathematical) were successfully fabricated onto 2D planar and 3D freeform workpiece. Figure 9 shows the mask properties of a 4x4 mm on 2D planar surface.

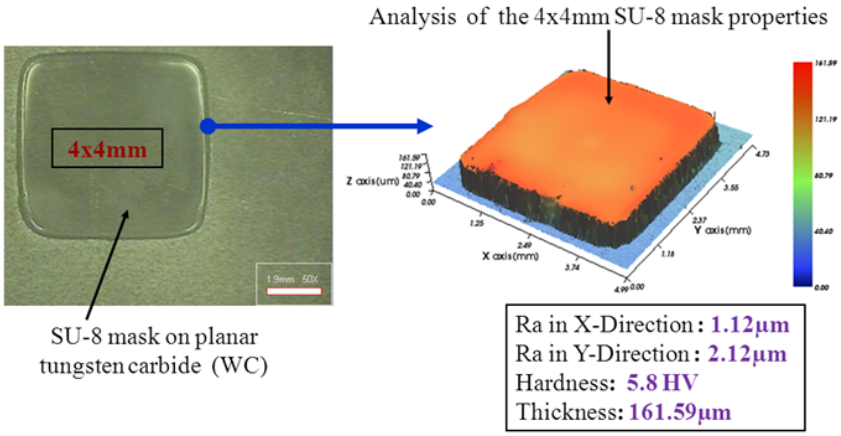

Figure 9: SU-8 mask properties (4x4mm on planar surface)

As shown also in the Figure 10 (a) and the Figure 10 (b), in the same fabrication conditions the photoresist masks have been successfully fabricated onto 3D curved glass (BK7) and tungsten carbide (WC). Moreover, various mathematical and non mathematical shapes have been successfully fabricated onto 3D curved tungsten carbide, as illustrated in the Figure 10 (c) and the Figure 10 (d).

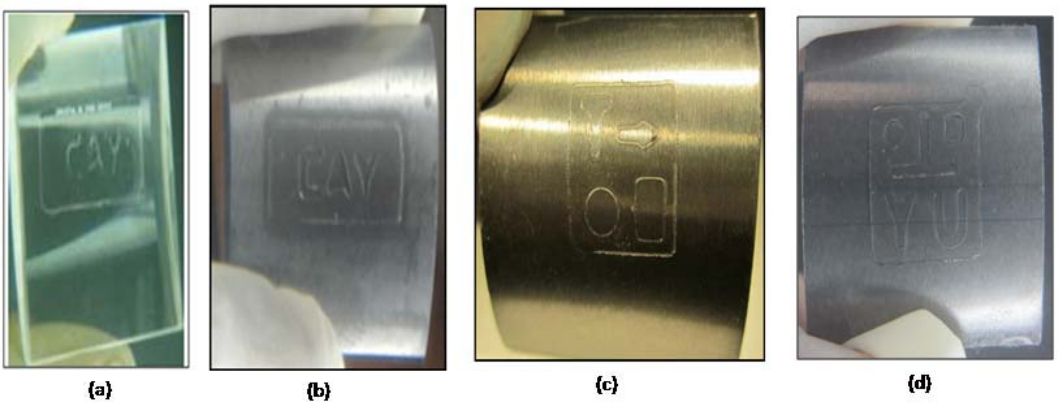

Figure 10: (a) Fabricated SU-8 resist mask onto 3D curved glass. (b, c, d) Fabricated SU-8 resist mask onto 3D curved tungsten carbide

In this work, it was observed that the photoresist mask fitted better onto the workpiece surface at the end point than at the starting point. This observation confirmed that a well stabilized mixed solution not only prevented a punched-like photoresist mask but also promoted a well-fitting mask onto a 3D curved workpiece surface.

4.1 Analysis of the SU-8 photoresist mask properties

The fabricated photoresist mask hardness was measured by using micro-Vickers (Figure 11), and more results on the optimal 3D freeform mask properties in terms of hardness are reported in table II [16]. Furthermore, it was also experimentally observed that when the photoresist mask was very rough (punched-like), the tiny highly pressurized abrasives were passing through the mask surface (just masked part) and striking the workpiece surface, making the mask useless.

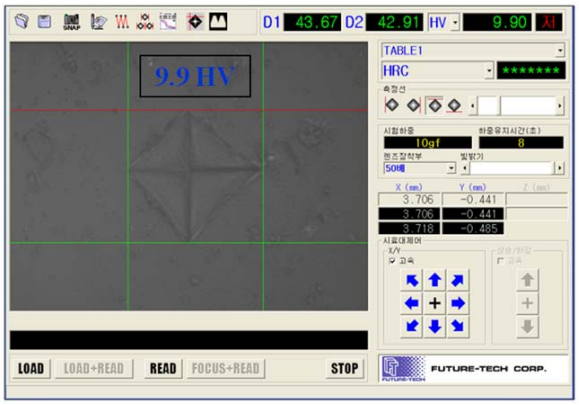

Figure 11: Result of the mask hardness

Since the photoresist mask surface was supposed to be very smooth, the non-contact method was used to measure the surface roughness (Figure12). Surface roughness measurements are reported in Table 2 as well.

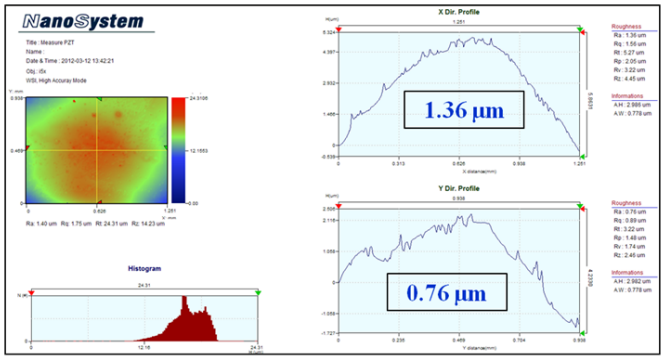

Figure 12: Result of the mask surface roughness

In addition to experimental observation, the Taguchi approach was used for further analysis of the mask hardness and surface roughness. For mask hardness, Figure 13 (a) shows main effects plot for signal to noise ratios while

Figure 13(b) shows the main effects for means. For mask surface roughness, Figure 14(a) shows main effects plot for signal to noise ratios while Figure 14(b) shows the main effects for means.

TABLE II
TAGUCHI ANALYSIS (L16) FOR MASK PROPEPERTIES

Dilute factor	UV Power (µW)	Scan speed (µm/s)	Area Factor	Hard baking at 100^0C (Min)	**Surface roughness: Ra_µm (X-Direction)**	**Surface roughness: Ra_µm (Y-Direction)**	**Mask hardness (HV)**
1	16	5	3.2	10	**1.40**	**0.27**	**4.95**
1	19	7	3.6	15	**1.57**	**1.01**	**5.80**
1	22	9	4	20	**1.66**	**2.17**	**0.92**
1	25	11	4.4	25	**0.297**	**0.55**	**1.12**
1.5	16	7	4	25	**0.95**	**0.498**	**5.84**
1.5	19	5	4.4	20	**1.98**	**0.25**	**1.44**
1.5	22	11	3.2	15	**1.36**	**0.78**	**9.90**
1.5	25	9	3.6	10	**3.72**	**0.90**	**5.45**
2	16	9	4.4	15	**0.92**	**1.05**	**5.23**
2	19	11	4	10	**0.82**	**1.38**	**1.47**
2	22	5	3.6	25	**0.461**	**0.57**	**2.52**
2	25	7	3.2	20	**2.28**	**1.23**	**5.34**
2.5	16	11	3.6	20	**0.86**	**0.82**	**4.77**
2.5	19	9	3.2	25	**2.85**	**1.87**	**1.69**
2.5	22	7	4.4	10	**2.09**	**2.67**	**1.52**
2.5	25	5	4	15	**1.25**	**0.174**	**0.96**

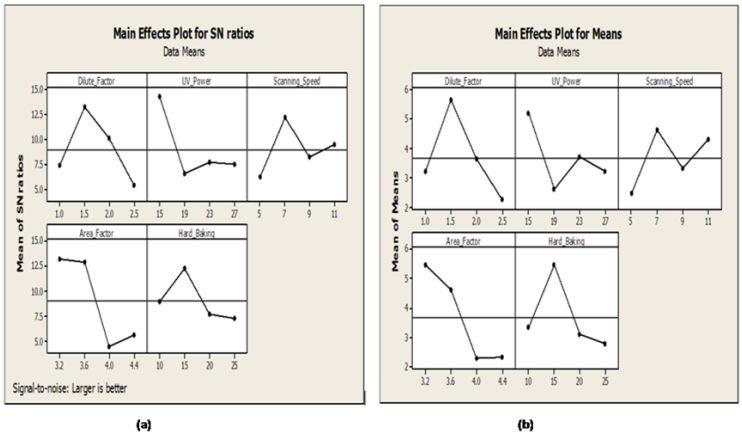

Figure 13: Taguchi analysis (Hardness of the fabricated mask)

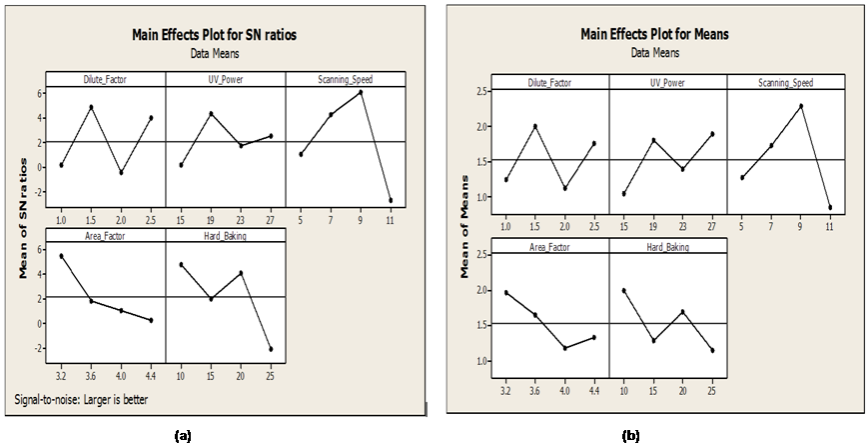

Figure14 Taguchi analysis (Surface roughness of the fabricated mask)

From the summarized results plotted in Figure 15 and Figure 16, the area factor and the dilute factor (Table 3 and Table 4) were ranked as the most influencing parameters of SU-8 photoresist mask hardness. And the scanning speed (Table 5 and Table 6) was ranked the most influencing of surface roughness.

TABLE III
MASK HARDNESS (SIGNAL TO NOISE RATIOS)

Level	Dilute factor	UV Power	Scanning speed	Area factor	Hard baking
1	7.355	14.290	6.183	13.228	8.901
2	13.284	6.585	12.196	12.899	12.299
3	10.074	7.713	8.233	4.399	7.641
4	5.353	7.477	9.453	5.540	7.225
Delta	7.931	7.705	6.013	8.829	5.075
Rank	**2**	3	4	**1**	5

TABLE IV
MASK HARDNESS (MEANS)

Level	Dilute factor	UV Power	Scanning speed	Area factor	Hard baking
1	3.197	5.197	2.468	5.470	3.348
2	5.657	2.600	4.625	4.635	5.473
3	3.640	3.715	3.322	2.297	3.117
4	2.235	3.218	4.315	2.328	2.793
Delta	3.422	2.597	2.157	3.173	2.680
Rank	**1**	4	5	**2**	3

TABLE V
SURFACE ROUGHNESS (S/N RATIOS)

Level	Dilute factor	UV Power	Scanning speed	Area factor	Hard baking
1	0.1745	0.1107	1.017	5.4622	4.7532
2	4.8924	4.3061	4.2585	1.8232	1.9507
3	-0.504	1.6875	6.0464	1.0420	4.046
4	4.032	2.4907	8.7734	5.1955	6.908
Delta	5.3962	4.1954	8.7734	5.1955	6.908
Rank	3	5	**1**	4	2

TABLE VI
SURFACE ROUGHNESS (MEANS)

Level	Dilute factor	UV Power	Scanning speed	Area factor	Hard baking
1	1.2317	1.0325	1.2728	1.9725	2.0075
2	2.0025	1.8050	1.7225	1.6528	1.2750
3	1.1203	1.3927	2.2875	1.1700	1.6950
4	1.7625	1.8868	0.8342	1.3218	1.1395
Delta	0.8822	0.8543	1.4533	0.8025	0.8680
Rank	2	4	**1**	5	3

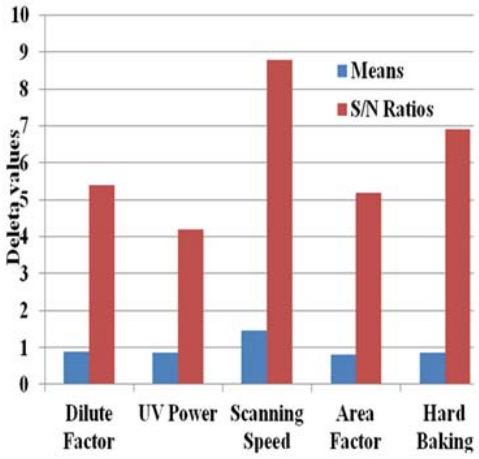

Figure 15 Mask roughness parameter's ranks

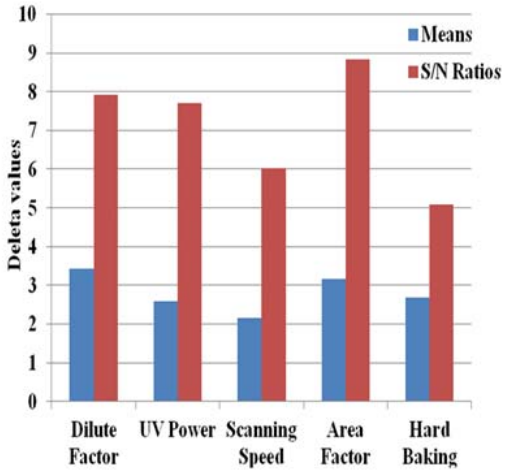

Figure 16 Mask hardness parameter's ranks

The heavily influencing parameter ranks for either mask hardness or surface roughness comply well with the design expectations. For instance, the area factor and dilute factor involved the most significant physical factors and chemical properties respectively in 3D fabrication. The area factor was the ratio of focal length and hatching space, whereas the dilute factor was the dilution ratio of cyclopentanone (C_5H_8O) and SU-8 photoresist. For surface roughness as well, scanning speed was a very important factor because as mentioned in the preliminary experimental observation, the mask surface was highly influenced by the stability of the mixed solution.

4.2 Validation of the mask hardness resuls

The Vickers hardness value (VHN) can be calculated from the applied load divided by areas of indentation, at which the latter is derived from the diagonals of the pyramid as expressed in the equation below

$$VHN = \frac{2P\sin(\theta/2)}{d^2} = \frac{1.854P}{d^2}$$

Where;

P is the applied load, kgf

D is the average length of the diagonals = $((d_1+d_2)/2)$, mm

θ is the angle between the opposite face of the diamond) =136^o

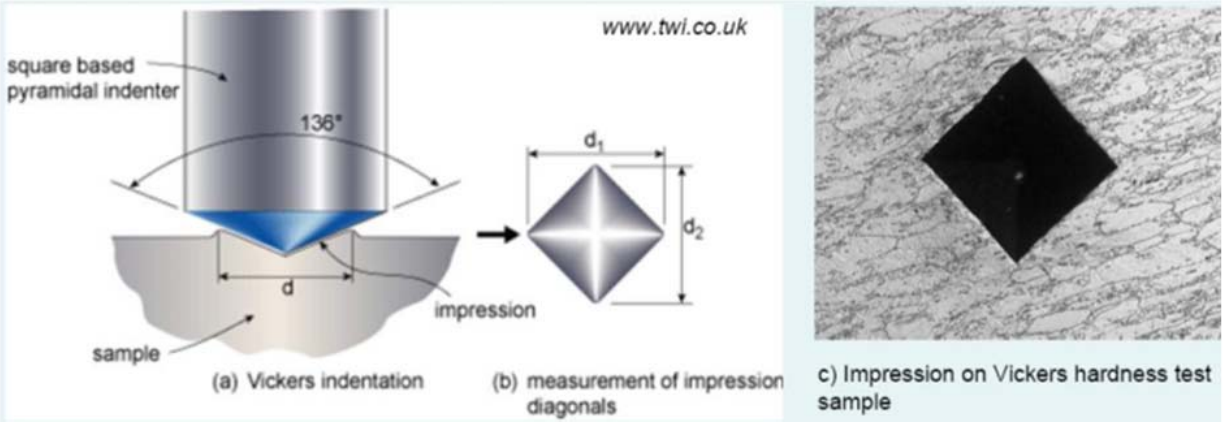

Figure 17: Measurement of hardness using micro-vickers [12, 16]

According to Vickers Hardness Test principle discussed above, we have confidence to confirm that our SU-8 photoresist mask results in the current paper are genuine as captured in Figure 11.

However, it is still very much challenging to find more accurate measuring strategies, the fabricated SU-8 photoresist mask onto 3D freeform workpiece has been found to be unique, flexible, and powerful. Under these settings, the attained mask hardness and surface roughness were 9.9 HV and 1.36 μm, respectively. To the authors' knowledge, there is no report found on 3D freeform resist mask experimentally fabricated.

5. **CONCLUSION**

In the previous work, an algorithm for rapidly modeling a mask for the micro-AJM process was introduced, but the algorithm was not tested and verified by mask fabrication experiments. This paper reported the successful verification of the developed modeling algorithm and fabrication of the SU-8 photoresist by using a tunable micro-SL system. Through Taguchi probability analysis, the area factor and the dilute factor were ranked as the most influencing input variables of mask hardness whereas the scanning speed was ranked as the most influencing of surface roughness.

ACKNOWLEDGEMENT

The authors acknowledge the support of Dedan Kimathi University of Technology, Kenya and Yeungnam University, South Korea.

REFERENCES

1. Lee S.P., Kang H.W., Lee S.J., Lee I.H, Ko T.J., and Cho D.W., "Development of rapid mask fabrication technology for micro-abrasive jet machining," J. of Mech. Sc. and Tech., Vol. 22, No.11, 2190-2196, 2008.
2. Saragih, A.S. and Ko, T.J, "A thick SU-8 mask for micro-abrasive jet machining on glass," Int. J. Adv. Manuf. and Techn. Vol.41, No.7-8, pp.734-740, 2009
3. Choi, J.S., Kang, H.W., Lee, I.H., Ko, T.J. and Cho, D.W., "Development of micro-SL technology using a UV lamp and optical fiber," Int. J. of Adv. Manuf. Techn., Vol. 41, No.3-4, pp.281-286, 2009.
4. Gelome, J.D., Cox, R.J. and Gutierrez, S.A.R. "Photoresist composition and printed circuit boards and packages made therewith," U.S Patent: 4882245, 1989
5. Lorenz, H., Despont, M., Fahrni, N., LaBianca, N., Renaudy, P., and Vettiger, P., "SU-8: A low-cost negative resist for MEMS," J.of Micromech. and Microeng., Vol.7, No.3, pp.121-124,1997.
6. Chan-Park, M.B., Zhang J., Yan Y. and Yue C.Y., "Fabrication of large SU-8 mold with high aspect ratio micro-channels by UV exposure dose reduction," Sens. and Act., Vol.101, No.1-2, pp.175-182, 2004.
7. Lee, I.H. and Cho, D.W., "An investigation on photopolymer solidification considering laser irradiation energy in micro-stereolithography", Microsystem Technol. Vol.10,pp. 592–598, 2004
8. Sun, C., Fang, N., Wu, D.M., and Zhang, X., "Projection microstereolithography using digital micro-mirror dynamic mask," Sens. and Act., Vol.121,pp.113-120, 2005
9. Choi, J.W., Wicker, R.B., Cho, S.H., Ha, C.S. and Lee, S.H., "Cure depth control for complex 3D micro-structure fabrication in dynamic mask project micro-SL," Rap. Prot. J., Vol.15, No.1, pp.59-70, 2009.
10. Choi, J.S., Kang, H.W., Lee, I.H., Ko, T. J., and Cho, D.W., "Development of micro-stereolithography technology using a UV lamp and optical fiber", Int. J. Adv. Manuf. Technol. Vol.41, pp. 281–286, 2009
11. Kim, H.C., Lee, I. H., T. J. Ko, "Direct 3D mask modeling for freeform workpieces in microabrasive jet machining", Int. J. Adv. Manuf. Technol., Vol. 58, No.1-4, pp.175-186, 2012
12. Byiringiro, J.B., Ko, T.J., Kim, H.C. and Lee, I.H., "Fabrication of the photo-resist mask onto 3D non-planar wafer for micro-abrasive jet machining," Proc. of the Mech. Eng. Conf. on Sust. Res. and Inn., ISSN 2079-6226, Vol. 4, pp. 155-16, 2012

13. Yang, R. and Wang, W. , "Out-of-plane polymer refractive microlens fabricated based on direct lithography of SU-8," Sensors and Actuators , Vol.113, pp.71–77, 2004
14. Stumbo, D. and Wolfe, J., "Ion exposure characterization of a chemically amplified epoxy resist," J. Vac. Scien. Technol. Vol.11, pp. 2432-2435, 1993
15. Micro-Chem, "SU-8 2000 permanent epoxy negative photoresist: processing guidelines for SU-2100 and SU-8 2150", http://www.microchem.com
16. Low, I.M. and Shi, C., "Vickers indentation responses of epoxy polymers," J. of Mat. Sc. L., Vol.17, No.14, pp.1181-1183, 1998
17. Unal, R. and Dean, E. B., "Taguchi approach to design optimization for quality and cost: an overview", Annual Conference of the International Society of Parametric Analysts ,1991

Effect of Syngas Composition on No_x Formation in Counterflow Syngas/Air Triple Flames

Stephen K. Musau, P. N. Kioni, A.Gitahi

kimayu07@gmail.com, ndirangukioni@yahoo.com, gitahi@eng.jkuat.ac.ke

Abstract

This paper presents numerical simulation of the effects of syngas composition on NO_x formation in counterflow syngas/air triple flames at atmospheric pressure. A detailed chemical kinetics mechanism, thermal and transport properties were used. The results indicate that hydrogen rich syngas triple flame produces more NO and NO2 than the hydrogen lean syngas flame. This is due to the appearance of the diffusion flame branch in the triple flame in which NO generation is through thermal route. Hydrogen has higher diffusivity and reactivity that cause higher flame temperatures resulting to more NO formation through thermal route. The heat transfer and radical diffusion between the diffusion flame branch and the premixed flame branches, the NO and NO_2 formation increases for both hydrogen rich and hydrogen lean syngas flames. NO_x formation in the premixed branches is by prompt route due to high concentration of CH radicals on those regions.

Keywords: Triple flame; premixed flame; NO_x; Hydrogen rich syngas; Hydrogen lean syngas

Sensitivity Analysis of Methane, Methanol and Methyl Formate Freely Propagating Flames

J. K. Tanui[1], P. N. Kioni[1], A. Gitahi[2]

[1]Mechanical Engineering Department, Dedan Kimathi University of Technology
[2]Mechanical Engineering Department, Jomo Kenyatta University of Agriculture & Technology

Email: josetanui@gmail.com, ndirangukioni@yahoo.com, gitahi@eng.jkuat.ac.ke

ABSTRACT

The local sensitivities of mole fraction of CH and NO in methane (CH_4)/air, methanol (CH_3OH)/air and methyl formate (CH_3OCHO)/air freely propagating flames have been done with an aim of establishing the important reactions in NO formation in these fuels. In this work, CH_3OCHO have been modeled using Dooley (2011) mechanism combined with Leeds NO_x mechanism while CH_4 and CH_3OH have been modeled using GRI mechanism. The numerical simulations have been performed at low pressure of 1 bar and the fuel air mixture is stoichiometric. It has been established that the most dominant radicals responsible for the CH production in a pure hydrocarbon (CH_4) are OH and CH_3 while in oxygenated fuel (CH_3OH and CH_3OCHO) are OH, H and HCO. The most influential reaction with high positive sensitivity in NO production zone in CH_4 is CH + N_2 = HCN + N. However, in oxygenated fuels, the dominant reaction in NO production zone is NNH + O = NH + NO.

Keywords: Sensitivity analysis; NO; CH; methyl formate; methane; methanol

1. INTRODUCTION

Over the last decade, utilization of biodiesel fuels in engines has been intensified. Biodiesel fuel burns efficiently in an engine and has reduced unburned hydrocarbon, carbon monoxide, and particulate matter. However, it has an increase nitrogen oxides (NO_x) emission as compared to fossil fuels.

To understand this phenomenon, several research works have been done [1,2]. Schonborn *et al.* [1] observed that molecular structure of the fuel significantly influence the formation of NO_x. Molecular structure affects the ignition delay of the fuel and the flame temperature attained. Fatty acid monohydric alcohol esters with shorter fatty acid chain lengths produced lesser amount of NO_x in their combustion than longer chained molecules, provided that their ignition delay is the same. Rao [2] observed that the higher levels of NOx emission in methyl esters is attributed to the combined effect of bulk modulus, cetane number, oxygen, and unsaturated fatty acids.

The objective of this paper is to further understand the high NO_x in a biodiesel fuel through chemical kinetics approach. This has been achieved by performing sensitivity analysis on a freely propagating flame for each of the fuel considered. Sensitivity analysis is carried out to predict the effect of variations of the rate constants on the dependent variables. Thus the important reactions as well as species responsible for NO_x formation are identified.

2. NUMERICAL MODEL

A freely propagating flame configuration has been used for all the three fuels. For this case, the flame is assumed to be one dimensional, and has low Mach number (deflagration). In addition, viscous dissipation, body forces, Dufour and Soret effects are neglected. Thus the general equations governing a multi-component reacting flow reduces to

$$\frac{\partial \rho}{\partial t} + \frac{1}{A}\frac{\partial}{\partial y}\left(\rho V_y A\right) = 0; \quad (1)$$

$$\rho\left(\frac{\partial Y_i}{\partial t} + V_y \frac{\partial Y_i}{\partial y}\right) = -\frac{1}{A}\frac{\partial}{\partial y}\left(\rho Y_i V_i A\right) + w_i$$

$$i = 1, \dots, N, \quad (2)$$

$$\rho c_p \left(\frac{\partial T}{\partial t} + V_y \frac{\partial T}{\partial y}\right) = \frac{1}{A}\frac{\partial}{\partial y}\left(\lambda A \frac{\partial T}{\partial y}\right) - \frac{\partial T}{\partial y}\sum_{i=1}^{N} c_{pi}\rho Y_i V_i - \sum_{i=1}^{N} h_i w_i + \frac{dp}{dt}$$

$$-\frac{1}{A}\frac{\partial}{\partial y}(q_R A) + A_s h_s (T - T_s), \quad (3)$$

$$p = \rho RT \sum_{i=1}^{N} \left(\frac{Y_i}{W_i}\right). \quad (4)$$

Here, ρ is the density, t is the time, p is the pressure, R is the universal gas constant, T is the temperature, N is the total number of species, A is the spatially variable cross sectional area, p is the pressure, V_y is the velocity in y direction, λ is the thermal conductivity, h_s is the heat transfer coefficient between gas and solid phase, q_R is the radiant heat flux, A_s is the local wetted surface area per unit void volume, T_s is the temperature at the solid surface, while w_i, Y_i, W_i, V_i, h_i, and c_{pi} represent the rate of production by chemical reactions, the mass fraction, the molecular weight, the diffusion velocity, the specific enthalpy, and the specific heat capacity at constant pressure of species *i*, respectively.

Sensitivity analysis is obtained by calculating the first-order sensitivity coefficients of the dependent variable, $\partial U/\partial K_k$, $k=1,\dots,l$. Here U denotes the vector of the unknown dependent variables, K_k denotes the rate constant for an elementary reaction k, and l denotes the total number of elementary reactions. The first order sensitivities are normalized to get the relative sensitivities or sensitivities coefficients, S^k. In this paper, the local sensitivities of mole fraction of CH and NO have been performed with respect to the rate constants of elementary reactions.

3. RESULTS AND DISCUSSIONS

3.1. Sensitivity of CH concentration in flames

The sensitivity of CH concentration towards the most important reactions in methane freely propagating flame is shown in Fig. 1. The graph shows that the dominant reaction is H + O_2 = O + OH. This is a very important chain branching step in every combustion process where H atoms are present [3]. The other reactions which have high positive sensitivity at the production zone of CH are OH + CH_3 = CH_2(S) + H_2O and OH + CO = H + CO_2. Therefore, from these reactions it is evident that OH and CH_3 are the most dominant radicals responsible for the CH production. Reactions which have high negative sensitivity at CH production zone are H + O_2 + H_2O = HO_2 + H_2O, OH + CH_4 = CH_3 + H_2O and H + CH_4 = CH_3 + H_2. Apparently, at the CH consumption zone the reactions which have positive sensitivity change to negative sensitivity and vice versa with the exception of reactions involving H abstraction in CH_4. These reactions also show that the consumption of CH_3 by OH, HO_2 and O promote the generation of CH. The generation of H radical increases CH production while the H consumption decreases its production. The plot also reveals that CO, H_2, CH_2(S), HCO, HO_2 and CH_2O are the other radicals which play an active role in the production and consumption of CH radical.

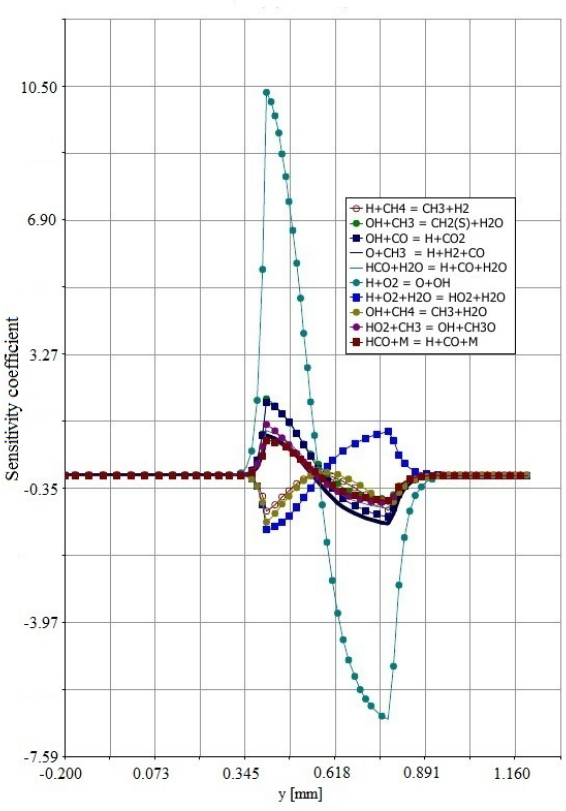

Figure 1: The sensitivity of CH concentration for a methane/air freely propagating flame, φ = 1

Sensitivity analysis of CH concentration in methanol freely propagating flame is presented in Fig. 2. Apart from H + O_2 = O + OH reaction, the other reactions which have high positive sensitivity at the CH production zone are H + HO_2 = 2OH, OH + CO = H + CO_2 and HCO + H_2O = H + CO + H_2O. Reactions: H + CH_3OH = CH_2OH + H_2 and HCO + O_2 = HO_2 + CO have high negative sensitivity at CH production zone. It is also important to note that the sensitivities of all these reactions change sign at the CH peak concentration position. OH, H and HCO are the dominant radicals which play an active role in the production and consumption of CH radical in this flame. Unlike in methane flame, CH_3 does not play a significant role in CH production in a methanol flame.

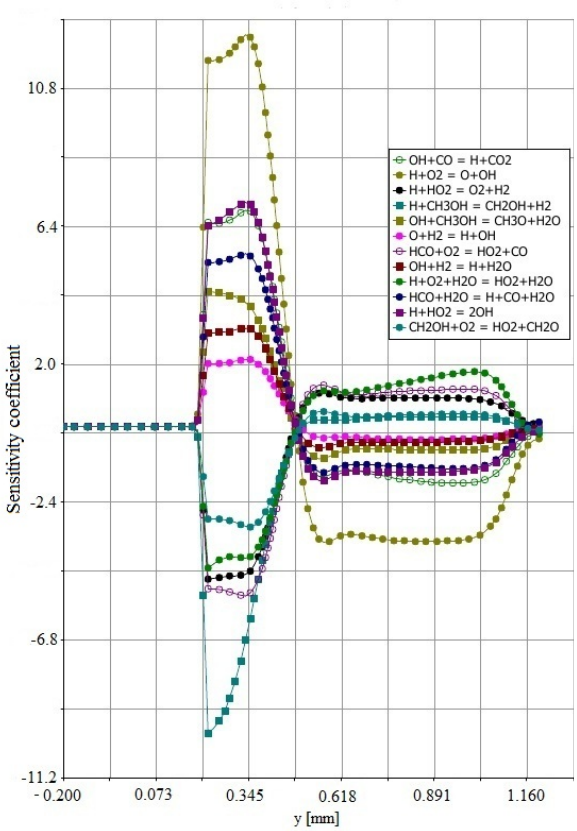

Figure 2: The sensitivity of CH concentration for a methanol/air freely propagating flame, φ = 1

Sensitivity analysis of CH concentration in methyl formate flame is shown in Fig. 3. Just like in the other two flames, H + O_2 = O + OH is the dominant reaction sensitive to the production of CH. Other reactions which have a bigger influence positively at CH production zone are CO + OH = CO_2 + H and HCO + M = H + CO + M. Reactions: H + OH +M = H_2O + M and H + CH_2OCHO = CH_3OCHO have high negative sensitivity at CH production zone. Similar to methanol flame, OH, H and HCO are the dominant radicals which play an active role in the production and consumption of CH radical in this flame. In particular, H radical dominates most of these reactions, with its generation promoting CH production and its consumption decreasing CH production. The plot also shows that CH_3 does not play a significant role in CH production in a methyl formate flame.

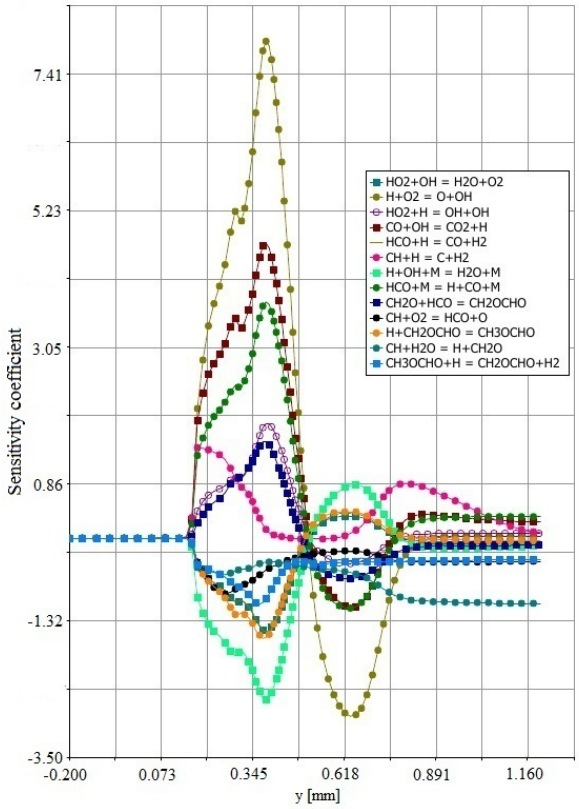

Figure 3: The sensitivity of CH concentration for a methyl formate/air freely propagating flame, φ = 1

3.2. Sensitivity of NO concentration in flames

The sensitivity of NO concentration towards the most important reaction in a methane flame is presented on Fig. 4. The most influential reaction with high positive sensitivity in NO production zone is CH + N_2

= HCN + N. This reaction is considered to be the dominant initiation reaction responsible for NO formation in flames [4,5]. The other reactions which have positive sensitivity are $CH + H_2 = H + CH_2$, $H + O_2 = O + OH$ and $OH + CH_3 = CH_2(S) + H_2O$. On the other hand, the reactions which have greater negative influence are $HO_2 + NO = NO_2 + OH$, $CH + O_2 = O + HCO$ and $O + CH_3 = H + CH_2O$. It is interesting to note that all these reactions have dominance effects even in the low temperature part of the flame zone where NO are produced at slow rate (as early as at -0.064 mm). At this zone, $HO_2 + NO = NO_2 + OH$ is the reaction which has high consumption of NO to form NO_2.

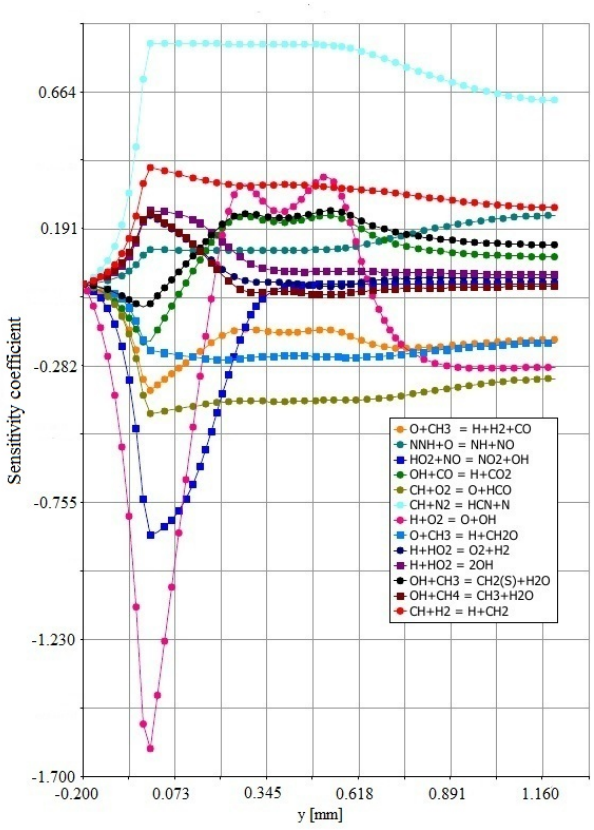

Figure 4: The sensitivity of NO concentration for a methane/air freely propagating flame, φ = 1

The sensitivity of NO concentration in a methanol flame is shown in Fig. 5. The plot shows a very interesting behaviour about the sensitivity of the reactions; highly sensitive at very low temperatures. This result in two regions of the flame zone where the rate constants of reactions are very sensitive; first region between -0.2 mm to 0.10 mm and the second region between 0.1 mm to 0.50 mm. Although the formation of NO in this flame starts at 0.30 mm, the first region sensitivity could indicate the formation and consumption of the precursor radicals responsible for NO formation. NNH + O = NH + NO is the only reaction which has positive dominance throughout the flame zone. This reaction has been identified by Hughes *et al.* [6,7] as the most sensitive in NO formation in H_2/air flame. The first region is characterized by reactions: $H + HO_2 = O_2 + H_2$, $2OH = O_2 + H_2O_2$, $HCO + O_2 = HO_2 + CO$ and $H + O_2 + H_2O = HO_2 + H_2O$ being most dominant on the positive side. The reactions which have the most positive influence in NO production in the second region are $H + O_2 = O + OH$, $OH + CO = H + CO_2$ and $HCO + H_2O = H + CO + H_2O$. All these reactions have antagonistic effects on both regions. It is also important to note that $HO_2 + NO = NO_2 + OH$ reaction contribute negatively to the production of NO in a methanol flame at low temperatures. Most of these reactions which have great influence in the low temperature region involve HO_2 radical. HO_2 radical is produced at low temperatures $T < 900$ K through hydrogen abstraction from the fuel via relatively slow reaction with oxygen [8].

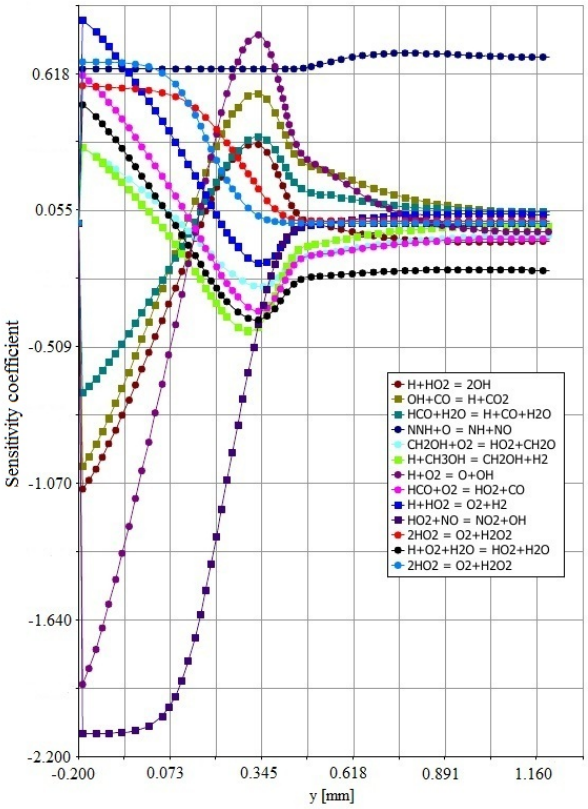

Figure 5: The sensitivity of NO concentration for a methanol/air freely propagating flame, φ = 1

The sensitivity of NO concentration in a methyl formate flame is presented on Fig. 6. Just like NO formation in a methanol flame, the behaviour of the sensitivity divide the flame into two regions; first region between -0.2 mm to 0.10 mm and the second region between 0.1 mm to 0.70 mm. Also NNH + O = NH + NO and N_2 + O = NO + N are the only reactions which have positive influence throughout the flame zone. Reactions: H + OH + M = H_2O + M, HO_2 + OH = H_2O + O_2 and HCO + H = CO + H_2 have high positive sensitivity in the first region. While reactions: CO + OH = CO_2 + H, H + O_2 = O + OH and HCO + M = H + CO + M have dominant positive sensitivity in the second region. It is also noted that HO_2 + NO = NO_2 + OH reaction contribute negatively to the production of NO in a methyl formate flame at low temperatures.

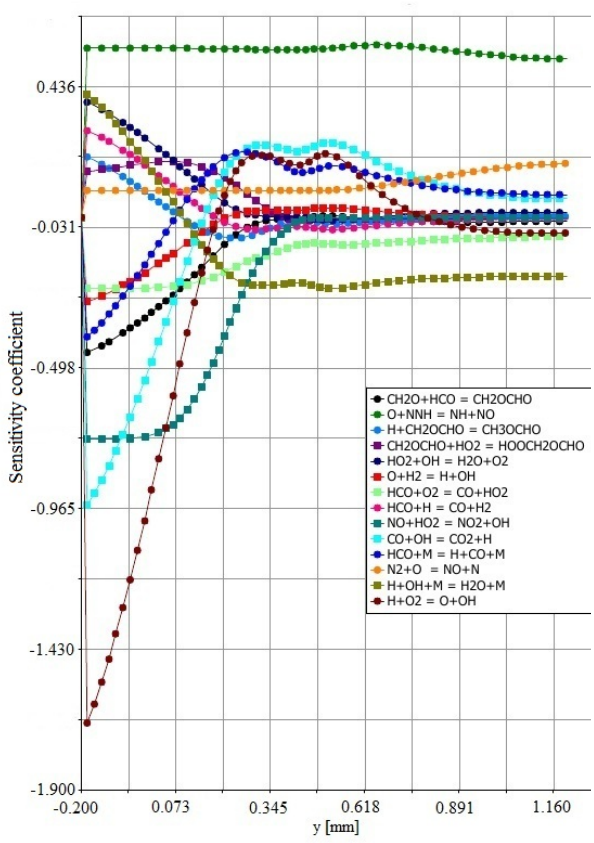

Figure 6: The sensitivity of NO concentration for a methyl formate/air freely propagating flame, φ = 1

4. CONCLUSION

The sensitivity analysis of CH and NO concentration in methane, methanol, and methyl formate freely propagating flames have been examined. The research has shown that unlike in methane flame, CH_3 does not play a significant role in CH production in a methanol and methyl formate flames. In addition, the sensitivity analysis has shown that prompt NO formation in oxygenated fuels follows a different route (NNH + O = NH + NO) as opposed to the well known route (CH + N_2 = HCN + N).

ACKNOWLEDGMENT

The authors gratefully acknowledge the financial support of the Dedan Kimathi University of Technology, whose Combustion Simulation Laboratory Software package (COSILAB) was used to carry out the Flame simulations.

REFERENCES

[1] A. Schonborn, N. Ladommatos, J. Williams, R. Allan, and J. Rogerson, "The influence of molecular of fatty acid monoalkyl esters on diesel combustion," *Combustion and Flame*, vol. 156, pp. 1396–1412, 2009.

[2] P. V. Rao, "Effect of properties of karanja methyl ester on combustion and NO_x emissions of a diesel engine," *Journal of Petroleum Technology and Alternative Fuels*, vol. 2(5), pp. 63–75, 2011.

[3] T. Turanyi, "Applications of sensitivity analysis to combustion chemistry," *Reliability Engineering and System Safety*, vol. 57, pp. 41–48, 1997.

[4] S. C. Li and F. A. Williams, "NO_x formation in two-stage methane-air flames," *Combustion and Flame*, vol. 118, pp. 399–414, 1999.

[5] S. Naha and S. K. Aggarwal, "Fuel effects on NO_x emmisions in partially premixed flames," *Combustion and Flame*, vol. 139, pp. 90–105, 2004.

[6] K.J. Hughes, A.S. Tomlin, E. Hamparsounmian, W. Nimmo, I. G. Zsely, M. Ujvari, T. Turanyi, A. R. Clague, and M. J. Pilling, "An investigation of important gas-phase reactions of nitrogeneous species from simulation of experimental measurements in combustion systems," C*ombustion and Flame*, vol. 124, pp. 573–589, 2001.

[7] I. Glassman and R. A. Yetter, *Combustion*. Elsevier, 2008.

[8] G. P. Merker, C. Schwarz, and R. Teichmann, *Combustion Engines Development.* Springer, 2009.

On modeling of sandwich panels with continuous piezoelectric PVDF cores

B. W. Nyota, B. Ikua and J. N. Keraita

brendanyota@yahoo.com

Abstract: Piezoelectric devices have been employed vastly in vibration energy harvesting applications. These devices are also employed in active, active-passive and passive vibration suppression. It is possible to combine the objectives of vibration suppression and energy harvesting, so as to achieve them simultaneously. Distributed devices show great potential in achieving this. The devices comprise of a distributed polyvinylidene fluoride spring layer with a mass layer atop. The geometrical intricacies of the spring layer coupled with the lack of symmetry in the placement of the device on the vibrating host structure make the modeling of such devices complex. This paper looks into the methods developed to circumvent the difficulties faced in modeling of the distributed devices so as to achieve accurate models with high computational efficiency.

Keywords

Energy harvesting, vibration suppression, distributed devices, piezoelectric devices

Effect of Pressure and Equivalence Ratio on Nitric Oxide Formation in Methane/Air Methanol/Air and Methyl Formate/air Homogenous Ignition

J. M. Ngugi, P.N. Kioni, A. Gitahi and S. K. Musau

johnmburungugi@gmail.com

Abstract: In this study, methane/air, methanol/air and methyl formate/air mixtures at equivalence ratios of 0.7, 1 and 1.3 have been numerically simulated at constant volume, pressures of 1 to 50 atm at initial temperatures of 1300K. The main aim of this study is to determine the impact of equivalence ratio and pressure on nitric oxide (NO) formation in oxygenated fuels. These conditions represent those behind a reflected shock in a shock tube, which is modeled as adiabatic homogenous system, with constant internal energy and constant volume. The chemical kinetic mechanisms employed in this study have been tested to ensure the validity of the results. NO mole fraction profiles and other radicals CH, HCN, N_2, N and O that are dominant in formation of NO have been compared in this study. The study has shown that that NO increases with increase in pressure for equivalence ratios of 0.7, and 1 and decreases with pressure increases at equivalence ratio of 1.3. No formation in methane is high at equivalence ratios of 0.7 and 1 while NO formation in methyl formate is higher at equivalence ratio of 1.3 for all pressures. The flame temperatures for all mixtures are high because of high initial temperatures. The study has also shown that temperature increases with increase in equivalence ratio at all pressures. Zeldovich (N_2+O=NO+N 318.4 Kj/mol) has been delineated as the rate determining steps for NO formation in this study.

Keywords: Homogenous mixture; NO; methane; methanol; methyl formate.

Design Optimization of a Renewable Hybrid Energy System

J. O. Obasi[1], L. M. Ngoo[2] and C. M. Muriithi[3]
[1]Electrical & Electronic Engineering Department, JKUAT
[2]Multimedia University of Kenya
[3]Electrical & Electronic Engineering Department, JKUAT
[1]jayobasi@gmail.com, [2]mwalungoo@yahoo.com, [3]cmaina77@yahoo.com

Abstract-This paper proposes the optimal design of a renewable hybrid energy system consisting of solar, wind energy with battery storage suitable for application in remote areas. The study investigates the possibility of reducing the overall size of a system already installed in a school in Maji Mazuri, Kiserian. The main aim of the study is to reduce size of the renewable systems and reduce energy storage. The study investigates the effects of reducing load demand on the size of the system components. DC LED lamps are proposed for all the lighting needs of the school in order to reduce the load demand especially during peak hours. The results show that the optimized system is able to meet the load demand. Homer software is used in the design and optimization of the renewable hybrid power system.

Keywords- Homer, Hybrid Energy System, Solar, Wind.

I. INTRODUCTION

With increasing concern on global environmental pollution and increased cost of electricity, hybrid energy systems based on renewable energy are now playing a key role in meeting current electricity demand. However, power produced from renewable sources such as solar PV and wind energy system is highly variable due to their intermittent nature. This poses serious technical and economic challenges when designing stand alone hybrid energy systems due to the uncertainties in the electricity generation. To provide balance between energy generation and load demand, energy storage systems are usually used [1]. Stand alone systems usually require large storage systems to cover for periods when there is no generation from the renewable resources [2]. Hybridizing solar PV and wind due to their complementary nature improves the system reliability and can significantly reduce the storage requirements [3] [4] [5].

A major challenge in the design of renewable resources is their intermittent nature which results in excess capacity and shortages. The challenge is reducing the shortages and excesses while ensuring the quality of supply [6]. Optimizing the size of the solar PV, wind generator and battery will improve the system reliability as well as reduce the overall cost of the system. Optimal sizing methods for standalone hybrid energy systems can either be single objective or multi-objective. In single objective the main aim is to ensure reliable supply while keeping the cost of the system at a minimum. In multi-objective optimization, the power supply reliability, the overall cost of the system and environmental considerations such as pollutant emissions are taken into account.

This paper proposes an optimal sizing method for an existing PV/wind/battery hybrid energy system by minimizing excess capacity and energy storage. The system was sized to meet all demand especially during peak hours, resulting in an oversized system. During mid-afternoon when the sun is overhead the power generated by PV exceeds the load demand, battery charging power and dump load power. The same case applies for the wind generator although the timing varies with the availability of wind. This paper proposes peak shaving by replacing all lighting loads with D.C. LED bulbs. LED lamps offer extraordinary power saving compared to fluorescent, compact fluorescent lamps and halogen lamps while giving the same light output.

II. ENERGY DEMAND AND RESORCES

A: Load demand

The objective of this study was to optimize the design of a renewable hybrid energy system by reducing excess capacity from the renewable resources. Maji Mazuri School in Kiserian, Kajiado County has been selected for study as it already has an existing system with a lot of excess electricity. Kajiado borders Nairobi to the South and lies in the expansive Great Rift Valley. The electrical load for the school is mainly for

lighting, electrical appliances such as radio, T.V, computers and water pumping. Daily load demand is illustrated in Fig 1.

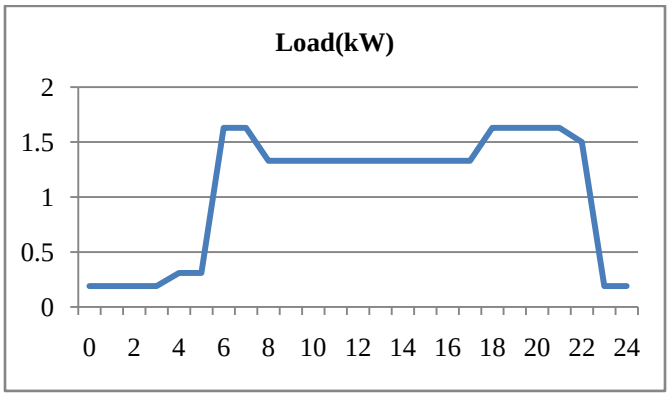

Fig. 1 Daily Load Profile

There are two peaks, one occurring between 6 and 8 am in the morning and 7 and 10pm in the evening.

B: Solar Radiation

Solar energy is a promising renewable energy resource because of its unlimited potential and availability. Solar radiation is determined by the location on the earth's surface, the season and time of day. Monthly averages of solar radiation was collected from the Kenya Meteorological Department and used as inputs to the Homer software. Monthly averages for the solar radiation for the year are illustrated in Fig. 2. The scaled annual average clearness index is 0.55 and daily radiation is 5.508 kWh/m^2.

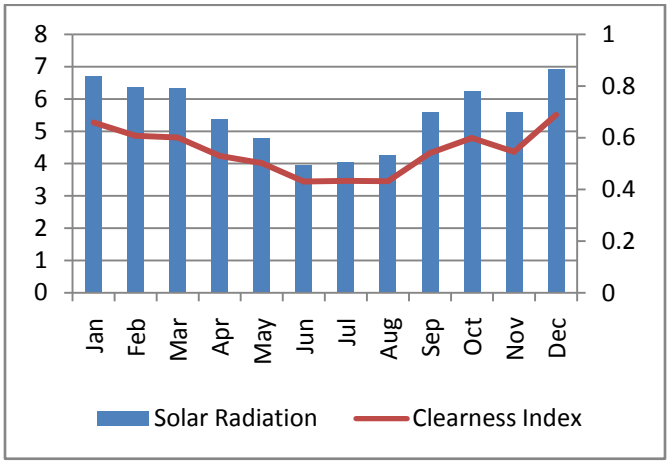

Fig. 2 Monthly average Solar Radiation

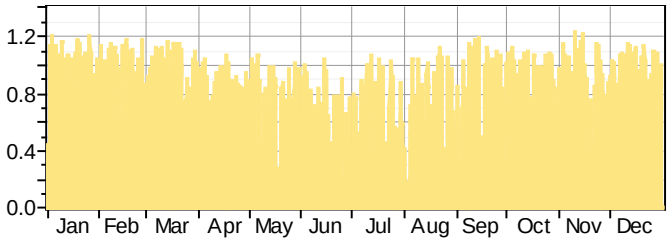

Fig. 3 Annual horizontal solar radiation

C: Wind Resources

Wind energy is the fastest growing among renewable energy technologies. The annual monthly wind speeds are shown in Fig. 3. Wind speeds suitable for power generation are observed between the months of Jan to May and Sep to Dec. The period between May and Aug on average there is very little wind speed about 3m/s which results in very low output from the wind generator.

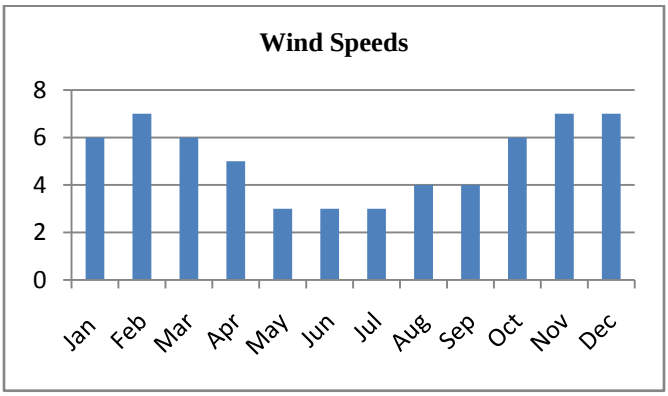

Fig. 3 Monthly average Wind Speeds

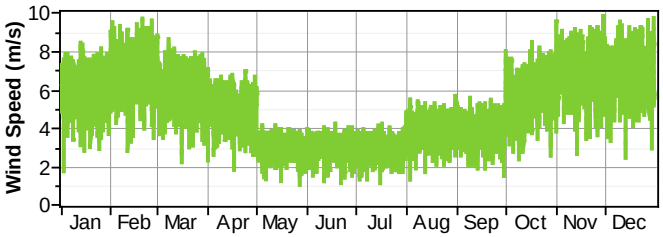

Fig. 4 Annual wind speeds

III. METHODOLOGY

This study seeks to optimize an existing hybrid energy system integrating wind energy, solar PV and batteries. The existing system consists of a 3.6 kW solar array, a 6 kW wind turbine and 30 batteries rated at 12v and 200Ah. The system is characterized by excess capacity

which cannot be utilized especially around midday resulting to a lot of wasted energy.

In order to optimize the system this study proposes to separate the loads into AC and DC, this will reduce the peak load due to a.c. lighting requirements. All electric appliances will be served by AC and all lighting will be replaced by DC LED lamps. LED lamps offer extraordinary power saving compared to fluorescent, compact fluorescent lamps and halogen lamps while giving the same light output. LED lamps rated 3watts have been chosen to replace the existing fluorescent and compact fluorescent lamps. Desktop computers have also been replaced with laptop computers while television sets have also been replaced with LCD televisions sets to reduce power consumption.

The new energy demand for the school is illustrated in the following figures

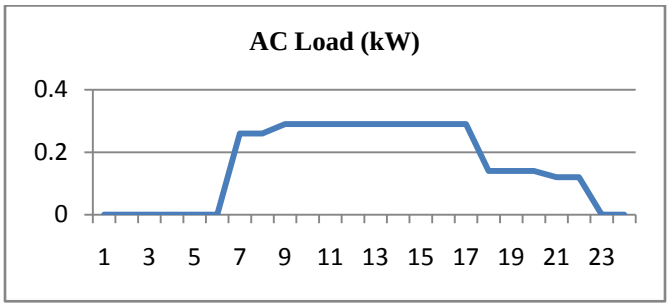

Fig. 5 Daily a.c load profile

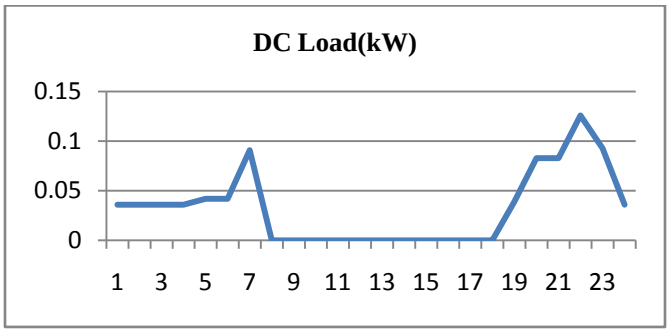

Fig.6 Daily d.c. load profile

The major components for the hybrid power system are solar PV panels, wind turbines, power converter and batteries. Solar panels are the primary source of power while the wind turbines and batteries provide electricity during periods of no generation from the solar panels. Homer requires the number of units to be considered, the capital costs, replacement costs, operation and maintenance costs and the lifetime of the components to simulate the system. The figure below shows the considered hybrid energy system.

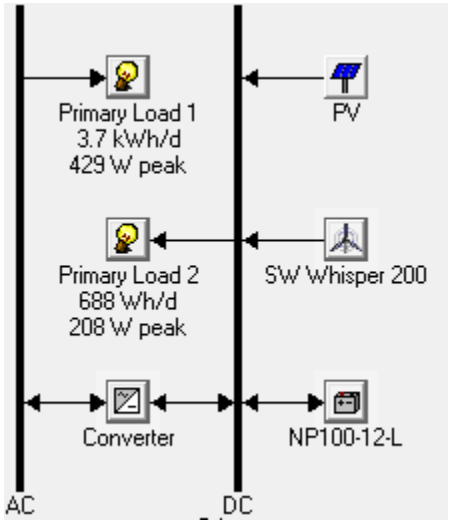

Fig. 7 Hybrid Energy System

The main aim of optimizing the system is to find the optimal decision variables of the system components that will match the load to the available wind and solar resources throughout the year. The various decision variables in the system to consider include:

- The size of the PV array
- The number of wind turbines
- The size of the converter
- The number of batteries

A. Solar Array

The Kyocera KD250GX-LFB 250 watt solar panel is considered for this study with one unit costing 375 dollars. The operation and maintenance costs are practically zero and the lifetime of the system is taken to be 25 years.

B. Wind Turbine

The 1kW DC SW Whisper 200 wind turbine with initial capital cost of 3,000 dollars is considered. The lifetime of the wind turbine is taken as that of the system to be 25 years.

C. Power converter

A power converter is required to convert DC to AC. A converter of 2.5kW is considered costing 950 dollars. The lifetime of the power converter is 25 years.

D. Batteries

Batteries are used in the hybrid power system to provide electrical power when there is little or no output from renewable resources. Batteries will supply electrical power when the renewable energy resources cannot meet the load requirements. The Dayliff Champion 12V 100Ah battery is considered in this study. Each battery costs 250 dollars and has an expected lifetime of about six years.

IV. RESULTS AND DISCUSSION

From the simulation the configuration containing one Whisper 200 1 kW wind turbine, 1.25 kW array, 10 batteries and 2.5kW inverter is found to be the optimum configuration. The optimized system is smaller in size compared to the existing system as shown in the following table.

Table 1: Comparison of designed systems

System	PV array	Wind Turbine	Batteries
Existing	3.6 kW	6 kW	30
optimized	1.25 kW	1kW	10

The Power generated from the wind generator and solar PV is sufficient for the better part of the year except during the months of May, June and July when the power generated is lower. The figure below shows the contribution of Solar PV and Wind energy resources to the total electricity production throughout the year.

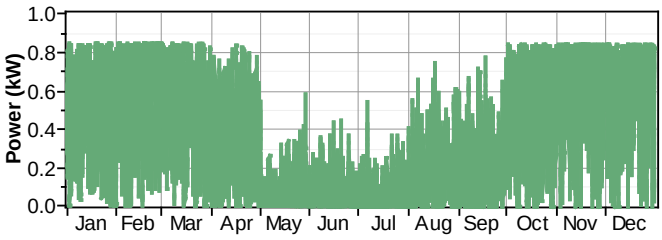

Fig. 8 Annual Wind Turbine Power

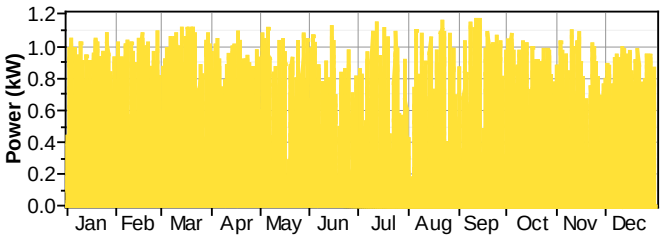

Fig. 9 Annual solar PV power

Batteries provide power during periods of little or no generation from the wind and solar generators. From the simulation the batteries operate optimally for most part of the year except during the months from May to September. The following figures show the batteries input power and state of charge (soc) throughout the year.

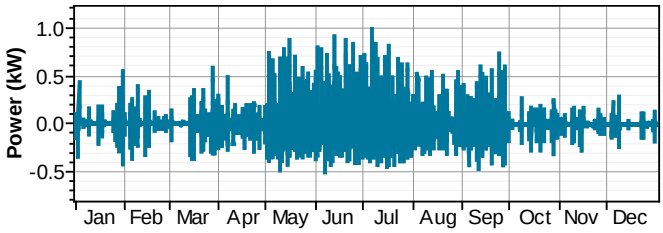

Fig. 10 Battery input power

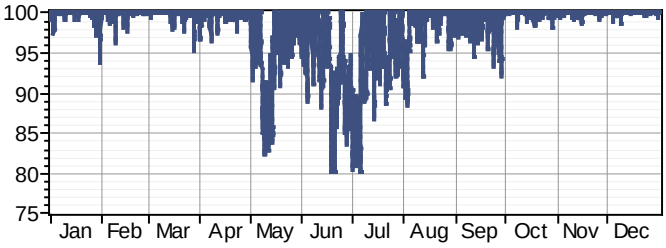

Fig. 11 Battery state of charge (%)

Between the months of May and September power from the renewable is reduced and the batteries have to be used regularly to provide power. There is also very little power generated such that the batteries are sometimes used to the lowest allowable SOC which is 80%.

Table 2: Comparison of Capital Cost

	Existing ($)	Optimized ($)
PV array	5,184	1.850
Wind Turbine	5,800	3,000
Batteries	4,200	2,500
Inverter	2,420	950
Capital cost	17,604	8,300

From the results the optimized system is cheaper by about 9,300 dollars. This is due to the reduced size of PV array, number of batteries, size of inverter and the size of wind turbine. The total cost of replacing the bulbs with LED bulbs, computers and television sets is about 6,245 dollars. The total savings realized is about

3,000 dollars. However, this does not include the salvage value of all the items being replaced.

V. CONCLUSION

Most remote areas are not connected to the grid because of the high costs involved in grid extension. Hybrid energy systems offer a promising alternative for electrification of these areas. The systems integrate locally available renewable resources with battery storage to ensure grid quality electricity supply.

From the simulation results a Solar-wind-Battery system consisting of a 1.25 kW solar array, one wind turbine, 10 batteries and a 2.5 kW inverter is found to be the optimum system. The system is able to reliably meet the load demand throughout the year and reduce excess capacity.

The analysis of results shows significant contribution of solar PV and wind turbines. Batteries are extensively employed between the months of May to September when the output from renewable sources is low.

Significant cost savings are realized by optimizing the system by reducing the peak loads which are associated with lighting and a.c appliances. This shows that demand side management can significantly reduce the load demand and thus reduce the overall size of the system.

ACKNOWLEDGEMENT

The authors would like to thank the National Commission for Science and Technology (NCST) of Kenya for their support in this project.

References

[1] Yuri V. M., Pengwei D, Michael C. W., and Chunlian J and Howard F. I, "Sizing Energy Storage to Accommodate High Penetration of Variable Energy Resources," *IEEE trans on Sustainable Energy*, vol. 3, no. 1, pp. 34-40, January 2012.

[2] Ruan X, Mao C, Zhang B and Luo Y Xu L, "An Improved Optimal Sizing Method for Wind-Solar-Battery Hybrid Power System," *IEEE Transactions on Sustainable enrgy Energy*, vol. 4, no. 3, pp. 774-785, March 2013.

[3] Perez E, Aparicio N and Rodriguez P Beltran H, "Daily Solar Energy Estimation for Minimizing Energy Storage Requirements in PV Power Plants," *IEEE Trans. Sustainable Energy*, vol. 4, no. 2, pp. 474-481, April 2013.

[4] Dong H and Xiaokang L Xiangjun L, "Battery Energy Storage Station (BESS)-Based Smoothing Control of Photovoltaic (PV) and Wind Power Generation Fluctuations," *IEEE Trans. Sustainable Energy*, vol. 4, no. 2, pp. 464-473, March 2013.

[5] Key Pour R, Shajari s, "Reduction of energy storage system for smoothing hybrid wind-PV power fluctuation," in *IEEE Conference Preceedings*, 2012, pp. 115-117.

[6] K. Suomalainen, C. Silva, and P. Ferrão and S. Connors, "Wind power design in isolated energy systems: Impacts of daily wind patterns," *Elsevier*, vol. 1, no. 1, pp. 533-540, 2013.

Static Voltage Stability Assessment of Nairobi Area Power Distribution Network

Oketch S.A[1], Muriithi C.M[2], Kaberere K.K[3]

Dept. of Electrical & Electronic Engineering, Jomo Kenyatta University of Agriculture & Technology
P.O. Box 62000, Nairobi, Kenya

[1]engsoketch@yahoo.com,[2]cmmuriithi@eng.jkuat.ac.ke,[3]kkkanuthu@eng.jkuat.ac.ke

***Abstract*-The Nairobi Area Power distribution network supplies over 50% of Kenya's national load demand. The increase in load demand in the network, over the years has generated interest to the network's voltage stability status. Voltage stability is an important factor that needs to be taken into consideration during the planning and operation of power systems in order to avoid voltage collapse and subsequently partial or full system blackout. The study of the voltage stability characteristics can provide a way to prevent this event from happening.**

This paper presents a study to assess the voltage stability of Nairobi Area Power distribution network using static analyses methods. The network power flow problem is formulated, and solution attained using Newton Raphson method to determine the base operating voltages and angles, the power flows, and to compute the full Jacobian matrix. The Sensitivity and Modal analyses methods are used to investigate the network weak buses and branches, and to analyse the response of network generators to incremental changes in reactive loadings. In the rest of this works, the P-V and Q-V curves analysis methods are used to compute the active and reactive power margins respectively, of the identified weak buses. The analysis is performed to simulate the peak loadings conditions of June, 2012

.

***Keywords*— Voltage stability, Sensitivity analysis, Modal analysis, Active power Margins and Reactive power margins.**

I. INTRODUCTION

In the last few years the need to increase the transfer capacity of the existing distribution networks without major investments and also without compromising the security of the power system has led to a situation where utilities operate power systems relatively closer to voltage stability limits [1].

The continued growth in load demand or contingency in the network may lead to a state of voltage instability, and eventually, voltage collapse.

Voltage stability is concerned with the ability of power system to maintain acceptable voltages at all buses under normal conditions and after being subjected to a disturbance [2]. Voltage stability can be attained by sufficient generation and transmission of energy. Generation and Transmission have definite capacities that are peculiar to them and should not be exceeded in a healthy power system. The main factor causing voltage instability is the inability of the power system to meet the demand for the reactive power in a heavily stressed system
[2], [3].

Therefore a power system is said to experience voltage instability when a disturbance or sudden increase in load demand or change in system conditions causes a progressive and uncontrollable decline in voltage levels. Voltage collapse refers to the process by which the sequence of events leading to voltage instability leads to low unacceptable voltages in a significant part of the power system [2]. It is the result of accumulative processes involving the actions and interactions of many devices, controls and protective systems.

Most utilities now consider Voltage stability in their planning and operation of the power systems in order to avoid voltage collapse and subsequently partial or full system blackout.

A number of techniques are available in literature for the analysis of voltage stability. These techniques are based on either steady state and/or dynamic analysis methods [2]. Since the system dynamics that influence voltage stability are usually slow, many aspects of the problem can be effectively analysed using static methods, which examine the viability of the equilibrium points represented by a specified operation of the power system. Static analysis methods, in addition to providing information with regard to the sensitivity or degree of stability, also involves the computation of only algebraic equations and are thus efficient and faster.

This paper presents an assessment of the voltage stability of the Nairobi Area Power Distribution Network using static analyses approaches. The power flow problem for the network configuration was formulated and solution attained by Newton

Raphson method, using a MATLAB based program. The VQ sensitivity and QV modal analyses methods are employed to investigate the network weak buses and branches, and also the response of the network generators to the incremental changes in reactive loadings. The buses identified as weak are further investigated by analysing their P-V and Q-V curve characteristics on PowerFactory DIgSILENT software, to determine their active and reactive power margins respectively. The analysis is performed to simulate the peak loading conditions of June, 2012.

The paper is organized as follows: Section I served as introduction. In section II we discuss the voltage stability analysis, section III presents a case study using the Nairobi Area Power Distribution Network, and in IV we outline conclusions and recommendations.

II. VOLTAGE STABILITY ANALYSIS

The linearized steady state system power voltage equations are presented by [2], [4]:

$$\begin{bmatrix}\Delta P\\ \Delta Q\end{bmatrix}=\begin{bmatrix}J_1 & J_2\\ J_3 & J_4\end{bmatrix}\begin{bmatrix}\Delta\delta\\ \Delta V\end{bmatrix} \qquad (1)$$

Where ΔP and ΔQ are the mismatch active and reactive powers, ΔV and $\Delta\delta$ are the unknown voltage and angle correction vectors, and

$\begin{bmatrix}J_1 & J_2\\ J_3 & J_4\end{bmatrix}$ - is the network full Jacobian matrix.

A. *Q-V Sensitivity Analysis*

The elements of Jacobian matrix give the sensitivity between the power flows and bus voltage changes [2], [5], [6].The system voltage stability is affected by both P and Q. However at each operating point if P is kept constant then voltage stability is evaluated by considering incremental relationship between Q and V.

Based on these considerations then, in equation (1) if $\Delta P = 0$, then

$$\begin{bmatrix}0\\ \Delta Q\end{bmatrix}=\begin{bmatrix}J_1 & J_2\\ J_3 & J_4\end{bmatrix}\begin{bmatrix}\Delta\delta\\ \Delta V\end{bmatrix} \qquad (2)$$

$$\Delta Q = \left[J_4 - J_3 J_1^{-1} J_2\right]\Delta V \qquad (3)$$

$$\Delta Q = J_R \Delta V \qquad (4)$$

$$J_R = \left[J_4 - J_3 J_1^{-1} J_2\right] \qquad (5)$$

J_R - is the reduced Jacobian matrix of the system.

From equation (4),

$$\Delta V = J_R^{-1}\Delta Q \qquad (6)$$

The matrix J_R^{-1} is the reduced V-Q Jacobian and its i^{th} diagonal element is the sensitivity at bus i.

The V-Q sensitivity at a bus represents the slope of Q-V curve at a given operating point. A positive V-Q sensitivity is indicative of stable operation; the smaller the sensitivity the more stable the system]. As the stability decreases, the magnitude of the sensitivity increases, becoming infinite at the stability limit. Conversely a negative sensitivity is indicative of unstable operation. A small negative sensitivity represents a very unstable operation [2], [7], [8], [9].

B. *Q-V Modal Analysis*

Voltage stability characteristics of the system can be identified by computing the eigenvalues and eigenvectors of the power flow (reduced) Jacobian matrix, J_R [2], [3], [5], [7], [9].

Let $J_R = \xi \Lambda \eta$ (7)

Where

ξ =Right eigenvector of matrix J_R

η =Left eigenvector of matrix J_R

Λ =diagonal eigenvalue of matrix J_R

From equation (7),

$$J_R = \xi \Lambda^{-1} \eta \qquad (8)$$

Incremental changes in reactive power and voltage are related by equation (6). Substituting equation (8),

$$\Delta V = \xi \Lambda^{-1} \eta \Delta Q \qquad (9)$$

Or

$$\Delta V = \sum_i \frac{\xi_i \eta_i}{\lambda_i} \Delta Q \qquad (10)$$

Where

λ_i - is the i^{th} eigenvalue

ξ_i - is the i^{th} right eigenvector of J_R

η_i -is the i^{th} row left eigenvector of J_R

Each eigenvalue λ_i and the corresponding right and left eigenvectors ξ_i and η_i define the i^{th} mode of V-Q response.

Since $\xi^{-1} = \eta$ equation (9) can be written as:

$$\eta \Delta V = \Lambda^{-1} \eta \Delta Q \qquad (11)$$

Or

$$v = \Lambda^{-1} q \qquad (12)$$

Where

$v = \eta \Delta V$ is the vector of modal voltage variations, and

$q = \eta \Delta Q$ is the vector of modal reactive power variations

The i^{th} modal voltage variation can therefore be written as:

$$v_i = \frac{1}{\lambda_i} q_i \qquad (13)$$

From equation (13) the stability of mode i with respect to reactive power changes is defined by the modal eigenvalue λ_i. Large values of λ_i suggest small changes in modal voltage for reactive power changes. As the system is stressed the value of λ_i becomes smaller and the modal voltage becomes weaker. If the magnitude of λ_i is equal to zero, the corresponding modal voltage collapses since it undergoes infinite changes for reactive power changes. A system is therefore defined as stable if all the eigenvalues of J_R are positive. The bifurcation or voltage stable limit is reached when at least one eigenvalue reaches zero; that is one or more modal voltages collapses. If any of the eigenvalues is negative the system is unstable. The magnitudes of eigenvalues provide a relative measure of the proximity of the system to instability.

1) Bus Participation Factors: The left and right eigenvectors corresponding to the critical mode in the system can provide information concerning voltage instability, by identifying the elements participating in these modes. The relative participation of bus k in mode i, is given by bus participation factor:

$$P_{ki} = \xi_{ki} \eta_{ik} \qquad (14)$$

Bus participation factors corresponding to the critical modes can predict nodes or areas in a power system susceptible to voltage instability. Buses with large participation factors to the critical mode correspond to the most critical of system buses. In practical systems with several thousand buses, there is usually more than one weak mode associated with different parts of the system, and the mode associated with the minimum eigenvalue may not be the most troublesome mode as the system is stressed [2].

2) Branch Participation Factors: If we assume vector of modal reactive power variations, q corresponding to mode i to have all elements equal to zero except the i^{th}, which equals to 1, then the corresponding vector of bus reactive power variations is

$$\Delta Q^{(i)} = \eta^{-1} q = \xi q = \xi_{(i)} \qquad (15)$$

Where ξ_i is the i^{th} right eigenvector of J_R

The vector of bus voltage variations is

$$\Delta V^{(i)} = \frac{1}{\lambda_i} \Delta Q^{(i)} \qquad (16)$$

The corresponding vector of bus angle variations is

$$\Delta \theta^{(i)} = -J_1^{-1} J_2 \Delta V^{(i)} \qquad (17)$$

The linear relationships for the real and imaginary powers at a bus can be obtained for small variations in variables θ and V by forming total differentials [10] as follows:

For a PQ bus bar

$$\Delta P_k = \sum_{m \in k} \frac{\partial P_k}{\partial \theta_m} \Delta \theta_m + \sum_{m \in k} \frac{\partial P_k}{\partial V_m} V_m \qquad (18)$$

$$\Delta Q_k = \sum_{m \in k} \frac{\partial Q_k}{\partial \theta_m} \Delta \theta_m + \sum_{m \in k} \frac{\partial Q_k}{\partial V_m} V_m \qquad (19)$$

For PV bus bar, only equation (18) is used since Q_k is not specified. For slack bus bar, no equation is used.

With angle and voltage variations for both the sending end and the receiving end known, the linearized change in branch reactive loss can be calculated [2].

The relative participation of branch j in mode i is given by the participation factor:

$$P_{ji} = \frac{\Delta Q_{loss} \text{ for branch j}}{\text{maximum } \Delta Q_{loss} \text{ for all branches}} \quad (20)$$

Branch participation factor indicates for each mode which branches consume the most reactive power in response to an incremental change in reactive load. Branches with high participations are either weak links or are heavily loaded [2].

3) Generator Participation Factor: The relative participation of machine m in mode i, is given by generator participation factor [2].

$$GPF_{m.i} = \frac{\Delta Q_m \text{ for machine m}}{\max\text{imum } \Delta Q \text{ for all machines}} \quad (21)$$

The generator participation factor indicates for each mode which generator supply most reactive power in response to an incremental change in system reactive loading.
Generator Participation factors provides important information regarding proper distribution of reactive reserves among all machines.
Generators with high $GPF_{m.i}$ are important in maintaining stability of mode i [2].

C. *P-V and Q-V curves Analysis*

At the voltage collapse point, the maximum power transfer limit has been reached, and therefore operation of power system faces difficulties. For a satisfactory operation, a sufficient power margin must be allowed [2]. In assessing the network proximity to voltage collapse point, P-V and Q-V curves are plotted and analysed.
It has been argued in literature that Q-V curve technique is preferable when determining the reactive supply problems, whereas the P-V curve analysis is preferable for providing power loading and transfer indications [11].

1) P-V Curves: The P-V curves have been used widely for predicting the margins of voltage stability. For a given value of active power, there are two possible voltages (higher voltage with lower current or lower voltage with higher current). The normal operation corresponds to higher voltage solution [2], [9], [12], [13].

The P-V curve at a load bus is produced by incrementally increasing the active power, P and performing series of power flow solutions for the different loading levels, until the maximum power transfer limit is reached.

The P-V curve is plotted using the calculated values of voltages corresponding to the incremental changes of P values at the candidate bus. A typical P-V curve is shown in Fig 2.1

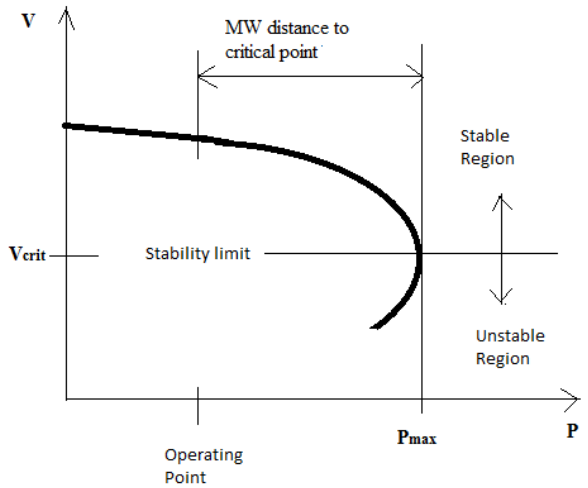

Fig. 2.1: Typical (P-V) Curve

As shown in Fig 2.1 the real power margin at a load bus is the Megawatt (MW) distance from the operating point to the voltage collapse point.

2) Q-V Curves: The Q-V relationship represents the sensitivity and variation of a bus voltage with respect to reactive power injections or absorptions [2]. A system is voltage stable if V-Q sensitivity is positive for every bus and voltage unstable if V-Q sensitivity is negative for at least one bus.

The Q-V curves are used by many utilities for determining proximity to voltage collapse so that operators can make good decision to avoid losing system stability [11].

The Q-V curves are produced by incrementally increasing the reactive power demand, Q at the candidate bus, and running series of power flows with each change until the power system is not able to meet the demand for the reactive power.

A typical Q-V curve is shown in Fig. 2.2. As seen in the figure, the Reactive Power Margin is the Mega Volt Ampere reactive (MVAr) distance from the operating point to the critical voltage.

III. CASE STUDY

Figure 1 shows the single line diagram of the Nairobi Area supply distribution network. It consists of 66kV radial distribution lines originating from four bulk power supply points. Rings of transmission lines at 132kV and 220kV supplies the bulk supply points from six hydroelectric and two geothermal power stations. The network also has two Diesel generators and one small hydroelectric power plants injecting power at 66kV.

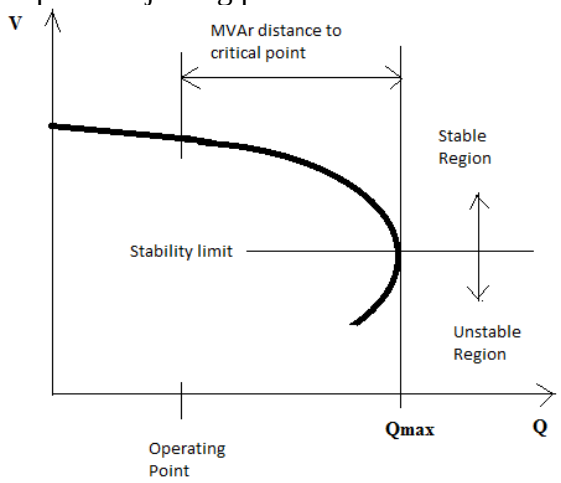

Fig.2.2: Typical (Q-V) Curve

Apart from the 66kV voltage level, the distribution network has other voltage levels: 33kV, 11kV and the low voltages. But this study is mainly on the 66kV network.

A. *Network voltage operating conditions*

The power flow problem was formulated and solved by Newton Raphson method using a MATLAB based program to obtain the operating voltages and angles, line flows and the full Jacobian matrix.

The voltage variation criteria in Kenya are +/- 6% for distribution networks and +/- 10% for transmission networks [14]. Table I of section IV shows buses operating outside this criterion.

B. *Q-V Sensitivity analysis*

The MATLAB program further computed the Reduced Jacobian and the reduced V-Q Jacobian matrices from the full Jacobian matrix.

The sensitivity factors of the load buses are evaluated from the diagonal elements of the reduced V-Q Jacobian matrix. Figure 2 of section IV shows the buses with highest sensitivity factors in the network.

C. *Q-V Modal analysis*

The MATLAB program was used to compute the eigenvalues, the right and left eigenvector matrices of the reduced Jacobian matrix, from which the bus and branch participation factors were evaluated.

Table III and IV of section IV shows the smallest modal eigenvalues for the network operating condition.

Figure 3 of section IV shows buses with highest bus participation factors for the network operating condition.

Figures 4 of section IV shows the branches with highest branch participation factors in the network.

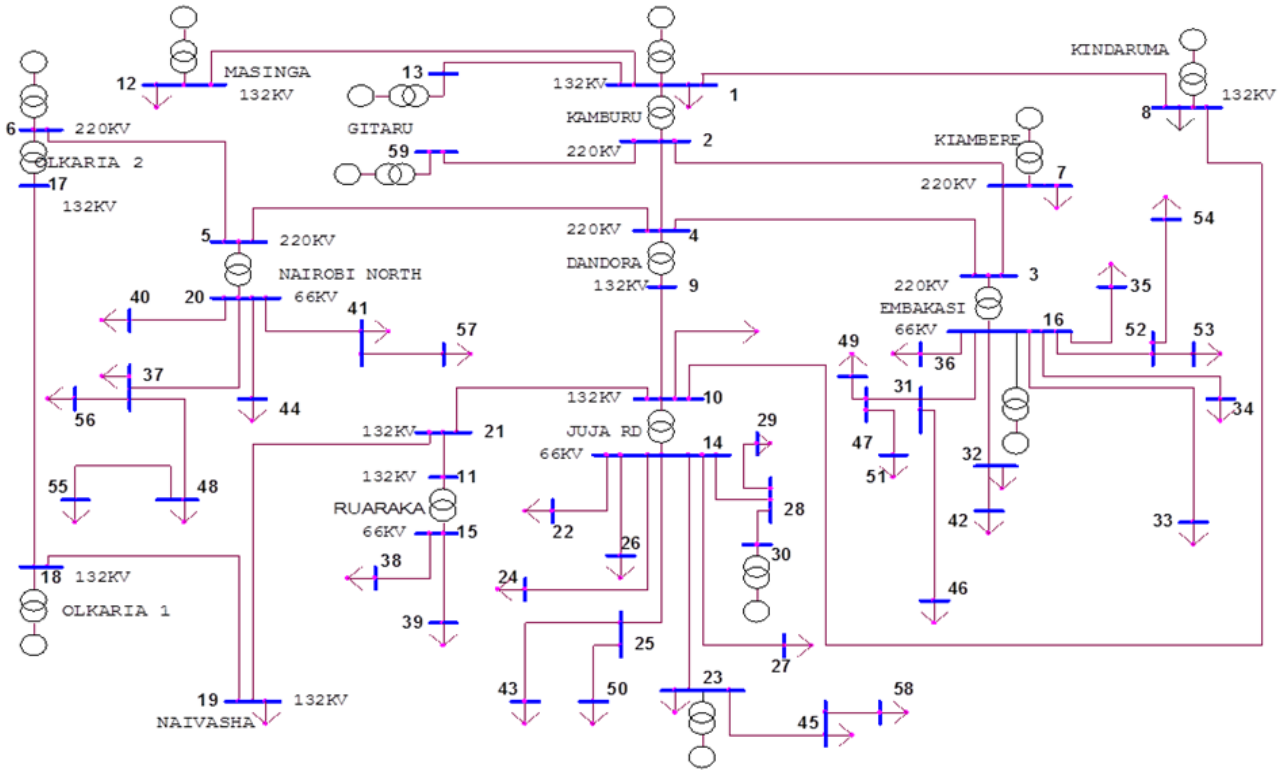

Figure 1: Nairobi Area Power Supply Distribution Network as at July, 2012.

Figures 5 of section IV shows the generator buses with highest generator participation factors in the network.

D. *Determination of Active Power Margins.*

The P-V curves in this research were plotted in PowerFactory DIgSILENT software, after modelling the network shown in Fig 1. The plotting is done by the software based on the principles outlined in section II.

The real power margin is calculated by subtracting the P value at the base operating point from the maximum permissible real power, P_{max} , which is at the collapse point, as illustrated in Fig 2.1 of section II.

Figure 6 of section IV shows the P-V curves for the buses considered weak in the network.

E. *Determination of reactive Power margins*

The data for plotting the Q-V curves were obtained by recording the reactive power demands corresponding to active power increments in part D, until the maximum loading limit is reached.

The reactive power margin, Q is computed by subtracting the Q values at the operating point from the maximum reactive power, Q_{max} which is at the maximum loading limit, as is illustrated in section II. Figure 7 of section IV shows the Q-V curves of the buses considered weak in the network.

IV. Results and Analysis

The buses which are operating outside the recommended voltage criteria are shown in Tables I.

TABLE I
BUSES OPERATING OUTSIDE VOLTAGE CRITERIA

BUS	27	29	42	51	55
VOLT. (P.U)	0.913	0.932	0.936	0.938	0.927

Figure2 shows the buses with the largest Q-V sensitivity factors for the network. Buses with high sensitivity factors are comparatively weaker in the network. The study shows buses 42(Magadi), 55 (Karen), 27 (EPZ) and 48 (Kikuyu) are the most sensitive buses in the network, and therefore weak nodes.

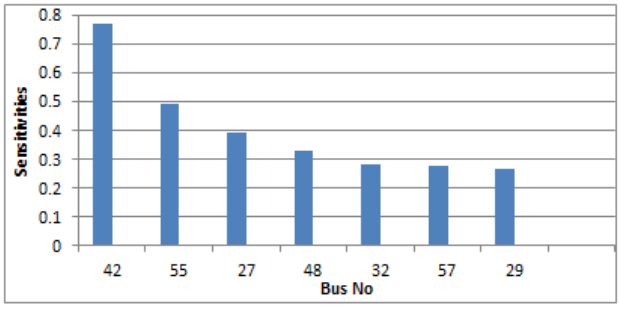

Fig2: Largest Bus sensitivity Factors

Tables II shows the magnitudes of smallest modal eigenvalues. The magnitude of the smallest eigenvalue gives indication of the network proximity to voltage collapse.

TABLE II
THE SMALLEST EIGENVALUE

MODE	30	39	40	33	34	32	31	35
EIGENVALUE	0.7	1.1	2.2	2.6	2.6	3.1	3.3	5.3

Figure3 shows buses with dominant bus participation factors. Buses with high participation factors are weak nodes in the network. The study shows buses 55(Karen), 48(Kikuyu), 56(KPC Ngema) and 57(Gigiri W/Works) are the weak nodes in the network.

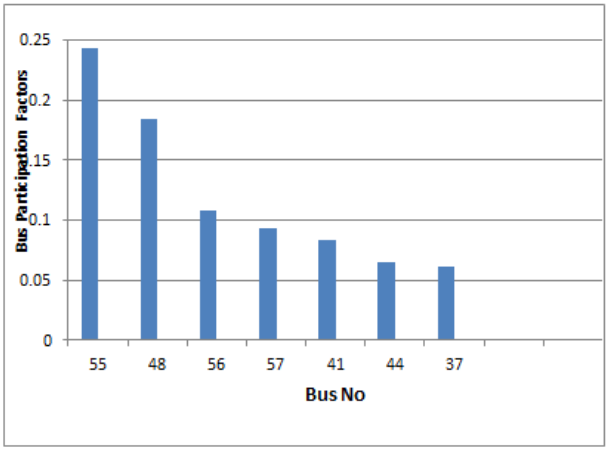

Fig. 3: Largest Bus Participation Factors

Figure 4 shows the network branches which have dominant participation factors. Branches with higher participation factors are weak links in the network. They are either overloaded or consumers of most reactive power. The study shows branches 37-48(Limuru-Kikuyu), 37-20(Limuru-Nairobi North) and 48-55 (Kikuyu-Karen) are the weak links in the network.

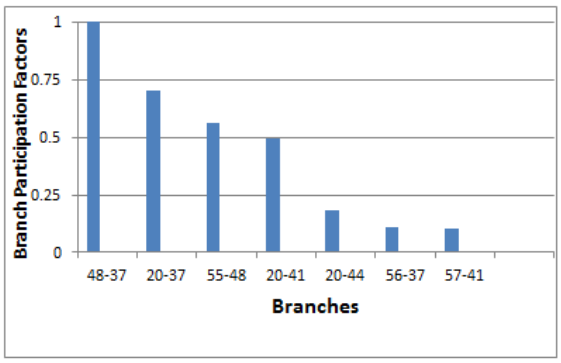

Fig. 4: Largest Branch Participation Factors

Figure 5 shows generator buses with the highest Generator participation factors. The Generators participation factors indicate for each mode, which generators supply the most reactive power in response to the system incremental reactive power loadings. The result shows that generators 6 (Olkaria II) and 7 (Kiambere) have the highest participation factors. These generators are important in maintaining the stability of the critical mode.

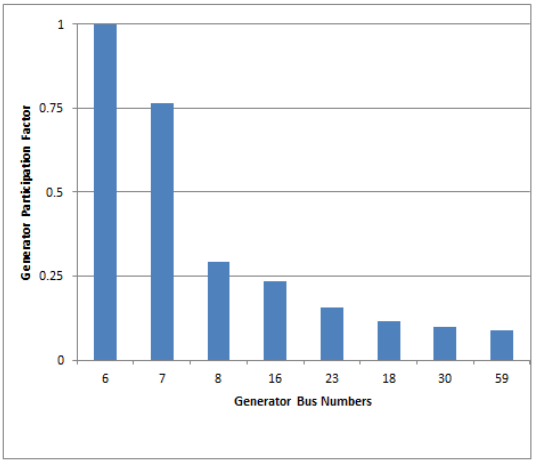

Fig. 5: The Largest Generator Participation factors

Table III shows the active and reactive power margins for the buses considered weak in the network.

TABLE III
ACTIVE AND REACTIVE POWER MARGINS FOR NETWORK WEAK BUSES

Bus No.	Voltage (p.u)	Active Power Margin (MW)	Reactive Power Margin (MVAr)
42	0.936	14.3099	2.9058

55	0.927	51.2375	10.4042
27	0.913	81.2871	16.5084
48	0.947	84.5555	21.2667

Figure 6 shows the P-V curves for the network weak buses. Bus 42 (Magadi) which is located further away from the Bulk supply source at Embaksi has the least active power margin.

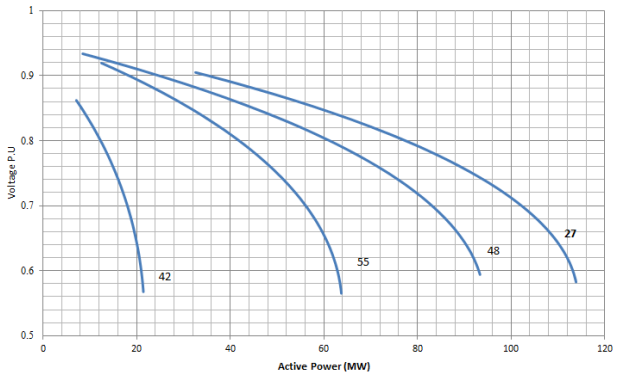

Fig 6: P-V Curves for the network weak buses

Figure 7 shows the Q-V curves for the network weak buses. Again bus 42 has the least reactive power margin.

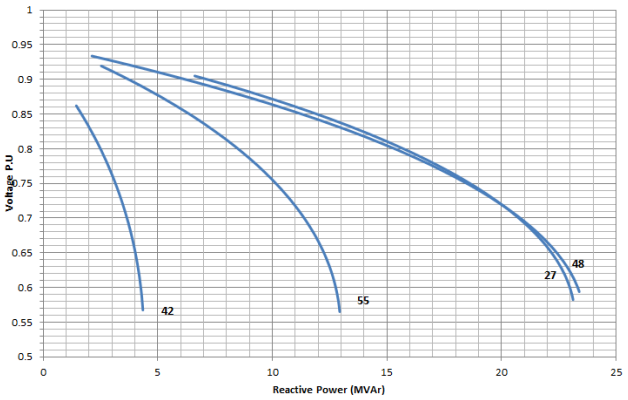

Fig 7: Q-V Curves for the network weak buses

V. Conclusions

Based on this study, the following conclusions can be made

1) The Q-V sensitivity analysis has shown that the Nairobi Area network is voltage stable since all the sensitivity factors are positive and greater than zero. The result showed buses 42 (Magadi), 55(Karen) and 27(EPZ) in the reducing order of sensitivities to have the largest sensitivity factors. These are weak buses in the network.

2) The modal analysis showed that all the eigenvalues are positive and greater than zero. This confirms that the network is indeed voltage stable. However, the minimum eigenvalue was 0.7, which implies operation very close to voltage collapse point.

3) The result of the bus participation factors showed buses 55(Karen), 48 (Kikuyu), and 56 (KPC Ngema) in order of decreasing participations, had the largest participation factors. These are the buses that participate in the critical mode, and therefore they are the weak nodes in the network.

4) The branch participation factors showed the branches (48-37) (Kikiyu-Limuru), (20-37) (Nairobi North-Limuru) and (48-55) (Kikuyu-Karen) in the order of decreasing participations, had the largest participation factors. These are the branches that consume most reactive power when the critical mode is excited. They are therefore the weakest links in the network.

5) The study of P-V curve characteristics of the identified buses provided the active power margins, which is the MW distance to critical voltage point. The analysis showed that bus 42 (Magadi) followed by buses 55 (Karen), 27 (EPZ) and 48 (Kikuyu) in the order of increasing margins, had the least active power margins.

6) The Q-V curve characteristics of the identified buses provided their Reactive power margins, which is their MVAr distance to critical voltage point. The analysis again showed that bus 42(Magadi) followed by buses 55 (Karen), 27 (EPZ) and 48 (Kikuyu) respectively, had the least reactive power margins.

APPENDIX

A. LOAD DATA

BUS NO	**BUS NAME**	**P_L (MW)**	**Q_L (MVAR)**
10	JUJA RD 132kV BUS	3	0.0
19	NAIVASHA 132kV BUS	23.25	8.10
22	BABA DOGO	22.39	7.36
23	NBI SOUTH	59.52	19.56
24	EMCO	25.25	8.29
26	PARKLANDS	44.80	14.72
27	EPZ	32.58	10.71
29	THIKA	37.06	12.17
31	NBI WEST	34.59	12.06
32	MATASIA	9.375	3.26
33	ATHI RIVER	34.21	11.21
34	NEW AIRPORT	14.66	4.82
35	NSSF	30.14	9.90

36	MSA RD	21.99	7.23
37	LIMURU	13.25	4.71
38	RUIRU STEEL MILLS	8.71	3.07
39	RUARAKA	23.36	8.14
40	CIANDA	12.23	3.19
41	KITSURU	15.75	5.49
42	MAGADI	7.13	1.45
43	JIVANJEE	18.5	6.45
44	WESTLANDS	15.75	5.49
45	KPC NBI	1.3	0.66
46	CATHEDRAL	14.06	4.90
48	KIKUYU	8.5	2.1
49	NGONG RD	12.75	4.45
50	KIMATHI	10.73	3.74
51	KILELESHWA	17.25	6.02
53	NEW INDUSTRIAL	26.93	9.39
54	FIRESTONE	2.61	1.26
55	KAREN	12.5	2.50
56	KPC NGEMA	2.16	0.50
57	GIGIRI W/PUMP	3.40	1.74
58	MORRIS & CO	1.00	0.22

B. Generator Data

Bus No.	BUS NAME	V (p.u)	P_G (MW)	Qmax (MVAr)	Qmin (MVAr)
1	KAMBURU	1.090	0	0	0
6	OLKARIA II	1.052	89	69	-33
7	KIAMBERE	1.095	130	40	-16
8	KINDARUMA	1.094	45	8	-1
12	MASINGA	1.093	28	20	-16
13	GITARU 132KV	1.080	73	80	-20
16	EMBAKASI	1.000	60	19.2	0
18	OLKARIA I	1.031	44	15	0
23	NBI SOUTH	1.010	100.5	33	0
30	TANA	1.015	20	6.6	0
59	GITARU 220KV	1.042	60	20	-10

D. Line Data

From Bus	**To Bus**	**R (p.u)**	**X (p.u)**	**$1/2B_C$ (p.u)**
1	8	0.0190	0.0443	0.0086
1	12	0.0076	0.0456	0.0052
1	13	0.0040	0.0093	0.0030
2	4	0.0081	0.0484	0.1389
2	7	0.0074	0.0302	0.0459
3	4	0.0013	0.0054	0.0164
3	7	0.0232	0.1357	0.1939
4	5	0.0009	0.0056	0.0159
5	6	0.0060	0.0377	0.0079
8	10	0.1229	0.2868	0.0558
9	10	0.0004	0.0024	0.0009
10	21	0.0029	0.0060	0.0012
21	19	0.0414	0.0863	0.0323
11	21	0.0009	0.0018	0.0007
18	19	0.0096	0.0572	0.0106
14	22	0.0225	0.0434	0.0006
14	23	0.0084	0.0163	0.0002
14	24	0.0059	0.0110	0.0001
14	25	0.0128	0.0247	0.0003
14	26	0.0372	0.1567	0.0007
14	27	0.1680	0.2887	0.0030
14	28	0.0757	0.1522	0.0019
15	38	0.0492	0.0952	0.0012
15	39	0.0011	0.0020	0.0001
16	31	0.0247	0.0478	0.0006
16	32	0.1395	0.2644	0.0032
16	33	0.0396	0.0766	0.0007
16	52	0.0159	0.03075	0.0004
16	34	0.0120	0.0219	0.0004
16	35	0.0341	0.0621	0.0007
16	36	0.0011	0.0020	0.0001
17	18	0.0012	0.0081	0.0013
20	37	0.02952	0.05712	0.0007
20	40	0.0258	0.0499	0.0006
20	41	0.0572	0.1106	0.0014
20	44	0.0396	0.0766	0.0009
23	45	0.0071	0.0152	0.00022
25	43	0.0128	0.02475	0.00035
25	50	0.0197	0.0381	0.0005
28	29	0.0787	0.1522	0.0019
28	30	0.0877	0.1691	0.0021
31	46	0.0087	0.0093	0.0001
31	47	0.0323	0.0624	0.0008
32	42	0.2214	0.4284	0.0054
37	48	0.0693	0.1340	0.0017
37	56	0.0258	0.0499	0.0006
41	57	0.0258	0.0499	0.0006
45	58	0.0083	0.016	0.0002
47	49	0.0323	0.0634	0.0008
47	51	0.0323	0.0624	0.0008
48	55	0.0693	0.1340	0.0017
52	53	0.0237	0.04585	0.0005
52	54	0.0056	0.01085	0.0001
59	2	0.0040	0.0093	0.0030

ACKNOWLEDGMENT

The authors wish to acknowledge the Engineers at KPLC Nairobi Area System Control Centre, and the operation Engineers based in Nairobi Region for their support.

REFERENCES

[1] M.J.Khani, B.T.Atiyah, K.M Ashem "Computer Aided Stability Analysis in Power System "Journal of Thi-Qar University, Vol.15, 2010.

[2] P. Kundur "Power System Stability and Control" McGraw Hill I, 1994.

[3] M. B Keskin ''Continuation Power Flow and Voltage Stability in Power systems'' MSc Thesis, Middle East Technical University, 2007.

[4] S. Hadi, "Power System Analysis", McGraw-Hill, 2002

[5] V Ajjarapu "Computational Techniques for Voltage Stability assessment and Control" Springer, 2006.

[6] F. Larki, M. Joorabian, H. M. Kelk, M. Pishvaei "Voltage Stability Evaluation of the Khuzestan Power System, Iran Using CPF Method and Modal analysis" Proc. Power and Engineering Conference (APPEEC),2010.

[7] F.A. Althowibi, M.W.Mustafa “Maximum power system Loadability to detect Voltage Collapse” Proc. Power Engineering and Optimization Conference (PEOCO2010), 2010
[8] C.A. Aumuller, T.K. Saha “Determination of Power System Coherent Bus groups by Novel Sensitivity- based Method for Voltage Stability Assessment” IEEE Transactions on Power systems, Vol.18, No.3, August 2003.
[9] C. Reis, A. Andrade, F.P.M. Barbosa “Methods of Preventing Voltage Collapse” Proc. International Conference on Electrical and Electronics Engineering, 2009.
[10] J. Arrillaga, C.P Arnold “Computer Analysis of Power Systems” John Willey & Sons, 1994.
[11] C.A. Aumuller, T.K. Saha “Determination of Power System Coherent Bus groups by Novel Sensitivity- based Method for Voltage Stability Assessment” IEEE Transactions on Power systems, Vol.18, No.3, August 2003.
[12] P. Mustapha, G. Murugesan “Transmission Line Stability Improvement Using TCSC” International Journal of Advanced Engineering Sciences and Technologies, vol. No.3, Issue no.2, 165-173, 2011.
[13] Sitiki Guner, Bulent Bilir, “Analysis of transmission Congestion using power flow solutions” Proc.. 5th IASME/WSEAS international conference on Energy & environment, 2010.
[14] Kenya Electricity Grid Code-Draft One-November, 2004

IMPROVEMENT OF VOLTAGE PROFILE AND POWER SYSTEM LOSS REDUCTION BY USE OF FACTS DEVICES

IRENE MUISYO, C. M. MAINA, ROY ORENGE

muisyoirene@gmail.com, cmaina77@yahoo.com, samroyoin@gmail.com

EEE SEEIE JKUAT, EEE SEEIE JKUAT, EEE DeKUT

P.O. Box 62000 – 00200, Juja, Nairobi, Kenya.

ABSTRACT - Flexible AC Transmission System (FACTS) devices in a power system play an important role in improving the power system performance, both the static and dynamic, reducing losses and the cost of generation. In order to benefit from them, these devices must be located optimally. This paper proposes a method by which optimal location of series and shunt FACTS devices can be achieved, leading to reduction of losses and cost of generation. Congestion rent is used to pinpoint the lines which are more suitable for TCSC location, while benefit factors are used for SVC location. Proposed algorithm is tested on WSCC 9-bus and IEEE 30-bus test systems and results show that with optimal location, FACTS devices can improve the voltage profile, reduce losses and cost of generation.

Keywords — FACTS devices, TCSC, SVC, optimal location

I. INTRODUCTION

Deregulation of the electricity market over the last two decades has led to extensive use of transmission grids. The increase in power demand, scarce natural resources and slow expansion of transmission networks are some factors contributing to transmission systems being operated near their limits.

In the open power market, control of active and reactive power flow in a transmission line becomes a necessity. Entry of more power generation companies has increased the need for secure operation of power systems.

The stable operation of the power system networks revolves around improving voltage profile and minimizing power transmission loss. Minimization of active power losses can also lead to reduction in electricity cost (Rakhmad Syafutra Lubis, 2012).

FACTS devices are said to effectively control power flow, providing the possibility of operating the transmission grid with increased flexibility and efficiency (P R Sharma, 2012) (Rakhmad Syafutra Lubis, 2012) (F. Rezvani Gilkolaee, 2013).

In last two decades, a number of Flexible AC Transmission System (FACTS) devices have been proposed and implemented. These include Static Var Compensator (SVC), Thyristor Controlled Series Capacitor (TCSC) and Unified Power Flow Controller (UPFC). These devices can control power flow in the network, reduce the flow in heavily loaded lines there by resulting to increased load ability, low system losses, improved stability of network and reduced cost of production (Rakhmad Syafutra Lubis, 2012).

A number of studies devoted to the application of FACTS devices are ongoing, with the aim of obtaining the optimal location, type and size of the appropriate device for utilization. (Ch.Rambabu, 2011) uses the Newton-Raphson algorithm for optimal location of FACTS devices in load flow analysis, while (J.Sridevi, 2012) proposes the application of TCSC & SVC for congestion relief and voltage stability under contingencies. The optimal location of TCSC and SVC is determined based on performance index.

Evolutionary techniques have also been proposed for optimization. (Kalaivani R., 2012) uses Particle Swarm Optimization (PSO) and Genetic Algorithm (GA) to find optimal location and value of Static Var Compensator (SVC) which minimizes voltage stability index in power systems. (Amit Debnath, 2013) investigates the effect of UPFC on voltage profile of modified IEEE 30-bus system while Eigen value analysis was employed in (P R Sharma, 2012) to show the performance of UPFC for stability enhancement.

In this paper, optimal location of TCSC is by use of congestion rent method while benefit factors are used for SVC placement. A combined installation is undertaken afterwards, where SVC is given priority. Tests have been performed on WSCC 9-bus and modified IEEE 30-bus systems. It is shown that installing FACTS devices in the proper location will improve voltage profile, reduce losses and cost of generation.

This paper is organised as follow: Section I gives introduction of the work. Section II presents FACTS devices and their mathematical models. Section III presents the proposed algorithm. Section IV shows results and discussion while V concludes the paper.

II. FACTS DEVICES

Power flow can be controlled and optimized by modifying system parameters. This can be achieved by use of FACTS devices. They can act by supplying or absorbing reactive power, or controlling the series impedance or phase-angle. Two types of FACTS have been used in this study: Thyristor Controlled Series Capacitor (TCSC) and Static Var Compensator (SVC).

Mathematical model of FACTS Devices

TCSC is modelled simply to modify the reactance of a transmission line while SVC is modelled using the power injection models (Jigar S.Sarda, 2012). Mathematical models of FACTS devices are implemented in MATPOWER version 2, a toolbox of MATLAB programming language.

a) TCSC model

TCSC is a series compensation component which consists of a series capacitor bank shunted by thyristor controlled reactor. It acts by decreasing or increasing the overall effective series transmission impedance of a line, by adding a capacitive or inductive reactive correspondingly.

In this paper, TCSC is modelled as a variable reactance shown in fig. 1.

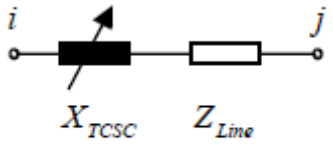

$$X_{TCSC} = X_{Min} \sim X_{Max}$$

Figure 1: TCSC model

As shown in Fig. 1, the reactance of the line can be changed by TCSC as:

$$X_{ij} = X_{Line} + X_{TCSC} \quad (1)$$

$$X_{TCSC} = r_{tcsc} . X_{Line} \quad (2)$$

where X_{Line} is the reactance of the transmission line and r_{tcsc} is the coefficient which represents the compensation degree of TCSC (A. Esmaeili Dahej, 2012).

To avoid overcompensation, the working range of the TCSC is between $-0.7X_{Line}$ and $0.2X_{Line}$

$$r_{tcsc,min} = -0.7, \quad r_{tcsc,max} = 0.2$$

b) SVC model

The primary purpose for SVC application in a transmission network is the rapid control of voltage at weak points in a network. SVC can be used for both inductive and capacitive compensation (Ch.Rambabu, 2011). In this paper SVC is modelled as an ideal reactive power injection at a bus.

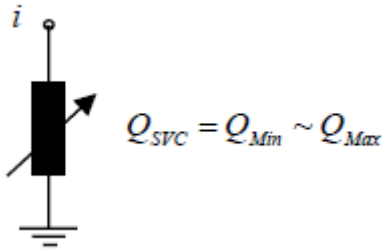

Figure 2: SVC model

III. FORMULATION

The objective function is to obtain the best location and size of FACTS devices in order to minimize cost of generation.

Mathematically, we have:

$$F = min\big(F(P_G)\big) = \sum_{i=1}^{NG} a_i P_{Gi}^2 + b_i P_{Gi} + C_i \quad (3)$$

Subject to

Equality constraints (power balance)

$$P_G = P_D + P_L \quad (4)$$

$$Q_G = Q_D + Q_L \quad (5)$$

Inequality constraints

Real power generating limits: $P_{Gi,min} \leq P_{Gi} \leq P_{Gi,max}$

Reactive power generating limits: $Q_{Gi,min} \leq Q_{Gi} \leq Q_{Gi,max}$

Transmission line limits: $S_{ij} \leq S_{ij\ max} \quad i \neq j$

Voltage limits: $V_{i,min} \leq V_i \leq V_{i,max}$

a) OPTIMAL LOCATION OF TCSC

Transmission lines are many in interconnected systems. Congestion rent can be used to pinpoint lines which are more suitable for TCSC location. Congestion rent is simply the product of Locational Marginal Price (LMP) difference and power flowing through a given line.

The congestion rent of an individual line is

$$CC_{ij} = \Delta\rho_{ij} P_{ij} \quad (6)$$

where P_{ij} is power flow of line $i\,j$ and $\Delta\rho_{ij} = |LMP_i - LMP_j|$

LMP is the Lagrangian multiplier associated with the active power flow equations for each bus in the system, also known as spot price. It is composed of three components, a marginal energy component (same for all buses), a marginal loss component and a congestion component.

$$\rho_i = \lambda + \lambda_{L,i} + \lambda_{C,i} \quad (7)$$

Thus, the price at each bus differs by the loss component and the congestion component (Murillo-Sanchez, 2011) (Hossein Hashemzadeh, 2009).

PROCEDURE

Step 1: Run the base case OPF to calculate the LMPs at all buses and the power flow across all line sections.

Step 2: Obtain the absolute value of LMP difference and calculate congestion rent of individual lines.

Step 3: Form a suitable list of the lines with large congestion rent. For each line in the list, run OPF with TCSC in that line and obtain the value of the objective function and real power loss.

The best location of TCSC is the one which gives the minimum losses and cost of generation (Hossein Hashemzadeh, 2009).

b) OPTIMAL LOCATION OF SVC

The SVC should be placed at a bus with the highest benefit factor in terms of loss and voltage. Placement of SVC is considered for load buses only. Two benefit factors are obtained:

I. Voltage Benefit Factor (VBF)

$$VBF_i = \sum_i \frac{(V_i(Q_{si}) - V_{io})}{Q_{si}}\ x\ 100\% \quad i \in n \quad (8)$$

where $V_i(Q_{si})$ and V_{io} is the voltage magnitude at load bus i, with and without VAR compensation respectively and Q_{si} is the amount of VAR support in the bus. n is the number of load buses.

II. Loss Benefit Factor (LBF)

$$LBF_i = \sum_i \frac{\big(P_{Lo} - P_L(Q_{si})\big)}{Q_{si}}\ x\ 100\% \quad i \in n \quad (9)$$

where $P_L(Q_{si})$ and P_{Lo} is the power transmission loss in the system with and without VAR compensation respectively (Zhu, 2009), (Jigar S.Sarda, 2012), (J.Vivekananthan, 2013). The optimal location is obtained by weighting the two factors.

CASE STUDY

WSCC 9-bus and the modified IEEE 30-bus system whose data is found in (Zhu, 2009), (Murillo-Sanchez, 2011) were used to test the effectiveness of the proposed method.

IV. RESULTS AND DISCUSSION

Simulations were done for four different scenarios in both systems.
Scenario 1: normal operation (without FACTS devices).
Scenario 2: one TCSC optimally placed.
Scenario 3: one SVC optimally placed.
Scenario 4: both TCSC and SVC optimally placed.

a) WSCC 9-BUS SYSTEM

This system has 9 lines and 6 load buses. A priority list for TCSC location is formed with four candidate lines, which are then tested and optimal location identified. Among 9 lines in WSCC 9-bus system, the top four candidates selected for TCSC placement by use of congestion rent method are lines 4, 6, 7 and 8, and results obtained are shown in table 1.

Load buses are evaluated for SVC placement and the optimal location obtained too.

	Compensation	Loss (MW)	Generation Cost ($/hr)
Line 4	-70%	11.984	12677.50
Line 6	-30%	12.211	12686.36
Line 7	-30%	12.168	12684.93
Line 8	-60%	12.183	12685.66

Table 1: Location candidates for TCSC placement

Among the candidates, line 4 gives the minimum cost of generation and lowest value of total system loss, hence it is the optimal location for TCSC.

SVC placement

SITE	VBF	LBF	AHP WEIGHTS
Bus 4	0.001453	0.003917	0.127922
Bus 5	0.002176	0.012744	0.249117
Bus 6	0.00215	0.009415	0.219598
Bus 7	0.00137	0.004973	0.131354
Bus 8	0.001795	0.005784	0.165977
Bus 9	0.001241	0.002955	0.106004

Table 2: Location candidates for SVC placement

Below is a summary of the system operation with device location, size, corresponding loss and cost of generation.

Device	Site	Size
None	-	-
TCSC	Line 4	Xline = 0.0255 p.u
SVC	Bus 5	QSVC= 106.64 MVAR
TCSC & SVC	TCSC line 8, SVC bus 5	Xline = 0.0255 p.u, QSVC =105.36 MVAR

Device	Loss (MW)	Generation cost ($/hr)
None	12.247	12688.26
TCSC	11.985	12677.50
SVC	10.889	12632.40
TCSC & SVC	10.862	12631.40

Table 3 & 4: Summary of system loss and cost of generation with FACTS devices

In WSCC 9-bus system, the first simulation without any compensation has the highest system loss and cost of generation. Scenario 2 which utilizes TCSC alone has the best location for TCSC as line 4, and both loss and cost of generation goes down. Scenario 3 which utilizes SVC alone has bus 5 as the appropriate location for SVC, loss and cost of generation go down too. For scenario 4, SVC is placed in the optimal location, the TCSC located afterwards. Voltage profile is shown in fig 3.

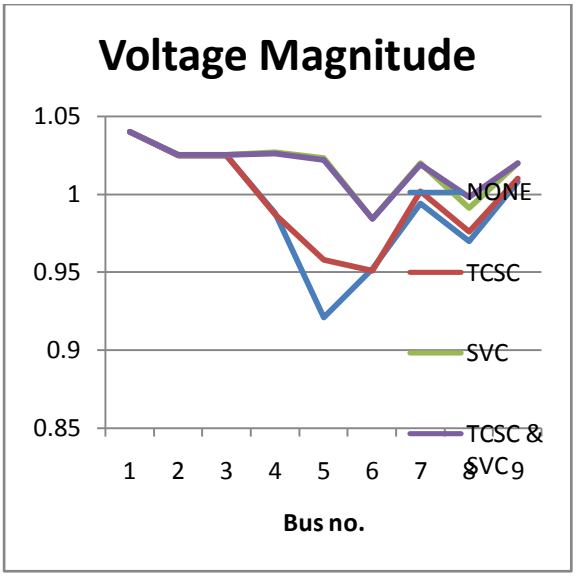

Figure 3: WSCC 9-bus system Voltage magnitude plot

Voltage magnitude of the system is plotted for different scenarios. Results in fig. 3 show that installing TCSC slightly improves the voltage profile and reduces losses. SVC gives much better results while a combination of both give the best results. Bus 5 has the lowest voltage magnitude of 0.921p.u., which significantly goes up after system compensation.

b) IEEE 30-BUS SYSTEM

OPTIMAL LOCATION OF TCSC

Among 41 lines in this system, the top 8 candidates selected for TCSC placement by use of congestion rent method are shown in table 5.

Line	Compensation (%)	Generation cost ($/hr)	Total losses (MW)
1	20%	1017.96	12.743
2	-10%	1017.98	12.749
3	20%	1017.96	12.744
4	-70%	1017.99	12.75
5	-30%	1017.62	12.69
6	20%	1017.9	12.728
9	20%	1017.92	12.733
18	10%	1018.03	12.762

Table 5: Candidate lines for TCSC placement

Line 5 is the best location for TCSC location.

SVC PLACEMENT

Benefit factors are obtained in a similar manner for modified IEEE 30-bus system. The optimal location for SVC is bus 26 as it has the highest voltage and loss benefit factors.

Below is a summary of the system operation with device location, size, corresponding loss and cost of generation.

Device	Site	Size
None	-	-
TCSC	Line 5	Xline = 0.013881 p.u
SVC	Bus 26	QSVC = 4.96 MVAR
TCSC & SVC	TCSC line 5, SVC bus 26	Xline = 0.013881 p.u, QSVC=4.94MVAR

Device	Loss (MW)	Cost of generation ($/hr)
None	12.763	1018.04
TCSC	12.658	1017.62
SVC	12.662	1017.65
TCSC & SVC	12.559	1017.23

Table 6 & 7: Summary of system loss and cost of generation with FACTS devices

Similarly, the voltage magnitude of the system is plotted below for the various scenarios.

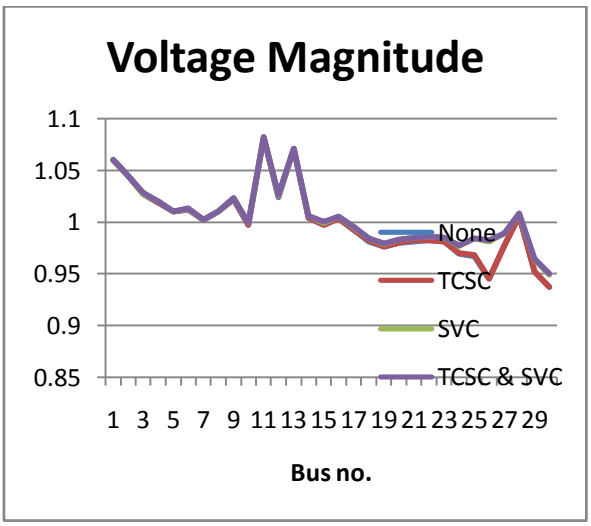

Figure 4: Modified IEEE 30-bus system Voltage magnitude plot

Without FACTS devices, the lowest voltages are in bus 26 (0.945p.u.) and bus 30 (0.937p.u.), which increase to 0.982p.u. and 0.95p.u., respectively, when either SVC or both SVC and TCSC are installed.

V. CONCLUSION

This paper gives an idea on application of TCSC and SVC in power systems for voltage improvement, loss reduction and cost of generation reduction. Their individual contribution towards the improvement of voltage profile and reduction of power losses has been tested on WSCC 9-bus and IEEE 30-bus systems. The performance of SVC on the system, when located optimally is considered to be good while a combination of both devices is the best choice in terms of voltage profile, power loss and cost of generation.

REFERENCES

A. Esmaeili Dahej, S. E. (2012). Optimal Allocation of SVC and TCSC for Improving Voltage Stability and Reducing Power System Losses using Hybrid Binary Genetic Algorithm and Particle Swarm Optimization. *Canadian Journal on Electrical and Electronics Engineering* , 100-108.

Amit Debnath, C. N. (2013). Voltage Profile Analysis for IEEE 30 Bus System Incorporating with UPFC. *International Journal of Engineering and Advanced Technology* , 763-769.

Ch.Rambabu, D. D. (2011). Improvement of Voltage Profile and Reduce Power System Losses by using Multi Type Facts Devices. *International Journal of Computer Applications* , 37-42.

F. Rezvani Gilkolaee, S. H. (2013). Optimal Placement of TCSC and SVC for Enhancement of ATC and Improvement of Contingency Using Genetic Algorithm. *African Journal of Basic & Applied Sciences* , 156-60.

Hossein Hashemzadeh, S. H. (2009). Locating Series FACTS Devices Using Line Outage Sensitivity Factors and Particle Swarm Optimization for Congestion Management. *Power & Energy Society General Meeting*, (pp. 1-6). Calgary, AB.

J.Sridevi, J. G. (2012). ROLE OF FACTS DEVICES ON ZONAL CONGESTION MANAGEMENT ENSURING VOLTAGE STABILITY UNDER CONTINGENCY. *International Journal of Advances in Engineering & Technology* , 635-642.

Jigar S.Sarda, V. N. (2012). Genetic Algorithm Approach for Optimal location of FACTS devices to improve system loadability and minimization of losses. *International Journal of Advanced Research in Electrical, Electronics and Instrumentation Engineering* , 114-126.

Kalaivani R., V. K. (2012). Enhancement of Voltage Stability by Optimal Location of Static Var Compensator Using Genetic Algorithm and Particle Swarm Optimization. *American Journal of Engineering and Applied Sciences* , 70-77.

Murillo-Sanchez, R. D. (2011). *Matpower 4.1 User's Manual*. Washington: Power Systems Engineering Research Center.

P R Sharma, A. D. (2012). Location of SVC and UPFC for Real Power Loss Minimization and Stability Enhancement in a Multi Machine Power System using Parametric Approach. *International Journal on Advanced Electrical and Electronics Engineering* , 84-89.

Rakhmad Syafutra Lubis, S. P. (2012). Selection of Suitable Location of the FACTS Devices for Optimal Power Flow. *International Journal of Electrical & Computer Sciences* , 38-50.

S. B. Bhaladhare, P. B. (2012). Enhancement of Voltage Stability through Optimal Location of SVC. *International Journal of Electronics and Computer Science Engineering* , 671-678.

Zhu, J. (2009). *OPTIMIZATION OF POWER SYSTEM OPERATION*. New Jersey: John Wiley & Sons, Inc.

Nature Inspired Metaheuristic Optimization: A New Approach to Load Shedding

Charles Mwaniki[1]; Christopher Muriithi Maina[2]; Nicodemus Abungu[3]

[1]Electrical & Electronic Engineering Department, Thika Technical Training Institute,
P. O. Box 91-01000, Thika Kenya

[2]Electrical & Electronic Engineering Department, Jomo Kenyatta University of Agriculture and Technology,
P. O. Box 62000-00200, Nairobi Kenya

[3]Electrical & Electronic Engineering Department, University of Nairobi
P.O. Box 30197-00200, Nairobi, Kenya

e-mail:mwanikicharles2005@yahoo.com; cmmuriithi@eng.jkuat.ac.ke; abunguodero@uonbi.ac.ke

Abstract- Voltage stability has become a serious threat of modern power system operation nowadays. To tackle this problem properly, load shedding is one of the effective countermeasures. However, its consequences might result in huge technical and economic losses. Therefore, this control measure should be optimally and carefully carried out. Conventional methods of system load shedding are too slow and do not effectively calculate the correct amount of load to be shed. This results in either excessive or insufficient load reduction. Metaheuristic algorithms are becoming an important part of modern optimization. A wide range of Metaheuristic algorithms have emerged over the last two decades. This paper presents an overview of the extent to which metaheuristic algorithms have been utilized in optimal under frequency and under voltage load shedding**.**

Key-Words: - Cuckoo search, Metaheuristic optimization, Unconstrained optimization, Nature inspired algorithms

1. INTRODUCTION

Because of computational drawbacks of conventional numerical methods in solving complex optimization problems, researchers may have to rely on new algorithms. Heuristic algorithms typically intend to find a good solution to an optimization problem by 'trial-and-error' in a reasonable amount of computing time. Here 'heuristic' means to 'find' or 'search' by trials and errors. There is no guarantee to find the best or optimal solution, though it might be a better or improved solution than an educated guess. Any reasonably good solution, often suboptimal or near optimal, would be good enough for such problems. Broadly speaking, local search methods are heuristic methods because their parameter search is focused on the local variations, and the optimal or best solution can be well outside this local region. Metaheuristic algorithms are higher-level heuristic algorithms. Here, 'meta-' means 'higher-level' or 'beyond', so metaheuristic means literally to find the solution using higher-level techniques, though certain trial-and-error processes are still used. Broadly speaking, metaheuristics are considered as higher-level techniques or strategies which intend to combine lower-level techniques and tactics for exploration and exploitation of the huge space for parameter search [1-4].

There are two important components in modern metaheuristics, and they are: intensification and diversification, and such terminologies are derived from Tabu search . For an algorithm to be efficient and effective, it must be able to generate a diverse range of solutions including the potentially optimal solutions so as to explore the whole search space effectively, while it intensifies its search around the neibourhood of an optimal or nearly optimal solution. In order to do so, every part of the search space must be accessible though not necessarily visited during

the search. Diversification is often in the form of randomization with a random component attached to a deterministic component in order to explore the search space effectively and efficiently, while intensification is the exploitation of past solutions so as to select the potentially good solutions via elitism or use of memory or both [4-6].

Any successful metaheuristic algorithm requires a good balance of these two important, seemingly opposite, components [6]. If the intensification is too strong, only a fraction of local space might be visited, and there is a risk of being trapped in a local optimum, as it is often the case for the gradient-based search such as the classic Newton-Raphson method. If the diversification is too strong, the algorithm will converge too slowly with solutions jumping around some potentially optimal solutions. Typically, the solutions start with some randomly generated, or educated guess, solutions, and gradually reduce their diversification while increase their intensification at the same time, though how quick to do so is an important issue.

Another important feature of modern metaheuristics is that an algorithm is either trajectory-based or population-based. In trajectory-based algorithm, the path of the active search point (or agent) forms a Brownian motion-like trajectory with its movement towards some attractors. In population based algorithm, the parameter search is carried out by multiple agents in parallel. It is difficult to decide which type of method is more efficient as both types work almost equally successfully under appropriate conditions. A good combination of these two would lead to better metaheuristic algorithms.

2. NATURE INSPIRED METAHEURISTIC ALGORITHM

The naturally inspired metaheuristic algorithm includes genetic algorithms (GA), particle swarm optimization (PSO), simulated annealing (SA), ant colony optimization (ACO), bee algorithms (BA), harmony search (HS), firefly algorithms (FA), photosynthetic algorithm (PA), enzyme algorithm (EA) and Tabu search

3. APPLICATION OF METAHEURISTIC ALGORITHMS IN OPTIMAL LOAD SHEDDING.

In recent years, the word ‘metaheuristics’ refers to all modern higher-level algorithms [4], including Particle Swarm Optimization (PSO), Simulated Annealing (SA), Evolutionary Algorithms (EA) including Genetic Algorithms (GA), Tabu Search (TS), Ant Colony Optimization (ACO), Bee Algorithms (BA), Firefly Algorithms (FA), and, certainly Harmony Search (HS) and Cackoo search (CS)

Over the last decades, many meta-heuristic algorithms have been successfully applied to various engineering optimization problems. For most complicated real-world optimization problems, they have provided better solutions in comparison with conventional numerical methods. In regard to optimal load shedding the following nature inspired algorithm have been applied [1-4].

3.1 PARTICLE SWARM OPTIMIZATION

A new particle swarm optimization based corrective strategy to alleviate overloads of transmission lines is presented [6]. A direct acyclic graph (DAG) technique for selection of participating generators and buses with respect to a contingency is presented. Particle swarm optimization (PSO) technique has been employed for generator rescheduling and/or load shedding problem locally, to restore the system from abnormal to normal operating state. The effectiveness of the proposed approach is demonstrated for different contingency cases in IEEE 57 and modified IEEE 118 bus systems. The result shows that the proposed approach is computationally fast, reliable and efficient, in restoring the system to normal state after a contingency with minimal control actions.

Congestions or overloads in transmission network are alleviated by generation rescheduling and/or load shedding of participating generators and loads. The two

conflicting objectives 1) alleviation of overload and 2) minimization of cost of operation are optimized to provide pareto-optimal solutions. A multiobjective particle swarm optimization (MOPSO) method is used to solve this complex nonlinear optimization problem. A realistic frequency and voltage dependent load flow method which considers the voltage and frequency dependence of loads and generator regulation characteristics is used to solve this problem. The proposed algorithm is tested on IEEE 30-bus system, IEEE 118-bus system, and Northern Region Electricity Board, India (NREB) 390-bus system with smooth as well as nonsmooth cost functions due to valve point loading effect [7].

An optimal load shedding approach to enhance voltage stability employing a combination of modal analysis and particle swarm optimization (PSO) is presented[8],[19]. At first as a preventive control action the best transformers tap setting is indicated by PSO optimization to get the most possible voltage stability margin then as a corrective control action after contingencies the proposed approach is organized as a multi-objective optimization problem which reveals the best location and the lowest level of load shedding for special protection systems (SPS) in the direction of improving the voltage stability margin as well as the voltage profile.

A new optimization model to minimize power loss and the load curtailments necessary to restore the equilibrium of operating point is proposed [9]. The solution algorithm is based on the particle swarm optimization (PSO) method in which the load shedding would be considered as the penalty in the optimization cost function. The aim function would be optimized for minimum power loss under normal operating conditions and minimum load shedding during emergency conditions. In contrary to the other load shedding

A method for optimal allocation of fast and slow VAR devices using particle swarm optimization under different load levels is proposed [10]. These devices are supposed to be utilized to maintain system security in normal and contingency states, where corrective and preventive controls are implemented for the contingency cases. Load shedding and fast VAR devices are used in the corrective state in order to quickly restore system stability even they are expensive, while cheap slow VAR devices can be used in the preventive state to obtain the desired security level.

An approach to optimally allocate FACTS devices based on Expected Security Cost Optimal Power Flow (ESCOPF) under deregulated power system is proposed. The aims of the approach are both to minimize device investment cost and to maximize benefit defined as difference between Expected Security Cost (ESC) with and without FACTS installation. The problem is solved using Particle Swarm optimization (PSO) for attaining optimal FACTS allocation [11-13].

An automatic learning framework for the dynamic security control of a power system is presented. The proposed method employs a radial basis function neural network (RBFNN), which serves to assess the dynamic security status of the power system and to estimate the effect of a corrective control action applied in the event of a disturbance. Particle swarm optimization is applied to find the optimal control action, where the objective function to be optimized is provided by the RBFNN. The method is applied on a realistic model of the Hellenic Power System and on the IEEE 50-generator test system, and its added value is shown by comparing results with the ones obtained from the application of other machine learning methods [14].

3.2 GENETIC ALGORITHM

A new optimization approach for planning under-frequency load shedding using a variant of a genetic algorithm (GA) is described. The load shedding strategy consists of a given sequence of feeder disconnections, minimizing

total load curtailment while taking into account load dynamic characteristics [15-16].

A genetic algorithm (GA) is employed to search for the optimal supply restoration strategy in distribution networks. An 'integer permutation' encoding scheme is adopted in which each chromosome is a list of indices of switches. The status of each of these switches is decided according to graph theory subject to the radiality constraint of the distribution networks. Each chromosome then maps to a feasible network topology. A special gene '0' is also introduced into the chromosome. Instead of representing a switch, this is a flag that keeps some parts of the network disconnected enabling the GA to find the optimal load shedding strategy where necessary [17].

A novel planning method using genetic algorithm (GA) to achieve minimization of load shedding is proposed. The frequency of a power system declines rapidly when generator outage occurs. The general solution is to install sufficient under-frequency relays to pull frequency back to normal range. In this study, a single machine infinite bus (SMIB) is utilized to simulate system load with genetic algorithm for estimating the optimal load shedding and shedding ratio in each stage. Simulated results indicate that the proposed GA-based method is both feasible and effective to facilitate optimal load shedding planning [18].

3.3 ANT COLONY OPTIMIZATION

An ant colony optimization (ACO) based algorithm for solving the optimal load shedding problem is proposed. Two principal concerns of the problem are addressed. The appropriate load buses for the shedding are identified by sensitivities of voltage stability margin with respect to the load change at different buses. Then, the amount of load shedding at each bus is determined by applying ACO to solve a nonlinear optimization problem formulated in the optimal power flow framework. The performance of the proposed ACO based method is illustrated with a critical operating condition of the IEEE 30-bus test system [19].

4. DISCUSSION AND CONCLUSION

From the literature review described above it is evident that researchers have developed new optimization methods by imitating natural or behavioral phenomena on earth. The most commonly used metaheuristic being the particle swarm optimization. Genetic Algorithm and ant colony optimization have also been applied though not intensively. Although the HS algorithm has not been utilized at all in load shedding optimization, it has been successfully applied to a wide variety of practical optimization problems like pipe-network design [20], structural optimization [21], vehicle routing problem [22], combined heat and power economic dispatch problem [23], and scheduling of multiple dam system [24]. The Cuckoo search (CS) also has not been applied in optimization of load shedding. It is a newly evolved metaheuristic algorithm developed recently by Xin-She Yang and Suash Deb in 2009 [25]. It was proven in [18] that the CS was more generic and robust than the
PSO and GA in optimizing multimodal objective functions. Through simulations running on various standard test functions, CS was found to be more efficient in finding the global optima with higher success rates. This is partly due to the fact that there are fewer parameters to be fine-tuned in CS than in PSO and GA [26]. To the best of our knowledge, so far, CS was successfully used for mechanical engineering problems, which were spring design optimization and welded beam design [27]. Hence, CS has a great potential also to be as an effective alternative besides other evolutionary algorithms in handling load shedding optimization problems. There is therefore need for a research to be carried out to establish its feasibility in optimal load shedding.

5. REFERENCES

[1] Yang XS (2008) Mathematical Optimization: From Linear Programming

to Metaheuristics, Cambridge Int. Science Publishing, UK.

[2] Yang XS (2005) Biology-derived algorithms in engineering optimization. Handbook o]f Bioinspired Algorithms and Applications, Eds Olarius S and Zomaya A, Chapman & Hall/CRC

[3] Yang XS (2008) Nature-inspired Metaheuristic Algorithms. Luniver Press

[4] Glover F and Laguna M (1997) Tabu Search. Kluwer Academic Publishers

[5] Rad, B.F. ; Abedi, M. , "An optimal load-shedding scheme during contingency situations using meta-heuristics algorithms with application of AHP method", Optimization of Electrical and Electronic Equipment (OPTIM); 2008 , Page(s): 167 - 173

[6] Maharana, M.K., Swarup, K.S, "Particle Swarm Optimization based corrective strategy to alleviate overloads in power system" Nature & Biologically Inspired Computing, 2009. Pg 37 - 42

[7] Hazra, J. ; sinha, A. ,"Congestion management using multiobjective particle swarm optimization" Power and Energy Society General, 2008 IEEE , Pg: 1

[8] Jalilzadeh, S.; Hosseini, S.H.; Derafshian-Maram, M.,"Optimal load shedding to prevent voltage instability based on multi-objective optimization using modal analysis and PSO" Ultra Modern Telecommunications and Control Systems and Workshops (ICUMT), 2010 Page(s): 371 – 376

[9] He, Fei ; Wang, Yihong ; Ka Wing Chan ; Zhang, Yutong ; Shengwei Mei, "Optimal load shedding strategy based on particle swarm optimization" Advances in Power System Control, Operation and definition of optimal load shedding strategies" Electric Power Engineering, 1999

[17] Luan, W.P.; Irving, M.R.; Daniel, J.S., "Genetic algorithm for supply restoration and optimal load shedding in power system Management (APSCOM), 2009 , Page(s): 1 – 6

[10] Eghbal, M. ; El-Araby, E.E. ; Ito, Y. ; Zoka, Y. ; Yorino, N. , "A PSO Approach for VAR Planning Considering the Slow and Fast VAR Devices Prices", Systems, Man and Cybernetics(SMC), 2006, Page(s): 1849 - 1854

[11] Wibowo, R.S.; Yorino, N.; Zoka, Y.; Sasaki, Y.; Eghbal, M., "FACTS Allocation Based on Expected Security Cost by Means of Hybrid PSO" Power and Energy Engineering Conference (APPEEC), 2010, Page(s): 1 – 4

[12] Eghbal, M.; El-Araby, E.E.; Yorino, N.; Zoka, Y., "Application of metaheuristic methods to reactive power planning: a comparative study for GA, PSO and EPSO", Systems, Man and Cybernetics, 2007. Page(s): 3755 - 3760

[13] Eghbal, M. ; Yorino, N. ; El-Araby, E.E. ; Zoka, Y. , "Multi-load level reactive power planning considering slow and fast VAR devices by means of particle swarm optimisation" Generation, Transmission & Distribution, IET Volume: 2 , Issue: 5 ,2008 , pg 743 – 751

[14] Voumvoulakis, E.M.; Hatziargyriou, N.D., "A Particle Swarm Optimization Method for Power System Dynamic Security Control", Power Systems, IEEE Transactions Volume: 25 , Issue: 2 ; 2010 , Page(s): 1032 – 1041

[15] Mozafari, B.; Amraee, T.; Ranjbar, A.M., "An Approach for Under Voltage Load Shedding Using Particle Swarm Optimization ", Industrial Electronics, 2006 IEEE International Symposium ; 2006 , Page(s): 2019 – 2024

[16] Lopes, J.A.P.; Wong Chan Wa; Proenca, L.M. , "Genetic algorithms in the distribution networks" Generation, Transmission and Distribution, 2002, Page(s): 145 - 151

[18] Chao-Rong Chen ; Wen-Ta Tsai ; Hua-Yi Chen ; Ching-Ying Lee ; Chun-Ju Chen ; Hong-Wei Lan, "Optimal load shedding

planning with genetic algorithm", 2011 , Page(s): 1 - 6

[19] Nakawiro, W.; Erlich, I. "Optimal Load Shedding for Voltage Stability Enhancement by Ant Colony Optimization" Intelligent System Applications to Power Systems, 2009, Page(s): 1 - 6

[20] Z.W. Geem, J.H. Kim, and G.V. Loganathan, "Harmony search optimization: application to pipe network design", Int. J. Model. Simul, 22,(2), 125–133, 2002.

[21] K. S. Lee and Z.W. Geem, "A new structural optimization method based on the harmony search algorithm", Computers and Structures, 82, pp. 781–798, Elsevier, 2004.

[22] Z. W. Geem, K. S. Lee, and Y. Park, "Application of harmony search to vehicle routing", American Journal of Applied Sciences, 2(12), 1552-1557, 2005.

[23] A. Vasebi, M. Fesanghary, and S. M. T. Bathaeea, "Combined heat and power economic dispatch by harmony search algorithm", International Journal of Electrical Power and Energy Systems, Vol. 29, No. 10, 713-719, Elsevier, 2007.

[24] Z. W. Geem, "Optimal scheduling of multiple dam system using harmony search algorithm", Lecture Notes in Computer Science, Vol. 4507, 316-323, Springer, 2007.

[25] Cuckoo search. vol. 2011: Wikipedia, 2010.

[26] Yang, X.-S., Deb, S. Cuckoo Search via Lévy flights. In Proc.World Congr. on Nature & Biologically Inspired Computing (NaBIC 2009). India, 2009, p. 210-214.

[27] Yang, X.-S., Deb, S. Engineering optimization by cuckoo search. Int. J. Mathematical Modelling and Numerical Optimization, Dec 2010, vol. 1, no. 4, p. 330-343.

Analysis of Approximation Models of Power Coefficient Parameter in Variable Speed Wind Turbine Modeling

Ndirangu J.G[1], Nderu J.N[1], Muriithi C.M[1], Muhia A.M[2]
julzndirangu@gmail.com, adjainderuac@gmail.com,cmaina77@yahoo.com,ammuhia@gmail.com
[1]Department of Electrical and Electronic Engineering, Jomo Kenyatta University of Agriculture and Technology
[2]Department of Electrical and Electronic Engineering, Dedan Kimathi University of Technology

Abstract – Modeling a wind turbine is important in understanding its behavior especially for developing a controller for maximum power point tracking. The relationship between the various variables in a wind turbine and its output power constitutes the mathematical model of the wind turbine. Among these variables, the power coefficient is the most important especially for maximum power point tracking. It is a non linear function of tip speed ratio and blade pitch angle. This paper undertakes a survey of various numerical approximation models that have been proposed for the power coefficient parameter for given values of tip speed ratio and blade pitch angle. Maximum power point curves are then simulated using MATLAB and compared for the various models for a case study variable speed wind turbine. Simulation results and analysis show that one of the approximation models is the most appropriate for the case study wind turbine. This analysis will assist in development of a comprehensive control algorithm for maximum power point tracking for the variable speed wind turbine.

Keywords –wind turbine, power coefficient, maximum power point, tip speed ratio.

INTRODUCTION

Even though renewable energy is a good substitute for conventional sources, there is some skepticism associated with their performance and cost. Researchers have been working to address these concerns. A unique limitation of wind energy conversion systems is their inability to track peak power production efficiently at varying wind speeds. This has led to control algorithms referred to as Maximum power point (MPPT) algorithms[1].

MPPT involves optimizing the generator speed relative to the wind velocity intercepted by the wind turbine such that power extracted is maximized. MPPT methods can broadly be classified into those that use sensors and those that are sensorless. The sensorless methods track the maximum power point by monitoring the power variation [2], [3].

Methods that use sensors track maximum power point by control of rotor speed and torque to keep tip speed ratio at an optimal value. Tip speed ratio is the ratio of tip speed of rotor blades to the wind speed.

Sensorless MPPT methods have poor dynamic characteristics because they are not usually sensitive to variations in wind speed. Due to the non-negligible inertia of the wind turbine, the power output changes a bit lazily compared to change in wind speed, this challenge is overcome by the methods that use sensors since they directly measure the wind turbine speed and give the control reference instantaneously. However these methods require the characteristic of the wind turbine to be known.

Wind turbines may be variable pitch or fixed pitch meaning blades may or may not be able to rotate along their longitudinal axes [4]. For small wind turbines typically less than 10kW, the blade pitch is usually fixed to minimize design cost. They can also be variable or fixed speed. Variable speed wind energy systems have several advantages compared with fixed speed wind energy systems such as yielding maximum power output, developing low amount of mechanical stress, improving efficiency and power quality.

Maximizing power output from a wind turbine requires maximizing the power coefficient C_p for the varying wind speeds. Power coefficient is the ratio of the mechanical power at the turbine shaft to the power available in the wind, given as a function of tip speed ratio. To understand the behavior of C_p, numerical approximation models are used to simulate it for analysis. This paper carries out a comparison of several of these approximation models with the aim of

finding the appropriate one for a case study wind turbine.

According to [5],model validation involves defining the model and model structure to be used for modeling the device under study, collecting recorded or measured data from the actual device to be modeled, simulating the same events/ tests as occurred / forced during data collection using the model and then comparing the simulated results to recorded/ measured results.

WIND TURBINE MODELLING

Dynamic modeling and simulation is required to determine the effectiveness of a control strategy before deployment of a system.

The power extracted from the wind by a wind turbine rotor can be expressed as:

$$P_m = \frac{1}{2}\rho\pi R^2 v^3 C_p \quad (1)$$

Where

ρ = air density
R = radius of the rotor,
v = wind speed and
C_p = Power coefficient.

C_p represents the percentage of power available in the wind that is converted into mechanical power. It is a non linear function of the tip speed ratio λ as well as the blade pitch angle β i.e

$$C_p = C_p(\lambda, \beta) \quad (2)$$

Where

$\lambda = \frac{R\omega}{v}$ and

ω = rotation speed of the rotor.

The blade pitch angle is defined as the angle between the plane of rotation and the blade cross-section chord. As earlier stated, for small wind turbines, the blasé pitch angle is usually fixed.

A maximum for the function in equation (2) is known as Beltz limit. $C_{pmax} = 0.593$ [3]

This is the maximum possible turbine power coefficient. From equation (1) above, when controlling the wind turbine for power output maximization, C_p is useful as it is the only variable and controllable parameter. Wind speed v is a variable but not controllable.

There is a value of λ for which C_p is maximum, therefore yielding maximum power for a given wind speed v.

Because of the relationship between C_p and λ for each wind velocity, there is a turbine speed that gives maximum output power.

Modelling is essential in developing a controller for maximum power point tracking.

Various authors have proposed different numerical approximation models for the power coefficient parameter Cp for given values of λ and β . For a fixed pitch wind turbine as is the case with our case study wind turbine, β is set to a constant value.

The author in [6] proposes the model given by:

$$C_p = \frac{1}{2}\left(\frac{116}{\lambda_i} - 0.5\beta - 5\right)e^{-21/\lambda_i} \quad (3)$$

where

$$\lambda_i = \frac{1}{\frac{1}{\lambda + 0.089\beta} - \frac{0.035}{\beta^3 + 1}}$$

Similarly, the author in [7] used the model defined by:

$$C_p = 0.22\left(\frac{116}{\lambda_i} - 0.4\beta - 5\right)e^{-12.5/\lambda_i} \quad (4)$$

where:

$$\lambda_i = \frac{1}{\frac{1}{\lambda - 0.02\beta} - \frac{0.003}{\beta^3 + 1}}$$

According to the authors in [8] the $C_p(\lambda)$ curve of the wind turbine can be expressed approximately using the following polynomial:

$$C_p(\lambda) = a_1 + a_2\lambda + a_3\lambda^2 + a_4\lambda^3 + a_5\lambda^4 + a_6\lambda^5 \quad (5)$$

Through adjusting the coefficients a1-a6 in the above polynomial equation (5), the

shape of the $C_p(\lambda)$ curve can be modified.

For the case study wind turbine the appropriate coefficients are found to be:

$a_1 = 0.04, \quad a_2 = 0.133, \quad a_3 = 0.146,$
$a_4 = 0.602 \; a_5 = 0.104 \; a_6 = 0.0006$

SIMULATION RESULTS AND ANALYSIS

The specifications parameters for the case study commercial wind turbine are given in Table 1.

The parameters shown in Table1 were defined and the operating parameters set in MATLAB program code.

The three numerical approximation models described by equations (3) to (5) were then simulated using MATLAB.

The plots of interest are those on the maximum power point curves for various wind speeds.

Case study wind turbine	Rhino Rotor Wind Turbine
Manufacturer	PowerGen East Africa Ltd.
Rated Power	1Kw at 12.5m/s
Rotor Diameter	3.1m
Startup wind speed	3.2m/s
Over speed protection	Mechanical tail furling

Table1: Parameters of case study wind turbine

The plots for maximum power point curves and Cp vs λ are as shown in figures 1 to 4 below.

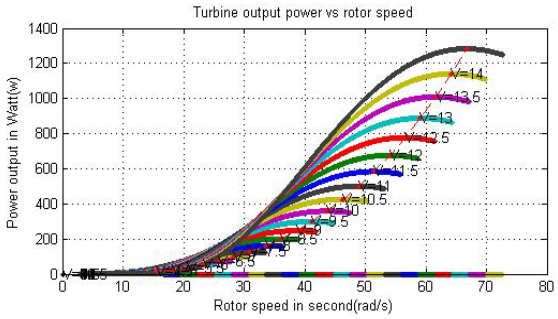

Fig.1: Power output vs rotor speed using approximation model in equation (3)

From the plot of Fig. 1 it can be seen that the power output at the rated speed of 12.5 m/s is 777.5W

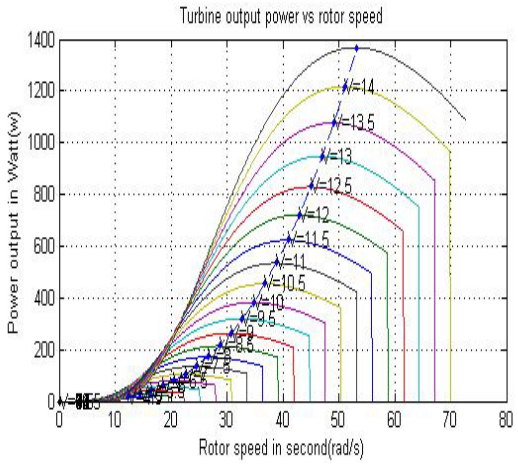

Fig.2 Power output vs rotor speed using approximation model in equation (4)

From the plot of Fig. 2 it can be seen that the power output at the rated speed of 12.5 m/s is 829.1W

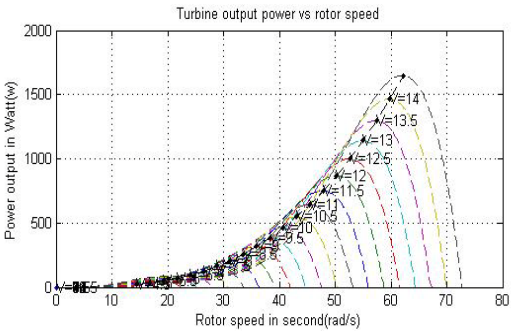

Fig.3 Power output vs rotor speed using approximation model in equation (5)

From the plot of Fig. 3 it can be seen that the power output at the rated speed of 12.5 m/s is 999.6W

Fig.4 shows power output vs rotor speed for all the 3 approximation models on the same scale.

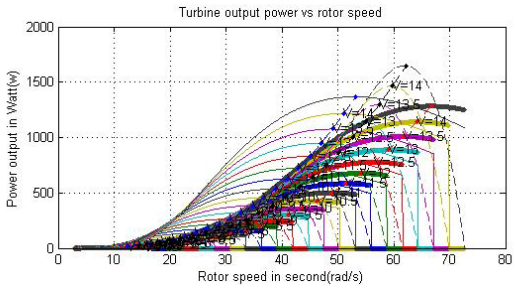

Fig.4. Power output vs rotor speed for all the 3 approximation models

Fig.4 shows that the three models are comparable for the case study wind turbine although giving different maximum power values.
From the results it can be seen that the different models give different values of maximum power points for the same wind speed.
To validate their accuracy, the maximum power point at the rated wind speed (12.5m/s) for the case study wind turbine as given by the various models was compared to the actual value from the manufacturer's datasheet.

The results are as shown in Table 2:

Model	Maximum power at 12.5m/s wind speed(W)	%Accuracy
1	777.5	77.75%
2	829.1	82.91%
3	999.5	99.95%

Table 2: Comparison of maximum power points at rated wind speed for the three models.

From the manufacturer's datasheet of the case study wind turbine, the power output at the rated wind speed is 1000W.
It can be seen that at rated wind speed, approximation model in equation (3) has 77.77% accuracy in predicting the power output. Approximation model in equation (4) has 82.91% accuracy while that in equation (5) has 99.95% accuracy.

A plot of Power coefficient C_p vs Tip speed ratio λ for the three models was also obtained as in figure 5.

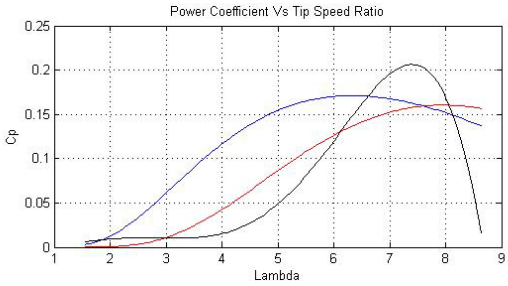

Fig.5 $C_p$vs λ for all the 3 approximation models.

The figure shows the maximum power coefficients of the three models. Approximation model in equation(1) gives maximum value of Cp as 0.1605, model in equation (4) as 0.1712 and that in equation (5) as 0.2063. It can be seen that model in equation (5) gives the highest value of Cp at 0.2063

CONCLUSION
For maximum power point tracking it is important to use a model that gives the maximum power for various wind speeds.
From the analysis, it can be seen that approximation model described by equation (5) is the one that best approximates power coefficient C_p for the case study wind turbine as well as giving highest power for all wind speeds as compared to the other models. It gives has an accuracy of 99.95% in giving power output at the rated wind speed.
It also gives the highest value of maximum C_p at 0.2063, hence giving maximum power output for the case study wind turbine.
This model will be used to develop a controller for maximum power point tracking for the case study wind turbine.

REFERENCES

[1] Shrikant S Mali1, B. E. Kushare, "MPPT Algorithms: Extracting Maximum Power from Wind Turbines," *International Journal of Innovative Research In Electrical, Electronics, Instrumentation and Control Engineering,* Vol. 1, Issue 5, August **2013**

[2] Xing –Peng et al, "A Fuzzy logical MPPT control strategy for PMSG wind generation systems", *Journal of Electronic Science and Technology*, Vol 11, No.1, March **2013**

[3] Kazmi S.M.R. et al, " A novel algorithm for fast and efficient speed-sensor less maximum power point tracking in wind energy conversion systems", *IEEE Transactions on Industrial Electronics.*. **2011**,

[4] Kathryn E. Johnson and Lucy Y. Pao, "A tutorial on the dynamics and control of wind turbines and wind farms", *Proc. American Control Conference*, **2009**.

[5] Mohamed Asmine et al, "Model validation for wind turbine generator models", *IEEE Transactions on Power systems*, **2010**

[6] R. Jagatheesan, K. Manikandan, "An Efficient Variable Speed Stand Alone Wind Energy Conversion System & Efficient Control Techniques for Variable Wind Applications", *International Journal of Advances in Engineering & Technology*, Nov. **2012**

[7] T. F. Chan and L. L. Lai, "Permanent-magnet machines for distributed generation: A review," in *Proc. IEEE Power Eng. Annu. Meeting*, **2007**.

[8]Bogdan S. Borowy and Ziyad M. Salameh,"Dynamic Response of a Stand-Alone Wind Energy Conversion System with Battery Energy Storage to a Wind Gust", *IEEE Transactions on Energy Conversion*, Vol. 12, No. 1, March **1997**.

The Impact of Using Auxiliary Service Voltage Transformer Sub-Station for Rural Electrification in Kenya

Michael J. Saulo, Marangi S. Mbogho, Joel Kitheka
Technical University of Mombasa
michaelsaulo@yahoo.com, marangimbogho@gmail.com, ctgaunt@uct.ac.za

***Abstract*- The majority of rural areas in Africa have low concentration of electrical energy users. As a result, most power utility will not be able to generate an adequate return on investment necessary to install a conventional distribution sub-station on the transmission line. Therefore, costs related to the deployment of a conventional distribution sub-station are prohibitive for most rural electrification projects. On the other hand, high voltage transmission lines on their path from the Generating stations to major urban centers typically transverse large spans of rural areas to which they do not supply electricity. The Auxiliary Service Voltage Transformers (ASVTs) have the ability to tap from high voltage lines and transform the voltage to a distribution class voltage. The technology to transform high voltage (HV) to medium voltage (MV) for delivering power in rural areas within the vicinity of the HV line is still a new concept in developing countries especially in Sub-Saharan Africa (SSA). In order to address the drawback associated with prohibitive costs of a conventional sub-station; this paper explores the impact of the ASVTs on a power network when used for rural electrification. The objective or contribution is to evaluate the impact and adoptability of the system in a Kenyan power network.**

Key words-- Auxiliary Service Voltage Transformers (ASVTs) Penetration level optimization, Sub Saharan Africa.

I. INTRODUCTION

The conventional distribution sub-stations are points in a large electrical power transmission network where high–level voltage is transformed into medium-level voltage, suitable for some industrial consumers, and for further transformation and distribution to low voltage end consumers [1].

Generally, rural areas in Sub Saharan Africa have low concentration of electrical energy users. As a result, most power utilities will not generate adequate return on investment necessary to install conventional distribution sub-station on the transmission line. Therefore, costs related to the deployment of a Grid based conventional distribution sub-station are prohibitive for most rural electrification programmes. Conversely, high voltage transmission lines from the Generating stations to major urban load centers typically transverse large spans of rural areas to which they do not supply electricity due to their typical high voltage capacities. In some developing countries where transmission systems are in place but a wide-spread distribution infrastructure is lacking, the Auxiliary Service Voltage Transformers (ASVTs) may be used as a compact transformer to greatly reduce the electrification costs for small villages [2]. The ASVT can either be used with its low voltage output to directly supply needed power for in-close loads near the transmission right of way, or simply step up the ASVT low voltage output through distribution transformers for a local distribution network [3].

Small sub-stations can be sited specific to the load requirements without a large distribution network. Tapping the high voltage transmission line and connecting an ASVT with a small footprint sub-station may provide affordable, readily-available electricity to many rural households living in close proximity to high voltage transmission lines who presently are without electricity. This paper explores the impact of the ASVTs on a power network when used for rural electrification. The proposed approach is achieved by a Compressive study to determine the level of harmonic current, the impact in the power system and possible suppression measures to be undertaken. In this paper, the design parameters considered are as follows; primary and secondary turns, number of coils per phase, number of turns per coil, conductor cross-sectional area, area of each strip, disposition of each strip, core diameter, core area, core stack, weight of the core, winding material, type of the coil, and the connection method used. The design parameters are eventually used for simulation and a comparison done. The results are tabulated and analyzed. The main objective is to evaluate the impact and adoptability of the system in a Kenyan power network.

II. AUXILIARY SERVICE VOLTAGE TRANSFORMER DESIGN

The developments of transformer design tools and their electrostatic field for finite elements as well as networks modeling programs allowed the transformers manufacturers to develop ASVTs which can transform high voltage energy from upto 230kV to (below 600V) in one step. ASVTs have high reliability and enough power to fulfill most of the low voltage load application, like control system, pump motors, instrumentation and illumination [4]. To develop an ASVT model it is first important to understand the magnetic circuit theory and finite element analysis. Ideally, a transformer stores no energy - all energy is transfered instantaneously from input to output. In practice, all transformers do store some undesired energy,through the following ways [5,8];

- Leakage inductance, which reperesents energy stored in the non-magnetic regions between Windings, caused by imperfect flux coupling. In the

equivalent electrical circuit, leakage inductance is in series with windings, and the stored energy is proportional to load current squared.

- Mutual inductance (magnetizing inductance), represents energy stored in the finite permeability of the magnetic core and in small gaps where the core halves come together. In the equivalent circuit, mutual inductance appears in parallel with the windings. The energy stored is a function of the volts-second per turn applied to the windings and is independent of load current.

Two models of analysing are considered for ASVTs design, the first model is based on the magnetic circuit theory and the second is based on magneto-static finite element analysis. In this research project the transformer reverse design method is incoperated for the two models. In the conventional method of transformer design, the terminal voltages, VA rating and frequancy are specified. In the reverse design approach the physical characteristics and dimensions of the windings and core are the specifications [6]. By manipulating the amount and type of material actually to be used in the transformer construction, its performance can be determined. This is essentially the opposite of the conventional transformer design. It allows for customized design, as there is considerable flexibility in meeting the performance required for a particular application.This type of design is suitable for ASVT models since they are meant for customized application [5]. In the reverse design method, the transformer is built up from the core outwards. The core cross section dimensions (diameter for a circular core and side lengths for a rectangular core) are selected from cataloques of available materials. A core length is chosen. Laminations that are availabe can be specified in thickness. A core stacking factor can be estimated from the ration of iron to total volume. Figure 3, shows a transformer profile of known material characteristics and dimensions [8].

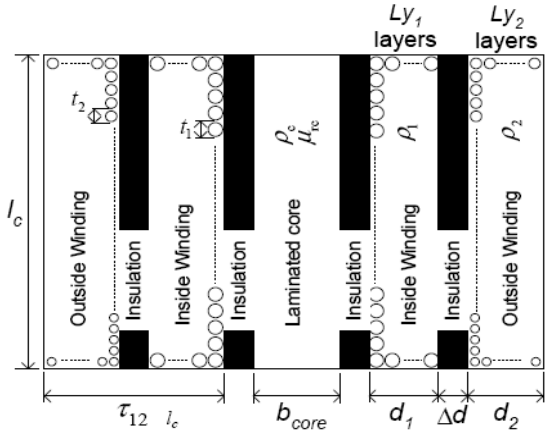

Figure 1 Component dimension and material properties of a transformer

Given the core length l_c and diameter,(or b_{core} and w_{core} for a rectangular core), the inside winding usually low voltage winding is wound on layer by layer. The wire size can be collected from catalogues. Insulation thickness is also specified. The designer can then specify how many layers of each winding are wound.

Insulation is placed between core and the inside winding (fomer) and between each layer for high voltage applications. The outer winding usually the HV windings is wound over the inside winding,with the insulation between layers according to the voltage between them. Windings current densities and volt per turn become a consequence of the design, rather than a design specification. The only rating requirements are the primary voltage and frequency.The secondary voltage and transformer VA rating are a consequence of the construction of a transformer. The number of turns are estimated to be[7][8] ;

$$N_1 = \frac{l_c L_1}{t_1}, N_2 = \frac{l_c L_2}{t_2} \tag{10}$$

Where;

l_c is the length of core

L_1, L_2 Number of primary and secondary winding layers

t_1, $t2$ axial thickness of primary and secondary wire

This calculation assumes that the winding length is equal to the core length. The actual winding lengths may be used if the primary and the secondary winding lengths are different and do not fully occupy the winding window height.
The transformer sub-station has the following technical features [8]

- A magnetic core with oriented gain and a high level permeability
- Electrolytic copper windings
- The primary winding is connected direct to the high voltage while the secondary winding supplies low voltage panels.
- The high voltage terminals are made of high conductivity aluminum and can be cylindrical or flat type.
- The external bushing is made of composite material in accordance with IEC 61642 standards suitable to be installed in highly polluted areas.

The sub-station offers the following advantages:

- It is suitable for both metering and low voltage power distribution.
- High Power availability as it directly tap power from overhead transmission lines

- High reliability due to reduced number of components used for energy conversion
- Wide range of power availability.

III. METHODOLOGY

The methodology involves selecting number of turns for the transformer based on $E_t = K\sqrt{Q}$.

Where; E_t

Established on the number of turns and the approximate flux density (assumed) the gross core area can be calculated. Once the core area is known, the core diameter can be determined using $A_g = k_1 \times \pi d^2$

Where *d* is the core diameter

K_1 is a factor to be selected from the number of core steps. Selection of the approximate area of winding wires and strip are done on the basis of the rated current and available current density, which is generally restricted to 1.5A/mm^2 for aluminum and 3.0A/mm^2 for copper material [10]

The diameter of round conductor for high voltage winding can be calculated from $Area = \pi \frac{d^2}{4}$.

The size of the strip and their disposition is very important to minimize the skin effect. When selecting the strip, the limitation of size as the ratio of width and depth must remain 2 and 4[8]. The following parameters where determined; core window height, core diameter, step width, core stack, core areas, coil diameter, weight of the core.

TECHNICAL SPECIFICATIONS

Power rating	250 KVA
No load voltage ratio	132,000/600 V
Number of phase/frequency	3 phase/ 50 HZ
Connection	delta/ star
Winding material	Aluminum
Tapping on HV	
For HV Variation	At+2.5%to 5%
No-load and load loss (max)	520/3520W
Impedance	4.5%
Maximum flux density	1.6%
Maximum current density	1.5A/sqmm

Figure 2, illustrates the ASVT design flow chart, the process is initialized by setting up the technical specifications, of the transformer to be designed, using the power rating of the transformer as captured in the technical specification, secondary volt/ turn is determined. This secondary volt/turn is then used to determine the secondary turns. By use of the secondary/primary voltage ratio, the primary turns are determined. The primary and secondary turns are then used to determine the transformation ratio. The calculated turns ratio is then compared with the turns ratio in the technical specifications, if not the processor transfers control to start off the process, if yes, the central processing unit proceeds to determine the core area then the core diameter, core stack, step width, number of coils per turn, weight of the core, conductor diameter and number of coils per turn.

The system is then constructed, operational test and current leakage test administered. If the required parameters have not been achieved the process is repeated. If the system operates as expected, the process is finished and the system dispatched.

For this reason, the system is usually referred as a capacitive transformer. The operating principle of the divider considering a phase to ground connection is as shown in Fig 2 [10] [13] [14].

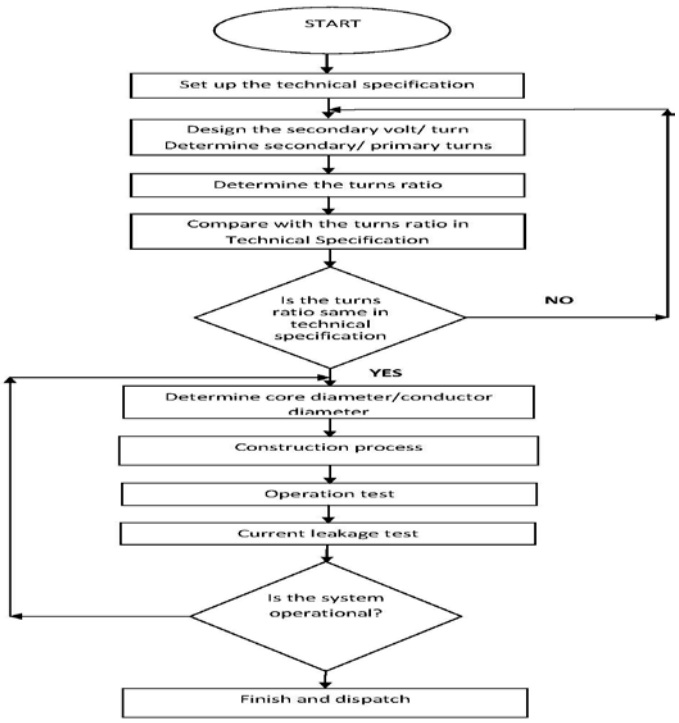

Figure 2. ASVT design flow chart.

IV. MODELLING AND ANALYSIS OF THE TRANSMISSION LINE

Traditionally, transmission lines may be modeled under the two possible scenarios i.e. steady and transient state. For transient analysis, a power line may be represented as a matrix of differential equations whereas for steady-state a set of hyperbolic equations may be used [17].

In order to achieve a model that is representative of an ASVT and their associated switch gears, analysis of mathematical equations are carried out. The approach taken in this paper is first to model the transmission line using actual data collected. In a transmission line, voltage and current are time and position dependent [18][19][20].

If dx = Small section of distance *x*

v,*i* = voltage and current respectively.

For a line of series resistance *r*, length *l,* shunt conductance and capacitance *g* and *c* respectively the series voltage for a section *dx* is given by;

$$V = \frac{V_R + I_R Z_C}{2}\varepsilon^{yx} + \frac{V_R - I_R Z_C}{2}\varepsilon^{yx}\varepsilon \quad (1)$$

$$I = \frac{V_R / Z_C + I_R}{2}\varepsilon^{yx} - \frac{V_R / Z_C - I_R}{2}\varepsilon^{-yx} \quad (2)$$

Where $Z_C = \sqrt{\frac{z}{y}}$ = the characteristic impendence

$y = \sqrt{yz}$ = the propagation constant

Re-arranging using hyperbolic functions

$$Sinh = \frac{z^{\theta} - z^{-\theta}}{2} \text{ and } Cosh = \frac{z^{\theta} + z^{-\theta}}{2} \quad (3)$$

$V = V_R \cosh yx + I_R Z_C \sinh yx$ (4)

the π model is used, since it gives a closer representation of an actual line. Figure 3, illustrated the line parameters.

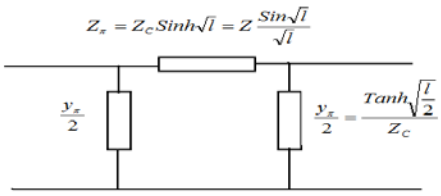

Figure 4 Equivalent circuit of a transmission line [16]

Where Z= *zl* and Y = *yl* are total series impedance and shunt admittance and $yl = \sqrt{zy}$

V. CASE STUDY

An ASVT acts as an inductive feeder, when integrated into a transmission line and may cause a significant change on long transmission line voltage stability limit depending on the penetration level of the ASVT units. Transmission lines utilize reactive power to support their magnetic fields. The magnetic field strength is dependent on the magnitude of the current flow in the line and line natural inductive reactance (X_L). It follows then that the amount of MVAr used by a transmission line is a function of current flow and inductive reactance ($MVAr = I^2X_L$) [17, 20].

In this case study, the 220kV, 440 km, (Kiambere – Rabai) line is used for the study and is integrated to ASVT units. First, the ASVT is designed using the reverse design

$I = V_R \cosh yx + V_R/Z_C \sinh yx$ (5)

If we let $x = l$ where *l* is the length of a transmission line; We can say;

$V_S = V_R \cosh yl + I_R Z_C \sinh yl$ (6)

$I_S = V_R \cosh yl + V_R / Z_C \sinh yl$ (7)

Where V_S and I_S are source voltage and current respectively and V_R and I_R are received voltage and current respectively. Alternatively these equations can be re-arranged to solve for received voltage and current given source voltage and current:

$V_R = V_S \cosh yl - I_S Z_C \sinh yl$ (8)

$I_R = V_S \cosh yl + V_S / Z_C \sinh yl$ (9)

These are standard equations used for solving problems for transmission lines. Since the study entailed tapping line to neutral voltage, a factor of $\sqrt{3}$ shall be multiplied to the line voltage to obtain the phase voltage value. For accurate representation of transmission line, lumped parameter equivalent circuit of π or T models are used. For this paper approach developed in the methodology and then integrated to the transmission line. System energisation at no-load and load on/off are carried out. Simulations are first done with the line not loaded followed by a loaded line and finally the line under short circuit conditions. Voltage and power variable constraints are taken into considerations. The ASVT units are included at different distances. The line is cascaded with PI sections to increase the speed of convergence and reduce delays in the Sim Power software used.

VI SIMULATIONS AND ANALYSIS

In this paper, a graphical icon based program under Sim Power Systems in MATLAB is used. This icon based simulation has been proved to be accurate [17][18].

The PI section line block model implements per phase transmission line with parameters lumped in PI sections. For a transmission line, the resistance, inductance, and capacitance are uniformly distributed along the line. An approximate model of the distributed parameter line is obtained by cascading several identical PI sections, as shown in Figure 5.

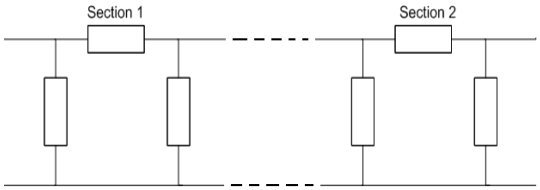

Figure 5 Sections of the π model (Source: Generated by the study)

The PI section linear model has a finite number of states that permit linear state-space model computation. The number of sections to be used depends on the frequency range to be represented. A good approximation of the maximum frequency range represented by the PI line model is given by the equation (10).

$$f_{\max} = \frac{Nv}{8l} \tag{10}$$

where
N: Number of PI sections

v: Propagation speed in km/s $= \frac{1}{\sqrt{LC}}$,

L in H/km, *C* in F/km
l: Line length in km.

For this paper, a section has a maximum of 110km. For example Kiambere – Rabai line being investigated is 440km length which is represented by approximately 4 PI sections.

VII. PENETRATION LEVEL OF ASVT IN TRANSMISSION NETWORK

In this section actual data collected are used to model multiple configurations of a real power network in the Kiambere–Rabai grid transmission network with varying topologies. The 3 phase, 220kV line is modeled per phase for the purpose of this study. The (Kiambere – Rabai) line under study has generation at both ends, with a load capacity of 210MW. Simulations are first done with the line not loaded followed by a loaded line at (125MVA, 10MVAR) and finally with the line under short circuit conditions. The Auxiliary Service Voltage Transformer (ASVT) units are included at different instances. The line is cascaded with PI sections to increase the speed of convergence and reduce delays in the Power Sim software used. Ode 23t, an integration algorithm (Runge and Kutta 2nd &3rd Order) and a stiff solver is used for simulation. It is fast and accurate with tolerance of 10e-4. Fig 6 to 10, show the ASVT model with sending/receiving end voltages waveforms respectively.

VII. RESULTS AND DISCUSSION

The results show that switching on a loaded transmission line reduce Ferranti effect as compared to when the line is not loaded. Penetration of a single ASVT along the line exhibit increased voltage distortion towards the end of the line as shown in fig 7. The impulse distortions which last for 6 cycles upon switching cumulatively could cause insulation failure of electrical equipment such as transformers connected to the line. However, penetration of two ASVTs provides much more improved characteristics for both transmission line and output of the sub-stations. The Ferranti effect was limited to less than two cycles (fig 8). With addition of an extra ASVT a smaller input capacitor was required. This would put a ceiling on what is possible for manufacture to produce with regard to standardization. It was also noted that with the penetration of a third ASVT (fig 9) the low voltage output shot to unacceptable level. The simulation results established that Ferranti effect problems persisted regardless of position of the ASVTs along the line. This meant that Ferranti effect was not a function of the distance of the line, but of the system equipments. Predominant, saturation in these equipments is due to the ferro-magnetic inductor and the distribution transformer used in the circuit. Due to Ferranti effect problems, only linear transformers or transformers close to that order may be used for ASVTs sub-stations. Saturating transformers must be avoided for such applications. Though these substations can be placed anywhere along the line. It would be more effective to install them in position where there is high density of rural communities living in close proximity to the line. The main observation was that reliable protection at both high and low voltage sides, in accordance to the thermal capacities of the sub-station elements needed to be incorporated due to severity of fault currents.

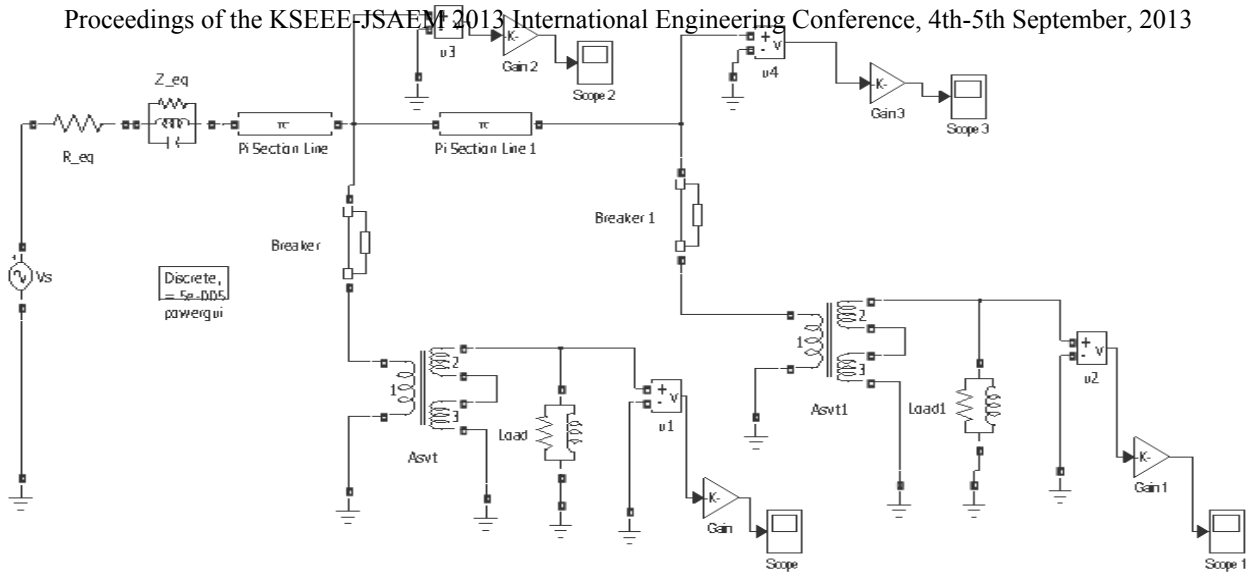

Figure 6 Model for two ASVT connected on the transmission line (Source: Generated by the study)

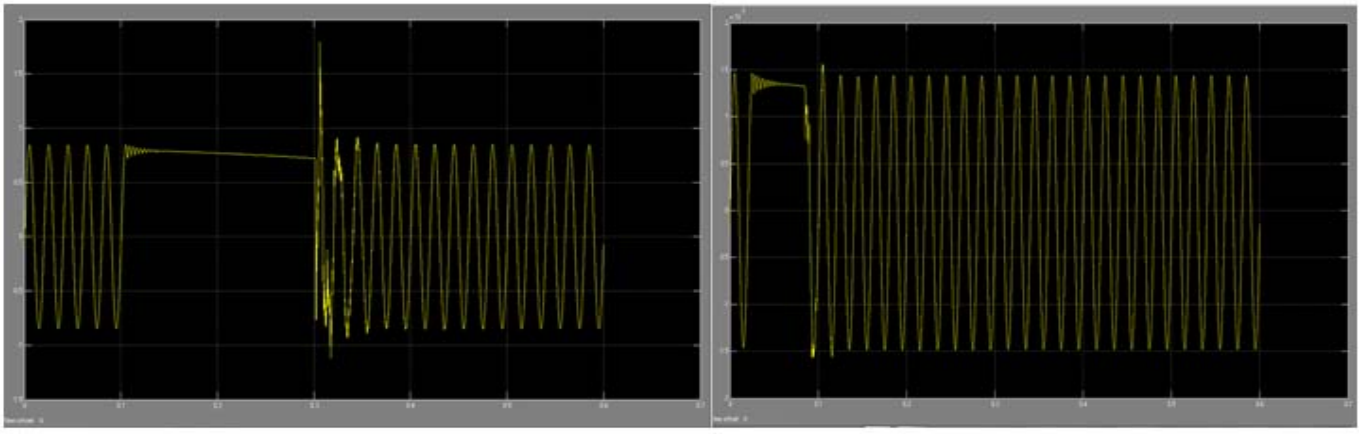

Figure 7 Tap-off voltage and load voltage waveforms for an ASVT.

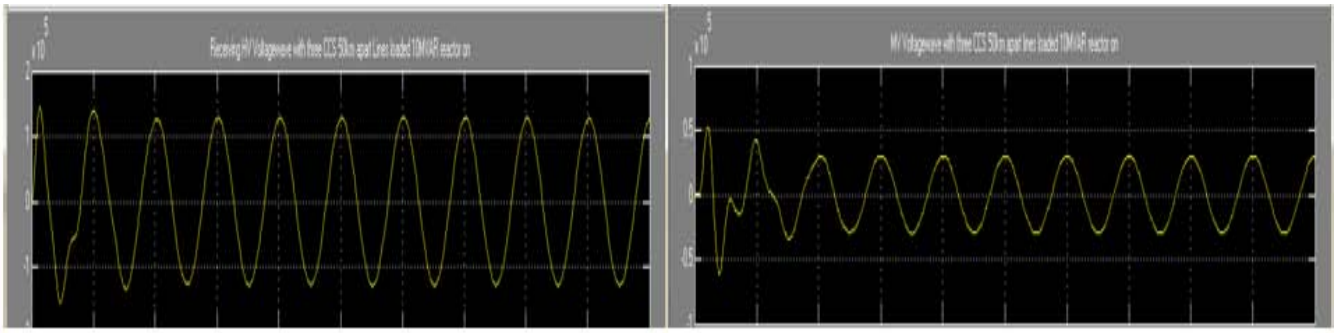

Figure 8. Sending and Receiving end Voltages for three ASVT at different distances

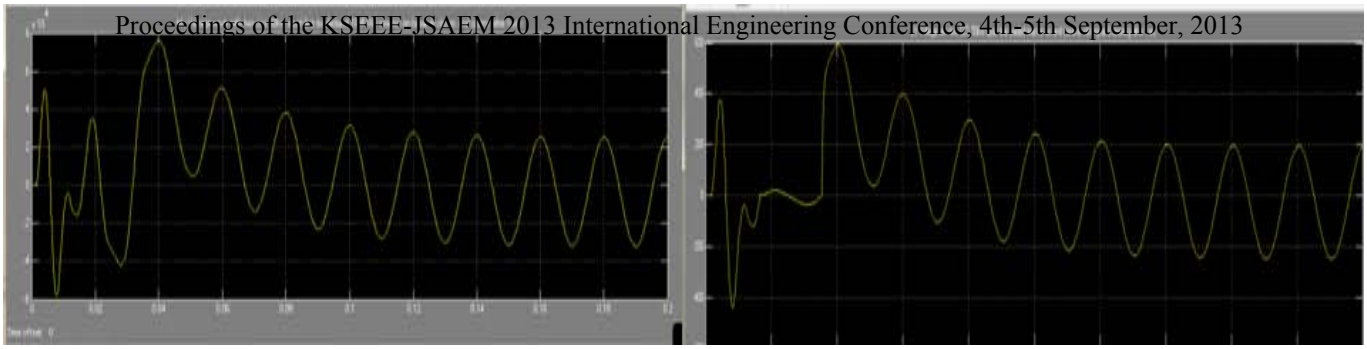

Figure 9. MV and LV Voltage with breaker closing after 1 second

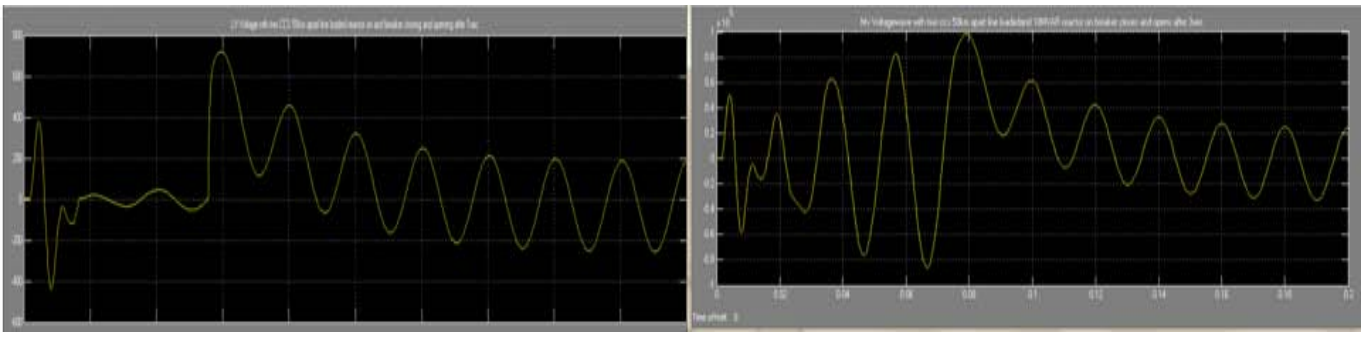

Figure 10. MV and LV Voltage with breaker closing after 2 second

VIII CONCLUSION AND RECOMMENDATIONS

It was established from the analysis and simulations, that there was no apparent optimum penetration point for installing ASVTs sub-station. The sub-station can be installed at any point along the transmission line. However, it was recognized that there is an optimum number of ASVT units that can be allowed to penetrate a particular line. The optimum penetration level of ASVT sub-station for the Rabai-Kiambere was determined as two sub-stations per phase. The creation of a third sub-station was possible if only the capacitive compensators were to be continuously in circuit to keep the voltage level within ± 5% limits. The following recommendation may be made;

(i) Where HV transmission lines traverse rural villages or pass in close proximity, it is recommended that an ASVT should be installed to tap power from the EHV lines and Single Wire Earth Return (SWER) system can be used to reticulate power in such villages.

(ii) When using the ASVT systems, the compensating capacitor should be split between both sides of the distribution transformer. This helps to coordinate the fault current protection as well as to regulate the voltage on the load side.

REFERENCES

1) V. Neimane, *On Development Planning of Electricity Distribution Networks* Doctoral Dissertation, Royal Institute of Technology Stockholm (2001).
2) M.S.Pasand, R. Aghazadeh., Capacitive Voltage Substations Ferro resonance Prevention using power electronics devices International *conference on power system transients- IPST 2003* in New Orleans, USA.
3) Gomez, R.G., Solano, A.S., Acosta E.A., (2010): *Rural Electrification Project Development, Using Auxiliary Transformers. Location of Tubares, Chihuahua, Mexico. CIGRE* C6-305- 2010 working group (Coll 2010) "Rural Electrification
4) G.O. Anderson, K.Yanev, Non-Conventional Substation and Distribution System for Rural Electrification. *3rd IASTED Africa PES 2010,* September 2010 Gaborone, Botswana.
5) Bell, S.C., Bodgers P.S., (2007) *Power Transformer Design Using Magnetic Theory Finite Element Analysis-Comparison of Techniques* Proceeding of AUPEC 2007 Perth, Western Australia 9-12 December 2007.
6) ASVT ' Auxiliary Service voltage Transformer models UTP-245 and UTP-145 manuals and technical brochures'.www.Arteche.com (accessed 20June 2012)

7) Calve R., Salvano A. , Acosta (2000) 'Rural Electrification in Chihuahua Mexico at one third of the cost versus conventional substation' *Eradicating energy poverty* pp1-10

8) Dasguta I.(2002) *Design of transformers* : Tata Mc Graw- Hill education

9) G., Ledwich, P. Martino, F.Calderon, and C.T. Gaunt, *International practices in Rural Electrification CIGRE* SC-C6 working group (Coll 2007) ...IWD Topic E.

10) IEG C57.13-1993, "IEEE Standard requirement for instrument transformer.

11) Rural areas: The Capacitor Voltage Divider. *IEEE Trans on power delivery*, Vol 5, No 1, pp259-265, January 1990.

12) T.V., Raphalalani, N.M., Ijumba, A.A. Jimoh, Capacitive Divider System for feeding a distribution network from an EHV line. *Powercon 2000.*

13) Simon, C.M, P.S., Bodges, Power Transformer Design using Magnetic circuit theory and Finite element analysis. *AUPEC 2007* Perth Western, Australia, December 2007.

14) Bodger, P.S., Liew, M.C., and Johnstone, P.T., A comparison of conventional and reverse transformer design *AUPEC 2000* Brisbane, Australia, September 2000

15) H.Daqing, and J.Roberts, Capacitive Voltage Transformers: Transient Overreach Concerns and Solutions for Distance Relaying. *Schweitzer Engineering Laboratories*, Inc. Pullman, WA USA.

16) Aweetana, Transient characteristics of Capacitive Potential Devices *IEEE Transaction on Power Apparatus,* vol 90 No 5 September/October 1971.

17) W.H. Kersting, Distribution *System Modelling and Analysis*, ISBN 0-8493-0812-7, CRC Press Boca Raton, Florida 33431, 2001.

18) K. P. Mrimal, Voltage *stability Condition considering load characteristics* IEEE Power Engineering Society 1991.

19) R.B. Arthur, and V. Vijay, (2000): *Power Systems Analysis.* 2nd edition ISBN 0-13-691990-1 Prentice Hall Inc 2000.

20) D.P. Kothariand, I.J. Nagrath, Modern *Power System Analysis* Mc Graw Hill, 2006.

OPTIMAL LOCATION OF SVC FOR MINIMIZING THE COST OF GENERATION

IRENE MUISYO, C. M. MAINA, ROY ORENGE

muisyoirene@gmail.com, cmaina77@yahoo.com, samroyoin@gmail.com

EEE SEEIE JKUAT, EEE SEEIE JKUAT, EEE DeKUT

P.O. Box 62000 – 00200, Juja, Nairobi, Kenya.

Abstract - Flexible AC Transmission System (FACTS) devices in power systems play a vital role in the power system performance, such as improving system stability, increasing system loading capability, reducing losses and the cost of generation. In order to maximize their benefits, these devices must be located optimally. In this paper, optimal location of SVC is obtained by use of two benefit factors which are obtained and weighted by Analytical Hierarchy Process (AHP). Placement of SVC is then done at the obtained location and Optimal Power Flow (OPF), voltage analysis and an estimation of the cost of investment recovery are performed. This proposed method is tested on WSCC 9-bus and modified IEEE 30-bus test systems. Results obtained show an improved voltage profile and minimization of generation cost.

Keywords: VAR compensation, FACTS devices, SVC, voltage profile.

I. INTRODUCTION

Transmission of reactive power results to increased losses in the transmission system, decrease in the real power transmitted, and changes in the voltage amplitude at the end of the line. It is therefore necessary to provide reactive power compensation, at the right location in the power system, in order to increase transmitted power, decrease losses and provide stability of voltage amplitude at the end of the line (Tosun, 2012).

Traditionally, the locations for placing new VAR sources were either simply estimated or directly assumed (Wenjuan Zhang, 2007). With the deregulation of the electricity market, the traditional concepts and practices of power systems are changing. FACTS devices such as Static VAR Compensator (SVC), Thyristor Controlled Series Compensation (TCSC) and Unified Power Flow Controller (UPFC) are being adopted in many countries.

FACTS devices are power electronic based devices which can change transmission system parameters like impedance, voltage and phase angle. This allows control of power flow in the network, reduction of flows in heavily loaded lines, lower system losses, improved stability of network and reduced cost of production. It is important to ascertain the location of these devices because of their significant costs (S. B. Bhaladhare, 2012) (Rakhmad Syafutra Lubis, 2012).

Optimal VAR location of different devices has been attempted using various techniques over the last few years. (N.M. Tabatabaei, 2011) presents PSO and APSO-SA methods for ascertaining optimal location of FACTS devices to achieve minimum VAR cost while satisfying the power system constraints, for single and multi-type FACTS devices. (S. B. Bhaladhare, 2012) discusses optimal placement of FACTS devices based on Voltage Stability Index (VSI) to obtain their location and operating parameters for improving voltage profile in a power system.

Location and type of various FACTS controllers has also been investigated in (Rakhmad Syafutra Lubis, 2012) using the sensitivity of system loading factor method and solved with the nonlinear predictor-corrector primal-dual interior-point optimal power flow (OPF) algorithm. Performance evaluation of Newton-Raphson power flow analysis method has been done on IEEE-30 bus system in (Amit Debnath, 2013) to investigate effect of UPFC on the voltage profile.

This paper seeks to obtain the optimal location of SVC by use of a real power loss minimization algorithm. Benefit factors are evaluated from the results and weighted by use of AHP. OPF is then done with SVC incorporation. Lastly, voltage analysis and comparison of savings made from their utilization will be done to determine if it is economical to invest in FACTS devices.

This paper is organized as follows: section II presents SVC modelling and its optimal location, while problem formulation and case study are in section III. Simulation results and discussion are found in section IV and conclusion section V.

II. FACTS DEVICES

FACTS devices can regulate the active and reactive-power flow as well as system voltage magnitude simultaneously by their fast control characteristics and their continuous compensating capability. Series compensation modifies line reactance X_{ij} while shunt compensation injects reactive power which improves the voltage (Rakhmad Syafutra Lubis, 2012) (J.Vivekananthan, 2013).

Static VAR Compensator (SVC)

SVCs regulate voltages at its terminals by controlling the amount of reactive power injected into or absorbed from the power system. If the power systems reactive load is capacitive (leading), the SVC will use reactors to consume VARs from the system, lowering the system voltage. Under inductive (lagging) conditions, the capacitor banks are automatically switched in, thus providing a higher system voltage (D. Murali, 2010). The model is incorporated into the sending end as a shunt element of the transmission line as shown in Fig. 1.

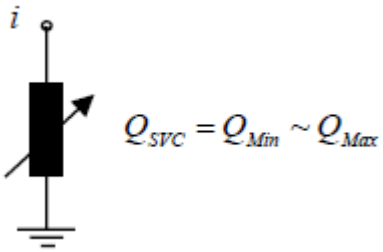

Fig 1: Power Injection Model of SVC

OPTIMAL LOCATION OF SVC

Due to the high cost of FACTS devices, it is necessary to locate them properly in order to maximize their benefits. Two benefit factors evaluated in this paper are:

a) Voltage Benefit Factor (VBF)

$$VBF_i = \sum_{i \in n} \frac{(V_i(Q_{si}) - V_{io})}{Q_{si}} \; x \; 100\% \; i \qquad (1)$$

where $V_i(Q_{si})$ and V_{io} is the voltage magnitude at load bus i, with and without VAR compensation respectively and Q_{si} is the amount of VAR support in the bus. n is the number of load buses.

b) Loss Benefit Factor (LBF)

$$LBF_i = \sum_{i \in n} \frac{(P_{Lo} - P_L(Q_{si}))}{Q_{si}} \; x \; 100\% \; i \qquad (2)$$

where $P_L(Q_{si})$ and P_{Lo} is the power transmission loss in the system with and without VAR compensation respectively (Zhu, 2009) (Jigar S.Sarda, 2012) (J.Vivekananthan, 2013).

Analytic Hierarchy Process (AHP)

The AHP is a decision making approach which presents an objective function, criterion and alternatives. It evaluates trade-offs and performs a synthesis to arrive at a final decision (Saaty, 2008). In this paper, the AHP technique is applied with the objective of identifying the optimal location of SVC. The criterion is VBF and LBF, while alternatives are the various load buses which are candidate sites for VAR support. The judgement matrix to be used (Zhu, 2009) is presented below:

	VBF_i	LBF_i
VBF_i	1	½
LBF_i	2	1

The weighting coefficients of the judgment matrix are computed through the sum method as

$$W = [0.667, 0.333]$$

III. PROBLEM FORMULATION

This is done in two stages:

a) Optimal location of SVC

Optimal location of SVC can be done using various objective functions as detailed in (Wenjuan Zhang, 2007). The approach taken in this paper is minimizing real power loss of the system while observing all system constraints. Mathematically, it is expressed as:

$$F = \min(P_{loss}) = \min\left(\sum_{i=1}^{NL} g_{i,j}\left(V_i^2 + V_j^2 - 2V_iV_j\cos(\delta_i - \delta_j)\right)\right) \quad (3)$$

where V_i is voltage magnitude at bus i; $g_{i,j}$ is conductance of line $i-j$; δ_i is voltage angle at bus i and NL is the total number of transmission lines in the system.

SVC constraint:

$$Q_{SCV,min} \leq Q_{SCV} \leq Q_{SCV,max} \quad (4)$$

where Q_{SCV} is the reactive power injected into the bus by SVC.

b) Generation cost minimization with SVC incorporated

This is the conventional OPF whose objective function is:

$$F = min\big(F(P_G)\big) = \sum_{i=1}^{NG} a_iP_{Gi}^2 + b_iP_{Gi} + C_i \quad (5)$$

Both objectives are subject to:

Power balance (equality) constraints: The total power generated by the units must be equal to the sum of total load demand and total real power loss in the transmission lines.

$$P_G - P_D - \sum_{j\in N} |V_i||V_j||Y_{ij}|\cos(\theta_{ij} + \delta_j - \delta_i) = 0 \quad (6)$$

$$Q_G - Q_D - \sum_{j\in N} |V_i||V_j||Y_{ij}|\sin(\theta_{ij} + \delta_j - \delta_i) = 0 \quad (7)$$

where P_G is the total active power generated and P_D is the total active power demand of the system. Q_G is the reactive power generated and Q_D is the reactive power demand of the system.

Inequality constraints

Power generating limits: each generator in operation has a minimum and maximum permissible output.

$$P_{Gi,min} \leq P_{Gi} \leq P_{Gi,max} \quad (8)$$

$$Q_{Gi,min} \leq Q_{Gi} \leq Q_{Gi,max} \quad (9)$$

Transmission line limits: this is the maximum power a given transmission line is capable of transmitting.

$$S_{ij} \leq S_{ij\ max} \quad i \neq j \quad (10)$$

Voltage limits: imposed for bus voltage magnitudes in order to maintain the voltage profile.

$$V_{i,min} \leq V_i \leq V_{i,max} \quad (11)$$

(D P Kothari, 2003)

Capital cost of SVC

The capital cost of SVC is given as:

$$C_{SVC} = 0.0003S^2 - 0.3051S + 127.38\ (US\$/kVAr) \quad (12)$$

where S is the operating range of device obtained as: $S = |Q_2| - |Q_1|$

Q_2 is the reactive power in the system after installing FACTS devices and Q_1 is the reactive power in the system before installing FACTS devices (N.M. Tabatabaei, 2011) (Kalaivani R., 2012).

CASE STUDY

Optimizing process and placement of SVC has been tested on two systems: Western System Coordinating Council (WSCC) 9-bus and modified IEEE 30-bus system. WSCC 9-bus test system has 3 generators on bus 1, 2 and 3 (S. B. Bhaladhare, 2012). Modified IEEE 30-bus system has 6 generators on bus 1, 2, 5, 8, 11, and 13 (Zhu, 2009). Generator data is found on the appendix. MATPOWER (v2), a toolbox of MATLAB, has been used for simulations.

IV. SIMULATION RESULTS

Case 1: Optimal location of SVC

SVC is placed at all load buses. LBFs and VBFs are calculated, then AHP used to determine the best location for SVC. The bus with the highest weight coefficient signifies the largest system benefit in terms of voltage, loss and cost of generation. Figure 2 shows the proposed VAR support sites and the corresponding weighting coefficients for the 9-bus system.

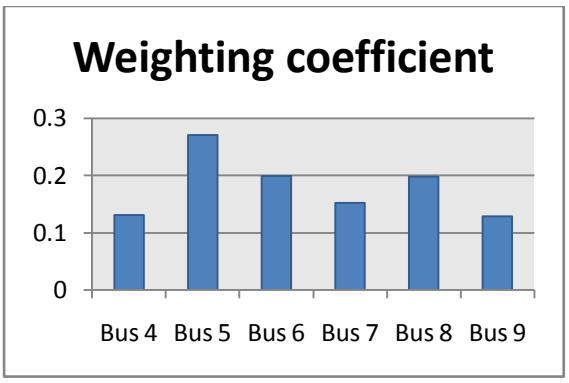

Fig 2: WSCC 9-bus test system

The top three sites in the WSCC 9-bus system for placing VAR compensation is bus 5, 8, and 6. Bus 5 has the highest weighting coefficient hence the optimal location of SVC.

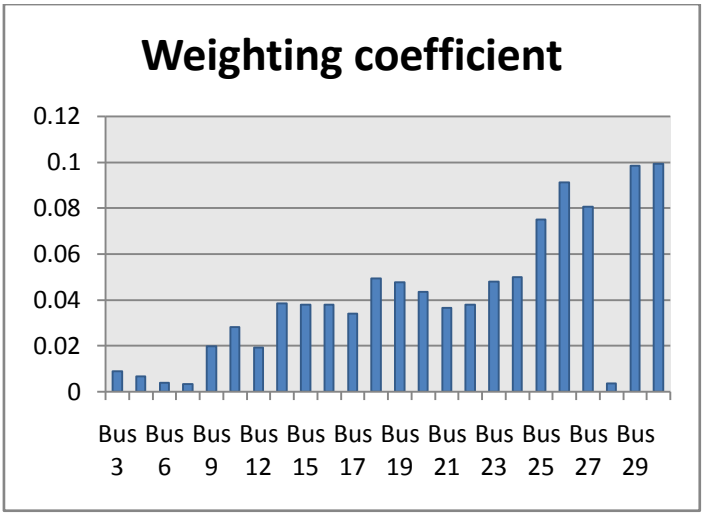

Fig 3: Modified IEEE 30-bus system

The top three sites in the IEEE 30 - bus system for placing VAR compensation is bus 30, 29 and 26, with the optimal location being bus 30.

Case 2: Voltage analysis

Plot of voltage magnitude for both systems, without and with SVC are shown in fig 4 and 5.

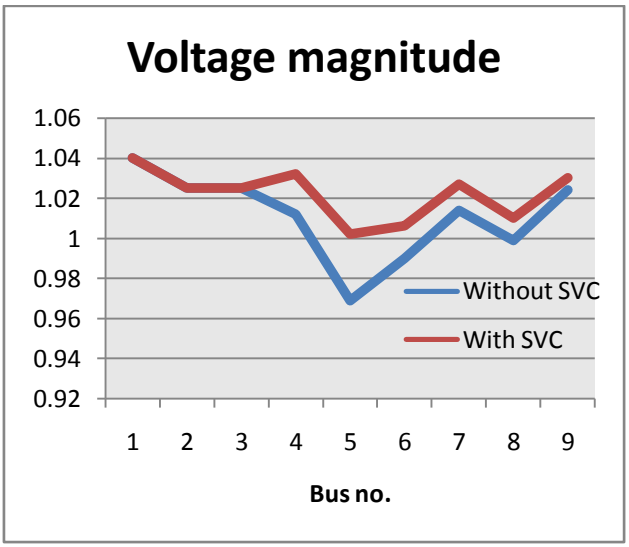

Fig 4: WSCC 9-bus system

The voltage profile has improved. Bus 5 had the lowest voltage magnitude of 0.969p.u., which rose to 1.002p.u. after SVC incorporation.

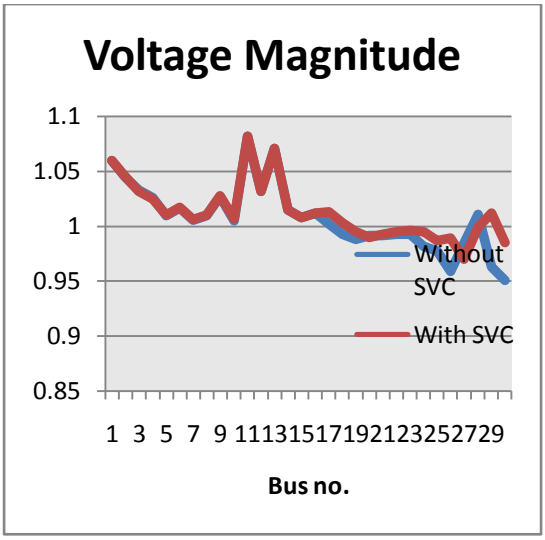

Fig 5: IEEE 30-bus system

Bus 30 had the lowest voltage of 0.951p.u., which rose to 0.985 p.u. after SVC incorporation.

POWER SYSTEM LOSS

The real and reactive total system losses for both systems are found in table 1 and 2 below, with and without SVC.

Table 1: WSCC 9 bus-system

	Without SVC	With SVC
Real power loss (MW)	7.437	6.86
Reactive power loss (MVAR)	77.63	71.63

Total system losses reduced with SVC incorporation for WSCC 9-bus system.

Table 2: Modified IEEE 30-bus system

	Without SVC	With SVC
Real power loss (MW)	9.251	9.569
Reactive power loss (MVAR)	39.2	40.02

From table 2, real and reactive power losses slightly increased with SVC incorporation. This is due to change in dispatch, whereby the cheapest generating unit increases real power production, resulting in higher power flows, hence losses in some lines.

The total cost of generation in both systems is however reduced and savings are used as signals for capital cost recovery, below.

Investment cost recovery

Table 3: WSCC 9-bus system

Cost of generation ($/hr)	
Without SVC	7805.95
With SVC	7754
Savings	51.95

Operating range is evaluated as $18MVAR$ and capital cost of SVC $US\$91{,}835.58$. With a utilization factor of 40%, payback period is 0.51 years.

Table 4: modified IEEE 30-bus system

Cost of generation ($/hr)	
Without SVC	883.74
With SVC	865.56
Savings	18.18

Operating range is evaluated as $8MVAR$ and capital cost of SVC $US\$16{,}886.58$. With a utilization factor of 40%, payback period is 0.26 years.

V. CONCLUSION

In this paper, a method for optimal placement of SVC has been proposed for reducing the cost of generation in a power system. The proposed method is tested on the WSCC 9-bus and modified IEEE 30-bus test systems and results obtained show that SVC placement on the appropriate bus results in a great reduction in cost of generation and improves the voltage profile.

Appendix

WSCC 9-BUS SYSTEM

Table A1 & A2: Generator Data

Bus. no.	Generator limits			
	Pmax	**Pmin**	**Qmax**	**Qmin**
1	250	10	300	-300
2	300	10	300	-300
3	270	10	300	-300

Bus. no.	Generator cost coefficients		
	a	**b**	**c**
1	0.150	5.0	150
2	0.085	1.2	600
3	0.123	1.0	335

MODIFIED IEEE 30-BUS SYSTEM

Table A3 & A4: Generator Data

Bus. no.	Generator limits			
	Pmax	**Pmin**	**Qmax**	**Qmin**
1	200	50	250	-20
2	80	20	100	-20
5	50	15	80	-15
8	35	10	60	-15
11	30	10	50	-10
13	40	12	60	-15

Bus. no.	Generator cost coefficients		
	a	**b**	**c**
1	0.020	2.00	0
2	0.018	1.75	0
5	0.063	1.00	0
8	0.008	3.25	0
11	0.025	3.00	0
13	0.025	3.00	0

References

Amit Debnath, C. N. (2013). Voltage Profile Analysis for IEEE 30 Bus System Incorporating with UPFC. *International Journal of Engineering and Advanced Technology* , 763-769.

D P Kothari, I. J. (2003). *Modern Power System Analysis.* New Delhi: Tata MCGraw Hill.

D. Murali, M. R. (2010). Comparison of FACTS Devices for Power System Stability Enhancement. *International Journal of Computer Applications* , 30-36.

J.Vivekananthan, R. (2013). VOLTAGE STABILITY IMPROVEMENT AND REDUCE POWER SYSTEM LOSSES BY BACTERIAL FORAGING OPTIMIZATION BASED LOCATION OF FACTS DEVICES. *International Electrical Engineering Journal* , 1034-1040.

Jigar S.Sarda, V. N. (2012). Genetic Algorithm Approach for Optimal location of FACTS devices to improve system loadability and minimization of losses. *International Journal of Advanced Research in Electrical, Electronics and Instrumentation Engineering* , 114-126.

Kalaivani R., V. K. (2012). Enhancement of Voltage Stability by Optimal Location of Static Var Compensator Using Genetic Algorithm and Particle Swarm Optimization. *American Journal of Engineering and Applied Sciences* , 70-77.

N.M. Tabatabaei, G. A. (2011). OPTIMAL LOCATION OF FACTS DEVICES USING ADAPTIVE PARTICLE SWARM OPTIMIZATION MIXED WITH SIMULATED ANNEALING. *International Journal on Technical and Physical Problems of Engineering* , 60-70.

Rakhmad Syafutra Lubis, S. P. (2012). Selection of Suitable Location of the FACTS Devices for Optimal Power Flow. *International Journal of Electrical & Computer Sciences* , 38-50.

S. B. Bhaladhare, P. B. (2012). Enhancement of Voltage Stability through Optimal Location of SVC. *International Journal of Electronics and Computer Science Engineering* , 671-678.

Saaty, T. L. (2008). Decision making with the analytic hierarchy process. *Internaional Journal Services Sciences* , 83-99.

Tosun, S. (2012). Investigation of controller effects of SVC and STATCOM on power systems. *Energy Education Science and Technology* , 749-760.

Wenjuan Zhang, F. L. (2007). Review of Reactive Power Planning: Objectives, Constraints, and Algorithms. *IEEE TRANSACTIONS ON POWER SYSTEMS* , 2177-2187.

Zhu, J. (2009). *OPTIMIZATION OF POWER SYSTEM OPERATION*. New Jersey: John Wiley & Sons, Inc.

Dynamic Voltage Stability Analysis of the Kenya Power System using VCPI Stability Index and Artificial Neural Networks

[1]Njoroge S. N, [2]Muriithi C. M, [3]Ngoo L. M

[1,2]JomoKenyattaUniversity of Agriculture & Technology

Department of Electrical & Electronic Engineering

snnjoroge@jkuat.ac.ke

[3]Multimedia University

***Abstract* - Dynamic voltage stability deals with the voltage levels and how they are affected by either faults or load changes within the system.Voltage instability has long been suspected in the voltage collapse and islanding of power systems. Identifications of operational conditions leading to voltage collapse is therefore critical in allowing for critical defensive measures by the system operator to avoid voltage collapse before it occurs. This paper examines the use of Voltage Collapse Proximity Indicator (VCPI) in conjunction with Artificial Neural Networks to predict conditions of voltage instability before they occur for load buses within the Kenya power system that can be used for online prediction of voltage stability within the system.**

Keywords – Voltage Stability, VCPI, ANN

I. INTRODUCTION

Voltage stability is the ability of a power system to maintain voltage magnitudes at all system buses within a specified margin both under normal operating conditions and after being subjected to a disturbance. Voltage instability has long been suspected in system wide blackouts. As a result, voltage stability has been studied in depth both for static and dynamic voltage stability. Static voltage stability is concerned with the system when operating under given loading and generation conditions while dynamic stability is concerned with the changes in the system when it undergoes significant load changes or contingencies in lines or generators. To evaluate how voltage stable a bus is, the Voltage Collapse Proximity Indicator (VCPI) is one of the tools employed recently.It incorporates elements of the Y-bus matrix to capture the network topology as well as the real and reactive power configurations both at the reference bus and within the system as a whole. The VCPI can however only be calculated for static conditions and in this paper minute load changes are used to simulate dynamic loading and contingency conditions.

Artificial intelligence techniques have also been used for a while to reduce the computation times in the power flow solution which is an iterative procedure. Artificial Neural Networks (ANN) are used to mimic human brain cognitive properties and can be trained to read patterns in related data that may be too complex to capture in mathematical terms. In this paper, ANNs are trained using data from the load flow simulations and the corresponding VCPI indices to give predictions of the corresponding voltage magnitudes to expect at each bus.

II. METHODOLOGY

A. POWER FLOW PROBLEM

The power flow solution is used to determine the voltage magnitude and angle at each bus within the system as well as the real and reactive power flows and losses along all lines within the system for a given configuration of loads and generation. Using the nodal current equations, the current entering the i^{th} bus of an n-bus system can be obtained by

$$I_i = V_i \sum_{j=0}^{n} Y_{ij} - \sum_{j=1}^{n} Y_{ij} V_j \qquad (1)$$

At bus I, the power injected is given by

$$\frac{P_i - jQ_i}{V_i^*} = I_i \qquad (2)$$

Equating the 2 equations gives

$$\frac{P_i - jQ_i}{V_i^*} = V_i \sum_{j=0}^{n} Y_{ij} - \sum_{j=1}^{n} Y_{ij} V_j \qquad (3)$$

Equation (3) is a system of algebraic non-linear equations that is solved by iterative techniques. The

most popular is the Newton-Raphson method which gives fast convergence on a solution due to its quadratic convergence.The powerflow equations (1) and (2) are solved to give

$$\begin{bmatrix} \Delta\delta \\ \Delta|V| \end{bmatrix} = \begin{bmatrix} J_1 & J_2 \\ J_3 & J_4 \end{bmatrix}^{-1} \begin{bmatrix} \Delta P \\ \Delta Q \end{bmatrix} \quad (4)$$

J is the Jacobian matrix while the left hand side gives the correction vector that updates earlier values of δ and ***V***. In this paper, the Newton Raphson is run for a maximum of 100 iterations to obtain a single solution convergence.

B. VOLTAGE STABILITY

A power system at a given operating state and subject to a given disturbance is ***voltage stable***if voltages near loads approach post-disturbance equilibrium values[2]. Voltages of the buses within a power system are required to remain within 4% or 5% of the nominal bus voltage in line with ANSI standard C84.1. Voltage Stability can broadly be classified into Static Voltage Stability and Dynamic Voltage Stability.

Static Voltage Stability evaluates the voltage magnitudes at all the buses in the system for a given loading and system configuration. The result only applies to that network topology and loading condition. Dynamic Voltage Stability is concerned with 2 aspects of voltage stability [1]

i. Distance to instability – this measures how close the system is to being voltage unstable. The distance is given in terms of system parameters like loading, power flow across a critical line or reactive power reserve.
ii. Mechanism of Voltage Instability – this investigates what system factors contribute to voltage instability and what indicates that the system is heading towards instability.

Previous studies on Dynamic Voltage Stability have used singular value decomposition, multi-variable control theory and bifurcation analysis[3-7]. Since voltage stability is affected by slow acting system dynamics which allows for the use of many static points to analyse Dynamic Voltage Stability. In this paper, the static points are evaluated by continuously varying loads at a high resolution of 0.001pu and carrying out power flow solutions at each loading configuration.

C. VOLTAGE COLLAPSE PROXIMITY INDICATOR (VCPI)

The VCPI is a relatively new indicator gaining popularity for Voltage Stability Studies. It can be calculated at each bus for each loading and contingency condition [8]. It is calculated at bus *j* as

$$L_j = \left| \frac{S_{j+}^*}{Y_{jj+} V_j^2} \right| \quad (5)$$

Where

$$S_{j+} = S_j + S_{jcorr} \quad (6)$$

$$S_{jcorr} = \left\{ \sum_{\substack{i \in Loads \\ i \neq j}} \frac{Z_{ji}^*}{Z_{jj}^*} \frac{S_i}{V_i} \right\} V_j \quad (7)$$

And

$$Y_{jj} = \frac{1}{Z_{jj}} \quad (8)$$

$S_{jcorr}$is a component of all the other loads in the system incorporated into the index at bus *j*. The VCPI is calculated for the load buses within the system. It has a value of 0 for stability and 1 for complete instability

D. ARTIFICIAL NEURAL NETWORKS (ANN)

These have previously been used for identifying weak buses within a system [9]. They are used to model complex relationships that are difficult to model with mathematical equations or for which relationships exist but are unknown. They mimic the human brain.An extremely important and human characteristic of ANN is their adaptive nature, where learning by experience replaces programming in solving problems. ANNs learn the pattern on which they are trained. An artificial neuron consist of synapses which apply weights to the inputs, an adder***(+)*** that sums the weighted inputs and an activation function ***g(v)*** that maps the sum to the output function of the neuron as shown in Fig. 1. ANNs are formed by arranging neurons in layers. The input layer has input neurons where each input into the network feeds into each of the neurons in the input layer. The input layer's output is fed into the middle layer containing several neurons. The middle layer's output is then fed into the output layer which normally has a single neuron with a single output. Varying the

number of neurons in the middle layer affects the accuracy of the whole ANN.

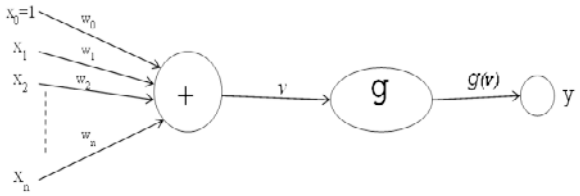

Fig.1: Artificial Neural Network

III. RESULTS

The 9-bus WSCC system was used to test the accuracy of the VCPI calculations using static load increments. The loading on Bus 5 was increased in steps of 0.001pu while maintaining pf until when the power flow solution did not converge. This occurred at 2.971pu loading and the corresponding plot of the VCPI and voltage magnitude was as in Fig 2.

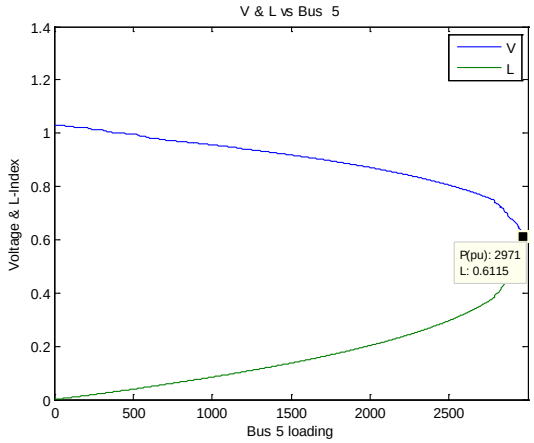

Fig.2 : Bus 5 V & L (WSCC 9-bus system)

This result matched previous studies using the VCPI [10] with the collapse point for Bus 5 occurring at 2.971pu (371+j149MVA).

Next the IEEE 14-bus system was studied. This involved iterations for the ideal case and with *n-1* contingency. The contingencies were selected as line contingences and for transformers the tap settings were varied between 90% and 110% of the nominal tap setting. At each iteration, 100 random loading configurations of between 30% and 200% at each load bus without maintaining pf. Within each of these iterations, a load flow study was run with the single contingency and load configuration. From the load flow, the voltage magnitudes, real and reactive power at each bus and for the whole system were recorded. Also, the L-index was calculated for that configuration. This data was then used to train an ANN with 100 neurons in the hidden layer. Previous studies [11] found bus 14 is the weakest bus in the system. A comparison of the VCPI calculated from the Power Flow and that predicted by the ANN is shown in Table 2

All Values in pu				n-1		
P_{14}	Q_{14}	P_{tot}	Q_{tot}		Method	VCPI
1	1	1	1	0	**Calculated**	0.0279
					ANN	0.0259
0.98	0.71	0.91	0.90	2	**Calculated**	0.0303
					ANN	0.0277
1.15	1.45	0.99	1.11	10	**Calculated**	0.0394
					ANN	0.0263
0.55	0.8	1.04	0.87	18	**Calculated**	0.0466
					ANN	0.0449
1.31	1.44	1.07	1.16	18	**Calculated**	0.0207
					ANN	0.0090

Table 1: VCPI for IEEE 14 bus System

From Table 1, it is clear that as the total system load increases, the VCPI value increases. Similarly, increased loading on bus 14 increases the VCPI value, indicating increased instability. The ANN values also follow the power flow calculated values. Since the VCPI varies from 0-1, the relative error is very minimal.

The same algorithm was then used on the 37-bus Kenyan system. Previous studies [12] identified buses 10,22,30,31 as the weakest buses in the system. The VCPI for the 3 buses using power flow and ANNs are shown in tables 2, 3 and 4.

All Values in pu				n-1		
P_{10}	Q_{10}	P_{tot}	Q_{tot}		Method	VCPI
1	1	1	1	0	**Calculated**	0.007928
					ANN	0.007935
1.04	1.50	0.86	1.08	20	**Calculated**	0.008729
					ANN	0.008658
1.40	1.15	1.02	0.86	20	**Calculated**	0.011047
					ANN	0.011137
0.57	0.53	1.01	1.05	1	**Calculated**	0.004443
					ANN	0.004390
0.71	0.73	0.88	0.91	33	**Calculated**	0.005663
					ANN	0.005570

Table 2: VCPI Values for Kenyan System Bus 10

The VCPI values in Table 2 indicate that in all the randomly selected cases the bus is stable even with the selected single contingencies. The ANN generated values also closely follow the power flow values to a very great extent. A comparison of a contingency on line 20 shows bus 10 stability drops with a relatively small increase in the total system real power loading even when the reactive power demand at the bus is reduced. This reinforces its classification as a weak bus.

All Values in pu				n-1		
P_{30}	Q_{30}	P_{tot}	Q_{tot}		Method	VCPI
1	1	1	1	0	**Calculated**	0.0059142
					ANN	0.0059142
0.76	1.13	0.81	0.97	8	**Calculated**	0.0049734
					ANN	0.0049744
0.95	1.05	1.19	0.94	34	**Calculated**	0.0057342
					ANN	0.005734
0.97	0.80	1.06	0.84	34	**Calculated**	0.005555
					ANN	0.005555
0.90	1.09	1.09	1.18	21	**Calculated**	0.005548
					ANN	0.0055493

Table 3:VCPI Values for Kenyan System Bus 30

From Table 3, a contingency on line 34 with 2 separate values of loading on bus 30 show slight drop in the stability of bus 30 with a similar slight increase in reactive power. This shows it is a weak bus though it doesn't evaluate the maximum reactive power the bus can support without voltage collapse. The VCPI values from the ANN are almost identical to the ones from the power flow.

All Values in pu				n-1		
P_{22}	Q_{22}	P_{tot}	Q_{tot}		Method	VCPI
1	1	1	1	0	**Calculated**	0.112534
					ANN	0.112534
0.00	0.00	1.16	0.94	11	**Calculated**	0.112534
					ANN	0.112534
0.00	0.00	0.99	0.89	11	**Calculated**	0.112534
					ANN	0.112534
0.00	0.00	0.92	0.73	7	**Calculated**	0.112534
					ANN	0.112534
0.00	0.00	1.01	0.91	33	**Calculated**	0.112534
					ANN	0.112534

Table 4: VCPI Values for Kenyan System Bus 22

Table 4 shows the unique case of bus 22 which is a node in the system without a direct load. The VCPI values for both the ANN and the power flow are identical. The stability index doesn't vary with the change in total system demand showing the sensitivity of the VCPI index to the load on a bus. This case is similar to bus 31 which is also a node.

A simulation of the VCPI using the load flow for buses 10 and 30was done with increasing loading till the voltage got to 0.95pu. It showed the VCPI being 0.02292 at 267% loading for bus 10 single loading (Fig. 3) and 0.04975 at 769% loading for bus 30 single loading (Fig. 4). While the loading may seem extreme, the buses are increasingly loaded alone while the rest of the system is maintained at the nominal values without any contingency. This shows the sensitivity of the VCPI index to the voltage magnitude of the buses.

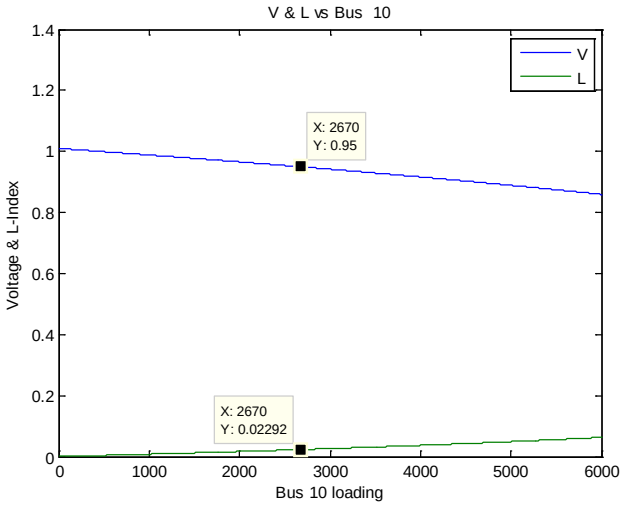

Fig.3: VCPI for Bus 10 Kenyan System

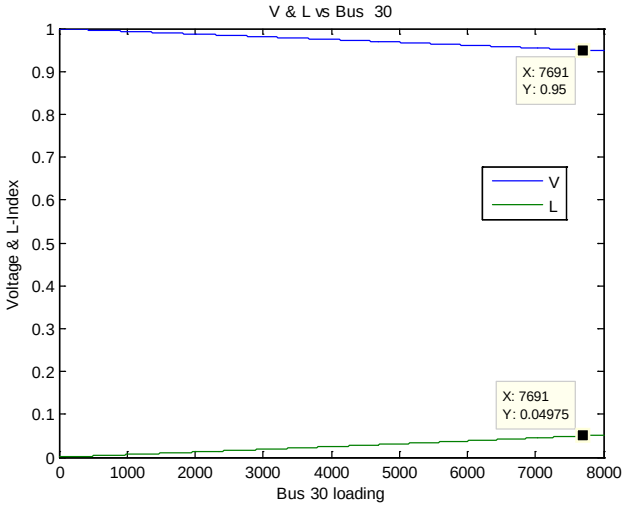

Fig.4: VCPI for Bus 30 Kenyan System

CONCLUSION

From the results, it has been shown that the VCPI index can be used as an accurate measure of voltage stability. The relationship between the VCPI values generated by the ANN and the actual values generated by carrying out load flows shows that ANNs can be trained for a bus which can then give a real time approximation of the stability of the bus using only 4 power measurements that are easy to read using a SCADA system which can lead to an on-line estimation of the stability at all the buses within the system using the VCPI. The VCPI for the weak buses within the Kenya Power system were also evaluated and the ANN values for VCPI found to very accurately track the actual values calculated using the power flow.

A major short coming of the VCPI is that while it may indicate increasing instability, it doesn't indicate the

distance to instability. This is an area that can be studied further.

REFERENCES

[1]P. Kundur , Power System Stability and Control , McGraw-Hill Inc ; 1994

[2]IEEE/PES Power System Stability Subcommittee, Voltage Stability Assessment: Concepts, Practices and Tools, IEEE Catalog IEEE Catalog Number SP101PSS, August 2002.

[3] L. Cai, and I. Erlich, Power System Static Voltage Stability Analysis Considering all Active and Reactive Power Controls - Singular Value Approach, IEEE Power Tech – IEEE Lausanne 5th July 2007

[4] K. Ioannis and O. Konstadinos, An Analytical approach for Dynamic Voltage Stability Analysis in Power Systems, Proceedings of the 5th WSEAS International Conference on Applications of Electrical Engineering, Prague, Czech Republic, March 12-14, 2006 (pp36-38)

[5] B. N. Soni, Bifurcation Analysis for Voltage Stability of Power System, National Conference on Recent Trends in Engineering & Technology, 13-14 May 2011

[6] L. Cai*et al*, Power System Dynamic Voltage Stability Analysis for Integration of Large Scale Wind Parks, 9th International Workshop on Large-Scale Integration of Wind Power into Power Systems as well as on Transmission Networks for Offshore Wind Power Plants, Quebec City, Quebec, Canada, October, 2010

[7] L. Cai, and I. Erlich, Dynamic Voltage Stability Analysis In Multi-Machine Power Systems, IEEE Power Tech – IEEE Lausanne ,5th July 2007

[8]G. M. Haung and N. Kumar, Detection of Dynamic Voltage Collapse, Power Engineering Society Summer Meeting, IEEE 2002, 25th July 2002, ISBN 0-7803-7518-1

[9] Muriithi C. M., Ngoo L. M., Nyakoe G. N.,"Load Flow Analysis with a Neuro-Fuzzy Model of an Induction Motor Load", IEEE AFRICON 2009

[10] I. Kumarswamy*et al*, An Optimal Power Flow (OPF) method with Improved Voltage Stability Analysis, Proceedings of the World Congress on Engineering 2012 Vol II WCE 2012, July 4 - 6, 2012, London, U.K.

[11]G. Balamurugan and P. Aravindhababu, Ann Based Online Estimation of Voltage Collapse Proximity Indicator, International Journal of Engineering Science and TechnologyVol. 2(7), 2010, 2869-2875

[12]C. Muriithi and S. Njoroge, Voltage Stability Analysis Using Cp_ANN and Optimised Capacitor Bank Placement, JKUAT SRI Conference 2010

APPENDIX

Appendix 1 : Kenyan Power System

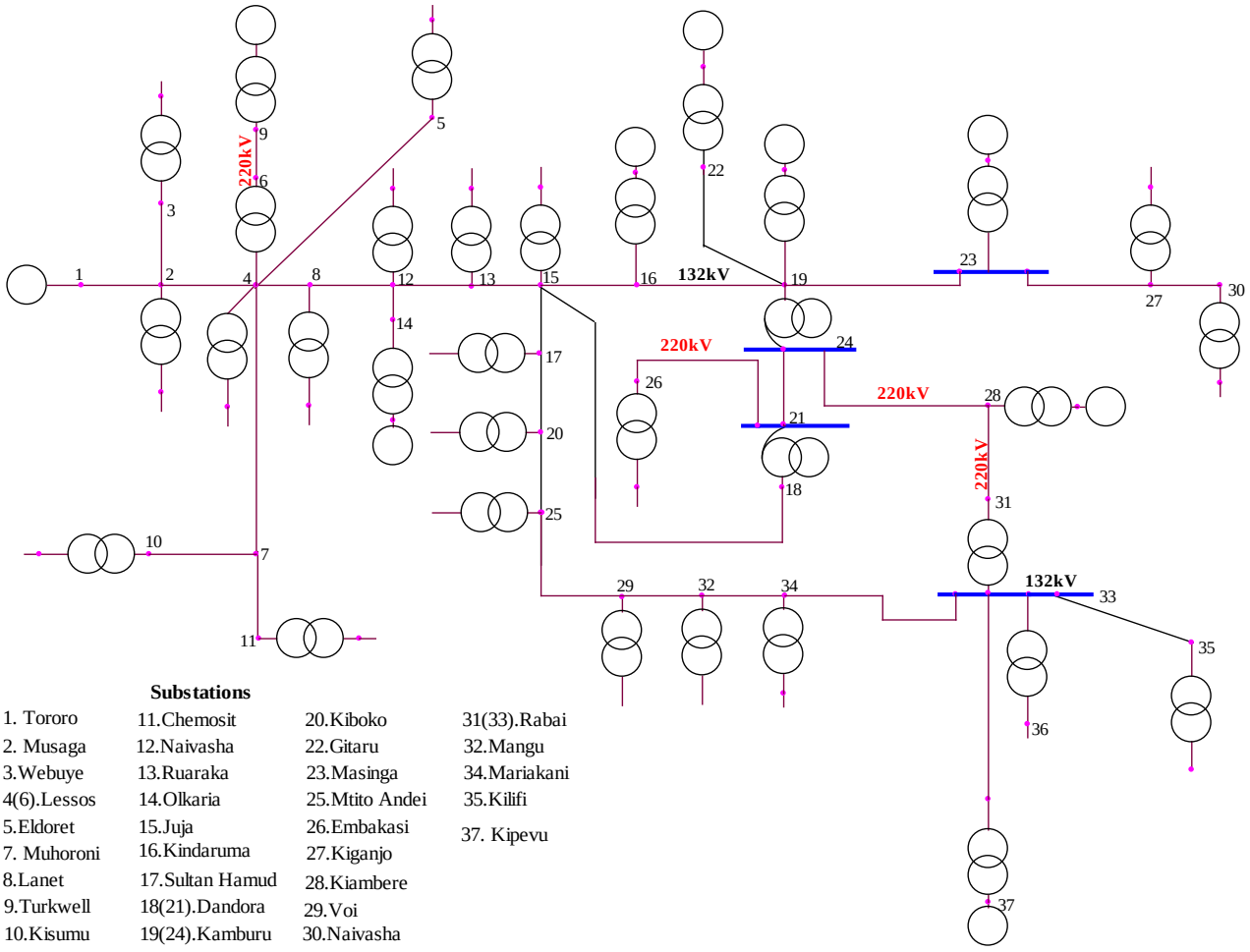

Substations

1. Tororo
2. Musaga
3.Webuye
4(6).Lessos
5.Eldoret
7. Muhoroni
8.Lanet
9.Turkwell
10.Kisumu
11.Chemosit
12.Naivasha
13.Ruaraka
14.Olkaria
15.Juja
16.Kindaruma
17.Sultan Hamud
18(21).Dandora
19(24).Kamburu
20.Kiboko
22.Gitaru
23.Masinga
25.Mtito Andei
26.Embakasi
27.Kiganjo
28.Kiambere
29.Voi
30.Naivasha
31(33).Rabai
32.Mangu
34.Mariakani
35.Kilifi
37. Kipevu

Securing Mobile Computing Applications-Implementing Intrusion Monitoring in Wireless Networks

C. K. Kihuha and E. K. Karari

cyrus.kamau@dkut.ac.ke, *ephantus.knyaujui@dkct.ac.ke*

Abstract: The rapid proliferation of wireless networks and mobile computing applications has changed the landscape of network security. The recent denial of service attacks on major Internet sites have shown us, no open computer network is immune from intrusions. The wireless ad-hoc network is particularly vulnerable due to its features of open medium, dynamic changing topology, cooperative algorithms, lack of centralized monitoring and management point, and lack of a clear line of defense. The traditional way of protecting networks with firewalls and encryption software is no longer sufficient and effective.

Majority of security threats arising from intrusion detection and un authorized access have been have been dealt with by developing solutions on fixed wired networks but they have with time turned not to be useful and inapplicable in this new wireless environments. The need to search for new architecture and mechanisms to protect wireless networks and mobile computing application from security threats cannot be understated.

In this research paper, we examine the vulnerabilities of mobile computing applications in wireless networks and improvise a solution to intrusion detection in the security architecture for mobile computing applications environment.

Keywords: network; security; mobile; vulnerabilities; intrusion; monitoring.